Switched Reluctance Machine Electromagnetic Design and Optimization

A Dissertation
Presented to
The Academic Faculty

by

Jie Dang

In Partial Fulfillment
of the Requirements for the Degree
Doctor of Philosophy in the
School of Electrical and Computer Engineering

Georgia Institute of Technology
August 2015

SWITCHED RELUCTANCE MACHINE ELECTROMAGNETIC DESIGN AND OPTIMIZATION

Approved by:

Dr. Ronald G. Harley, Advisor
School of ECE
Georgia Institute of Technology

Dr. Thomas G. Habetler
School of ECE
Georgia Institute of Technology

Dr. J. Rhett Mayor
School of ME
Georgia Institute of Technology

Dr. David G. Taylor
School of ECE
Georgia Institute of Technology

Dr. Maryam Saeedifard
School of ECE
Georgia Institute of Technology

Date Approved: [June 15th 2015]

To
my dear father, Yongming Dang
and my dear mother, Jue Wang

ACKNOWLEDGEMENTS

It would not have been possible for me to finish this doctoral dissertation without the guidance from my advisor, help from my friends, and support from my family.

First of all, I would like to give my deepest gratitude to my advisor, Dr. Ronald G. Harley. He is the kindest person in the world and the most knowledgeable professor in my life. He is always open-minded to listen to me, patient to advise me, and supportive to encourage me. He has always made himself available to provide insightful discussions about my research despite his busy schedules. He has constantly encouraged me to improve my communication skills and patiently helped me revise my papers. I feel so privileged to be his PhD student, and I cannot imagine having a better advisor and mentor in my life.

I would also like to take this opportunity to express my gratitude to Dr. Thomas G. Habetler and Dr. J.Rhett Mayor. Their invaluable guidance and constant encouragement help me overcome great challenges throughout the course of my research. They have always willing to share their wisdom and experience to me. I would never forget their support and caring. I would also like to thank Dr. Maryam Saeedifard and Dr. David Taylor to serve as my PhD committee members and provide valuable feedback.

I much appreciate Dr. Jose Restrepo for his selfless help in the past five years. He has played a crucial role in the completion of my research work. I have learned so much from his joy and enthusiasm in research. I enjoyed very much the time I worked with him when he visited Georgia Tech.

Dr. Saeid Haghbin is another important person I would like to thank. He has provided me much valuable guidance in the early stage of my PhD study. The work in this dissertation is much credited to their help.

I owe a great debt of gratitude to my labmate, Yi Du, a talented, reliable, and selfless mentor throughout my PhD study. I have enjoyed much from the discussions with him, and I have learned much from his experience and rich knowledge. I treasure the brotherhood between us throughout these years.

My time at Georgia Tech is unforgettable thanks to the many friends that have became a part of my life. I would give my deep thanks to some senior labmates, Siwei Cheng, Yao Duan, Andrew Semidey, Jiaqi Liang, Jing Dai, Bin Lu, Dustin Howard, Diogenes Molina, Stefan Grubic, Andrew Paquette, and John Seuss. Without their generous help, the completion of this dissertation would never have been possible. I would like to express my special thanks to Kevin Pham and James Steinberg for their help in my experimental work. I would ackowlodge Jill Auerbach and Julie Ridings for the happy memories in my participation of the ORS program. I also appreciate the help from Dr. Miroslac Begovic, Dr. Deepak Divan, Dr. A.P. Meliopoulos, and Dr. Santiago Grijalva. I will never forget them.

My gratitude is also given to other labemates, Sufei Li, Dawei He, Lijun He, Yi Deng, Nan Liu, Chen Jiang, Shen Zhang, Morteza Rezaee, Renke Huang, and Dongbo Zhao, who have helped me and provided collaborative efforts in the past few years. The lab has been a source of friendships, love and support. I feel grateful and wish them all the best.

I would acknowledge my supervisors, Mr. Rihong Mo at Ford Motor and Mr. Wayne Pon at ExxonMobil during my internships in 2013 and 2014.

There are numerous names of faculty, family, and friends that I should mention here. But most of all, I owe my greatest debt of gratitude to my parents, my dear Mom and Dad, who have stood by me through the good times and bad.

The financial supports from the National Science Foundation are gratefully acknowledged.

TABLE OF CONTENTS

Page

LIST OF TABLES

Page

LIST OF FIGURES

Page

LIST OF SYMBOLS AND ABBREVIATIONS

Abbreviation:

SRM	Switched reluctance machine
FEA	Finite element analysis
EV	Electric vehicle
HEV	Hybrid electric vehicle
IM	Induction machine
PM	Permanent magnet
PMSM	Permanent magnet synchronous machine
SynRM	Synchronous reluctance machine
FSM	Flux switched machine
IPMSM	Interior permanent magnet synchronous machine

Symbol:

θ_a	Aligned position
θ_u	Unaligned position
θ_{on}	Turn-on position (angle)
θ_{off}	Turn-on position (angle)
I_P	Peak current
θ_1	The position when the current first reaches I_P
θ_2	The position when the current drops to zero
θ_{1_est}	Estimated θ_1
θ_{off_est}	Estimated θ_{off}
V_{dc}	DC bus voltage
λ	Flux linkage
$\lambda_{I_P}(\theta_i)$	Flux-linkage at angle θ_i with constant current I_P

ω_r	Rotor speed
β_s	Stator pole angle
β_r	Rotor pole angle
b_{sy}	Stator back-iron thickness
b_{sy}	Rotor back-iron thickness
D_s	Stator diameter
D_r	Rotor diameter
D_{sh}	Shaft diameter
L	Stack length
N_{ph}	Number of turns for the coil winding per phase
l_g	Air-gap length
H_g	Magnetic field in the air-gap
B_m	Saturated flux density of the core material
μ_0	Magnetic constant
R_g	Flux path reluctance in the air-gap
R_s	Flux path reluctance in the stator pole
R_r	Flux path reluctance in the rotor pole
R_y	Flux path reluctance in the back iron
J_c	Current density
A_s	Stator coil area
Ff	Coil winding fill factor

SUMMARY

The objective of this dissertation is to study the switched reluctance machine (SRM) electromagnetic design and optimization. The research of electric machines is mostly driven by the motivation for higher efficiency and lower cost. The demands for high-performance electric machines also come from the development of emerging industries, such as electric vehicles (EV), hybrid electric vehicles (HEV), renewable energy conversion, energy storage and precision manufacturing. The additional requirements for those applications include volume, weight, speed, torque, reliability, fault tolerance capability, etc. The focus of the research effort is on the high speed and high torque applications, where the SRM stands out compared to other types of machines. The conventional design method significantly depends on the designer's experience, which uses equivalent magnetic circuit models, and therefore the SRM design is not well developed.

A novel SRM electromagnetic design and optimization method is developed, which uses the current-fed FEA simulation as the SRM performance estimation tool. This method serves as the main innovation of this research work. First, the proposed method is applicable to any SRM topologies and dimension, and no detailed modeling of a specific SRM configuration is required in advance. Therefore, an automated SRM design and optimization approach is developed. Secondly, great accuracy of the SRM electromagnetic analysis, e.g. flux density, torque, and current calculation, is achieved by using FEA simulation instead of simplified magnetic circuit approximations. This contribution is particularly significant when considering the poor accuracy of

conventional SRM analytical analysis methods, where several assumptions and approximations are used. Lastly, the proposed design method takes the typical SRM control strategy into account, where the excitation current profile is characterized as a trapezoid. This method adapts the flux linkage of the first FEA simulation result to specify the excitation current profile for the second FEA simulation, so the calculated SRM performance in FEA simulation agrees with the measurement on a practical machine.

The proposed SRM design and optimization method is used for a 12/8 SRM rotor design and for a complete 4/2 SRM design. These design examples validate the applicability of the proposed method to different SRM configurations and dimensions. Detailed design steps are presented for both design cases, and the selection of the parametric design variables are also discussed. The optimization results are demonstrated using multi-dimension diagrams, where the optimal design with the highest torque can be easily identified. The FEA simulation results are compared to the experimental results of a fabricated SRM prototype, and good agreement is found.

In addition, a new rotor configuration with a flux bridge is proposed for an ultra high speed SRM design. The primary motivation of this rotor topology is to reduce the windgae losses and the acoustic noise at a high speed of 50,000 rpm. However, care must be taken for the flux bridge design, and the impact of different flux bridge thicknesses to the SRM performance is studied. Meanwhile, the manufacturing difficulties and the mechanical stresses should also be considered when fabricating the flux-bridge rotor. As a result, two SRM prototypes are built, and the two rotors are one without a flux bridge and one with a flux bridge. The prototypes are tested at different speeds (10,000 rpm,

20,000 rpm and 50,000 rpm) respectively, and the experimental results show good agreement with the FEA simulation results.

CHAPTER 1 INTRODUCTION

1.1 Background

1.1.1 Electric machine applications

Electric machines are the primary energy conversion devices and consume about 85% of the electrical energy in the world [52]. The research of electric machines is mostly driven by the motivation for higher efficiency and lower cost. Higher efficiency brings benefits such as the reduction of the fossil fuel consumption and greenhouse gas emission. Lower cost makes electric machines more attractive in the extensive electrification advances in the automotive, transport and aerospace industries. The demands for high-performance electric machines also come from the development of emerging industries, such as electric vehicles (EV), hybrid electric vehicles (HEV), renewable energy conversion, energy storage and precision manufacturing. The additional requirements for those applications include volume, weight, speed, torque, reliability, and fault tolerance capability.

1.1.2 High speed machine applications

The interest in ultra high speed machines comes mostly from the spindle and drilling industry, including micro-machinery spindles, printed circuit board drillings, and dental drilling tools. In addition, emerging applications will in future be found in turbo compressor systems for fuel cells and heat pumps, generators/starters for portable gas turbines, electric-assisted turbochargers for car engines, and flywheel energy storage systems.

Sophisticated and precision manufacturing has attracted growing interest in mechanical engineering in recent years. Its considerable applications are found in biology, medical, material, aerospace and defense industries. Smaller and higher speed drilling, milling, and grinding tools are highly desired to fabricate high-precision

instruments [1]. For example, notch grinding of silicon wafers requires a spindle tool of up to 150,000 rpm [2].

With the advance of mobile devices, such as smart phones and tablets, tremendous demands are from the electronics industry for reduced size electronic packages. To achieve that, multiple layers (up to 12 layers) are used for the printed circuit board (PCB) designs. Between the layers, through-hole vias or more recently micro-vias are employed for the circuit connections. Nowadays, micro-vias with diameters of 75 μm are available economically with mechanical PCB drills (spindles), where a motor with speeds of up to 250,000 rpm is used [3]. The intensive competition of this industry is leading great efforts to look for drilling technology with the capability of making holes with diameters of 25 μm, or even 10 μm [4]. However, only laser drilling is possible for small hole diameters at the present stage, but it requires massive capital investment. Therefore, cheaper mechanical drilling is intuitively a better choice. As a result, increased drilling speeds are highly desired. Particularly, for holes with diameters of 10 μm, drilling tools with speeds over 1 million rpm are required [4].

A further potential application comes from the dental industry. Today, most dental drills use compressed air to drive air turbines to spin the drilling tip. The drawback of a compressed air drive is that the dental drills can only be operated at a single speed point, and there is not much control flexibility. The performance limitations include no accurate speed control, no adjustable speed capability, and no possibility for torque control. Therefore, speed-adjustable electrical drives are ideal to overcome these drawbacks, and to provide the dentist with much greater convenience. The currently available electrical dental drills are operated at speeds up to 40,000 rpm, and then a triple-gear system is used to step the speed up to a maximum of 200,000 rpm [5]. A direct drive system is highly desirable due to the incremental cost and the complexity of the step-up gears. To compete with the traditional compressed air drives, the specifications of an electrical drive would

be set at speeds of up to 400,000 rpm with power ranges between 10 and 20 W. Careful ergonomic considerations must be taken into account for such a drill design. Size requirements have to be satisfied to ensure the dentist hand operation custom and the patient's comfort when inserting the drill into his/her mouth.

In addition, the development of fuel cells for automotive applications has created great opportunity for high speed electrical drives. The operation of fuel cells, for example hydrogen-based fuel cells, requires a constant supply of pressurized air that is provided by an air compressor system. The employment of high speed electrical drives in those air compressors can provide good performance for the fuel cells. The benefits of increased speeds mostly come from the reduction of size. For example, a 120,000 rpm 12 kW air compressor is reported in [6].

Again in the automotive industry, turbochargers are another important technology progress in recent years. With the help of turbochargers, internal combustion engines can achieve better fuel economy and reduced emission. Turbochargers do not perform well at low speeds, and a turbo lag or a delay in the air boost exists. Therefore, electrically assisted turbochargers are under investigation, to improve the pressure boost at low speeds [7]. Particularly, an electrical machine is mounted on the same shaft between the turbine and the compressor, and to provide at least 1.5 kW to influence the acceleration performance of the vehicle [8]. So the electrical drive has to operate at the same rotational speeds of the turbocharger (up to 200,000 rpm), as well as in a harsh environment (high temperature). A commercial eBooster that has been developed by BorgWarner for the use with its turbochargers is reported in [9]. The operating speed is 86,000 rpm with a power of 720 W.

Moreover, the recent advance of wearable devices has called on portable, low-power gas-turbine-based power generation units. The electrical drive systems are mostly used for the chargers, and the increased speeds can significantly reduce the size. The power

level of such drives is around 100 W. At this power level, the ideal volume of the gas turbine system can be achieved if increasing the rotational speeds to over 500,000 rpm [10].

Furthermore, in the energy storage filed, flywheels are becoming a promising option and great research has been carried out in this area. Specifically, a motor/generator is needed in the flywheel system to store or extract electrical energy [11]. For applications in aerospace and transportation industries, high-speed flywheel systems have great significance. In particular, National Aeronautics and Space Administration (NASA) has performed a research project to study a 40,000 rpm 3 kW flywheel energy storage system, for satellites and the international space station applications. The stringent requirements on the weight and volume specifications have brought up great challenges for the electrical drive system. However opportunities still exist considering the operations in harsh environment, especially when comparing the electrical drives to other mechanical or hydraulic drives [12].

1.1.3 Electric machine design technology development

Given the great potential of ultra high speed machine applications, over the past 30 years, the research of electric machine and drives has made significant progress in areas of power electronics devices and excitation control. However, the conventional machine design processes evolve slowly and iterate through electromagnetic design by expert designers considering the traditional machine design equations with heuristics-driven estimation of either the specific electric loading, or the limiting current density in the stator windings, and subsequent thermo-mechanical validation.

The traditional machine design method gives the power output equation of (1.1) [13]:

$$S = C \cdot D_r^2 \cdot L \cdot \omega \tag{1.1}$$

where the power S available from an electrical machine can be written as where D_r is the rotor diameter, L the active length, and ω the rotational speed (in Hz or rpm, depending on the definition of C). Esson's utilization factor C depends on the machine type and other variables such as the cooling system and size of the machine [14], [15]. In this way, the active volume of the machine can be estimated for a given power and speed. The volume of a machine decreases with increasing speed, which leads to very small volume for ultrahigh speeds. Furthermore, for a given speed, the diameter of a rotor is limited by the maximum allowable mechanical stresses. Therefore, given a maximum length to diameter ratio, a relationship between the speed and the maximum available power can be derived. Scaling a machine with a constant power rating and efficiency, and therefore constant losses, to higher speeds leads to increased losses per surface area, since the size of the machine decreases. This leads to lower utilization factors and the need for more sophisticated thermal management for ultra high speed machines. In summary, for a given speed, there is a power limit depending on the machine design, materials used, rotor dynamics, and thermal constraints.

1.1.4 Ultra high speed electric machine design aspects

The design of ultra high speed machines is different from the regular speed electric machine design. The specific challenges include the mechanical design of the rotor, the lamination material selection, the power electronics design for the high frequency operation, and the type of bearings attached to the machine, as shown in Fig 1.1

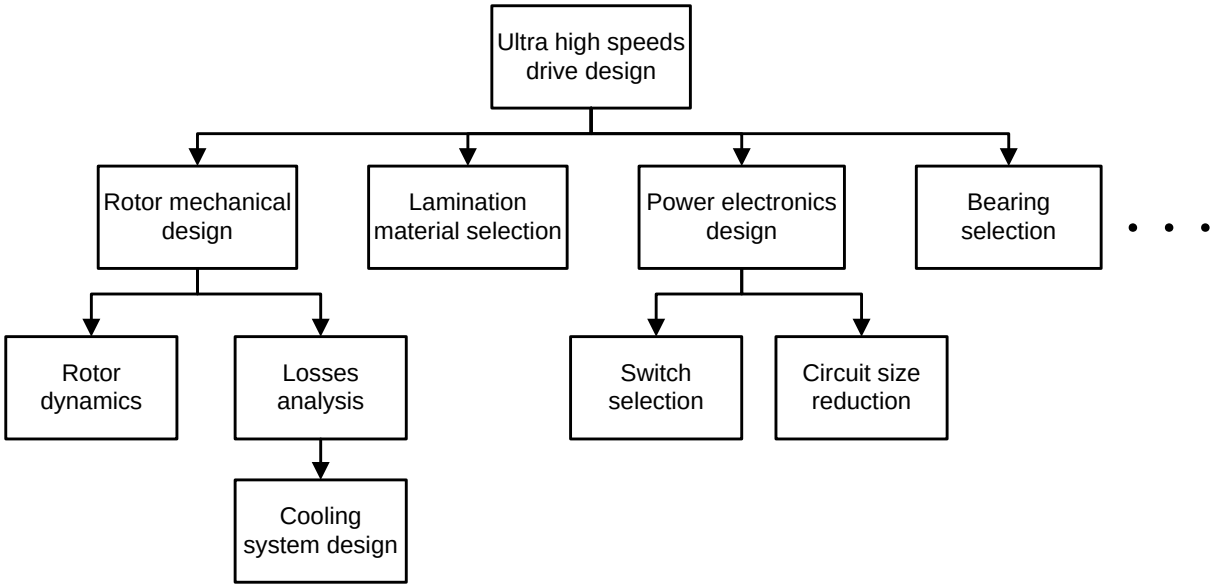

Fig 1.1 Ultra high speed machine design aspects

The rotor design usually requires strong interdisciplinary collaboration between mechanical engineers and electrical engineers. In many cases, the mechanical considerations are prior to the electromagnetic design. Particularly, the major mechanical concerns are the rotor construction design and the high frequency losses management.

First, for the rotor construction design, rotor dynamics and stress analysis studies need to be performed by mechanical engineers. In general, the first two rotor bending modes, associated two critical speeds, are mainly determined by the bearing stiffness and the mass of the rotor. Lower speed systems are operated below the first critical speed, whereas ultra high speed drives may run overcritical, which is in between those two critical speeds. Care must be taken to select the appropriate bearing system to damp the possible oscillations at the critical speeds, and the rotor should be controlled to accelerate through those critical speeds as fast as possible. Furthermore, the third bending mode is mainly dependent on the rotor geometry and material, which cannot be damped by the bearing system. However, for speeds less than 500,000 rpm, the rotor is usually operated

between the second and third critical speeds [29], so this issue is excluded from further discussion in this dissertation. Besides the bending modes, the stress points of the rotor at high speeds should be examined per mechanical simulations, and then be checked against the material specifications. Furthermore, manufacturing accuracy and tolerance margin should be provided before constructing the rotor.

On the other hand, with respect to the rotor losses, the copper loss, the core loss, the friction loss and the windage loss are the main loss components. The copper loss, which includs the skin effect, can be reduced by the adopting of Litz wire. The core loss can be analytically estimated by Steinmetz equations [13], and can also be calculated by electromagnetic simulations. Particularly, in the electromagnetic simulation, the weak points with high flux density can be observed in a straightforward way. Air friction loss is an important part of the total losses in an ultra high speed machine as they roughly scale proportional to the surface area and by the third power of the surface speed. For simple geometries, such as cylinders and disks, air friction loss can be calculated analytically with friction coefficients based on empirical data [14].

Given the specific losses analysis, appropriate cooling systems should be adopted depending on the applications to achieve effective thermal management. For example, in a turbo compressor system, there is additional cooling of the rotor and casing due to the air passing through the impeller and inlet. In contrast, in a gas turbine, there is a heat source in the rotor and housing due to the close proximity to the turbine. A machining spindle running on static air bearings has forced air cooling of the rotor due to the static air flow [29]. Furthermore, for a given power, the scaling of a machine to higher speeds leads to a lower volume due to the lower torque demand, which leads to a smaller cooling surface. Therefore, for higher speeds, an improved cooling concept has to be implemented or the machine efficiency has to be increased.

In the meantime, the selection of the lamination material is highly important in the rotor mechanical design, where the material stress and thermal specifications are frequently checked against. However, the final decision may be influenced by factors like cost and machining process difficulty. In reference [16], a comparison of different lamination materials is carried out for the efficiency improvements. As a result, within a small loading and speed variation range, the first test machine which used amorphous iron core material, was found to have the highest efficiency of 95.6%. It was followed by a machine made with high silicon steel, which had an efficiency of 95.1%. For the conventional low-loss silicon steel, the maximum efficiency was 89%. However, from a practical consideration, the relative high cost of amorphous iron is a problem. Thus, high silicon steel is recommended.

Next, for the power electronics design, it has been shown that scaling a machine to higher speeds leads to a smaller volume, which is advantageous in many applications. In order to obtain a small and lightweight total system, the power electronics interface must also be optimized for a low volume and weight. In contrast to electrical machines, the size of the power electronics mainly scales with power ratings and it can be minimized by choosing a proper inverter topology and the use of high switching frequencies. Reference [17] studies the converter topologies in terms of the number of semiconductor devices, size of passive components, control complexity, and ease of implementation of sensorless control. Particularly, in order to drive the machine with a pulse width modulation (PWM) inverter, a very high switching frequency (at least ten times higher than the fundamental frequency of the machine) is needed. However, the high control dynamics that can be achieved with a PWM inverter are not required for the majority of high speed applications, so the adoption of high switching frequency is not necessarily required.

Finally, for ultra high speed operation, the selection of a suitable bearing is a key issue. The possible candidates include ball bearings, air bearings, and magnetic bearings, and they are discussed respectively as following.

Ball bearings are the most common choice, and they are available for speeds up to 500,000 rpm [13]. The main advantages of ball bearings are the robustness and small size. The main disadvantages are the limited operating temperature and a lifetime dependency on lubrication, load, and speed.

Air bearings work with the principle of levitating the rotor with air pressure, either generated with an external supply (static) or by spinning the rotor (dynamic and foil). They all demonstrate low friction loss and a long lifetime, but they add to the complexity of system integration.

Magnetic bearings levitate the rotor using magnetic forces and have similar advantages as air bearings [18], [19]. However, active magnetic bearings require sensors, actuators, and control, which results in high complexity and increased bearing volume.

Besides the aforementioned types, a compromised alternative is using hybrid bearings, which can incorporate the advantages and eliminate the drawbacks of different bearing types. For example, a combined aerodynamic and magnetic bearing [18] can eliminate the wear of the air bearing at start and stop and provide a control and stabilization possibility, whereas the air bearing can take the main load.

1.1.5 Electric machine type comparison

After understanding the general idea of electric machine design for ultra high speed applications, the respective characteristics of different machine types are outlined in the following. Induction machines (IM) and permanent magnet (PM) machines are the two types of electric machines which are most widely used and available in the market. However, the switched reluctance machine (SRM) stands out in recent years due to its

advantages such as robust rotor and reliable performance. A picture of a regular 4/2 SRM is shown in Fig 1.2, which has 4 stator poles and 2 rotor poles. The rotor structure is extremely simple. There are no magnets or windings on the rotor, and it is simply made of a stack of steel laminations.

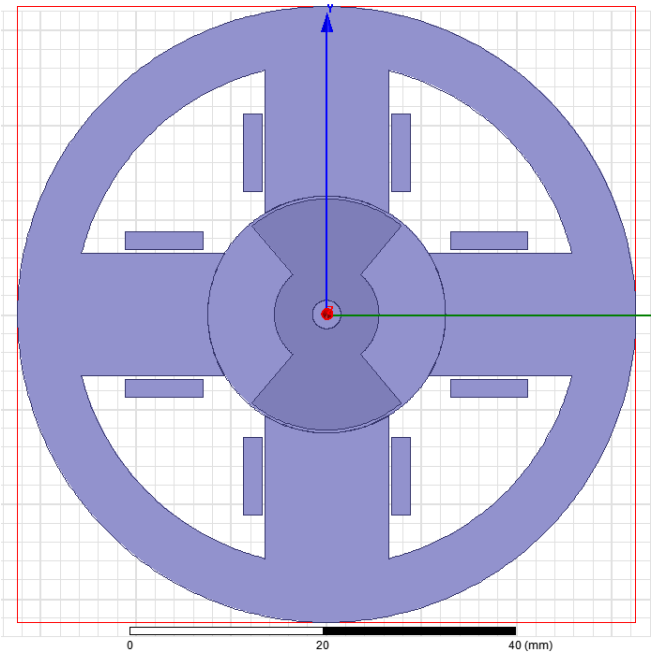

Fig 1.2 Cross section view of a regular 4/2 SRM

The rotor is aligned whenever diametrically opposite stator poles are excited. In a magnetic circuit, the rotating member prefers to come to the minimum reluctance position at the instant of excitation. While two rotor poles are aligned to the two stator poles, another set of rotor poles is out of alignment with respect to a different set of stator poles. Then, this second set of stator poles is excited to bring the rotor poles into alignment. Likewise, by sequentially switching the currents into the stator windings, the rotor is rotated. The movement of the rotor, hence the production of torque and power, involves switching of currents into stator windings when there is a variation of reluctance. Therefore, this type of machine is referred to as switched reluctance machine.

Particularly, a typical drive circuit for a 4/2 SRM is shown in Fig 1.3. An asymmetric bridge converter is used, which has two switches and two freewheeling diodes for each

phase. Turning on transistors T1 and T2 circulate a current in Phase A of the SRM. When they are turned off, the energy stored in the motor winding of Phase A keeps the current in the same direction until it is depleted. Hence, diodes D1 and D2 become forward biased leading to recharging of the source.

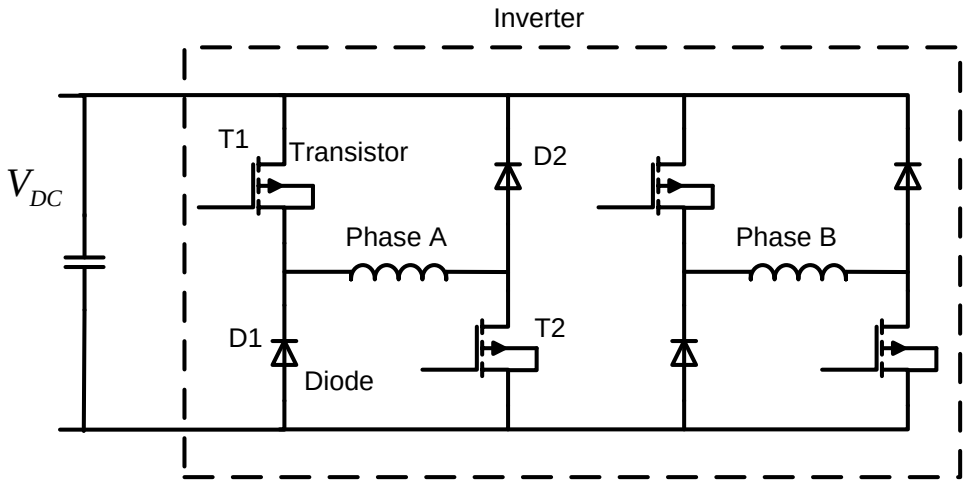

Fig 1.3 Typical drive circuit for a 4/2 SRM

The SRM torque production is illustrated in Fig 1.4 showing a relationship of different rotor positions and stator coil current values. Degree 0 and 180 indicate two aligned positions for phase B, and degree 90 indicates the aligned position for phase A. DC current from 0 A to 5 A is applied to the phase A windings. When the rotor pole approaches the aligned position with respect to the phase A stator poles (from 0 ºto 90 º), positive torque is generated, and the torque increases with the current. Otherwise, when the rotor pole leaves the aligned position with respect to phase A (from 90 º to 180 º), negative torque is generated.

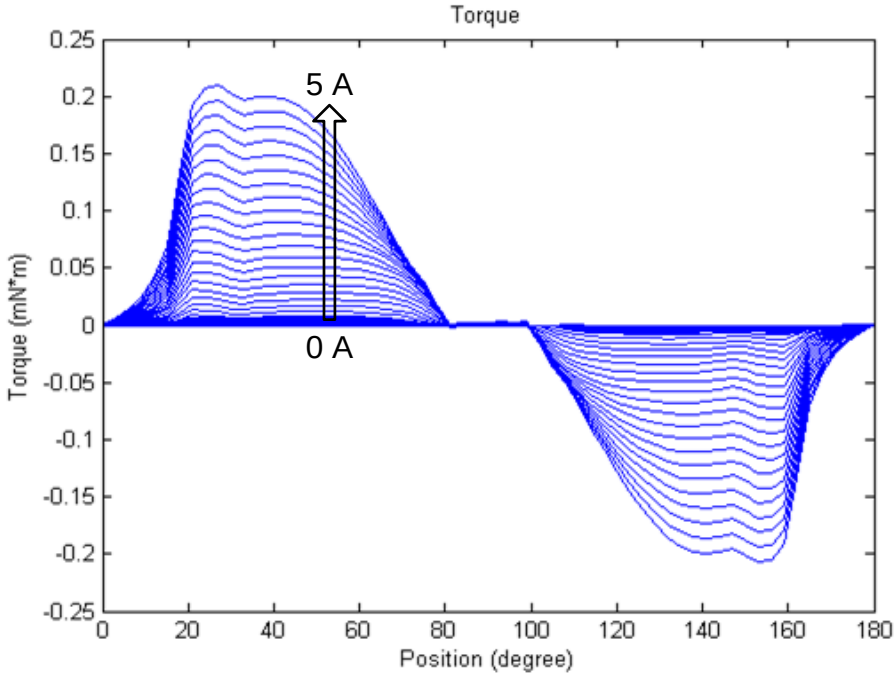

Fig 1.4 SRM torque vs. rotor position vs. current relationship

In general, the common perception is that SRM efficiency is rather low, especially compared with PM machines; hence, they are usually considered as low cost and low performance motors. However, in the recent decade, SRM efficiency has improved to a level that is comparable to the PM motor when the magnetic steel, machine design, and control method issues are addressed. Therefore, efficiency improvement is the key concern for the promotion of the SRM applications. Besides the efficiency deficit, the most well-known drawbacks with SRMs are high torque ripple and high acoustic noise.

The specific comparison between different machine types for high speed applications are presented in Chapter 2. However, in general, the issues of PM machine compared to SRM include:

1). Mechanical locking of magnets at high speeds;

2). Temperature rise and magnet property decay with high temperature;

3). Voltage runaway problem during speed reduction from high speed due to the field retention by the magnets [20];

4). High current for the flux weakening operation at high speed [21].

On the other hand, the problems of the IM compared to the SRM are:

1). Inability of the SRM to run when one phase is out of order (fault tolerant capacity or reliability);

2). Shoot through problem of drives (SRM uses H-bridge inverter);

3). Common mode voltage and bearing current and bearing failure (SRM runs by DC switched supply);

4). Fixed torque vs. speed characteristics (SRM can achieve speed and torque independent control, so high torque at low speed is achievable) [20].

5). Higher rotor losses (difficult to dissipate the heat) [21].

As a result, the SRM offers an alternative option in areas which have been dominated by the PM and IMs in the past, especially for harsh environment operations and high reliability requirements. However, not enough attention has been paid to the SRM study compared to the well developed research in IM and PM machines. Therefore, the design and optimization of a high speed SRM are studied in this dissertation.

1.2 Problem statement

The SRM design task can be broken down into electromagnetic, thermal, and mechanical aspects, so it is an interdisciplinary subject. However, the studied SRM design framework in this work aims to identify an optimal parametric electromagnetic design; a parameter set that defines active components of the machine design. The thermo-mechanical analysis of the identified optimal machine and the rapid identification from the entirety of the design domain using computational intelligence driven by numerical optimization techniques should still be anticipated and are not the focus of the

research effort. Rather, the research effort pursues the automatic and rapid SRM design approach with roots in electromagnetic fundamentals and takes the SRM control into the design considerations. Furthermore, close-loop control for high speed operations is also investigated. The proposed SRM design method and control scheme are tested on a fabricated SRM prototype, with the experimental results presented at the end of this dissertation.

1.3 Dissertation outline

This dissertation is organized as follows: the literature survey of the SRM design and optimization is presented in Chapter 2, with the focus on the high speed application; next a new SRM design method using current-fed FEA simulation is proposed in Chapter 3; and then the new method is applied to a high speed SRM design in Chapter 4; after that, a novel rotor design with a flux bridge for the high speed SRM is investigated in Chapter 5; then, the control scheme for the high speed SRM operation is studied and presented in Chapter 6, as well as the experimental results of a fabricated SRM prototype; thereafter, the proposed SRM design method is applied to a high torque application, considering the overlap of excitation current in Chapter 7; finally, the conclusions and contributions are presented in Chapter 8.

CHAPTER 2 LITERATURE SURVEY

2. 1 High speed machine research overview

High speed SRM research is the major objective of this work. Ultra high speed motor drives offer some interesting features like lower size, higher power density, and higher efficiency [21]. However, increased speed has some adverse impacts such as excessive core loss due to higher excitation frequency [22-25], more complicated bearings, increased motor windage loss, and more mechanical stress on the rotor due to the high centrifugal forces.

The progress of high speed machines is summarized in Fig 2.1, where the horizontal axis denotes the speed and the vertical axis denotes the power. The solid line in the graph indicates the output power limit as a function of rotational speeds in the available technology of 1995 [26]. However, this line has shifted toward the left since then. The rotor peripheral speed is a function of rotor rpm and rotor diameter, and values in the range of 100−250 m/s are classified as high speed [14].

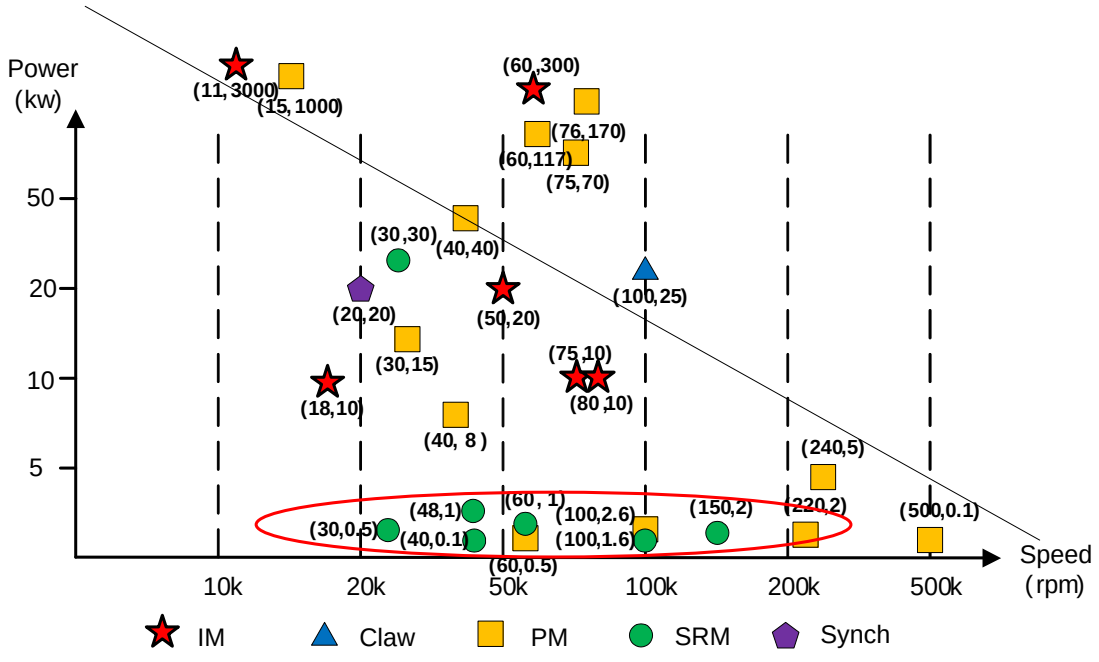

Fig 2.1 High speed machine examples in the literature [27]

In the ultra high speed area, induction machines (IMs), permanent magnet (PM) motors, and SRMs are dominant options. For low power but at a speed range of more than 500,000 rpm PM motors seem to be the only choice [13]. The study of high speed PM machines focuses on a rotor sleeve, which is used to contain the magnets [28]. However, at high speeds, the mechanical locking of magnets as well as the high current required for the flux weakening are the major issues for PM machines.

The red circle in Fig 2.1 indicates that SRMs are competitive with PM machines in the high speed low power region. The highest speed reported for a SRM is 200,000 rpm presented in [18, 19] in a university research application. Nevertheless, an SRM designed for a speed of 750, 000 rpm is reported in [29].

A number of research groups are investigating different application areas for high-speed electrical machines and drive systems. The most challenging aspects of this research occur when the operating speed is above 100,000 rpm. Various gas turbine and compressors systems are reported in [30]. The design target is for 240,000 rpm at a power level of 5 kW. Currently, this machine is operating at 180,000 rpm at no load. A fuel cell air compressor operating at 120,000 rpm and 12 kW is reported [6]. A 1 kW generator operating at 452,000 rpm is reported in [3] as the world's fastest PM brushless dc (BLDC) motor/generator in production. At the lower power level, MIT is developing portable power gas turbines on a microscale [32]; the target speed for their electric generator is 1.2 million rpm, while they have presently achieved 15,000 rpm. A micro fabricated axial-flux permanent magnet (PM) generator is reported in [33]; this generator is fabricated using a combination of micro fabrication and precision machining. At a rotational speed of 120,000 rpm, the generator produces 2.5 W of electrical power [34]. For dental hand pieces, a design target of 150,000 rpm at a power level of 10 W is reported in [35]. In the application area of machining tools, a design target of 150,000 rpm, 5 kW is reported [1]. The achieved speed is 100,000 rpm at no load and 60,000 rpm

under load. Commercially available products from company ATE obtain speeds of around 200,000 rpm at power levels between 200 and 900 W [36]. Application areas for these machines include grinding and PCB drilling. For electrically assisted turbochargers, the target speed for the electric drive is 120,000 rpm at a power level of 7.5 kW. In the area of energy storage and attitude controlled flywheels for aerospace applications, the only reported system above 100,000 rpm is that in [12]; the design target is 300,000 rpm at a power level of 100 W; but only 32,000 rpm has been currently achieved in a test run.

In summary, commercial drives are readily available at speeds below 100,000 rpm. Above 100,000 rpm and less than 250,000 rpm special industrial drives are available. Above 500,000 rpm, there are only a handful of pure research projects being undertaken, although there have not been conclusive results. A 500,000 rpm 100 W electrical drive is reported in [17] and [38], and recently, a 500,000 rpm 1 kW drive system and a 1 million rpm 100 W drive system are realized.

Particularly, the high speed SRM research focuses on the improvement of the rotor. The principle of operation of a SRM requires a certain amount of magnetic saliency of its rotor poles. However, this salient pole shape may cause great windage loss, noise, and vibrations at high speeds unless covered by a smooth sleeve. A cylindrical rotor is proposed in [39] as shown in Fig 2.2, and it is magnetically identical to a conventional rotor because the ribs are magnetically saturated when they are aligned with the stator poles.

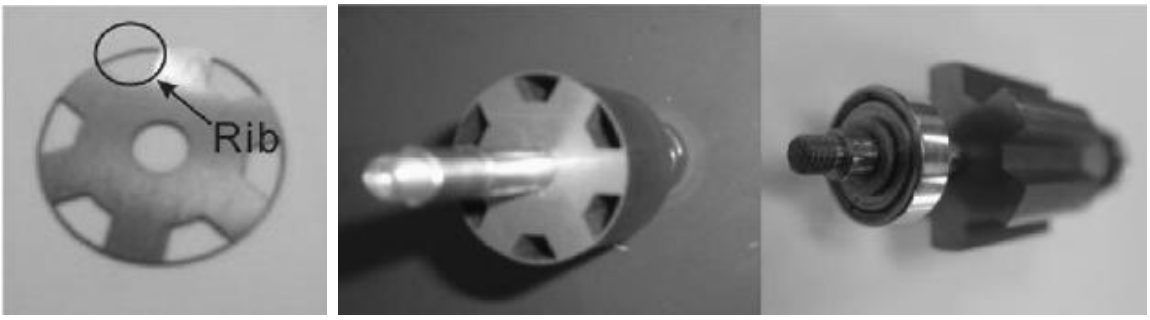

Fig. 2.2 High speed SRM with a rib on the rotor [39]

Using this rotor, the windage loss can be reduced significantly at high speeds as shown in Fig 2.3. At 40,000 rpm, the total power consumption is reduced from 118 W for the regular rotor to 78 W for the cylindrical rotor by 33.9%.

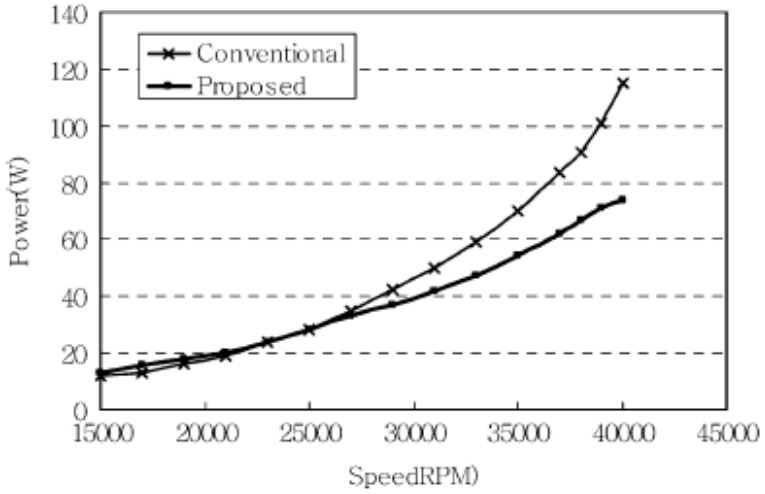

Fig 2.3 Windage loss reduction with the wrapped rotor [39]

Similar cylindrical rotor designs can be found in PM machines and IMs for high speed applications. A picture of a 10 kW 80,000 rpm induction machine rotor is shown in Fig 2.4. For the fabrication of this rotor, traditional die casting cannot be used as melting the alloy would result in the dispersion (and hence mechanical strength) being lost. Therefore the rotor has to be of a fabricated construction, whereby individual bars are machined and

inserted into punched slots inside the lamination stack. The bars are then brazed to the end-rings to create the required electrical short-circuiting connection.

Fig 2.4 Cylindrical rotor design of a high speed induction machine [40]

For the high speed PM machine rotor design, a wrap or sleeve is usually used to contain the PM in the rotor, as shown in Fig 2.5 [41]. An analytical magnetic model is used to investigate the effects of the magnetically permeable sleeve. The electromagnetic behavior of the rotor, particularly the modified BH curve due to the adding of the sleeve is compared with FEA results. In addition, the thermal effects and mechanical strength are also investigated to define a safe operating envelope.

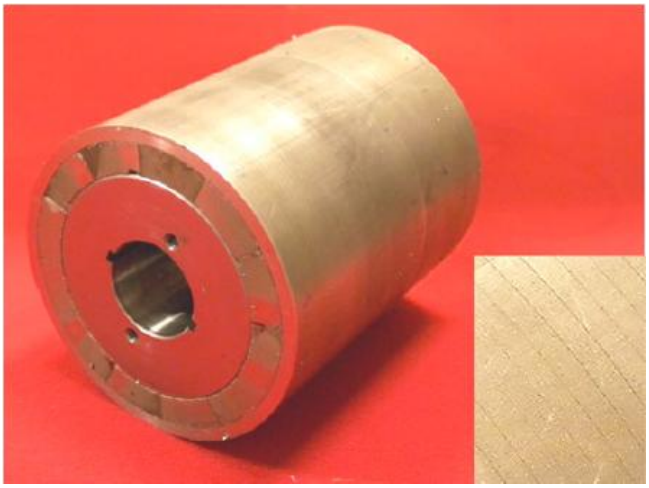

Fig 2.5 Rotor sleeve for a high speed PM machine [41]

Reference [41] reports that the ideal rotor wrap or sleeve should be as thin as possible to be magnetically transparent, but the mechanical stress is the major constrain for this

design due to the high centrifugal force at high speeds. Without a careful design, catastrophic rotor damage can happen at high speeds as shown in Fig 2.6. This rotor failure is a synthesized result of mechanical overstress and thermal overheating.

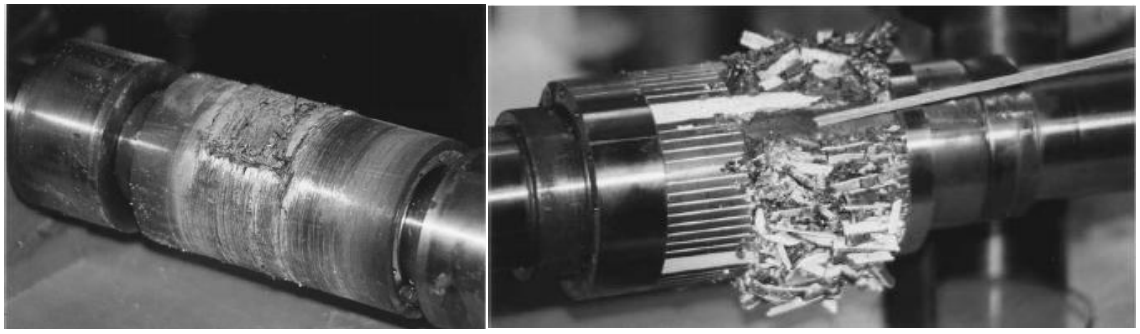

Fig 2.6 Rotor damage due to the mechanical design failure [42]

As a result, different sleeve materials (carbon fiber, copper, copper iron alloy, stainless steel) are compared in [28], where the sleeve eddy current loss, permanent magnet loss, thermal conductivity, and flux permeability are studied. In the conclusion of [28], the total rotor eddy current loss of the carbon fiber sleeve is the smallest. Although the thermal conductivity of the fiber sleeve is poor, the rotor temperature is relatively low. In the case of a copper sleeve, the maximum temperature of all rotor parts is the lowest compared with other material sleeves, due to the high thermal conductivity of the copper sleeve and the low eddy current loss.

Therefore, although it offers some windage loss reduction, the rotor design with a sleeve causes additional eddy current loss in the sleeve. It increases not only the magnetic air-gap length but also the costs of raw materials and the special shrink fitting.

Besides the modification of the rotor design, innovative topologies have also been proposed for the stator design. A lateral stator motor is reported in [43] as shown in Fig 2.7, which pushes the stator to one lateral side. A parametric FE analysis is undertaken in [43] allowing the selection of an ideal machine topology concerning torque and loss characteristics. The optimal design can deliver 8.6 mN-m torque at low speeds and has

only 1.15 W of no-load losses at 200,000 rpm. Compared to a regular PM motor with the same size, the lateral stator machine produces 17 times more torque with the same copper loss of 8 W.

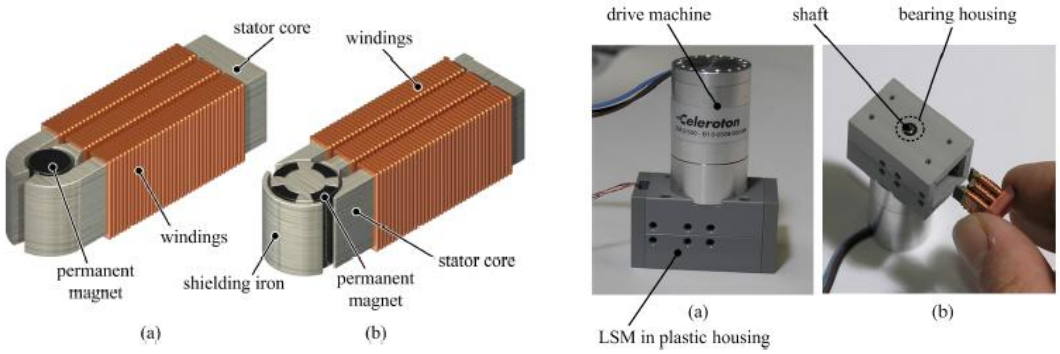

Fig 2.7 Lateral stator design for a high speed PM machine [43]

Research effort has also been made to reduce the winding manufacturing cost. Reference [44] presents an enhanced SRM configuration for low-cost production that possesses high slot space for ease of coil winding (Fig 2.8). For high power applications, such a structure can be easily augmented by stacking more modules together. Finally, a traditional SRM of the same size is simulated and compared with the enhanced SRM; the simulation results show that the enhanced SRM has better characteristics in terms of torque and efficiency, and there is a degree of flexibility in the design of the phase winding since the available slot area for the coils is higher.

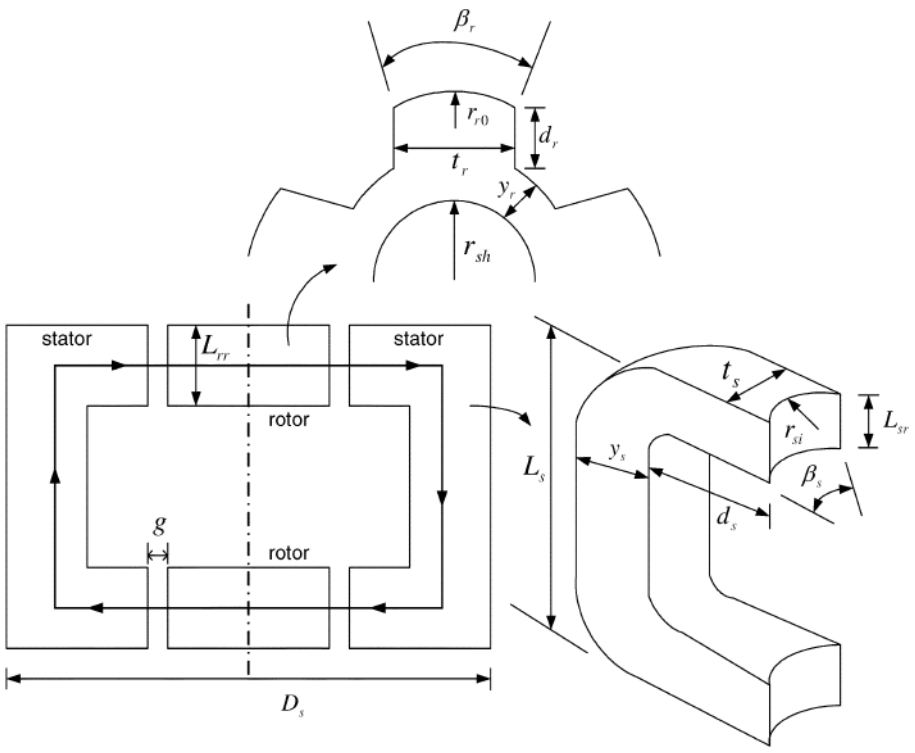

Fig 2.8 A novel SRM configuration for the ease of winding manufacturing [44]

While SRMs have several distinctive advantages in many potential areas of applications, their widespread market acceptance is still limited and slow due to torque ripple, lack of self starting capability and acoustic noise. A SRM design of asymmetric inductance profile with non-uniform air gap is investigated in [45] for the purpose of torque ripple reduction. A rotor pole shaping method is studies in [46] to produce overlapping torque and provide self starting capability. For the acoustic noise issue, many researches and papers show that the main source of the acoustic noise and vibration in the SRM is the abrupt change of the radial magnetic force when the switch is turned off. A design consideration employing the stator and rotor laminations of a single-phase 6/6 SRM with the same skew angle θ for both stator and rotor is presented in [47], as shown in Fig 2.9. In that way, it manages to mitigate acoustic noise and vibration by distributing the radial force widely on the yoke and reducing abrupt changes of the radial force. The

radial magnetic force of the yoke can be dispersed by skewing the rotor and stator and hence the acoustic noise and vibration of the SRM is reduced.

Fig 2.9 A 6/6 SRM prototype with different skew angles (0 º, 30 º, 64 º) [47]

In conclusion, the focus of the high speed machine research is on the rotor structure, and particularly, the rotor sleeve is a common option due to the reduction of the high windage loss. However, the modification of other parts (stator, rotor pole shape and skew angle) can also contribute to the SRM performance improvement, such as torque ripple, self-starting capability and acoustic noise. According to the literature survey in Fig 2.1, the target SRM specification is set as 50,000 rpm and 1 kW. A detail design procedure is presented in Chapter 4 and Chapter 5, where an automatic SRM design and optimization approach is proposed as well as a novel SRM rotor design.

2. 2 The traditional SRM design approach

Given the target specifications, the traditional SRM design methods are summarized first. The constraints and issues of the traditional methods are presented in this section. Particularly, only the electromagnetic design is discussed.

The conventional SRM design procedures are summarized in Fig 2.10 [48-51].

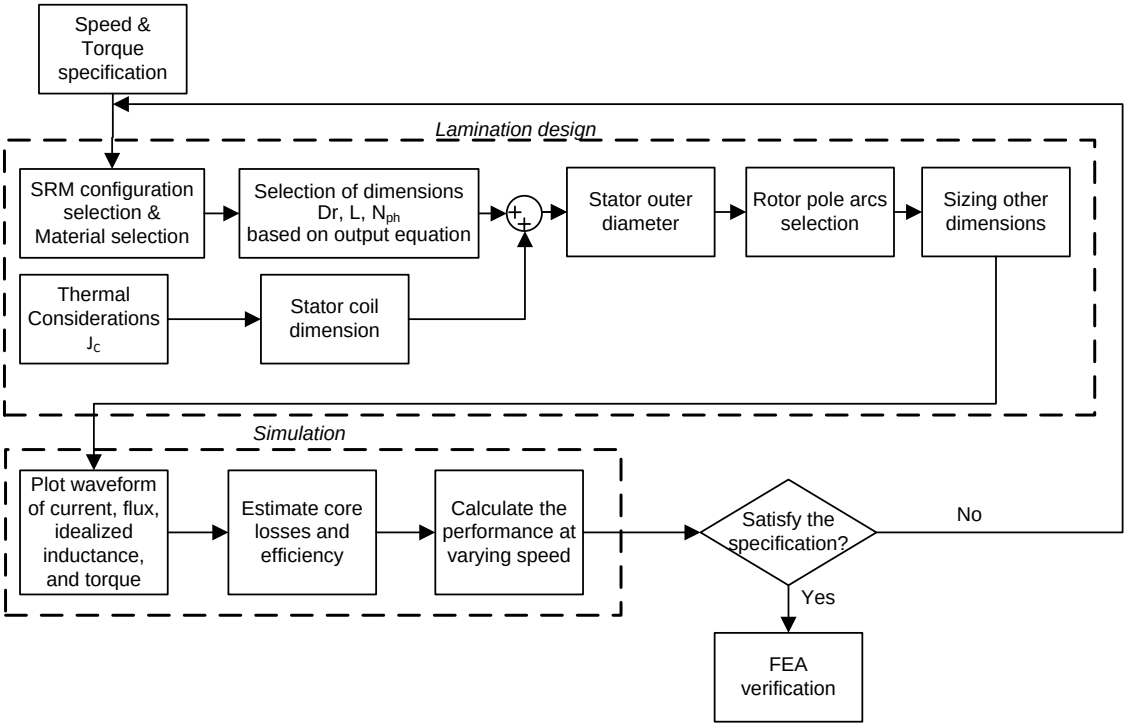

Fig 2.10 Conventional SRM electromagnetic design procedures

The design procedures can be divided into three parts: lamination design, simulation and FEA verification. At the beginning, the speed and torque specification are given as the design inputs, and the design procedures start with the lamination design, which includes:

1). Select the SRM configuration and the lamination material. The choice of the SRM configuration is mainly based on the consideration of the fundamental frequency and the torque ripple specification. The fundamental frequency is determined by the SRM operational speed. The higher the fundamental frequency is, the higher the SRM switching loss and core loss are. On the other hand, in general, a SRM configuration with more poles means less torque ripple, and this is an important specification for some applications, for example, the traction motor of an electric

vehicle. In most cases, the initial choice of the SRM configuration is highly dependent on the designer's experience.

2). Calculate the rotor outer diameter D_r and the stack length L according to the well-known torque output equation $T = K \times D_r^{\,2} \times L$, where T is the rated torque and K is a constant. The empirical values of K and the ratio between D_r and L are variables depending on the machine type and the operational conditions (speed and loading). The typical values of K for a SRM design are listed in Table 2.1.

Table 2.1 Typical values of K for a SRM design [48]

	Typical values of K (lbf-in/in3)
Small totally-enclosed motors	0.15 - 0.8
Integral-hp industrial motors	0.8 - 3
High-performance servomotors	1.5 - 5
Aerospace machines	3 - 7.5
Large liquid-cooled machines	15 - 200

3). Calculate the number of turns N_{ph} based on the magnetic circuit including the air-gap. For the sake of simplicity of the initial design, it is assumed that the reluctance on the air gap is much greater than that of the core. So the MMF, which is generated by the current in the coil winding, is approximated to be consumed by the air gap reluctance twice for a complete flux path, which gives the following equations:

$$2H_g \cdot l_g = N_{ph} \cdot I_{\max} \tag{2.1}$$

$$H_g = B_m / \mu_0 \tag{2.2}$$

where H_g is the maximum magnetic field in the air-gap, l_g is the air-gap length, I_{max} is the maximum current in the coil winding, B_m is the saturated flux density of

the core material and μ_0 is the magnetic constant. B_m is specified by the material property, l_g is an empirical value based on the designers' experience and manufacturing conditions, and I_{max} is calculated by using the power specification divided by the voltage used in the SRM drive. In this way, the initial value of N_{ph} is found.

4). Determine the current density J_c according to thermal considerations which depends on the SRM cooling system. For a regular air cooling system, J_c is usually around 5 A/mm^2.

5). Calculate the stator coil dimension (the stator pole height h_s and the width w_s between two adjacent stator pole tips), and then calculate the stator outer diameter D_s. The geometric parameters of a 4/2 SRM lamination are illustrated in Fig. 2.11.

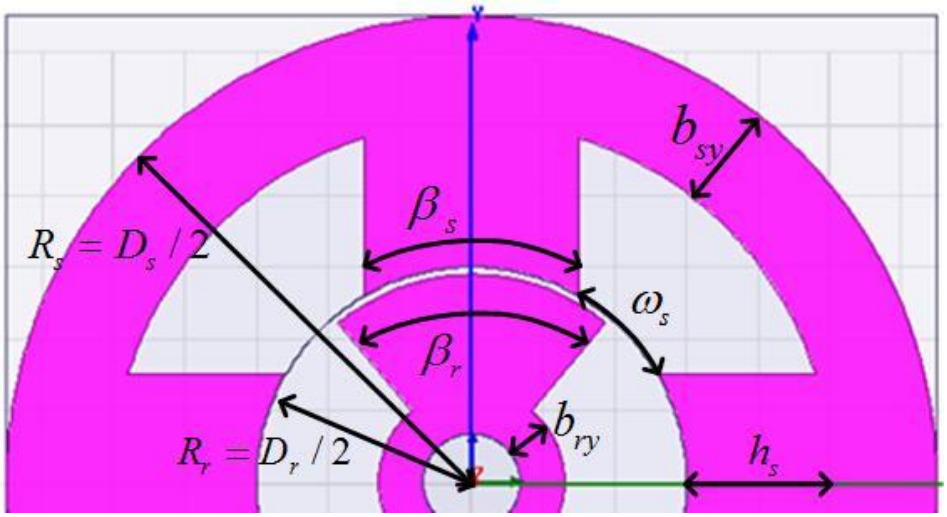

Fig 2.11 Geometric parameters of a 4/2 SRM lamination

Given the maximum current value I_{max}, the number of turns N_{ph} in step 3, and the current density J_c in step 4, the coil winding area can be calculated by equation:

$$A_s = \frac{N_{ph} \cdot I_{\max}}{J_c} \tag{2.3}$$

With the choice of a typical value for the stator pole angle β_s, the width w_s can be calculated by:

$$w_s = \frac{D_r}{2} \cdot \left(\frac{2\pi}{N_s} - \beta_s \right) \tag{2.4}$$

where N_s indicates the stator pole number. Next the stator pole height h_s is approximately equal to A_s divided by w_s, and then the stator backiron thickness b_{sy} is usually selected to be half of the stator pole width as the following:

$$b_{sy} = \frac{D_r \cdot \beta_s}{2} \tag{2.5}$$

Afterwards, the stator outer diameter D_s can be found as:

$$D_s = D_r + 2l_g + 2h_s + 2b_{sy} \tag{2.6}$$

6). Calculate other SRM dimensions, such as the rotor pole angle β_r, the rotor back-iron thickness b_{ry}, and the shaft diameter D_{sh}. Those values are mostly estimated based on the SRM designer's experience. These 6 steps complete the initial design of the SRM lamination geometry.

After sizing all the lamination variables, the step of simulation is carried out to check whether the empirical values of the geometric variables in steps 1-6 are correct, otherwise they are tuned accordingly. For example, a linearized inductance profile of the initial SRM design is calculated using a lumped element model of the SRM magnetic field in the core. Given the linearized inductance profile and a specific current profile, the SRM torque can be estimated as well as power. In addition, the power loss and efficiency at this operating point can be calculated. Finally, this simulation is repeated for other speeds, and finally it plots the SRM speed-torque/power characteristics over the entire operational range.

If the simulation results satisfy the input specifications, the FEA verification can be performed to obtain more accurate knowledge of the SRM performance. For example, the inductance profile can be improved by using the FEA method rather than a linearized profile from the lumped element model. However, in general, the FEA approach is very time-consuming, so it is only used at the final step to check the design candidate's performance.

Although the initial SRM design can be found in a conventional way where many empirical values are used, the optimal design can only be identified by comparing considerable design candidates, or searching over the design space, as shown in Fig 2.12.

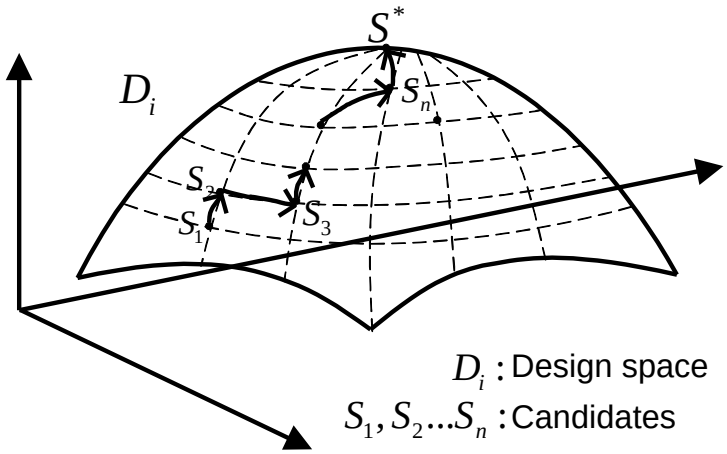

Fig 2.12 Design space for the SRM optimization

Each design candidate is defined as a set of geometric variables, and the corresponding SRM performance (torque, power, weight, size, efficiency) can be calculated for given values of those geometric variables. Particularly, the value of each variable is varying within its respective range, so the design space is a multiple-dimensional space with many design candidates. Therefore, there are two challenges to find the optimal design. The first one is to identify the optimal design among those great amounts of candidates in

a short time, where the optimality is defined by a given objective function. Some typical objective functions are given in (2.7) and (2.8) [52].

$$\text{Obj1} = \text{Volume}*20000 + \text{Weight}*2 + (1 - \text{Eff})*200 + \text{WtMgt}*5 - \text{TperA}*5 \quad (2.7)$$

$$\text{Obj2} = \text{Volume}*10000 + \text{Weight} + (1 - \text{Eff})*1000 + \text{WtMgt}*5 - \text{TperA}*20 \quad (2.8)$$

where the five performance indexes are, volume (m^3), weight (*kg*), efficiency (*0-100%*), weight of the magnets (*kg*) (for PM machines) and the torque per ampere at the rated condition (*Nm/Arms*).

However, with the advance of artificial intelligence algorithms, many computational intelligent optimization techniques have been utilized in this area. Particularly, genetic algorithm (GA), particle swarm optimization (PSO) and differential evolutionary (DE) algorithms are the most used ones. Therefore, the efficiency of searching the entire design space is greatly improved.

On the other hand, the estimate of the SRM performance is still a challenge that has not received much attention in the literature yet. For example, the aforementioned simulation method, which is used in the machine design software SPEED, adopts a lumped element magnetic circuit to calculate the performance, but it is not accurate. Besides this method, much effort has been spent to calculate the SRM performance in an analytical way by using a function of the geometric variables. The most well-known work in this area has been done by Dr. Krishnan, and a specific example of an 8/6 SRM design is presented in [50]. The cross section views of the 8/6 SRM at the aligned position and at the unaligned position for Phase A are shown in Fig 2.13 respectively, where the flux paths are plotted by using FEA.

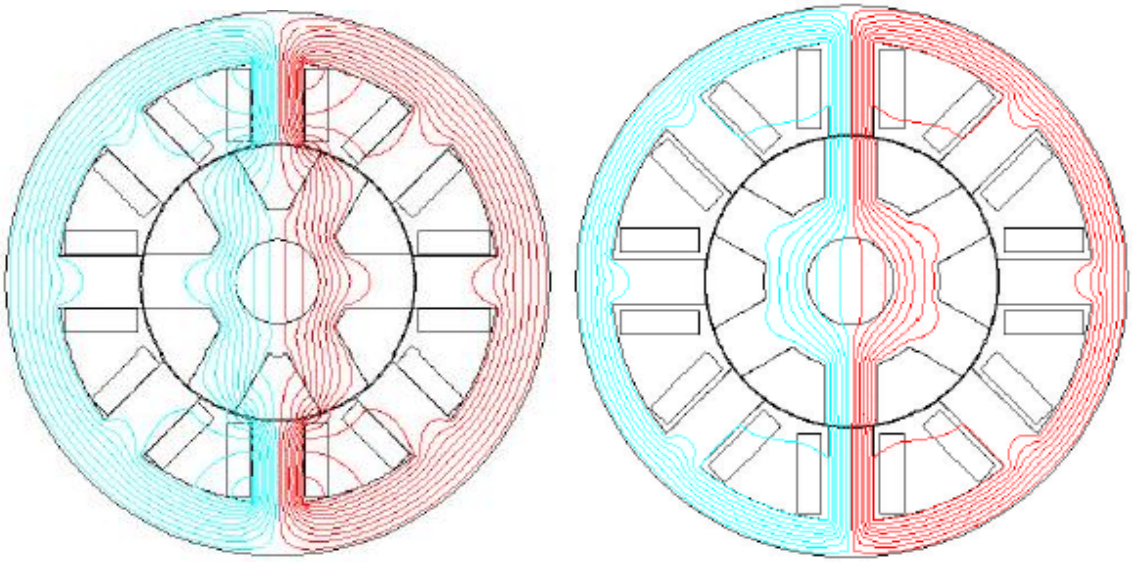

Fig 2.13 8/6 SRM flux paths at the aligned and unaligned positions [50]

Next, the flux paths for the unaligned position are sorted into nine groups as shown in Fig 2.14, and each group is defined as a flux tube.

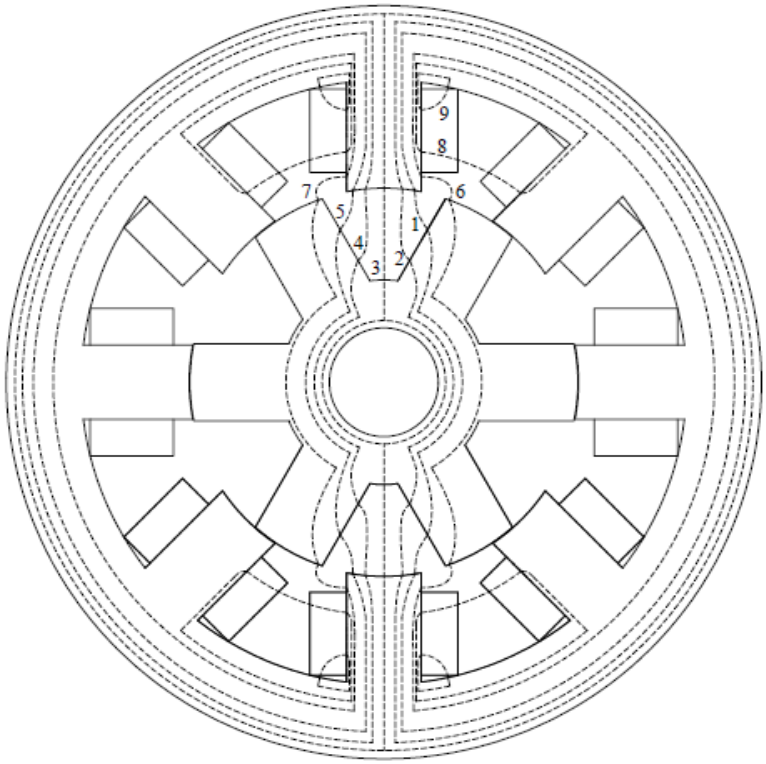

Fig 2.14 The flux paths for the unaligned position [50]

Then the flux path of each tube is described as a function of the SRM geometric variables, and an enlarged view of Tube 2 is shown in Fig 2.15. Then the entire SRM flux path or magnetic field for the unaligned position can be described by combining all the flux tubes. So the inductance for the unaligned position can be expressed as a function of the geometric variables. In this way, the inductance for different rotor positions (usually one aligned position, one unaligned position, and two positions in between) can be calculated, and the performance of the given SRM can be estimated.

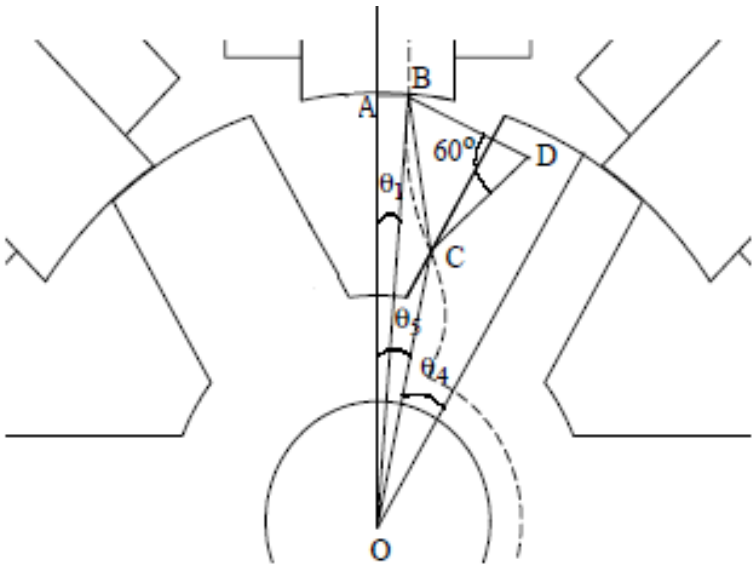

Fig 2.15 Enlarged view of Tube 2 [50]

Therefore, for this method, only one FEA simulation needs to be performed at the beginning in order to know the flux tubes distribution, and then a specific model can be established in an analytical way to calculate the SRM performance. Then, by varying the geometric variable values and assuming the consistence of the flux tubes, the SRM performance of different design candidates can be calculated, and a numerical optimization can be performed to find out the optimal design.

The main advantage of this method is the computational efficiency of calculating the SRM performance due to the analytical expression, and good agreement between the

analytical calculation result and the FEA simulation result has been verified in [50]. On the other hand, the drawback of this method is the tedious modeling of the flux tubes by describing them as a function of the geometric variables. Most importantly, the assumption for the consistency of the flux tubes does not hold if the geometric variable values are changed by a large amount. Therefore, this method, especially the tedious modeling of the flux tubes, is not portable to other SRM configurations (4/2, 6/4, or 10/8), or other SRM designs with significant geometric variation (for example, if the stator outer diameter is increased by a factor of two).

2. 3 Chapter summary

In conclusion, the problem of the conventional SRM design methods is that there is no appropriate tool available to estimate the SRM performance. The method used in [51] adopts a simplified linear inductance profile for the performance calculation, but a significant error exists. Other methods such as in [48-51] have the drawback of lacking versatility. At this moment, the finite element analysis (FEA) method is the most accurate approach to calculate the SRM inductance or other characteristics, but an FEA simulation requires much computing effort.

Therefore, the focus and innovation of the research effort in this dissertation is the development of a generic SRM performance estimation approach for the SRM design and optimization. In order to be suitable for different SRM configurations, the proposed method may sacrifice some computational time to achieve satisfactory accuracy for different cases. However, research effort has been made to reduce the computation cost as much as possible in this work.

CHAPTER 3 SRM Optimization using Current-fed FEA Simulation

3. 1 Introduction

The design procedures for conventional machines use extensive knowledge and experience in machine design, particularly for IMs and PM machines in [64]; in those designs an analytical estimation starts from a so-called output equation and in the end the design is verified by FEA simulation. However, this chapter describes a SRM design method which uses FEA as a performance estimator from the beginning, and achieves the optimal design by searching the entire design space.

First of all, it is required to establish a FEA simulation model which can calculate the performance by using the geometric variables, and the geometric variables constitute the design space. The challenge of the SRM modeling lies in the high non-linearity of the electromagnetic analysis, as the SRM's electromagnetic behavior is determined by the rotor position and the excitation current, not only by the geometric variables. For the IM and PM machine design, one can assume a sinusoidal power supply waveform applied to the stator winding, and the rotor is automatically aligned with the d axis of the sinusoidal waveform. However, the SRM excitation control is highly dependent on the rotor position, and it is required to be specified before calculating the SRM performance. Therefore, a new method to specify the SRM current shape is proposed in this chapter. It is accurate (FEA based calculation) and has wide applicability (portable to any SRM configurations and dimensions)

This chapter is organized as follows: the current-fed FEA simulation approach for the SRM design is presented in Section 3.2; a novel analytical method to calculate the excitation current profile for the current-fed FEA simulation is described in Section 3.3; the simulation results to verify the proposed analytical approach are presented in Section

3.4; a case study of a 12/8 SRM rotor design is described in Section 3.5; finally, chapter summary is presented in Section 3.6.

3. 2 Current-fed FEA simulation for SRM design

The FEA simulation is chosen as the SRM performance estimator mostly due to its accuracy. To carry out a FEA simulation, it is needed to specify the excitation method, which represents the strategy of controlling the SRM. Then the FEA simulation can be performed to calculate the torque, losses, efficiency, and etc. However, in this work, the investigation focuses on the torque calculation.

A typical current profile for the SRM excitation is shown in Fig. 3.1. The top trace denotes the ideal linearized inductance profile and the bottom trace denotes the ideal current profile. Both horizontal axes are the rotor position, and the rotor is moving from the unaligned position θ_u to the aligned position θ_a. As shown in the typical SRM drive circuit of Fig 1.3, the switch is turned on at θ_{on} and positive DC link voltage V_{DC} is applied to the phase winding. The current ramps up to the predefined peak current I_p at position θ_1, and then the current hysteresis control is adopted to keep the current at I_p. At position θ_{off}, the switch is turned off and negative DC voltage is applied to the phase winding. The current then freewheels and drops from θ_{off} to zero at position θ_2. The trapezoidal shape of the current profile $A^*B^*C^*D^*$ can be defined by the four positions $\theta_{on}, \theta_1, \theta_{off}$ and θ_2, and the peak current I_p.

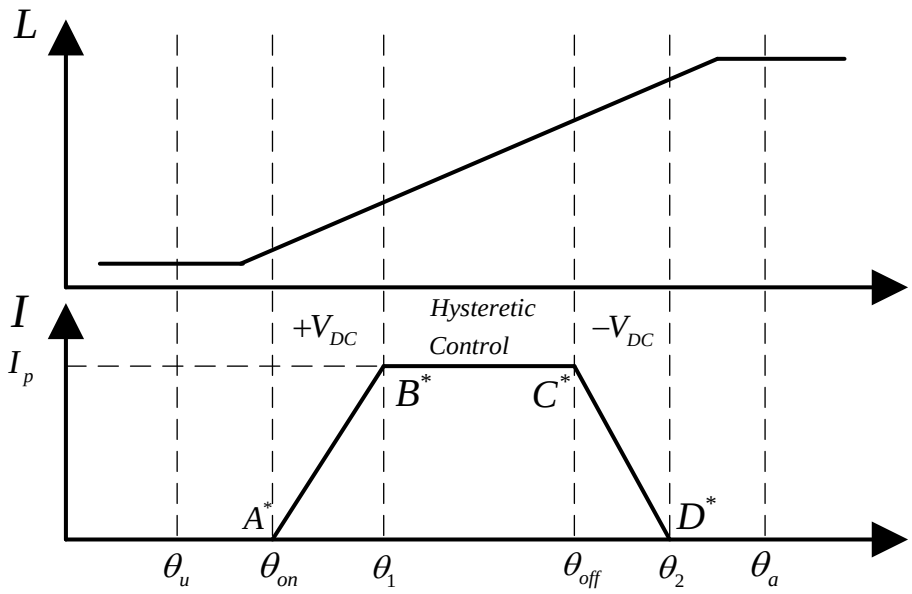

Fig 3.1 Typical SRM excitation current profile

For the FEA simulation software, such as Ansoft/Maxwell, there are two ways to define the excitation method, a) the voltage-fed mode, where the excitation input is a voltage profile; b) the current-fed mode, where the excitation input is a current profile. The current–fed mode is preferred rather than the voltage-fed mode because the FEA solution is faster. For the voltage-fed mode, the FEA simulation tool first estimates the current according to the input voltage, and calculates the flux distribution and the instantaneous inductance, and then checks whether the estimated current and the computed inductance satisfy the voltage equation. The iterations are repeated until the estimated current error converges to zero, and then the simulation moves to the next time point. According to Ampere's circuital theorem, it is the current which determines the flux spatial distribution. It is therefore more time efficient to run the FEA simulation based on a current-fed mode, which directly defines the excitation current profile.

The next step is how to specify the excitation current profile for the FEA simulation. Particularly, as shown in Fig. 3.1, the trapezoidal current profile is determined by the four

angles, θ_{on} , θ_1 , θ_{off} and θ_2 . So now the challenge is to calculate the four angles. A novel method to calculate the angles based on another current-fed FEA simulation result is to be described in the next section.

Therefore, for every design candidate (a set of specific geometric variables), the proposed design method needs to perform only two current-fed FEA simulations to estimate its performance. The first one uses constant-current (I_p) as the excitation current input and calculates the flux-linkage at the different angles. Then the flux-linkage is used to calculate the four angles in an analytical way (Section 3.3). The second current-fed FEA simulation uses the trapezoidal current profile (which is defined by the four angles) as the excitation current input to calculate the SRM performance. After analyzing the performance for this design candidate, the optimization can move to the next design candidate by changing the geometric variables. In this way, the design space is searched and an optimal set of dimensions is found.

3. 3 Angle calculation for the trapezoidal excitation current profile

Instead of searching all the possible angle combinations for θ_{on} , θ_1 , θ_{off} and θ_2 , this section describes a method to calculate the four angles analytically.

The flux-linkage with respect to different current and rotor positions is illustrated in Fig. 3.2. The horizontal axis denotes the current and the vertical axis denotes the flux-linkage. The curve OE indicates the flux-linkage at position θ_u , and the curve OF indicates the one at position θ_a . The curve AB in Fig. 3.2 corresponds to the segment A^*B^* in Fig. 3.1, as the rotor position moves from θ_{on} to θ_1 , and the current increases

from zero to I_p. The curve BC in Fig. 3.2 corresponds to the segment B^*C^* in Fig. 3.1, and the curve CD in Fig. 3.2 corresponds to the segment C^*D^* in Fig. 3.1.

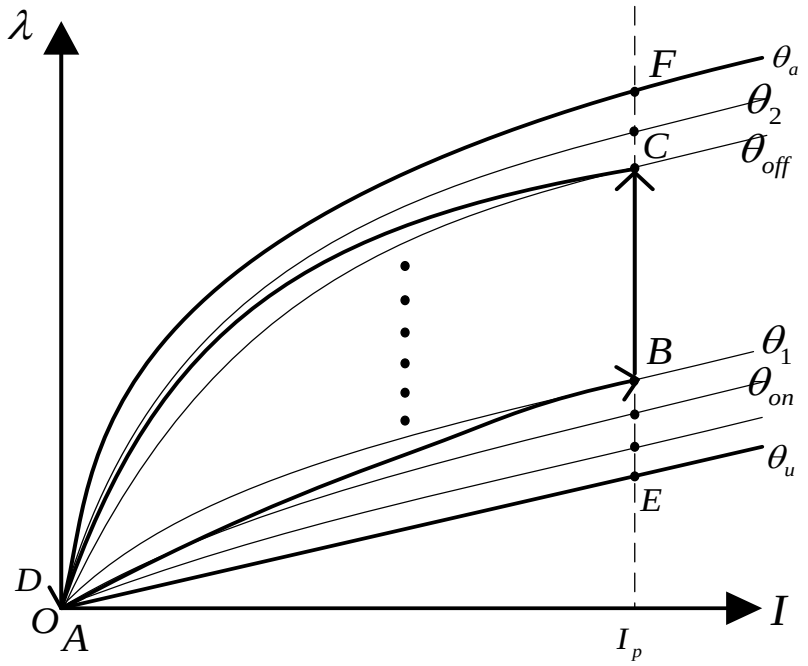

Fig 3.2 SRM flux-linkage for different rotor positions and current

The segment *EF* in Fig. 3.2 is very important for determining the angles $\theta_{on}, \theta_1, \theta_{off}$ and θ_2. The dependence of the four angles on each other is determined by the flux-linkage at these angles. The flux-linkage is again determined by the current. Therefore, the segment *EF*, which is the flux-linkage for different rotor positions (from θ_u to θ_a) with constant excitation current (I_p), is calculated using the first FEA simulation operating in the current control mode, and the result is shown in Fig 3.3. In Fig 3.3, $\lambda_{I_p}(\theta_i)$ indicates the flux-linkage at angle θ_i with constant excitation current I_p.

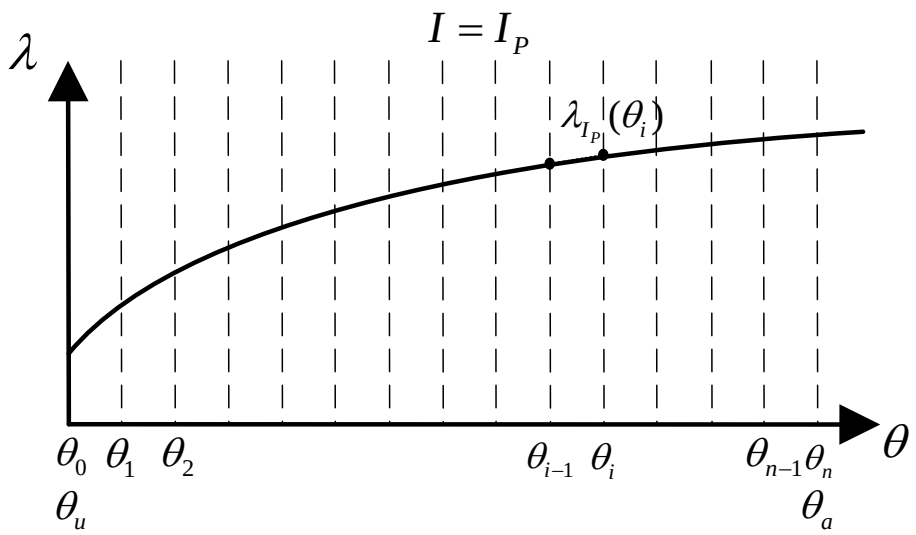

Fig 3.3 Flux linkage for different rotor positions with constant current

With the information of $\lambda_{I_P}(\theta_i)$, the time between θ_{on} and θ_1 (the time period when the current increases in Fig 3.1), and the time between θ_{off} and θ_2 (the time period when the current decreases in Fig 3.1) can be calculated analytically using a method presented as following.

3.3.1 Current increase time calculation

The *current increase time* denotes the time interval between θ_{on} and θ_1, which corresponds to the segment A^*B^* in Fig. 3.1. When the rotor moves from θ_{on} to θ_1, the machine state (indicated by the current and flux-linkage) moves from *A* to *B* in Fig. 3.4. Specifically, the current increases from zero to I_P, and the flux-linkage increases from zero to $\lambda_{I_P}(\theta_1)$ at point *B*. In most cases, $\theta_{on} = \theta_u$ to avoid producing negative torque.

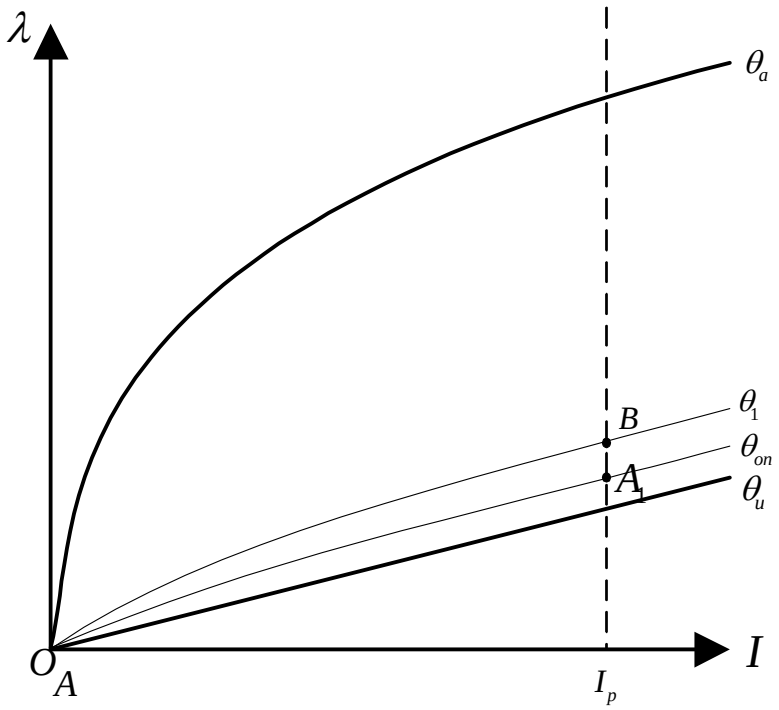

Fig 3.4 Current increase phase machine state diagram

Recall that the phase voltage is given by (3.1). Ignoring the phase resistance R, the phase flux-linkage λ is calculated by using (3.2).

$$V_{DC} = R \cdot i + \frac{d\lambda}{dt} \tag{3.1}$$

$$\lambda = \int V_{DC} \cdot dt = V_{DC} \cdot \Delta t \tag{3.2}$$

When the flux-linkage increases from 0 to $\lambda_{I_P}(\theta_1)$, the time interval between θ_{on} and θ_1 is calculated by (3.3), and the angle $\Delta\theta$ between θ_{on} and θ_1 is calculated by (3.4):

$$\Delta t = \frac{\lambda_{I_P}(\theta_1)}{V_{DC}} \tag{3.3}$$

$$\Delta\theta = \theta_1 - \theta_{on} = \Delta t \cdot \omega_r = \frac{\lambda_{I_P}(\theta_1)}{V_{DC}}\omega_r = \frac{\omega_r}{V_{DC}} \cdot \lambda_{I_P}(\theta_1) \tag{3.4}$$

Then, the block diagram of the current increase time calculation is illustrated in Fig 3.5. θ_1 is estimated to be θ_{on} at first so $\lambda_{I_P}(\theta_{1\_est}) = \lambda_{I_P}(\theta_{on})$, and θ_1 is calculated by

(3.5). Then $\lambda_{I_P}(\theta_1)$ is found from the corresponding value of θ_1 in Fig 3.3, and $\lambda_{I_P}(\theta_{1\_est})$ is replaced by $\lambda_{I_P}(\theta_1)$. This process is repeated until the value of θ_1 converges to a stable value.

$$\theta_1 = \frac{\omega_r}{V_{DC}} \cdot \lambda_{I_P}(\theta_{1\_est}) + \theta_{on} \tag{3.5}$$

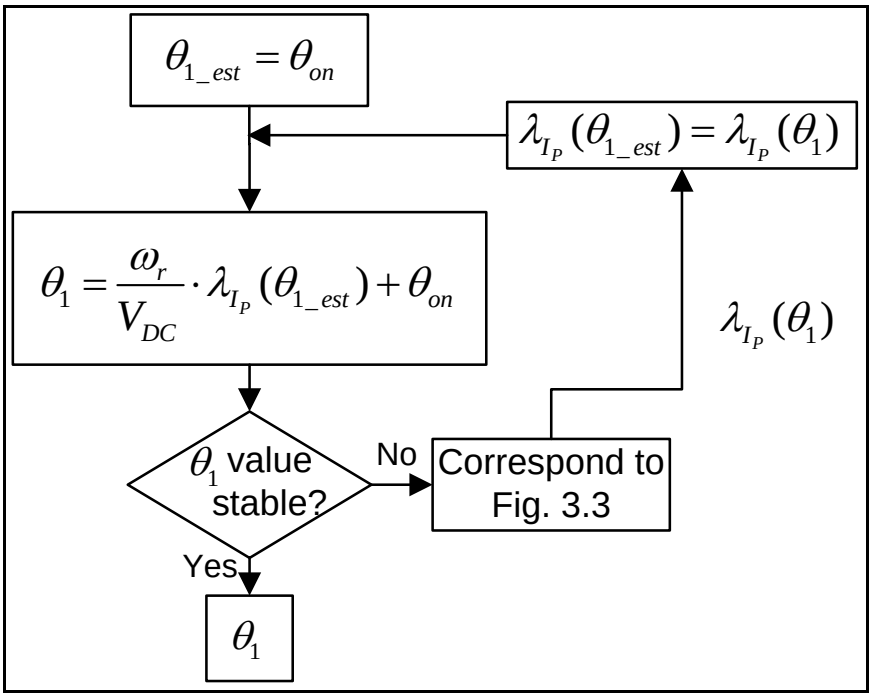

Fig 3.5 Current increase time calculation flow chart (from θ_{on} to θ_1)

3.3.2 Current decrease time calculation

The *current decrease time* denotes the angle between θ_{off} and θ_2, which corresponds to the segment C^*D^* in Fig. 3.1. The calculation is similar to that of the current increase time, and the machine state diagram is shown in Fig 3.6.

When the current decreases from I_P to zero, the machine state (indicated by the flux-linkage and current) moves from point *C* to *D* in Fig 3.6, and the flux-linkage drops by the distance of segment *CH*. The angle $\Delta\theta$ between θ_{off} and θ_2 is calculated using (3.6).

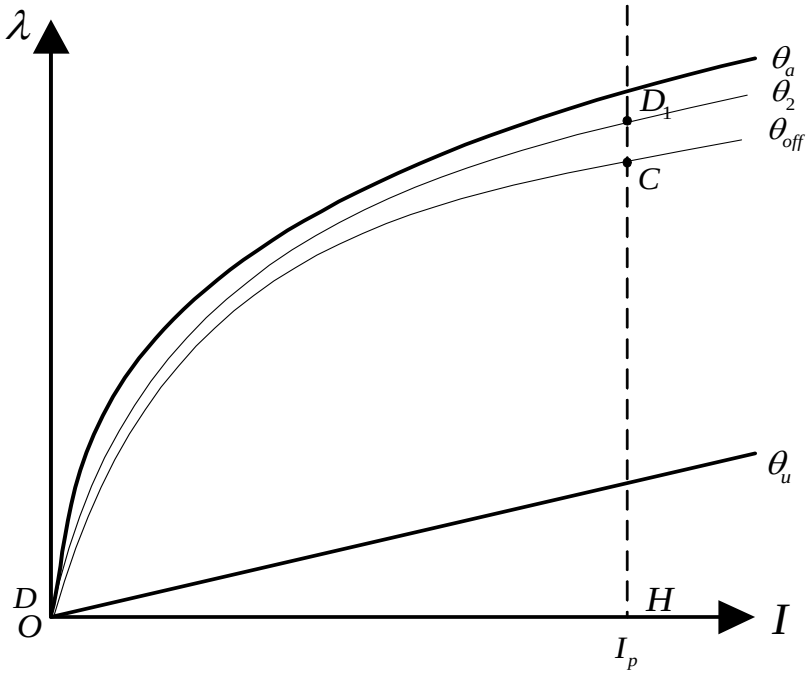

Fig 3.6 Current decrease phase machine state diagram

$$\Delta\theta = \theta_2 - \theta_{off} = \Delta t \cdot \omega_r = \frac{\lambda_{I_P}(\theta_{off})}{V_{DC}} \cdot \omega_r = \frac{\omega_r}{V_{DC}} \lambda_{I_P}(\theta_{off}) \tag{3.6}$$

For the SRM design optimization purpose, θ_2 is usually desired to be equal to θ_a. In this way, no negative torque is produced and the SRM operates at a high efficiency. The current decrease time calculation method is illustrated in Fig 3.7. At the beginning of each iteration $\theta_{off\_est} = \theta_2$, so $\lambda_{I_P}(\theta_{off\_est}) = \lambda_{I_P}(\theta_2)$. Next, θ_{off} is computed by (3.7), and $\lambda_{I_P}(\theta_{off})$ is found from the corresponding value of θ_{off} in Fig 3.3. Then $\lambda_{I_P}(\theta_{off\_est})$ is updated, and θ_{off} is re-calculated. The process is repeated until the value of θ_{off} converges to a stable value.

$$\theta_{off} = \theta_2 - \frac{\lambda_{I_P}(\theta_{off\_est})}{V_{DC}} \omega_r \tag{3.7}$$

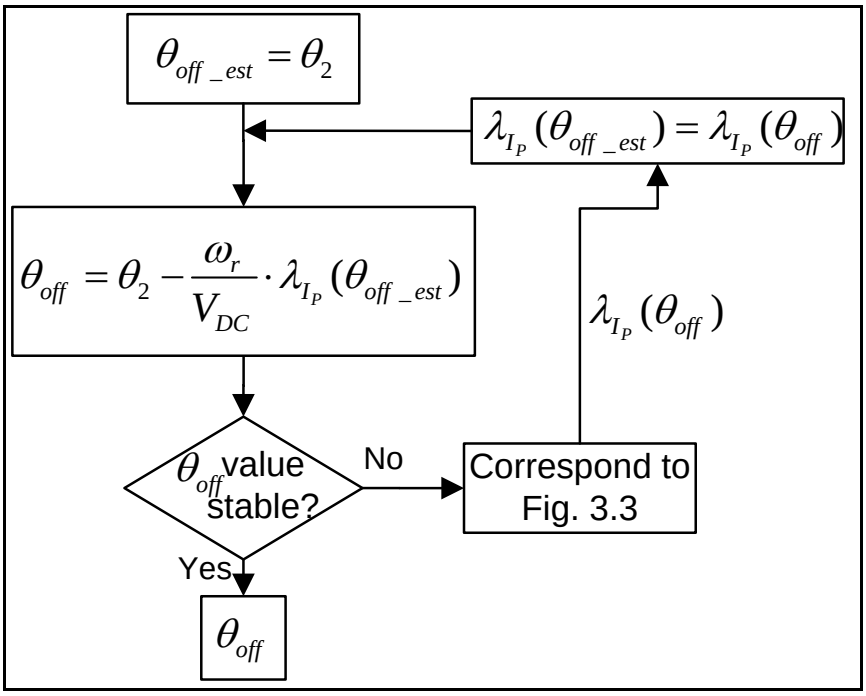

Fig 3.7 Current decrease time calculation flow chart (from θ_{off} to θ_2)

In summary, the position θ_1 and θ_{off} can be computed analytically using (3.3)-(3.7) if θ_{on} and θ_2 are given ($\theta_{on} = \theta_u$ and $\theta_2 = \theta_a$). The only data needed for the calculation is the FEA-simulated flux-linkage $\lambda_{I_P}(\theta_i)$ (Fig 3.3). The angle difference between θ_{on} and θ_1 is determined by ω_r, $\lambda_{I_P}(\theta_{on})$ and V_{DC}, and the one between θ_{off} and θ_2 is determined by ω_r, $\lambda_{I_P}(\theta_2)$ and V_{DC} according to (3.5) and (3.7). The peak current I_P can be known by using the specified power divided by the voltage used in the SRM drive.

3. 4 Verification with voltage-fed FEA simulation

To verify the aforementioned angle calculation method, the four angles calculated by the current-fed FEA are compared to the angles in a practical SRM current profile (using generic SRM control) in this section.

The generic SRM control strategy is shown in the top diagram of Fig 3.8 (top trace: voltage, bottom trace: current). However, a voltage-fed FEA simulation, where the speed ω_r, the flux-linkage $\lambda_{I_P}(\theta_{on}) = \lambda_{I_P}(\theta_2) = 0$ and the voltage $\pm V_{DC}$ are the same as the generic SRM control is used here as shown in Fig 3.8 bottom diagram. According to the conclusion of Section 3.3, the angles θ_{on}, θ_1, θ_{off} and θ_2, should be the same. Therefore, the current profile obtained by the voltage-fed FEA simulation can be used to represent the practical SRM current profile; and the practical angle values are used to verify the analytical calculation results (using current-fed FEA simulation).

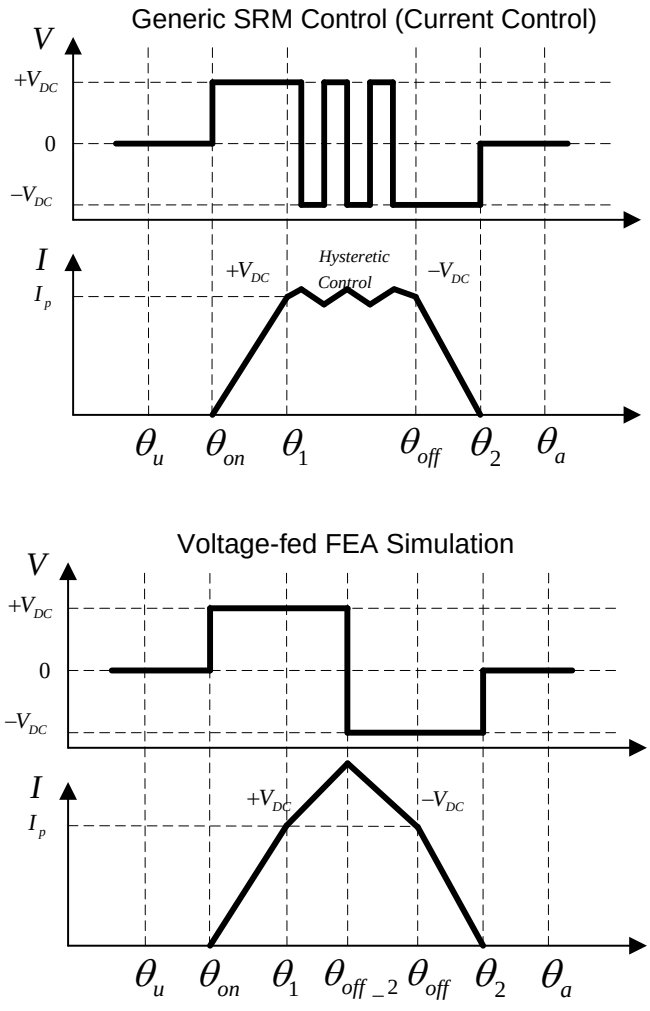

Fig 3.8 Generic SRM control (top) and voltage-fed FEA simulation (bottom)

First the voltage-fed FEA simulation is carried out in the *external circuit mode*. Constant DC voltage is applied to a phase winding between θ_{on} and θ_{off_2} (Fig. 3.8 bottom diagram). The time for the current to rise from zero to I_p is obtained from *the current profile* (Fig. 3.8 bottom diagram), by using the angle value θ_1 when the current first reach I_p to minus the turn-on angle value θ_{on}. The current decrease time can be calculated by using the angle value θ_2 when the current drops to zero to minus the angle value θ_{off} when the current first drop below I_p. Then, the current-fed FEA simulation is performed in the *current control mode*, with constant excitation current I_p = 5 A. The calculated flux-linkage $\lambda_{I_p}(\theta_i)$ is used to calculate the current increase and decrease time analytically as presented in Section 3.3. The results (actual values in the voltage-fed FEA vs. analytical values in the current-fed FEA) are compared to each other. The comparisons are done for different cases, with different speeds and different DC bus voltages.

3.4.1 Case 1: 3600 rpm, 600V DC bus voltage

In the first case, the simulation is performed for a constant speed of 3600 rpm, and a DC bus voltage of 600 V. For the FEA simulation in the *voltage control mode*, the excitation voltage profile is illustrated in Fig 3.9, and the resulting current profile is shown in Fig 3.10 and 3.11.

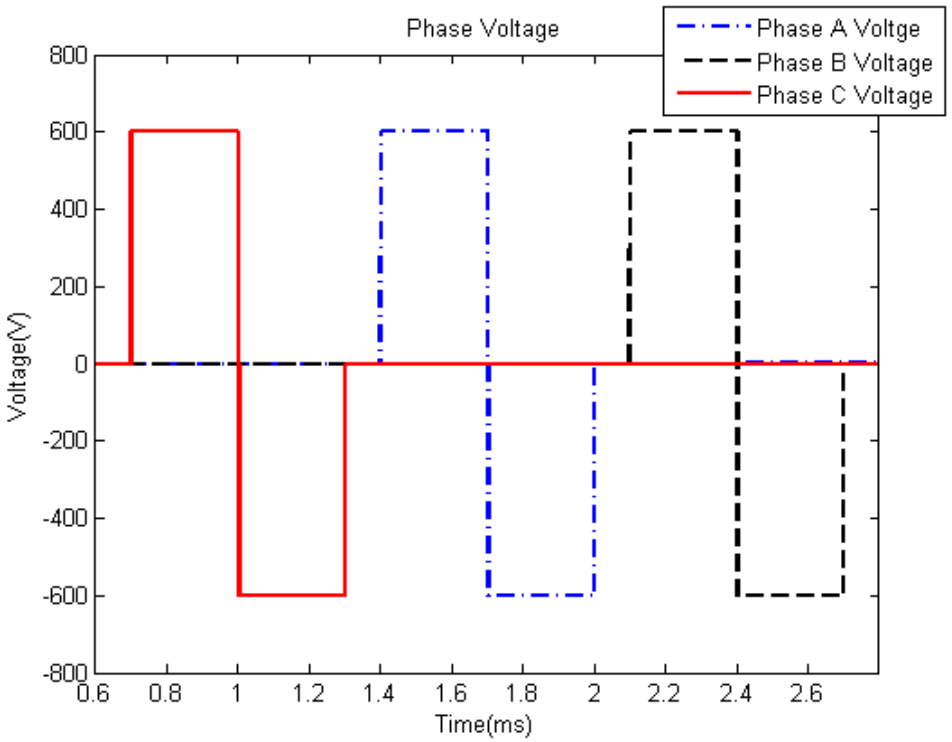

Fig 3.9 Voltage-fed FEA simulation voltage profile (3600 rpm, 600 V DC bus)

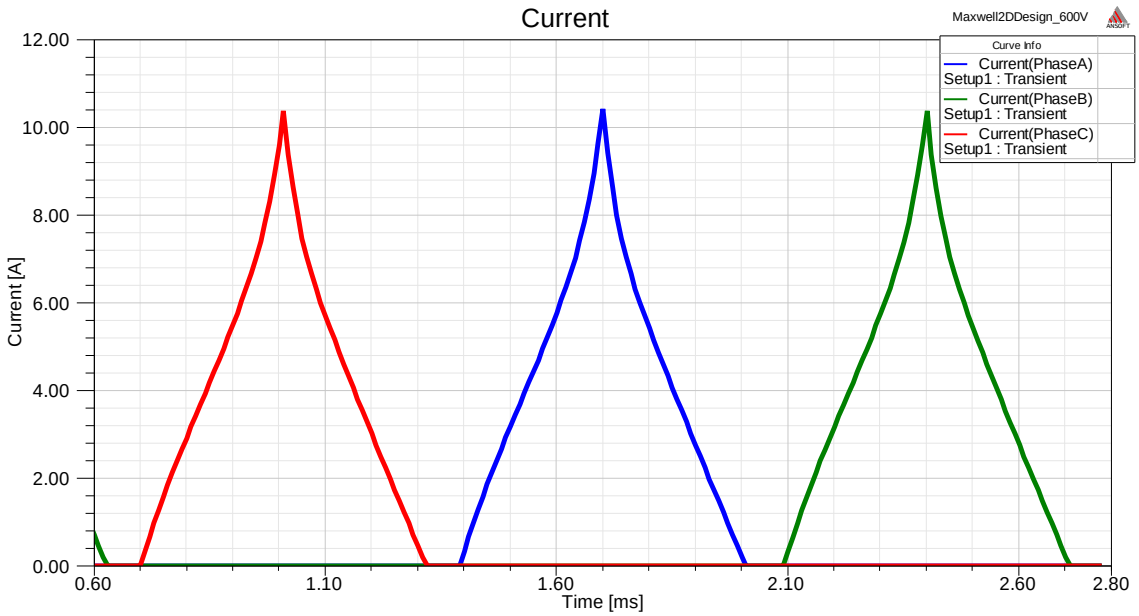

Fig 3.10 Voltage-fed FEA simulation current profile (3600 rpm, 600 V DC bus)

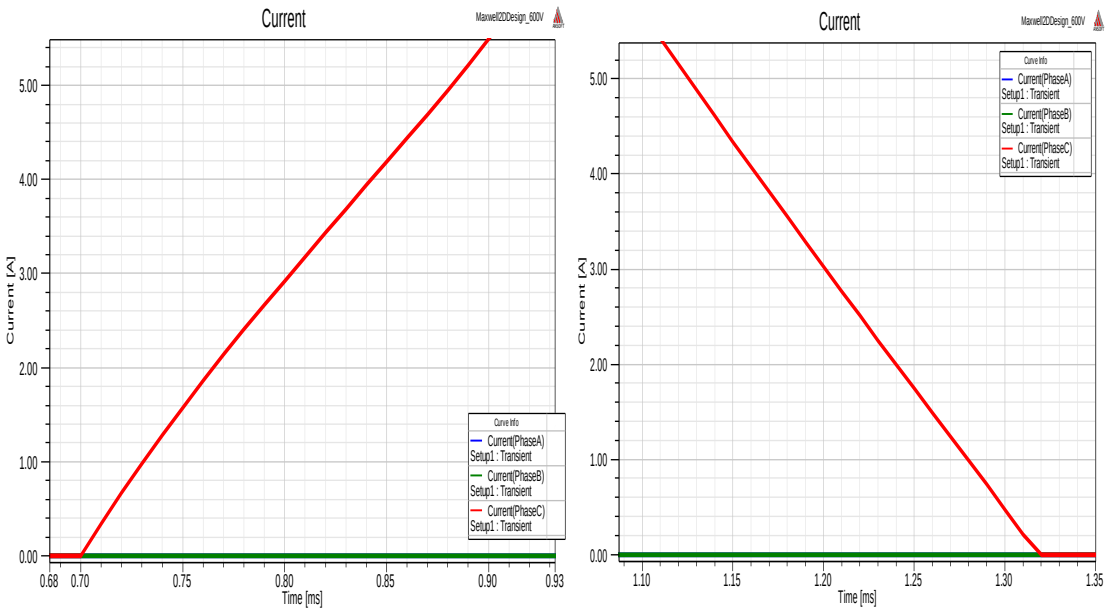

Fig 3.11 Enlarged view of the current profile (3600 rpm, 600 V DC bus)

In Fig 3.11, when positive DC bus voltage is applied to the phase C winding, the current begins to rise from zero at 0.7 ms, and reaches 5 A at 0.882 ms. When negative DC bus voltage is applied to the phase C winding, the current drops to 5 A at 1.125 ms, and decreases to zero at 1.32 ms. Therefore, the current increase time (0.7 ms to 0.882 ms) is 0.182 ms, and the current decrease time (1.125 ms to 1.32 ms) is 0.195 ms.

Next, the FEA simulation in the *current control mode* (I_p) is carried out. The flux linkage with respect to different rotor positions is shown in Fig 3.12. Specifically, the unaligned position is 0 º, and the aligned position is 15 º.

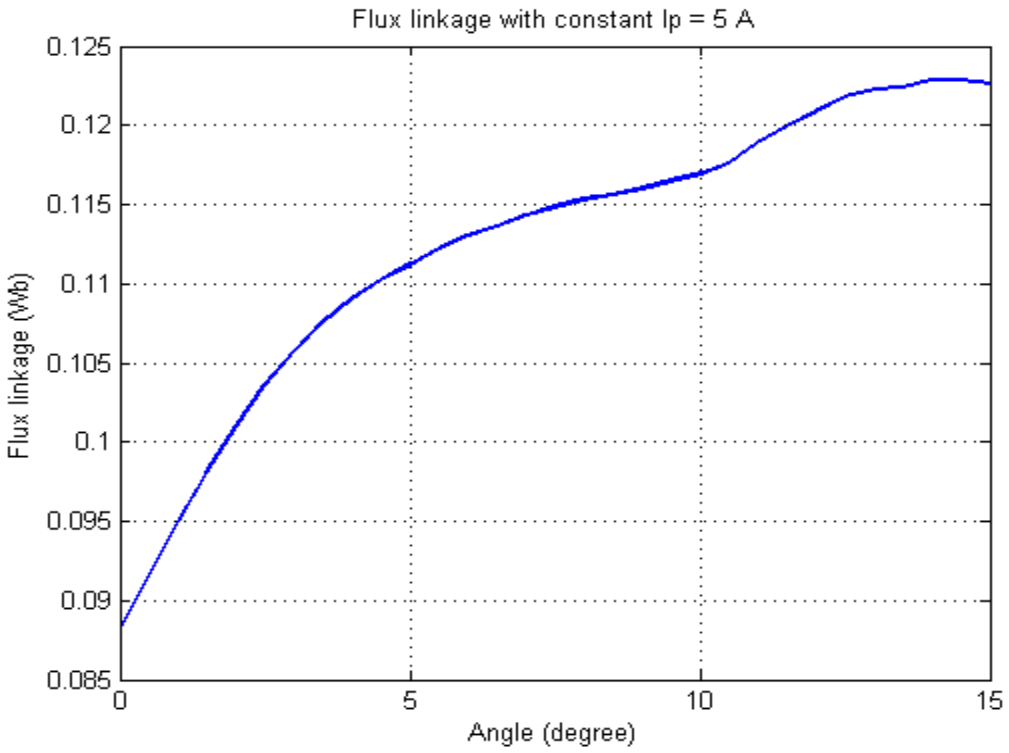

Fig 3.12 Current-fed FEA simulation flux linkage profile

Based on the flux-linkage results, the current increase time is calculated to be 0.181 ms as shown in the flow chart of Fig 3.13, and the current decrease time is 0.193 ms as shown in the flow chart of Fig 3.14. Therefore, the error of the current increase time is $\frac{0.182-0.181}{0.182}=0.5\%$, and the error of the current decrease time is $\frac{0.195-0.193}{0.195}=1\%$.

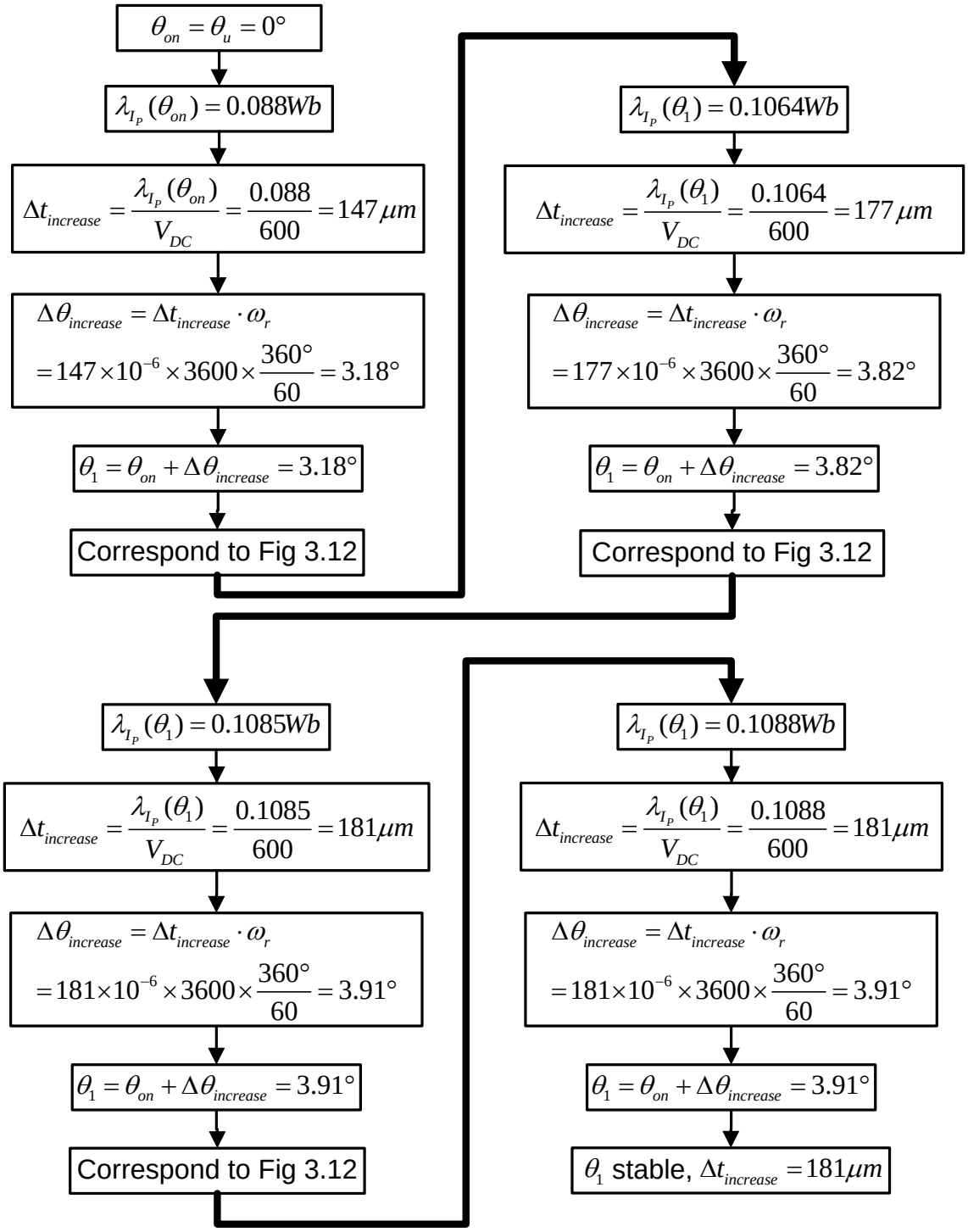

Fig 3.13 Current increase time calculation flow chart (3600 rpm, 600 V DC bus)

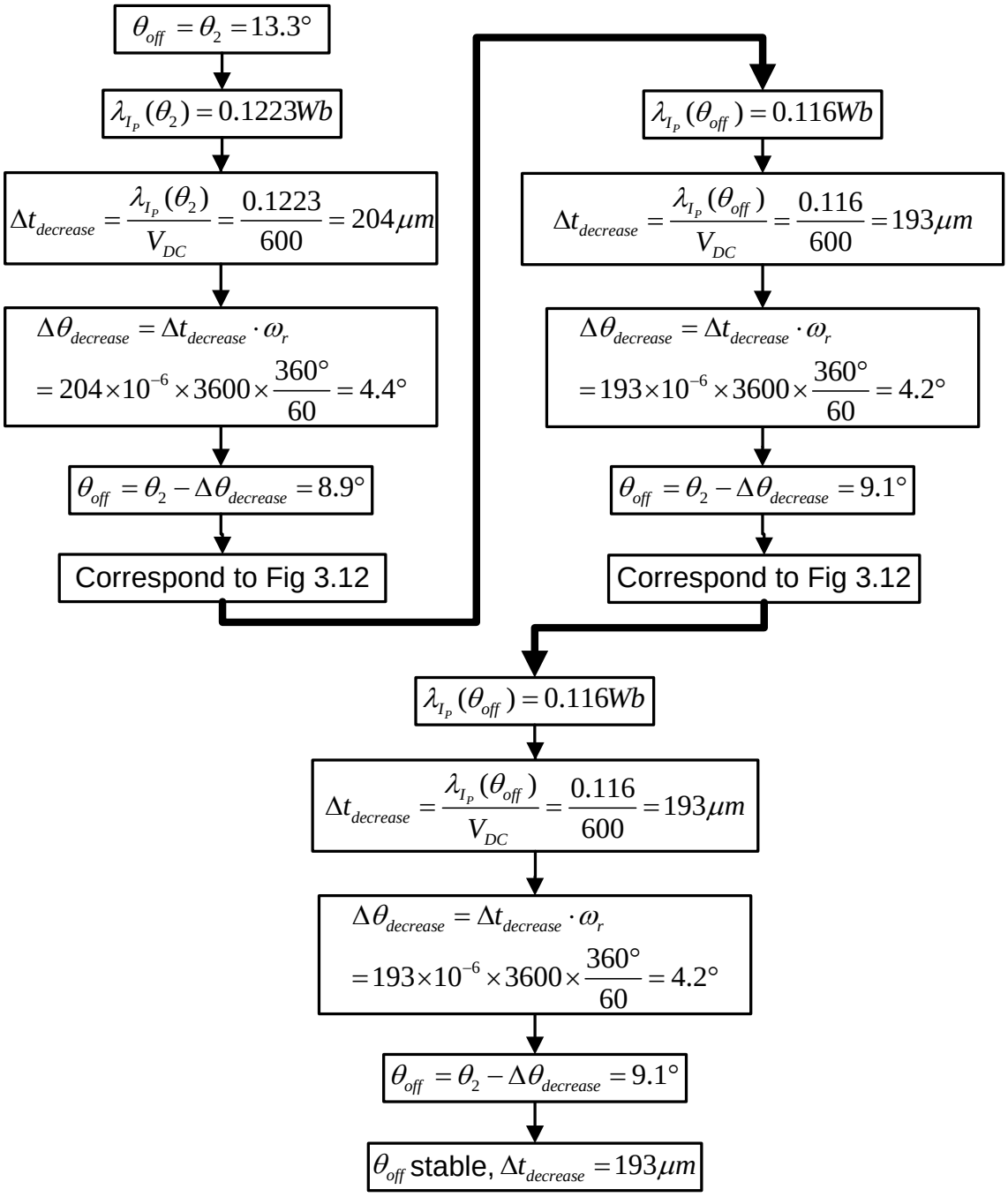

Fig 3.14 Current decrease time calculation flow chart (3600 rpm, 600 V DC bus)

3.4.2 Case 2: 2000 rpm, 350 V DC bus voltage

In the second case, the simulation is performed with a constant speed of 2000 rpm, and a DC bus voltage of 350 V. As shown in Fig 3.16, the current increase time (1.26 ms to 1.57 ms) is 0.31 ms, and the current decrease time (2.05 ms to 2.38 ms) is 0.33 ms.

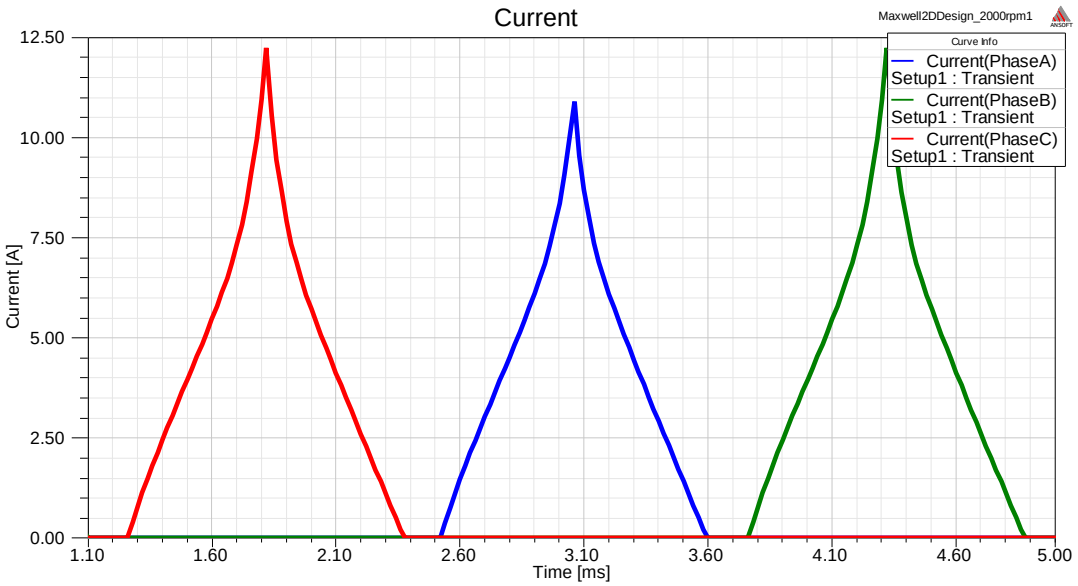

Fig 3.15 Voltage-fed FEA simulation current profile (2000 rpm, 350 V DC bus)

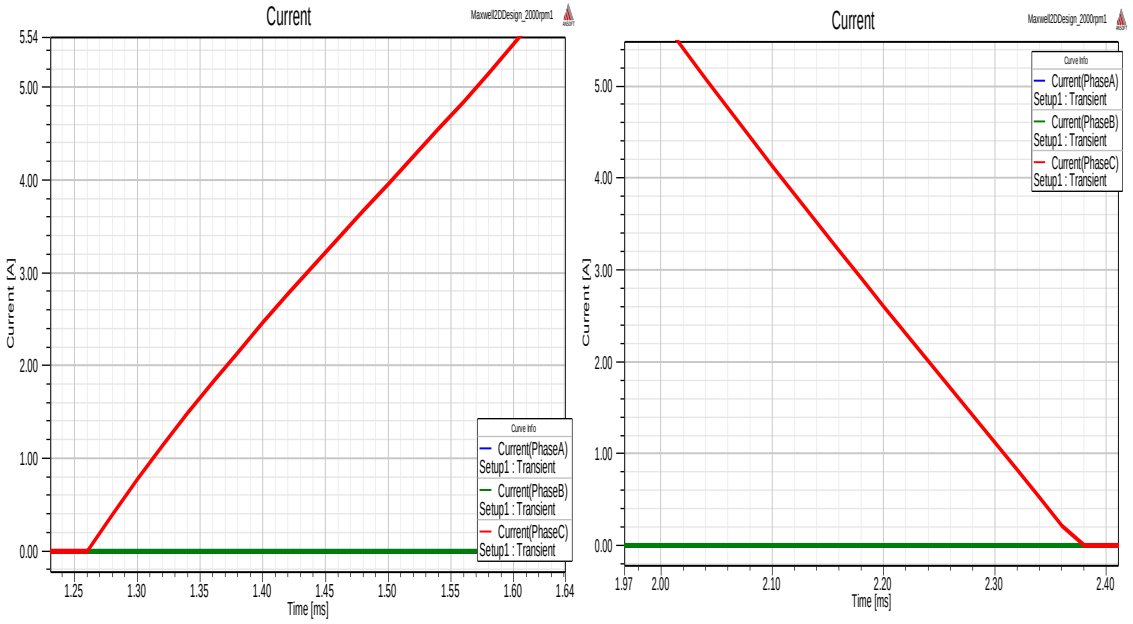

Fig 3.16 Enlarged view of the current profile (2000 rpm, 350 V DC bus)

Based on the flux-linkage in Fig 3.12, the current increase time is calculated to be 0.309 ms (Fig 3.17), and the current decrease time is 0.331 ms (Fig 3.18). Therefore, the error of the current increase time is $\frac{0.31-0.309}{0.31}=0.3\%$, and the error of the current decrease time is $\frac{0.33-0.331}{0.33}=-0.3\%$.

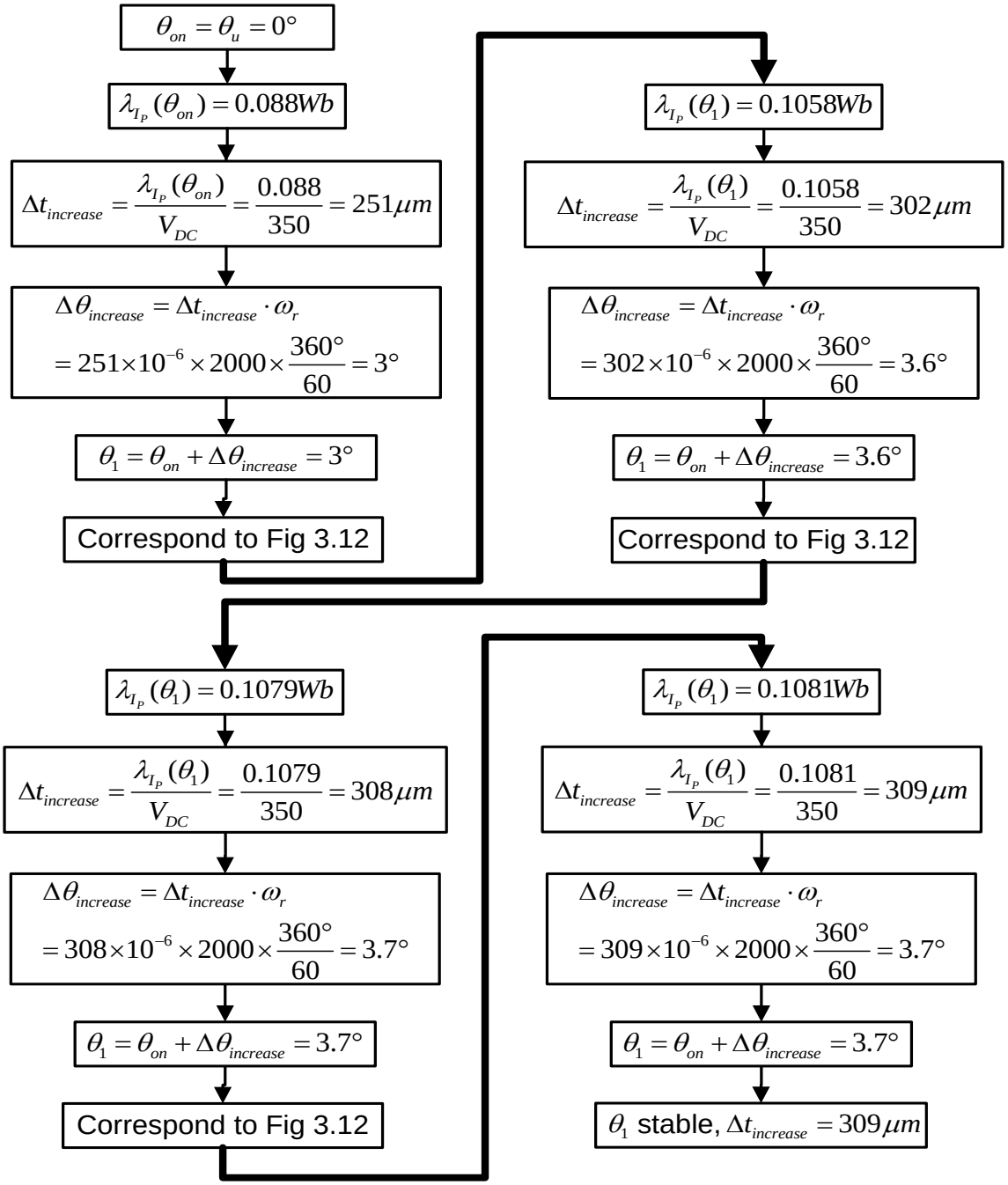

Fig 3.17 Current increase time calculation flow chart (2000 rpm, 350 V DC bus)

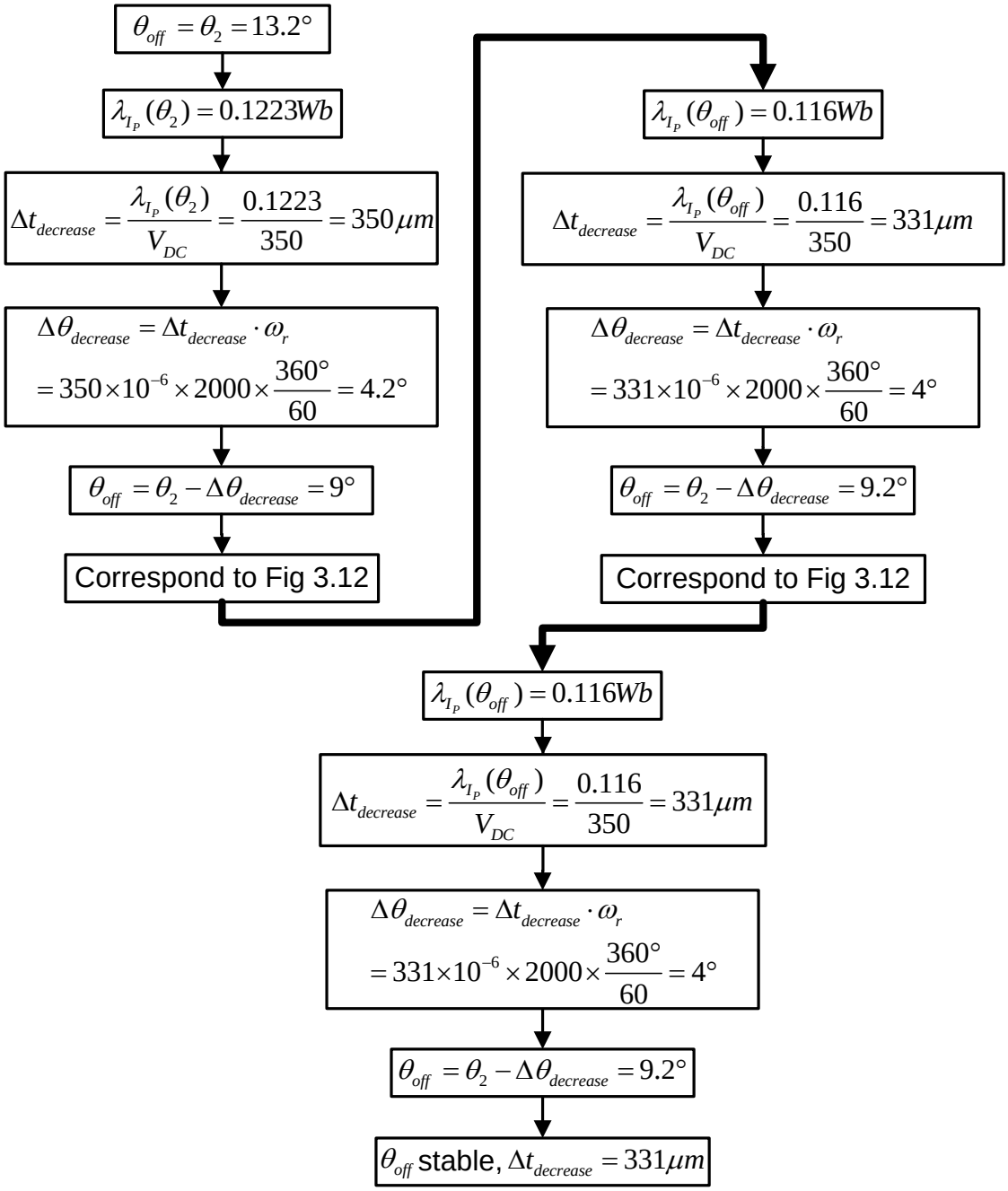

Fig 3.18 Current decrease time calculation flow chart (2000 rpm, 350 V DC bus)

3.4.3 Case 3: 1000 rpm, 150 V DC bus voltage

In the third case, the simulation is performed with a constant speed of 1000 rpm, and a DC bus voltage of 150 V. As shown in Fig 3.20, the current increase time (2.52 ms to 3.25 ms) is 0.73 ms, and the current decrease time (4.13 ms to 4.9 ms) is 0.77 ms.

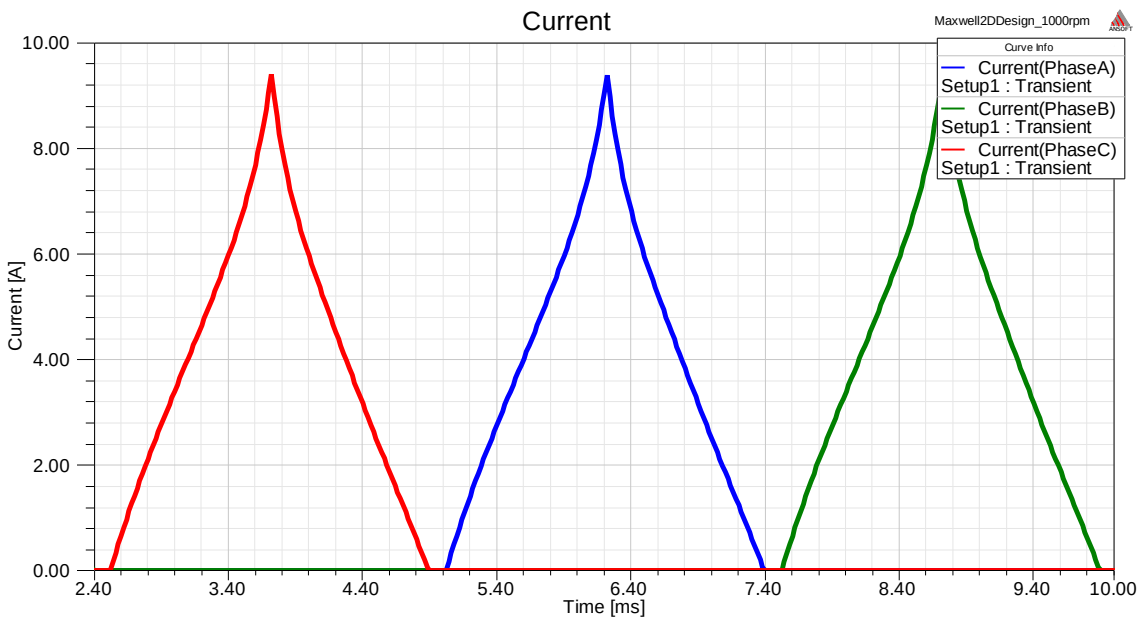

Fig 3.19 Voltage-fed FEA simulation current profile (1000 rpm, 150 V DC bus)

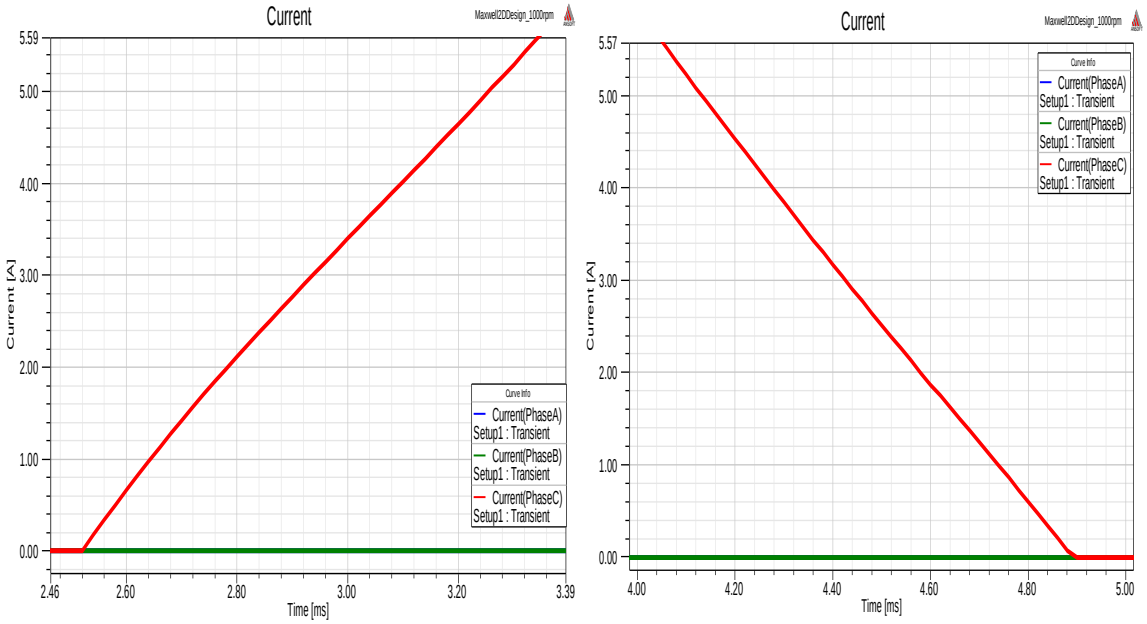

Fig 3.20 Enlarged view of the current profile (1000 rpm, 150 V DC bus)

Based on the flux-linkage in Fig 3.12, the current increase time is calculated to be 0.733 ms (Fig 3.21), and the current decrease time is 0.778 ms (Fig 3.22). Therefore, the

error of the current increase time is $\frac{0.73-0.733}{0.73}=-0.4\%$, and the error of the current decrease time is $\frac{0.77-0.778}{0.77}=1\%$.

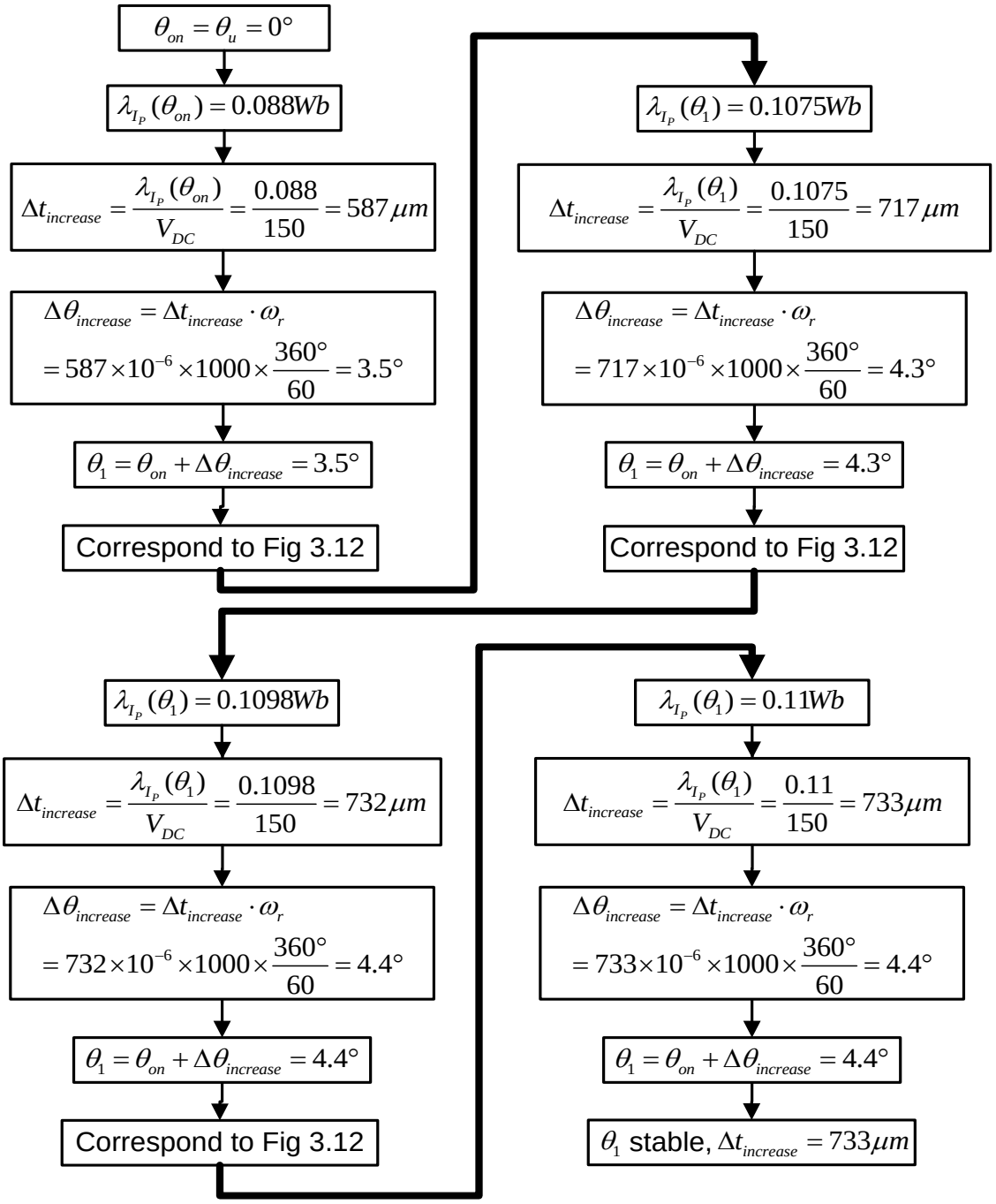

Fig 3.21 Current increase time calculation flow chart (1000 rpm, 150 V DC bus)

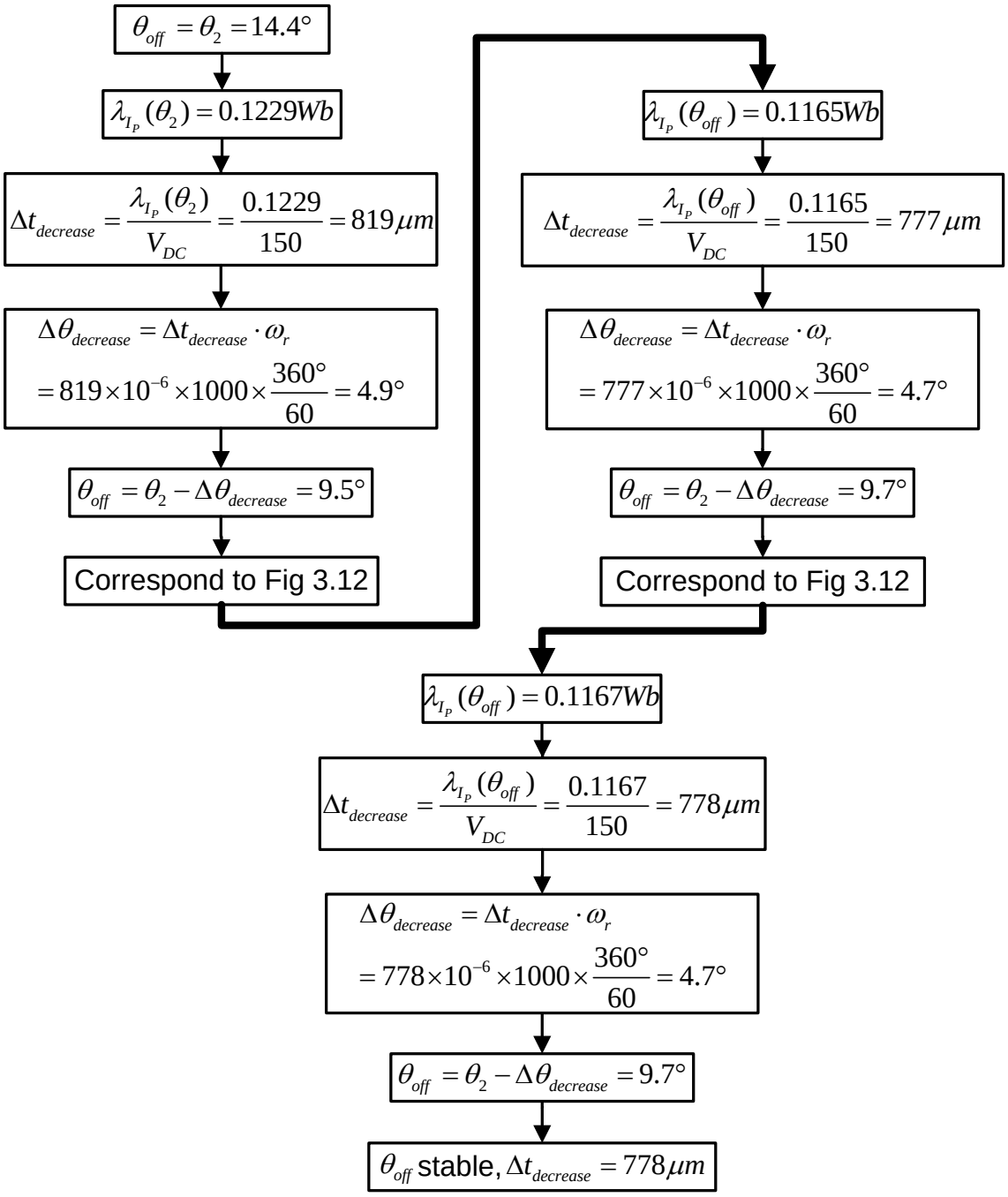

Fig 3.22 Current decrease time calculation flow chart (1000 rpm, 150 V DC bus)

In summary, the errors of the current increase and decrease times are within 1%. The accuracy can be improved by increasing the number of simulation steps in the FEA simulation with a sacrifice of simulation time. Therefore the angle calculated by the

proposed analytical approach is verified to agree with the one using the generic SRM control strategy. Afterwards, this method is used for the SRM design optimization in the following section.

3. 5 Case study of a 12/8 SRM rotor design

In this section, the proposed SRM design method using the current-fed FEA simulation is applied to a 12/8 SRM rotor design case study. The flow chart of the SRM design method is illustrated in Fig 3.23. For each design candidate, a constant-current-fed FEA simulation is performed to calculate the flux-linkage. Next, this flux-linkage is used to calculate the four angles of the excitation current profile. Then, the second current-fed FEA simulation is carried out to calculate the design candidate's performance. Finally, the optimization process moves to analyze the next design candidate. For the studied 12/8 SRM design, the stator is designed using the method in Yao's PhD dissertation [23], and no further optimization is done for the stator. In addition, the shaft is determined from the mechanical considerations and the diameter is fixed for the rotor design.

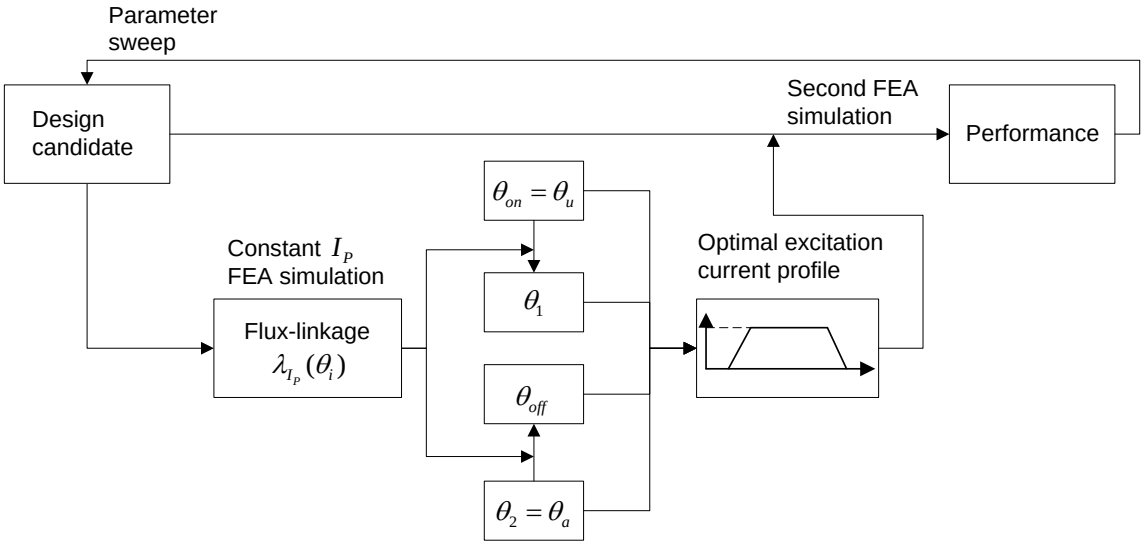

Fig 3.23 The proposed SRM design method flow chart

A lamination of the target SRM design is shown in Fig 3.24. The optimization variables are the rotor pole angle β_r and the rotor back-iron thickness b_{ry}.

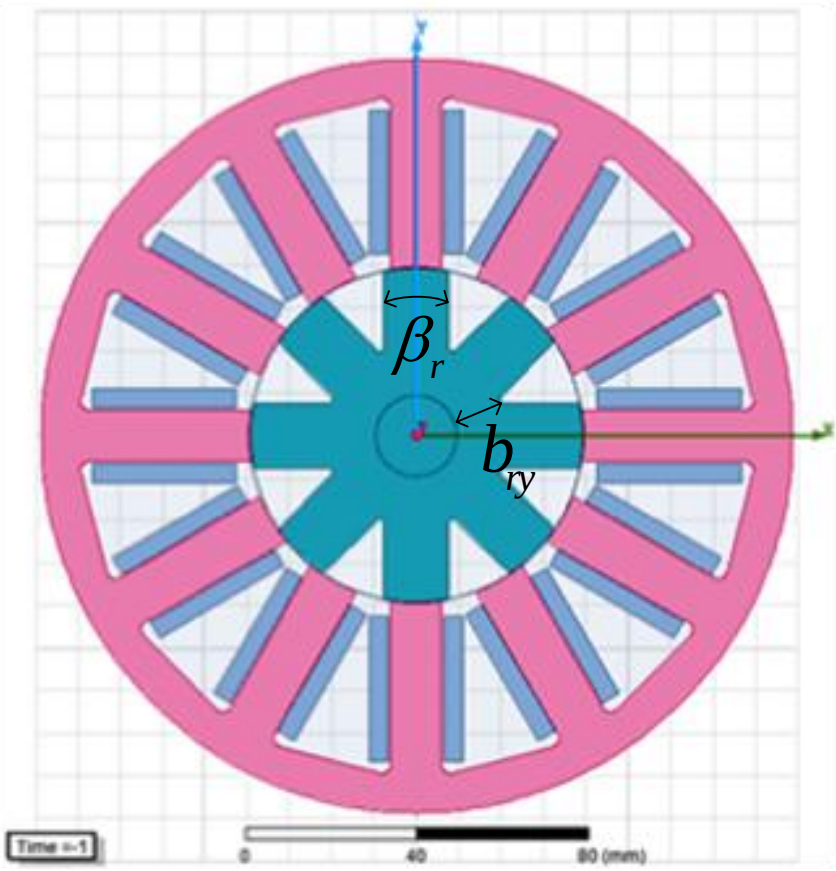

Fig 3.24 The 12/8 SRM lamination cross section view

Both β_r and b_{ry} are swept through their respective ranges to search for the optimal combination to have the highest torque. As the stator pole angle β_s is 18 ºand β_r needs to be greater than β_s, the sweep range of β_r is between 20 ºand 24 º, with steps of 1 º. For the back iron thickness b_{ry}, the minimum value is set as 14 mm according to the mechanical considerations. The sweep range of b_{ry} thus is between 14 mm and 22 mm, with steps of 2 mm.

Then, the design optimization is performed in a Matlab-Maxwell coupled simulation. A Matlab program calls Maxwell to run the FEA simulation, and then the simulation result is exported back to Matlab for the data processing. The Matlab program functions with respect to the design flow chart are shown in Fig 3.25, and they are listed in Appendix A at the end of this dissertation.

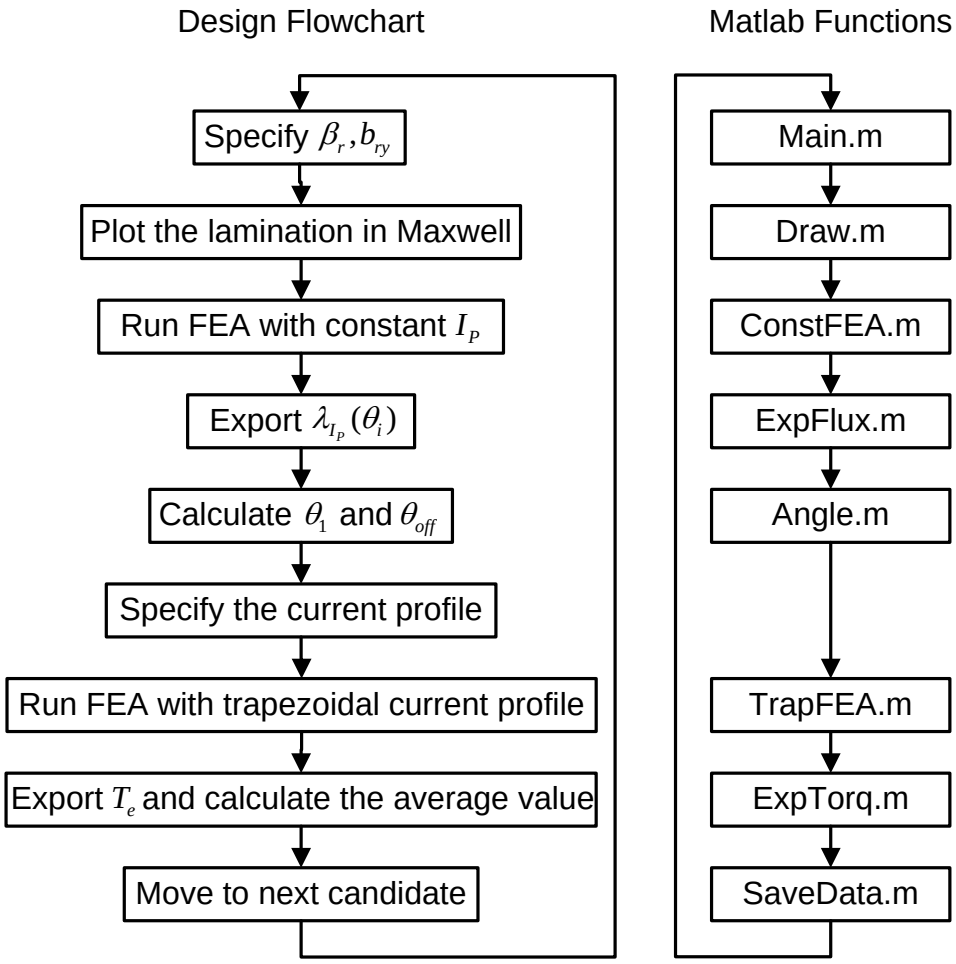

Fig 3.25 The 12/8 SRM rotor design flow chart and Matlab program functions

The optimization results are demonstrated in Fig 3.26.

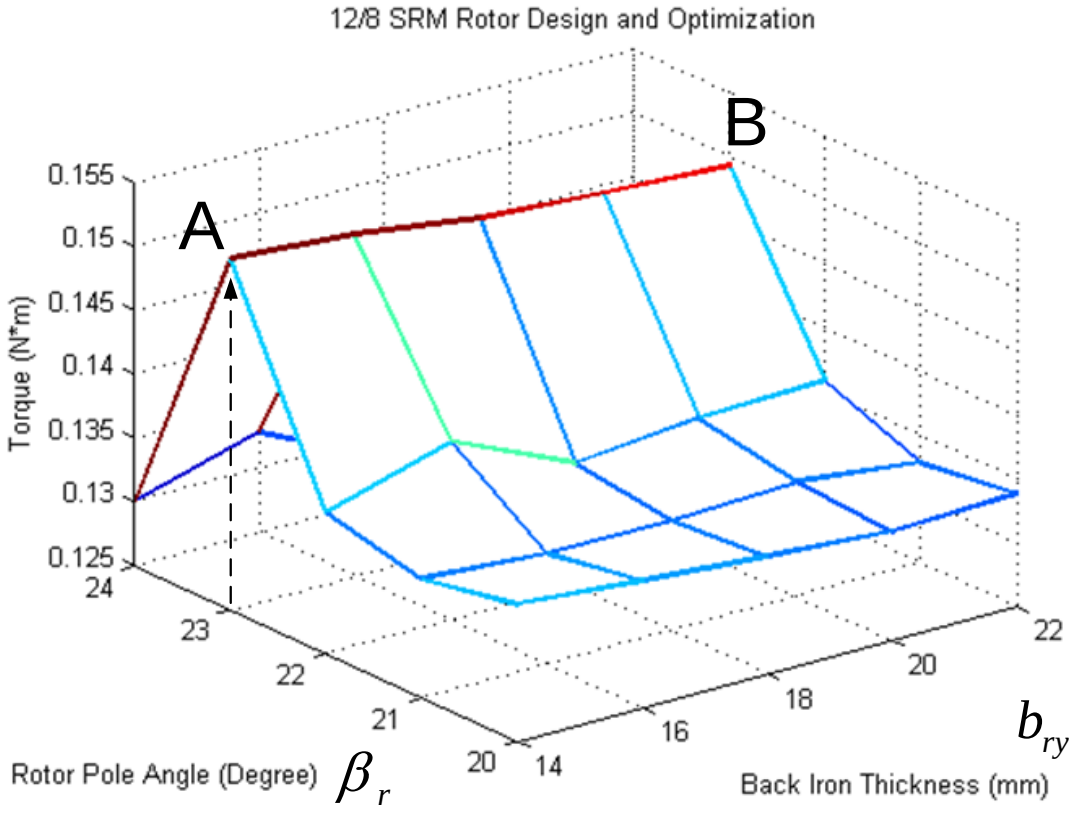

Fig 3.26 The 12/8 SRM rotor design optimization result

In Fig 3.26, the X and Y axes denote β_r and b_{ry}, and the Z axis denotes the average torque for each design. It is shown that along the line AB, the designs with $\beta_r = 23°$ have the highest torque value, which is about 0.15 N-m. The value of b_{ry} (between 14 mm and 22 mm) does not have much impact on the torque. Therefore, the optimal rotor design is $\beta_r = 23°$ and b_{ry} can be any value between 14 mm and 22 mm.

Particularly, for the design with $\beta_r = 23°$ and $b_{ry} = 20mm$, the trapezoidal excitation current profile and the resulting torque profile are shown in Fig 3.27 and 3.28 respectively. The current profile in Fig 3.27 is not a standard trapezoid because of the

linearized approximation between two simulation steps. For this design, the average torque is 0.154 N-m as indicated in Fig 3.28.

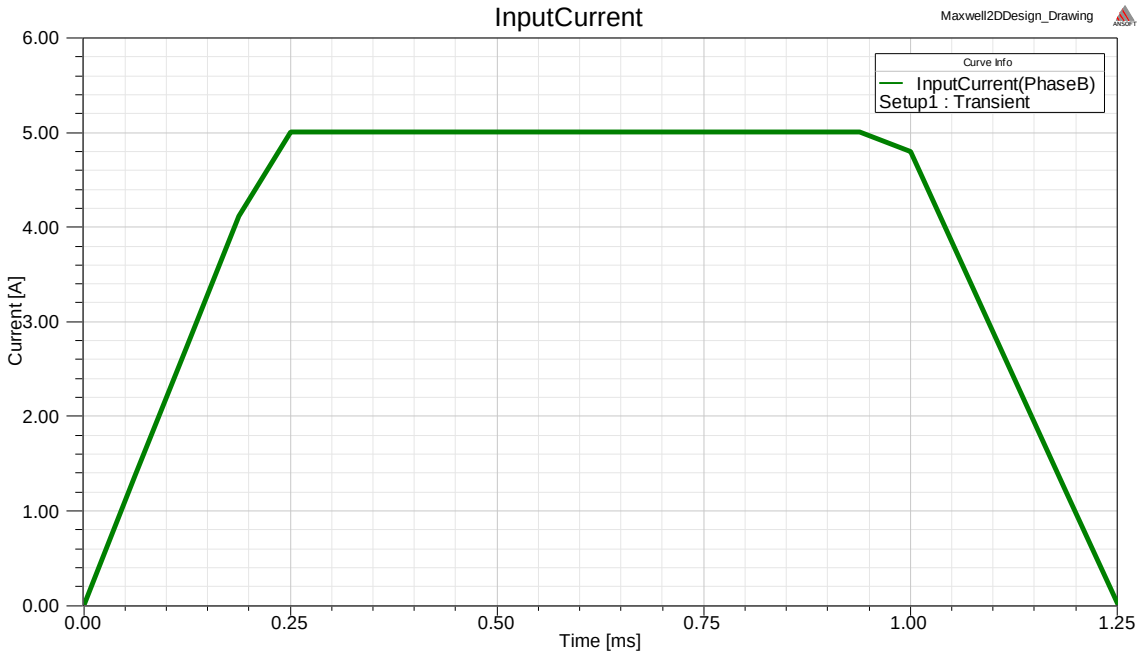

Fig 3.27 Trapezoidal excitation current profile ($\beta_r = 23°$ and $b_{ry} = 20mm$)

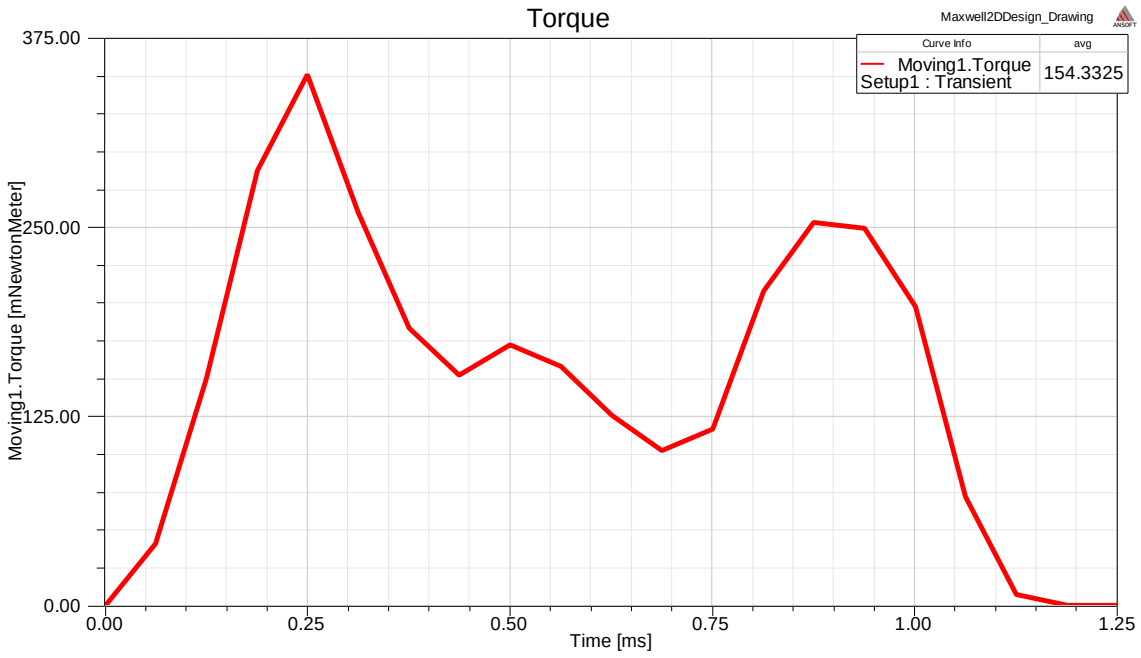

Fig 3.28 FEA calculated torque profile ($\beta_r = 23°$ and $b_{ry} = 20mm$)

The whole optimization process only takes about 75 mins to complete, and a total of 25 design candidates are swept during this time. So for each of the 25 design candidates, the proposed method takes less than 3 mins to yield the optimal excitation current profile and calculate the average torque.

3. 6 Chapter summary

In this chapter, a novel SRM design method using current-fed FEA simulation is proposed. The new method can first calculate the SRM excitation current profile by using a constant-current-fed FEA simulation, and then calculate the SRM performance with a second current-fed FEA simulation. The SRM design and optimization are achieved by running an automatic Matlab-Maxwell coupled simulation program, without the tedious modeling of a particular SRM. So it is portable to any SRM configurations and any dimensions. The proposed excitation current profile calculation approach is verified with FEA simulation results, and good accuracy is observed. At the end, this method is used to design a 12/8 SRM rotor, and an optimal design is found that has the highest average torque.

CHAPTER 4 High Speed SRM Design using Current-fed FEA Simulation

4. 1 Introduction

SRMs are attractive in the low power and high speed region. Therefore the SRM design and optimization method using the current-fed FEA simulation in Chapter 3 is applied to high speed machine design, in particular, a 50,000 rpm SRM design.

First the SRM configuration needs to be determined by selecting the stator and rotor pole numbers. The generic choice for ultra high speed applications is a 4/2 configuration. The lowest value of rotor poles minimizes the fundamental frequency of the SRM, and therefore the core losses and the switching losses. The SRM dimensions can be optimized based on the specific performance objective. In this work, the stator outer diameter D_s is fixed at 65 mm, because this allows the lamination steel sheet to be cut optimally. The stack length L and the shaft diameter D_{sh} are then determined and fixed from the mechanical considerations. The other geometric parameters of the lamination are the optimization variables, and the optimization objective is the torque. In other words, the goal is to optimize the geometric parameter values to have the maximum torque.

4. 2 High speed SRM design using current-fed FEA simulation

The target 4/2 SRM lamination (Fig. 4.1) is described by 7 geometric variables, which are the stator and rotor diameter D_s and D_r, the stator and rotor pole angle β_s and β_r, the stator and rotor back iron thickness b_{sy} and b_{ry}, and the shaft diameter D_{sh}. D_s is fixed at 65 mm, and the other parameters are the optimization variables.

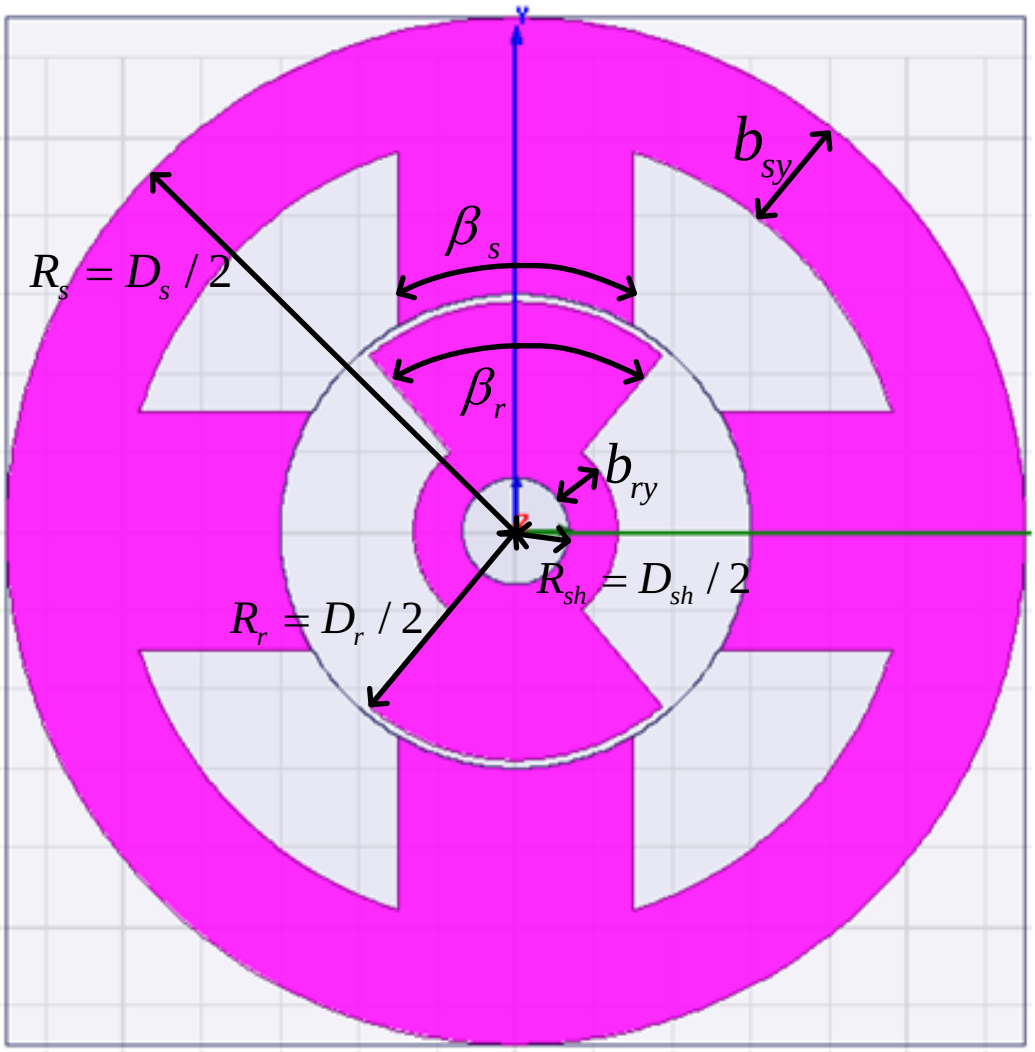

Fig 4.1 4/2 SRM lamination cross section view

At first, the initial design is found by using empirical values and equations. For example, a typical value [48] for the ratio of D_r over D_s is 0.5, so D_r is calculated to be 0.5*65=32.5 mm. The initial design's parameter values are listed in Table 4.1.

Table 4.1 Initial 4/2 SRM geometric variable values

D_r	β_s	β_r	b_{sy}	b_{ry}	D_{sh}
32.5 mm	60 º	80 º	10 mm	4 mm	12 mm

Next, the values of the geometric variables and other SRM design parameters are investigated as follows.

- b_{sy} b_{ry} and D_{sh}

The impact of b_{sy} and b_{ry} on the SRM performance (torque) is very small, as shown in the optimization results of Chapter 3 (Fig 3.26). In addition, the value of D_{sh} is fixed due to consideration for mechanical stress. For the purpose of minimizing the design space, these three variables are not included in the optimization process. Their values are fixed as shown in Table 4.1.

- The number of turns for the coil winding per phase N_{ph}

The generic method to calculate N_{ph} is based on the magnetic circuit as shown in Fig 4.2 and Fig 4.3, where R_s, R_r, R_g, R_y indicate the flux path reluctance elements in the stator pole, rotor pole, air-gap and the back iron, and the total flux for one phase is $N_{ph} I_P$.

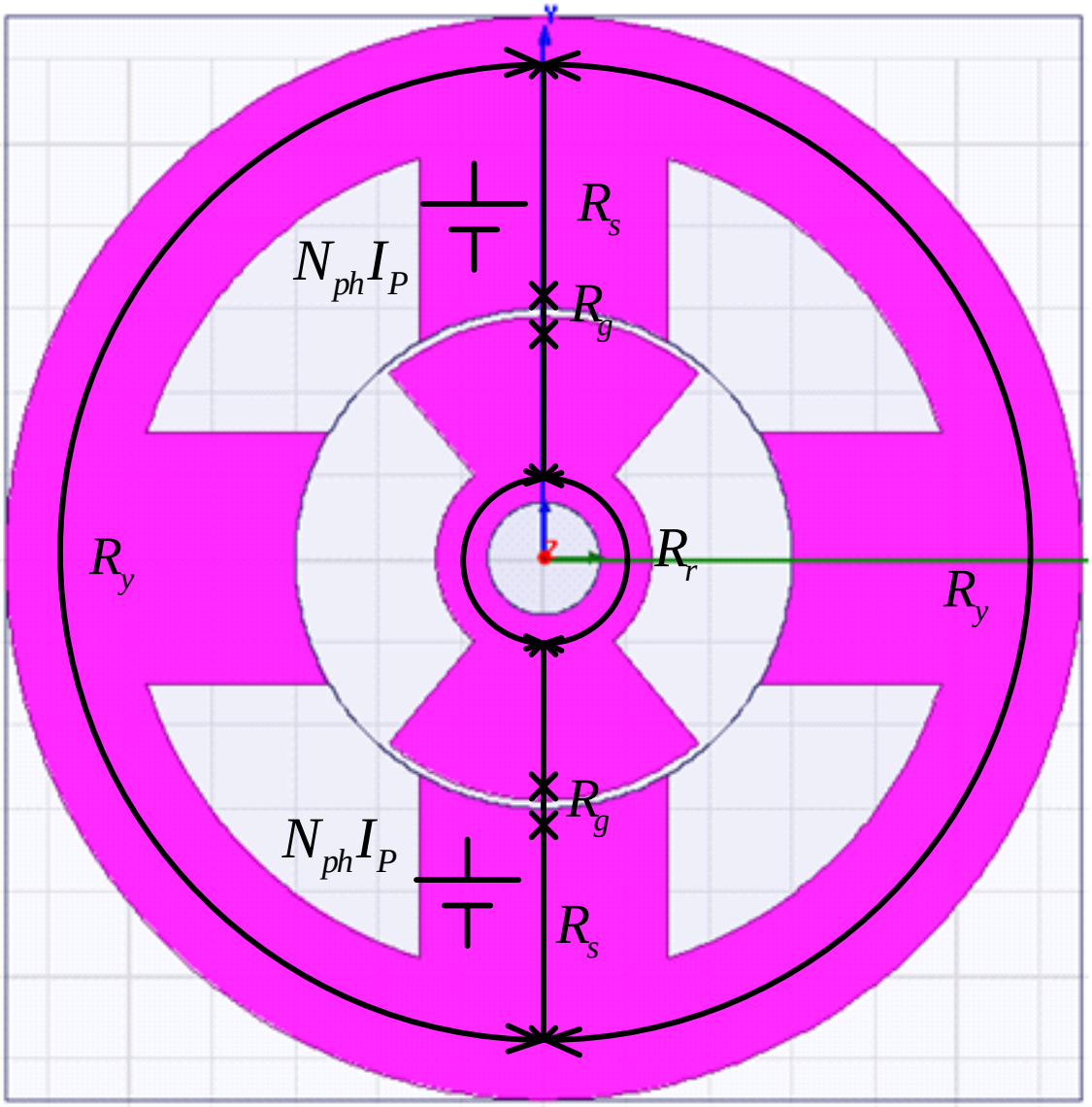

Fig 4.2 4/2 SRM lamination magnetic field (cross section view)

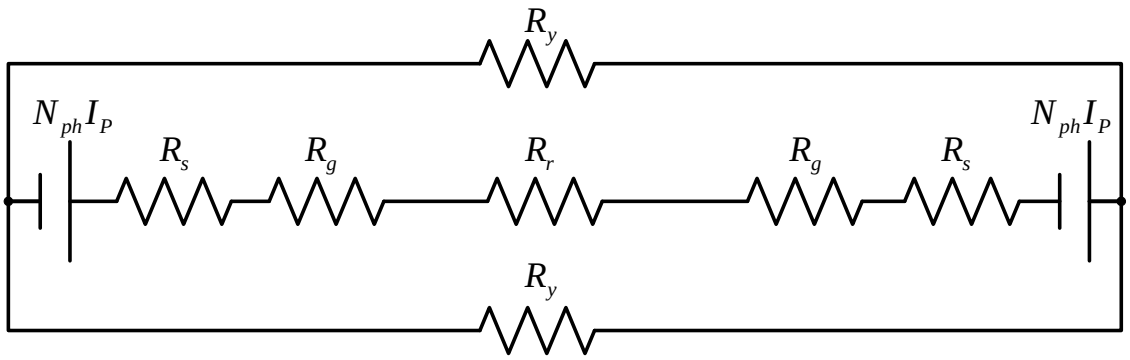

Fig 4.3 Magnetic circuit of the 4/2 SRM lamination

Because $R_g \gg R_s, R_r, R_y$, (4.1) is used to calculate N_{ph}, where $I_{\max}$ is the maximum current that the stator wire can carry, l_g is the air-gap length (l_g =0.5 mm for this work), and H_g is the maximum magnetic field strength in the air-gap. H_g is calculated by (4.2) where B_m is the saturated flux density of the core material (B_m =1.5 T for this work) and μ_0 is the magnetic permeability. Finally, N_{ph} is calculated to be equal to 70 for this work.

$$2H_g \cdot l_g = N_{ph} \cdot I_{\max} \tag{4.1}$$

$$H_g = B_m / \mu_0 \tag{4.2}$$

- Current-fed FEA simulation current peak value I_P

Because the values of b_{sy} b_{ry} and D_{sh} are fixed, the design space is reduced to three degrees of freedom (D_r, β_s and β_r). For each design candidate (defined as a set of D_r, β_s and β_r), the current-fed FEA simulation is carried out to calculate the average torque. However for the current-fed FEA simulation, the peak current I_P needs to be determined first.

The value of I_P is determined by the current density J_c and the stator coil area A_s. From a thermal consideration and for an air-cooled system, a typical value of J_c is 5

A/mm^2. Next, A_s is calculated based on the specific D_r, B_s and B_r values of each design candidate. The detail of A_s calculation can be found in Table 4.2.

The total current flowing in the stator coil is the product of J_c, A_s, and the fill factor constant Ff (Ff=0.3 for this work). The total current is calculated as the product of N_{ph} and I_p. Therefore, the value of I_p is calculated by (4.3):

$$I_p = \frac{J_c \cdot A_s \cdot Ff}{N_{ph}} \tag{4.3}$$

Table 4.2 4/2 SRM stator coil area calculation

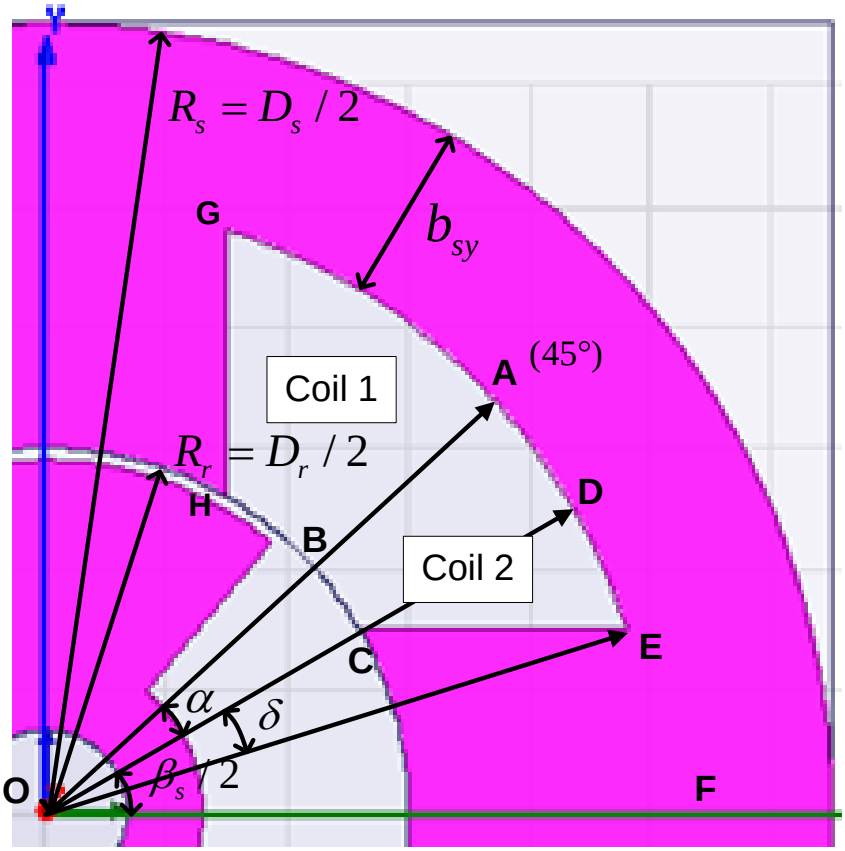

$\alpha = \pi / 4 - \beta_s / 2$	(4.4)
$S_{ABCD} = \alpha \cdot (AO^2 - BO^2) = \alpha \cdot ((D_s / 2 - b_{sy})^2 - (D_r / 2)^2)$	(4.5)

$$y_E = y_C = D_r / 2 \cdot \sin \frac{\beta_s}{2}$$	(4.6)
$$x_E = \sqrt{(D_s / 2 - b_{sy})^2 - y_E{}^2}$$	(4.7)
$$\angle EOF = \arctan(y_E / x_E)$$	(4.8)
$$\delta = \pi / 4 - \angle EOF$$	(4.9)
$$S_{DOE} = \delta \cdot (D_s / 2 - b_{sy})^2$$	(4.10)
$$S_{COE} = (x_E - x_C) \cdot y_C / 2 = (x_E - D_r / 2 \cdot \cos \frac{\beta_s}{2}) \cdot D_r / 2 \cdot \sin \frac{\beta_s}{2} / 2$$	(4.11)
$$S_{CDE} = S_{ODE} - S_{OCE}$$	(4.12)
$$A_s = S_{GHCE} = 2 \cdot (S_{ABCD} + S_{CDE})$$	(4.13)

Finally, the SRM lamination geometry variable optimization is carried out by way of sweeping the whole design space, as shown in Fig 4.4. Particularly, D_r is swept from 20 mm to 28 mm with steps of 2 mm; β_s is swept from 42 ºto 60 ºwith steps of 3 º; and β_r is swept from 65 ºto 80 ºwith steps of 3 º. For each design candidate, the current-fed FEA simulation is used to calculate the torque.

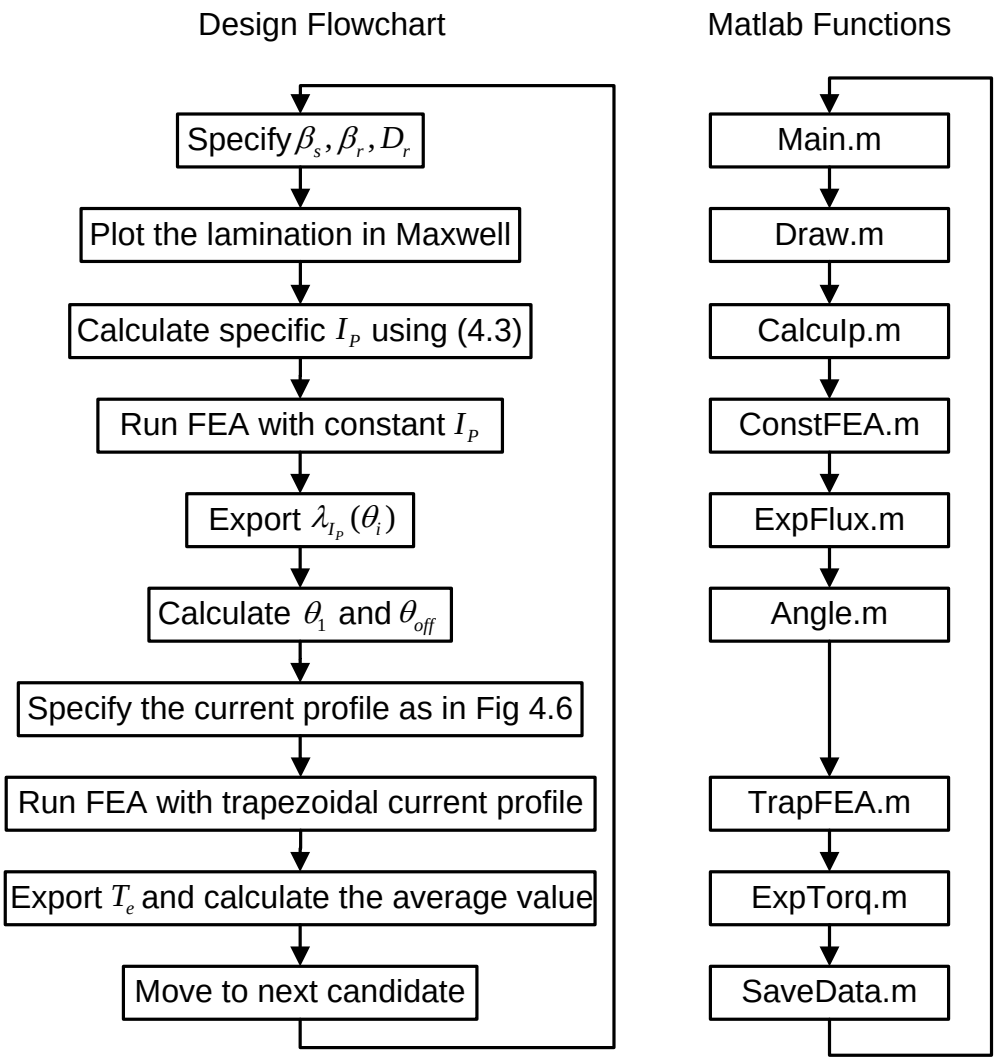

Fig 4.4 The 4/2 SRM design flow chart and Matlab program functions

The optimization results are presented in Fig. 4.5.

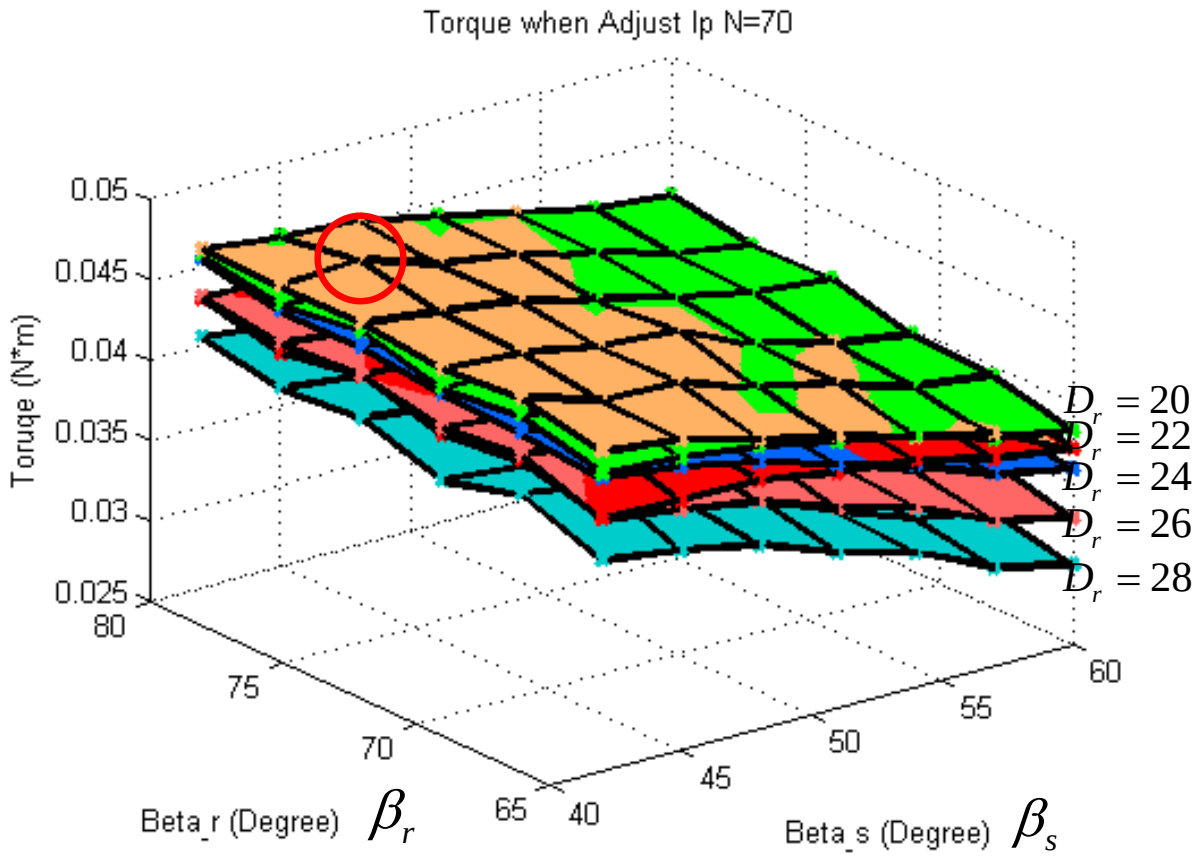

Fig 4.5 The 4/2 SRM design optimization results

In Fig. 4.5, the X and Y axes denote β_r and β_s respectively, the different layers denote different values of D_r, and the Z axis denotes the torque. The optimal design in terms of highest torque is identified by the circle on the top left, which is β_r = 77 º, β_s = 45 º, and D_r = 22 mm.

For the design with β_r = 77 º, β_s = 45 º, and D_r = 22 mm, the trapezoidal excitation current profile and the resulting torque profile are shown in Fig 4.6 and 4.7. For this design, the average torque is 0.046 N-m as indicated in Fig 4.7.

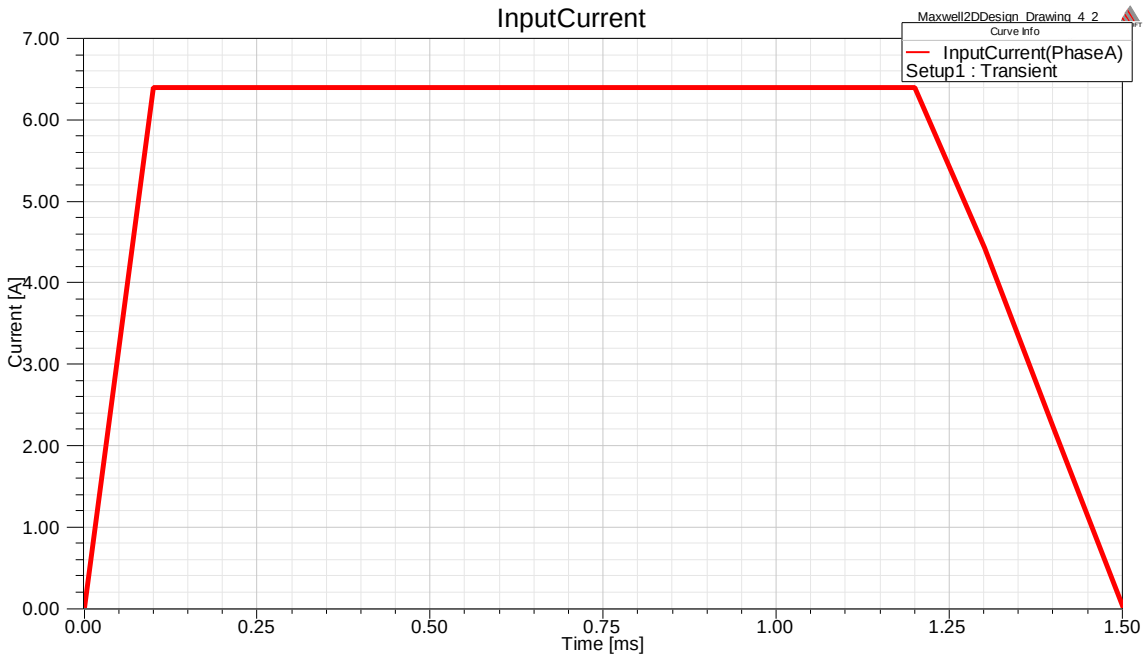

Fig 4.6 Trapezoidal excitation current profile (β_r = 77 º; β_s = 45 º; and D_r = 22 mm)

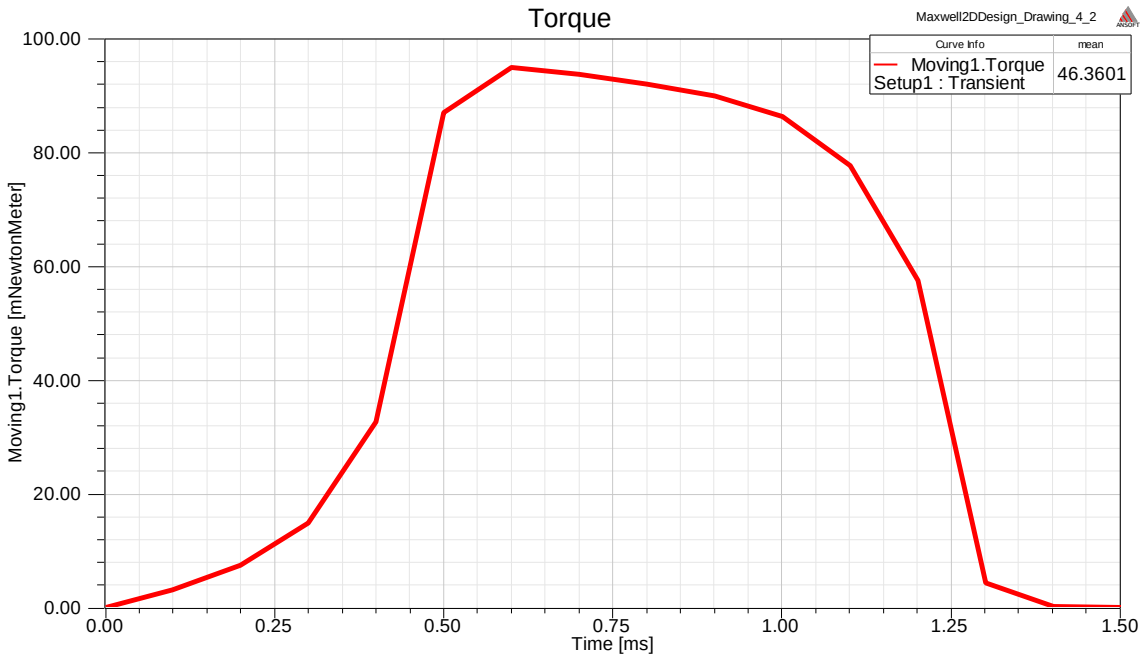

Fig 4.7 FEA calculated torque profile (β_r = 77 º; β_s = 45 º; and D_r = 22 mm)

4. 3 Sensitivity analysis of the optimal design

Due to reasons like modeling errors and manufacturing tolerances, the performance of a manufactured machine may vary from the design calculations. Therefore to investigate how those variations affect the machine performance, a sensitivity analysis is carried out in this section. The investigated variables in this section are the stator pole angle β_s, the rotor pole angle β_r, the rotor diameter D_r, the rotor back-iron thickness b_{ry}, and the stator back-iron thickness b_{sy}. The sensitivity analysis is performed in a numerical way. This means that the geometric variables are varied by small amounts around the value used in the optimal design, and the resulting machine performance is evaluated.

4.3.1 Stator pole angle β_s

The optimal stator pole angle β_s is found to be 45 ºin Fig 4.5 with steps of 3 ºin the range between 42 ºand 60 º. For the sensitivity analysis β_s is varied around the optimal value, particularly between 40 ºand 50 ºwith small steps of 1 º. The other variables remain the same as calculated in Section 4.2. The resulting variations of the SRM performance are presented in Fig 4.8. In the upper diagram, the horizontal axis is the stator pole angle β_s, and the vertical axis shows how the average torque varies with β_s. The lower diagram shows the variation percentage, which is defined as $(T_i - T_{avg})/T_{avg}$ ($T_{avg} = \sum T_i / 11$, and i = 1,2,…, 11). The percentage gives a straightforward indication of how significantly the average torque varies in the range between 40 ºand 50 º. Fig 4.8 shows that the SRM has the highest torque when β_s =46 º. In addition, the torque variation percentage is between -4% and 4%.

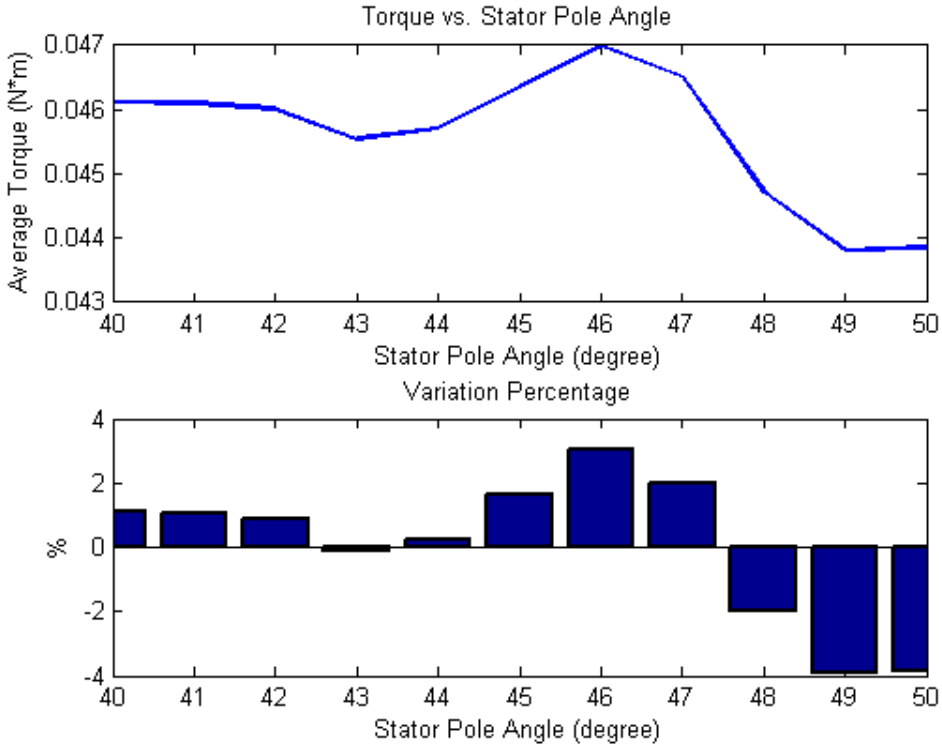

Fig 4.8 The sensitivity analysis of the SRM torque to the stator pole angle β_s

4.3.2 Rotor pole angle β_r

The stator pole angle β_s is now fixed at 45^0. The rotor pole angle β_r , which is found to be 77 ºin Section 4.2, is changed now. For the sensitivity analysis, β_r is varied with small steps of 1 ºbetween 72 ºand 82 º. The other variables are not changed. The resulting variations of the SRM performance are presented in Fig 4.9. It shows that the SRM has the highest torque when β_r =76 º. In addition, the torque variation percentage is between -2% and 3%.

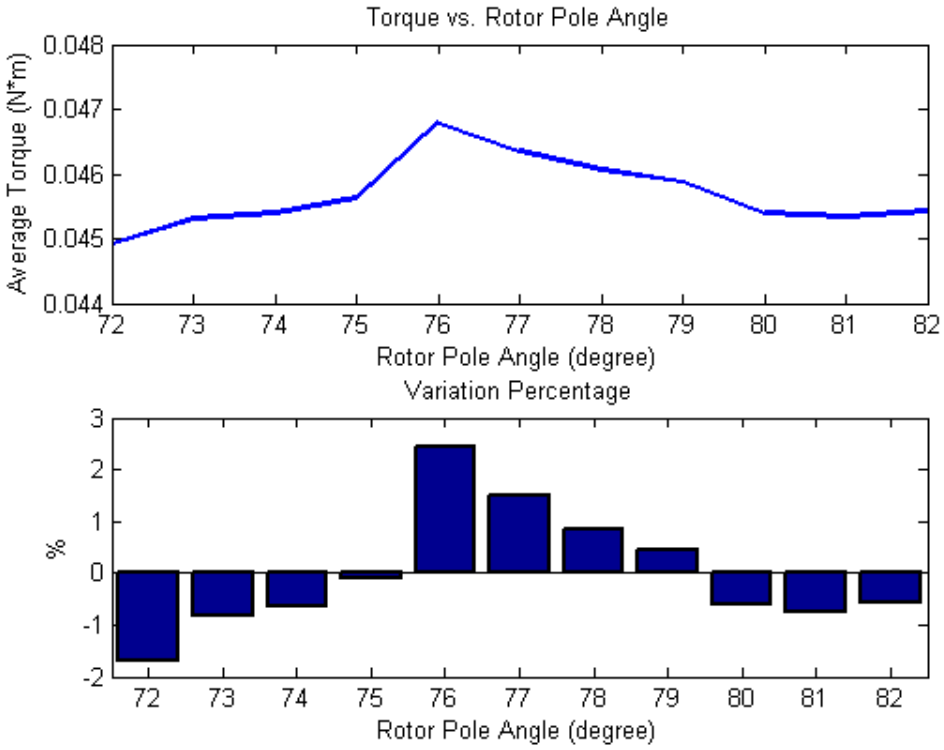

Fig 4.9 The sensitivity analysis of the SRM torque to the rotor pole angle β_r

4.3.3 Rotor diameter D_r

The rotor diameter D_r is found to be 22 mm in Section 4.2. For the sensitivity analysis, the values of β_s and β_r are fixed, and D_r is varied between 20 mm and 24 mm with small steps of 0.4 mm. The other parameters do not change. The resulting variations of the SRM performance are presented in Fig 4.10. It shows that the SRM has the highest average torque when D_r =21.2 mm. In addition, the torque variation percentage is between -2% and 2%.

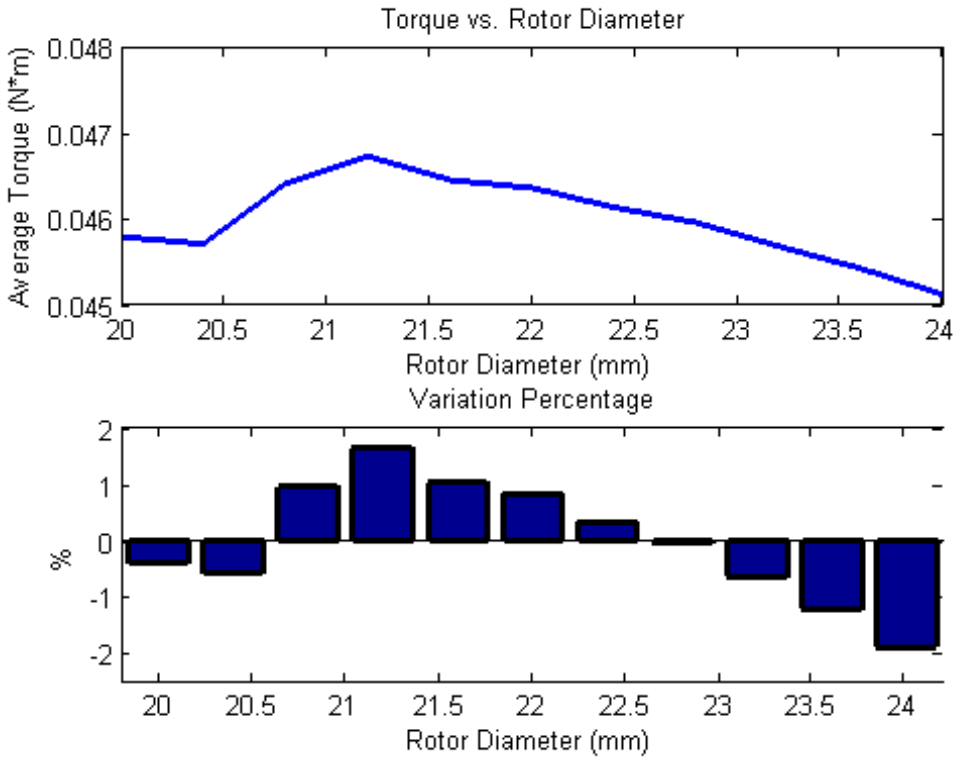

Fig 4.10 The sensitivity analysis of the SRM torque to the rotor diameter D_r

4.3.4 Stator back-iron thickness b_{sy}

The stator back-iron thickness b_{sy} remains constant at 4.5 mm in Section 4.2. For the sensitivity analysis, b_{sy} is varied between 4 mm and 5 mm with small steps of 0.1 mm. The resulting variations of the SRM torque are presented in Fig 4.11. It shows that the torque variation percentage is very small (between -0.6% and 0.5%).

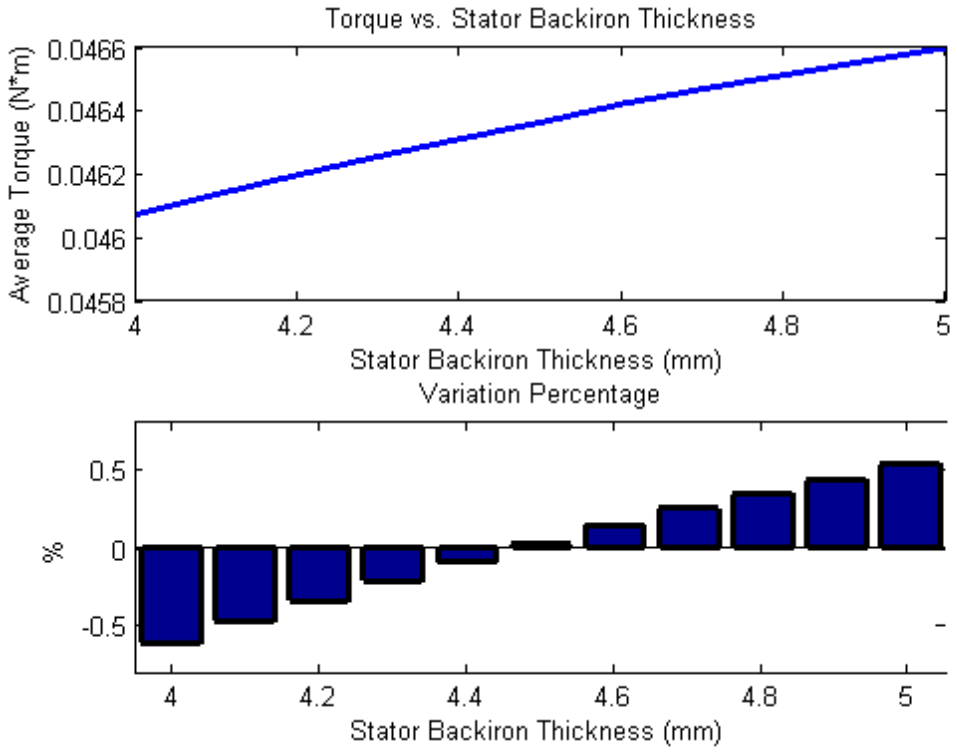

Fig 4.11 The sensitivity analysis of the SRM torque to the stator back-iron thickness b_{sy}

4.3.5 Rotor back-iron thickness b_{ry}

The stator back-iron thickness b_{ry} remains constant at 3.1 mm in Section 4.2. For the sensitivity analysis, b_{ry} is varied between 2.6 mm and 3.6 mm with small steps of 0.1 mm while keeping other variable values unchanged. The resulting variations of the SRM torque are presented in Fig 4.12. It shows that the torque variation percentage is also very small (between -0.5% and 0.5%).

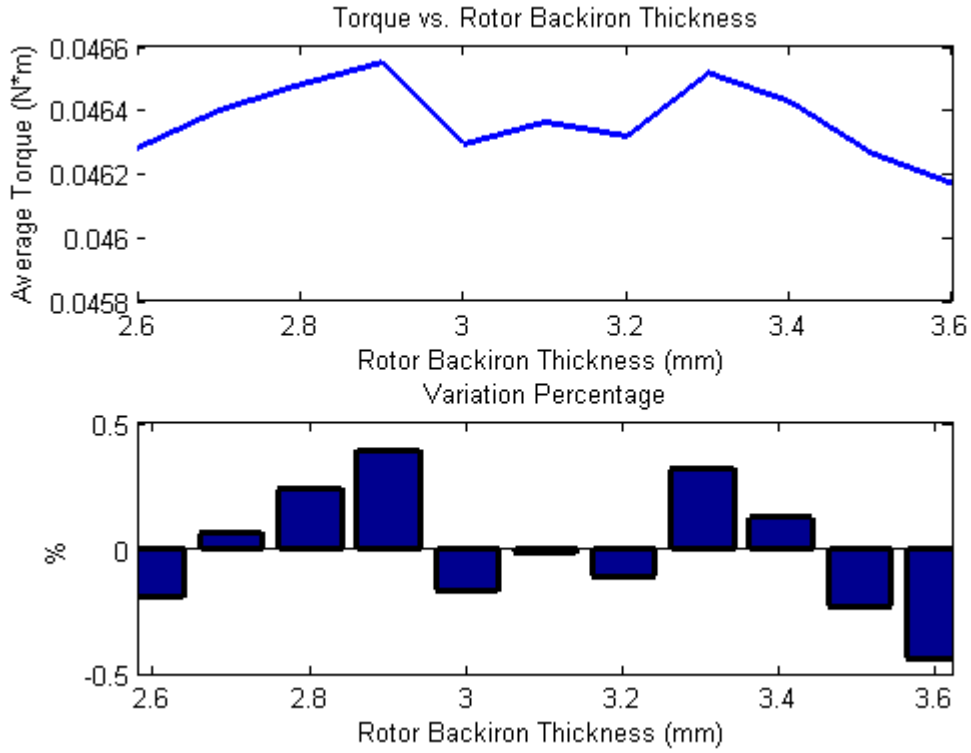

Fig 4.12 The sensitivity analysis of the SRM torque to the rotor back-iron thickness b_{ry}

The sensitivity analysis results indicate that the machine performance is mostly sensitive to the stator pole angle β_s (-4% and 4%). Therefore, more attention should be paid to β_s in order to ensure good agreement between the design calculation and the actual machine performance. Moreover the impact of b_{sy} and b_{ry} on the SRM torque is very small (-0.5% and 0.5%). Therefore b_{sy} and b_{ry} are excluded from the design space in Section 4.2, and only the optimization of β_s, β_r and D_r values are investigated.

4. 4 Chapter summary

In this chapter, the design of a complete 4/2 SRM is investigated, and the geometric variables are optimized to achieve the highest torque. First the SRM lamination is described using 7 geometric variables. Next the calculation of the b_{sy}, b_{ry}, D_{sh} and N_{ph} values is introduced, and the design space is reduced degrees of freedom (D_r, β_s and β_r). Then the SRM design optimization is carried out by sweeping the design space, and the current-fed FEA simulation is used. The optimal design in terms of highest torque is found to be β_r = 77 º, β_s = 45 º, and D_r = 22 mm. In the end, the sensitivity analysis of the SRM performance to the geometric variables is presented to identify that the stator pole angle β_s is the most influencing variable.

CHAPTER 5 High Speed SRM Design with a Flux-bridge Rotor

5. 1 Introduction

One of the challenges facing a high speed SRM is the high viscous drag on a rotor with an uneven surface. However by nature the rotor poles on a SRM must have sufficient saliency and therefore present an uneven surface. Several ideas proposed by others include wrapping some kind of non-magnetic tape [28] around the rotor in order to create some kind of cylindrical shape. This chapter focuses on creating a smooth rotor surface without requiring tape. Instead a very thin circular bridge is provided that connects the top of one rotor pole to the top of the next rotor pole, thus creating a cylinder as shown in the right hand diagram of Fig. 5.1. The regular rotor without a flux bridge is shown on the left as a comparison.

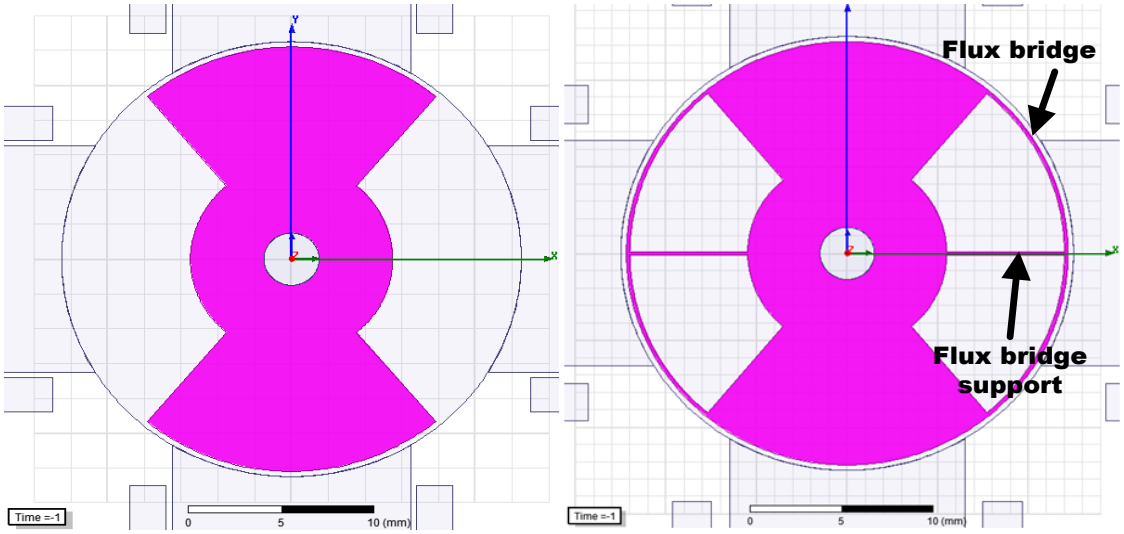

Fig 5.1 Cross section view of the SRM designs with (right) and without (left) flux bridge on the rotor

The benchmark design for a 50,000 rpm SRM is investigated in Chapter 4 as a first step towards machines that will run at much higher speeds. For the enhanced rotor design with a flux bridge, the flux bridge must be supported using one or more radial struts to account for centrifugal stress. Therefore a single radial strut located at the midpoint of the

flux bridge is considered. The flux bridges are thin enough to be sufficiently mechanically strong but also to saturate magnetically, thus behaving as air for the flux. This idea was first proposed in [58], but no in-depth research has been carried out in the literature. Therefore the electromagnetic behavior of the flux bridge topology and different flux bridge thicknesses are compared in the following section.

5. 2 50,000 rpm SRM design with a flux-bridge rotor

The electromagnetic characteristics of the proposed rotor design are studied using FEA simulation. The inductance and torque profiles of the design with the flux-bridge rotor are shown in Fig 5.2, and the design with a regular rotor are shown in Fig 5.3.

In Fig 5.2, when a rotor pole is at the aligned position (point X), for phase A for example, the phase A inductance is at the maximum value of 24 mH (Fig 5.2 top diagram). When that rotor pole leaves the aligned position (at point Y), the inductance does not drop symmetrically with respect to the increased slope, but remains at a high value. When the rotor pole comes to the unaligned position (point Z), the inductance has a little sag due to the existence of the flux bridge strut, shown by the circle in Fig 5.2. After the flux bridge support leaves the stator pole, the inductance recovers to around 21.5 mH at point W. Then, when the phase A is excited again, the inductance drops almost instantaneously to the minimum value of 5 mH at point S, and ramps up to the maximum value at point X’ as the rotor pole approaches the other stator pole of phase A.

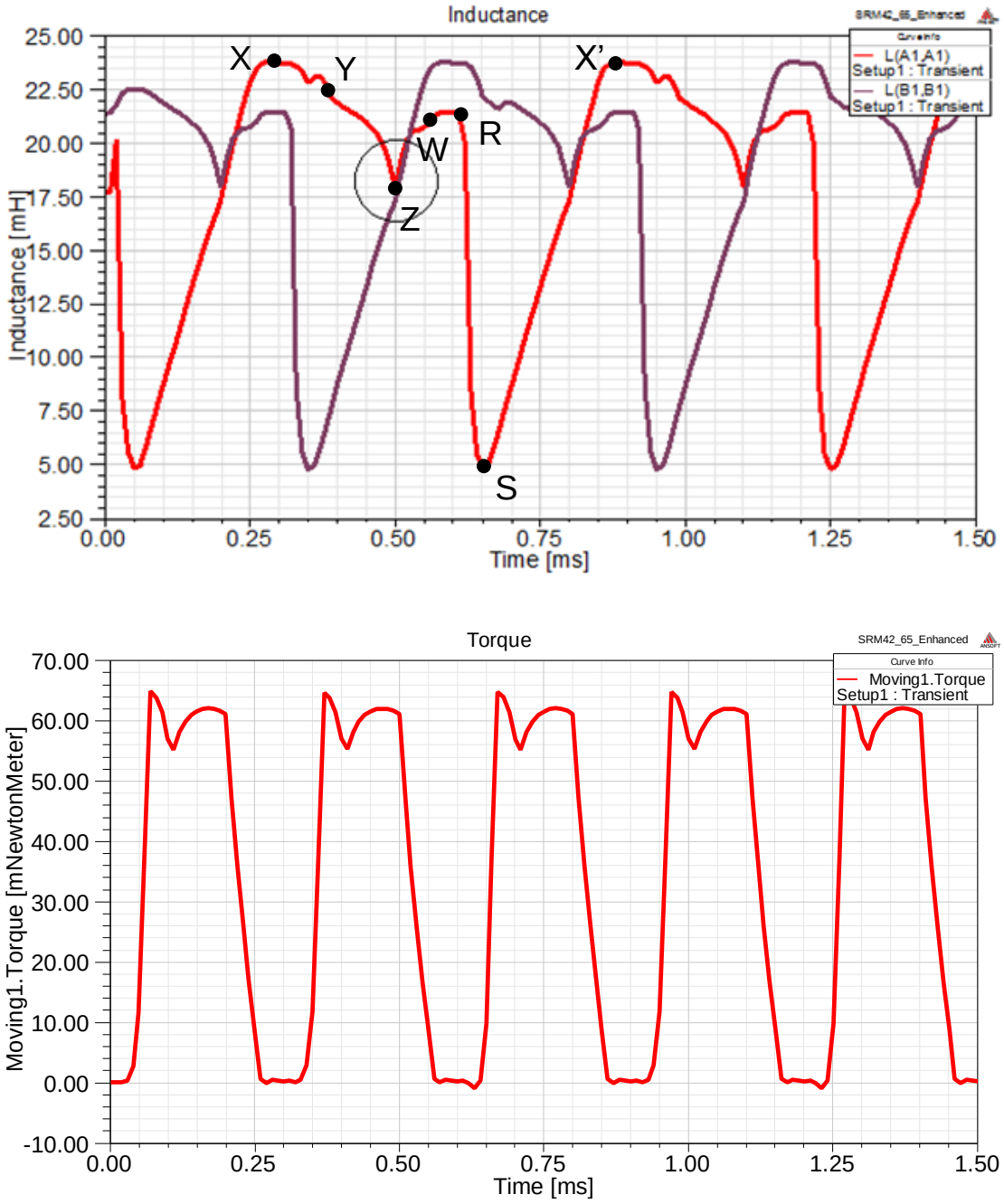

Fig 5.2 FEA simulation inductance (top) and torque (bottom) profiles for the flux-bridge rotor design as the rotor turns.

For the regular 4/2 SRM design, which has no flux bridge on the rotor, the inductance profile has symmetrically increasing and decreasing slopes when the rotor pole approaches and leaves the stator pole (Fig 5.3 top diagram). As shown in the top diagrams of Fig 5.2 and Fig 5.3, the inductance profiles are very different compared to each other, and so is the torque profile (bottom diagrams).

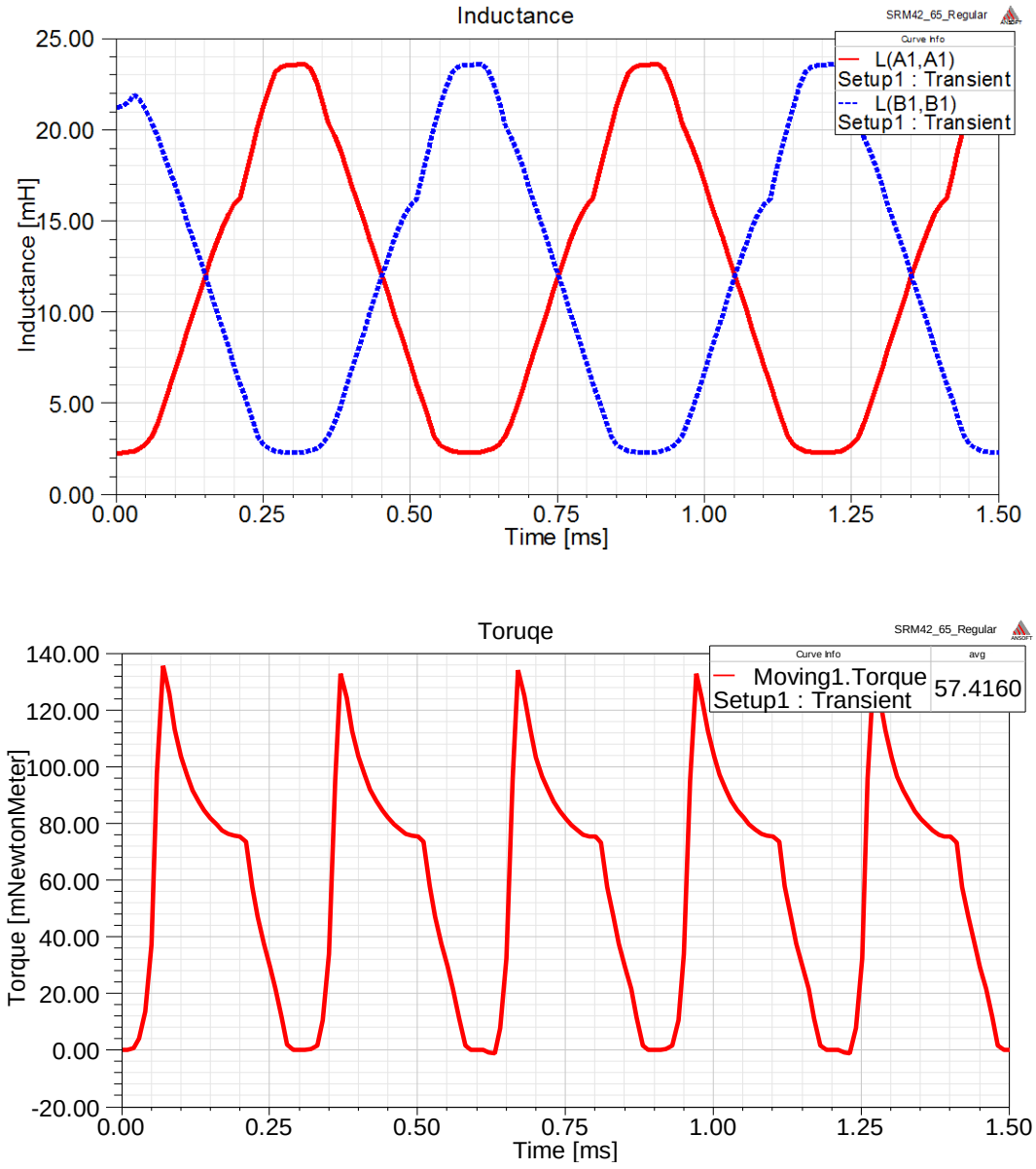

Fig 5.3 FEA simulation inductance (top) and torque (bottom) profiles for the regular rotor design.

To investigate the impact of different flux bridge thicknesses on SRM performance, the FEA simulation results of the SRM rotor design with different flux bridge thicknesses are presented in Fig 5.4. The inductance profile is shown on the top and the torque profile is shown on the bottom. The black dotted curve indicates the SRM design with the regular rotor (no flux bridge), the red solid curve indicates the design with a 0.2 mm thick flux bridge on the rotor, and the blue dash curve indicates the one with a 0.4 mm thick flux bridge on the rotor. Comparing the solid curve (0.2 mm flux bridge) to the dotted curve (regular rotor), there is an inductance sag in the decreasing slope as discussed in Fig 5.2 and 5.3, and the average torque is reduced from 57.4 mN-m (no flux bridge) to 34.6 mN-m (0.2 mm flux bridge) by 39.7%. Comparing the dash curve (0.4 mm flux bridge) to the solid curve (0.2 mm flux bridge), the inductance sag in the decreasing slope is smaller and the minimum inductance value is increased from 5 mH to 8.2 mH; the average torque is reduced by 35.2% from 34.6 mN-m to 22.4 mN-m.

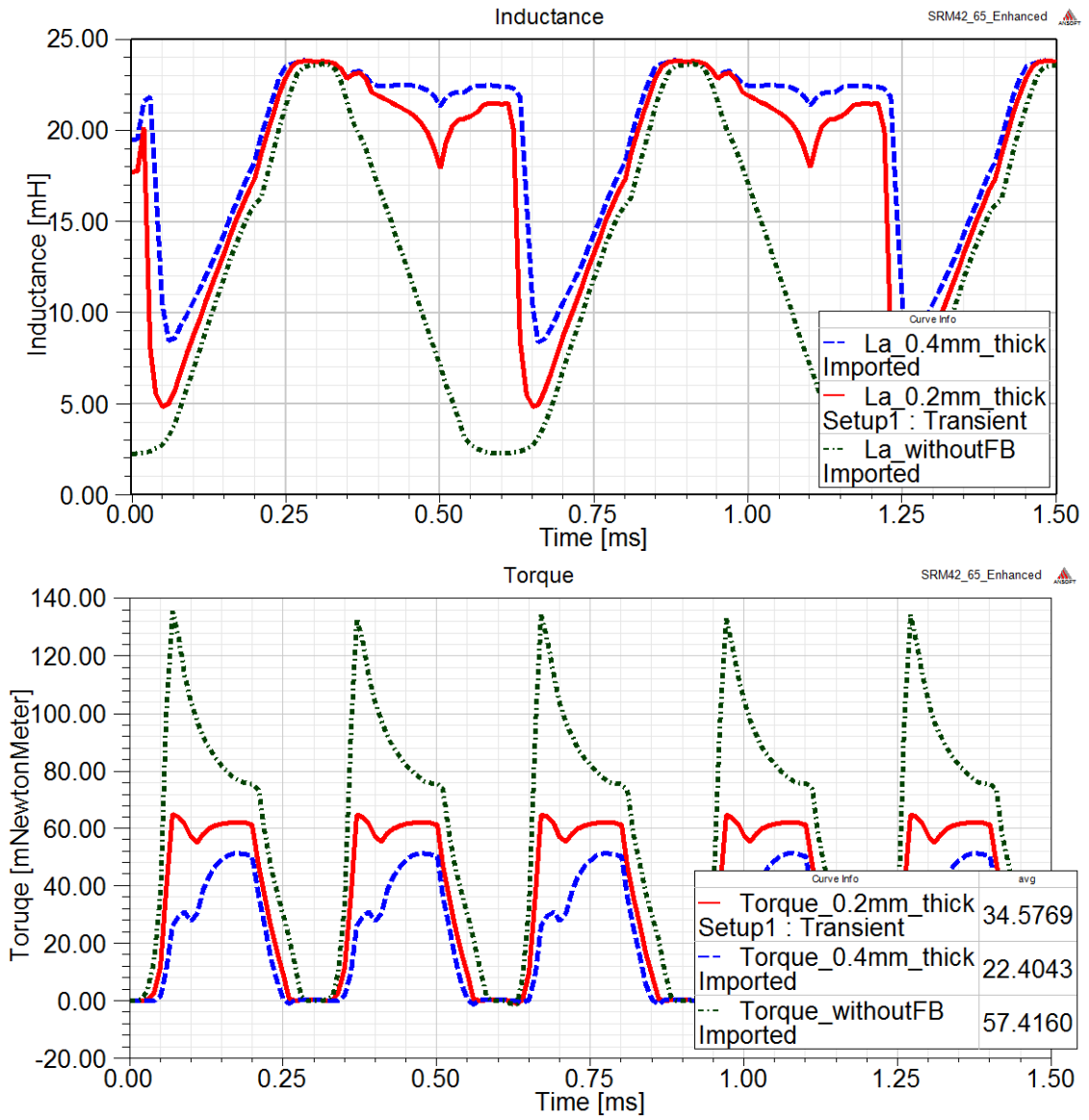

Fig 5.4 FEA simulation results for different flux bridge thickness comparison.

The reason behind the reduction of the average torque for a thicker flux bridge is the increase of the minimum inductance value. Recall that the ratio between the maximum and the minimum inductance values determines the torque that can be produced by a SRM. However in practice, the flux bridge thickness cannot be too small given the limitations from the mechanical strength considerations and the manufacturing capability. Therefore, the flux bridge of the SRM prototype rotor is chosen to be 0.5 mm, and the experimental results of the fabricated prototype is presented in the following section.

5. 3 Experimental results

To validate the FE analysis, a prototype is built and the rotor picture is shown in Fig 5.5. In order to compare the rotor with a flux bridge to the regular rotor, two rotors are fabricated. One rotor has a flux bridge (called the *enhanced rotor* for the rest of this dissertation), and the other does not (called the *regular rotor*).

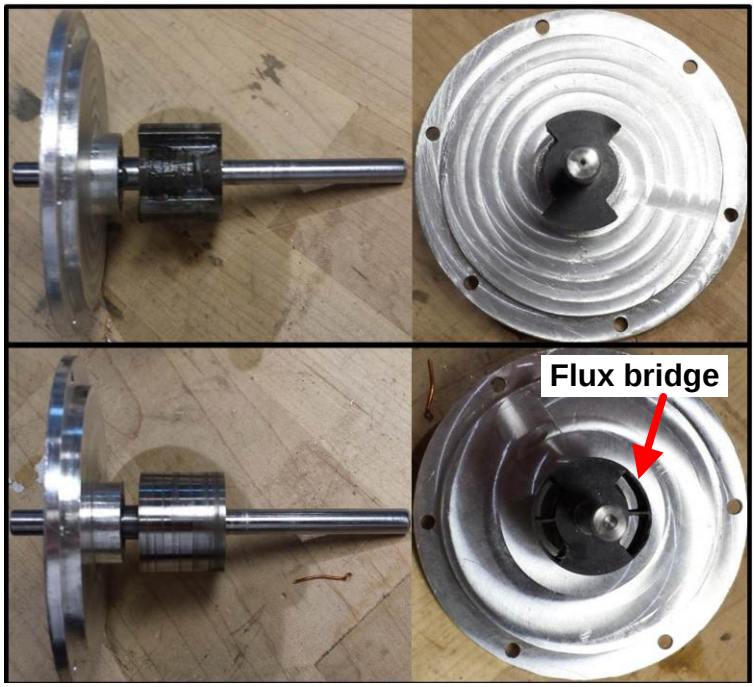

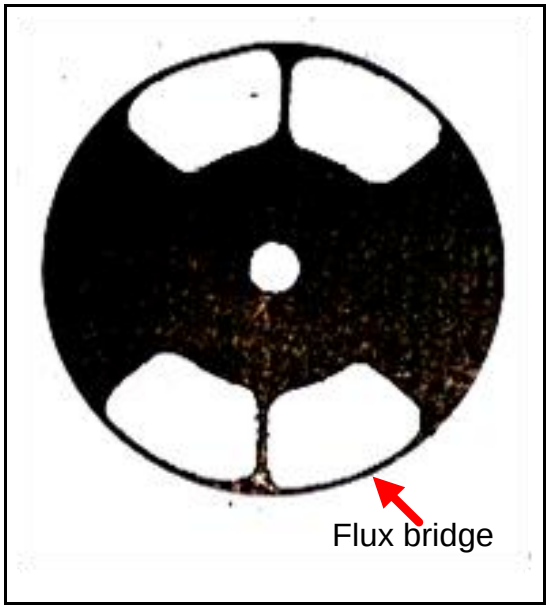

Fig 5.5 Photograph of the prototype motor: rotor (top), lamination (bottom)

The machine with a regular rotor is tested at a reduced initial speed of 10,000 rpm in order to validate the electromagnetic design before stressing the bearings. The experimental results of the current and voltage waveforms are shown in Fig. 5.6 (top diagram), where the upper two channels are the current traces and the bottom two channels are the voltage traces. For the test of 10,000 rpm, the period with respect to the fundamental frequency is $\frac{1}{\frac{10000\times 2}{60}} = 3ms$. In Fig 5.6, the interval between two vertical axes is 1 ms, and the interval between the two arrows is 3 ms, so the testing speed is 10,000 rpm.

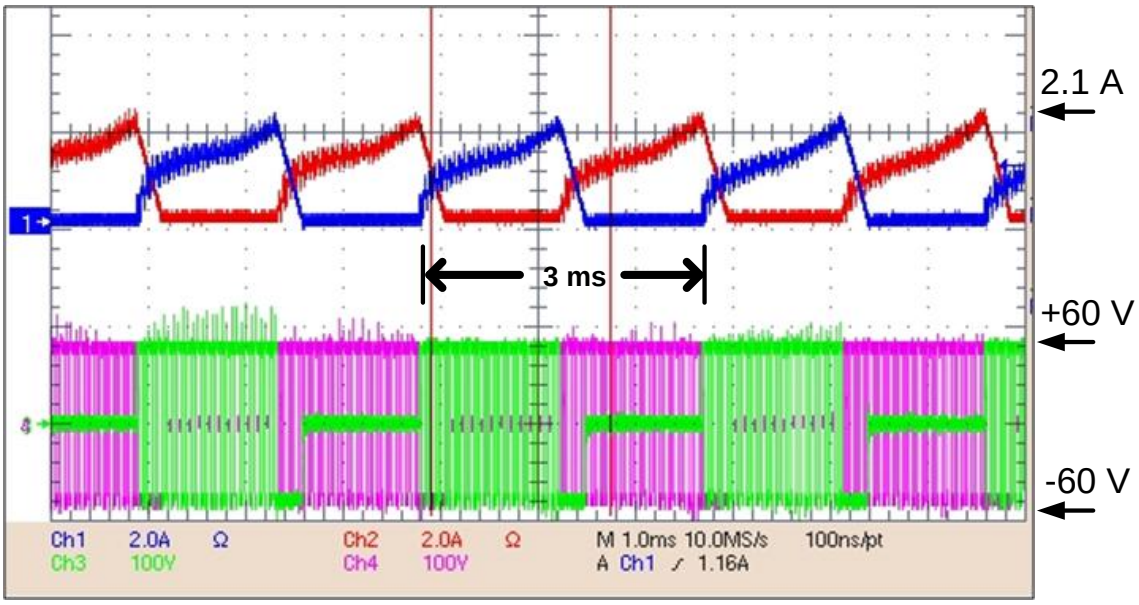

Fig 5.6 Experimental results for the SRM prototype with the regular rotor at 10,000 rpm.

In Fig 5.6, the red and purple traces are the phase A waveforms, and the blue and green ones are the phase B waveforms. There is good symmetry between the two phases, and the peak current is about 2.1 A. The machine is operated at no load, and an open-loop control is adopted for the control strategy. A FEA simulation for the prototype machine running at 10,000 rpm steady state is executed, and the results are presented in Fig 5.7.

The FEA simulated current profile shows that the peak current is about 2 A. This shows there is good agreement between the experimental current waveform and the simulation result. Therefore, the simulation provides sufficient confidence to predict the prototype machine performance, and it is used to further estimate the SRM prototype inductance and torque profiles.

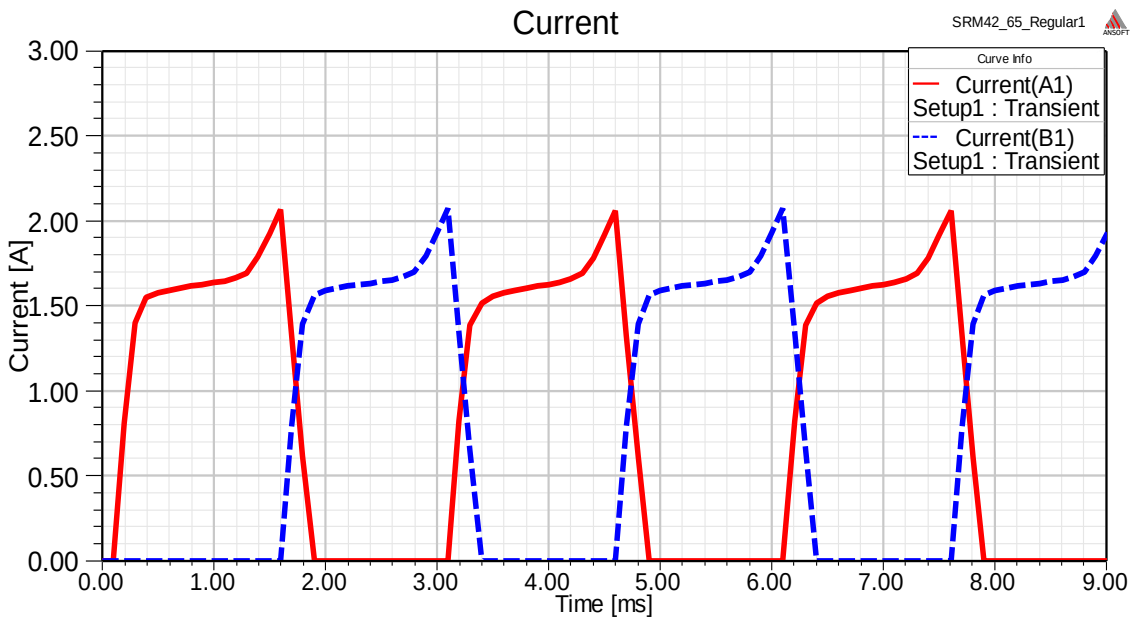

Fig 5.7 FEA simulation results for the SRM prototype with the regular rotor at 10,000 rpm.

The FEA simulation result of the inductance profile is shown in Fig 5.8, where the red curve denotes the Phase A inductance and the blue one denotes the Phase B inductance. The mutual inductance is denoted by the black curve, which is around zero. The maximum inductance for both phases is 12.5 mH, and the minimum inductance is 2.4 mH. Due to the manufacturing limitations, the prototype air gap is increased from 0.3 mm (the original design) to 0.5 mm, and this leads to the decrease of the maximum inductance value from 25 mH in the top diagram of Fig 5.3 to 12.5 mH in Fig 5.8.

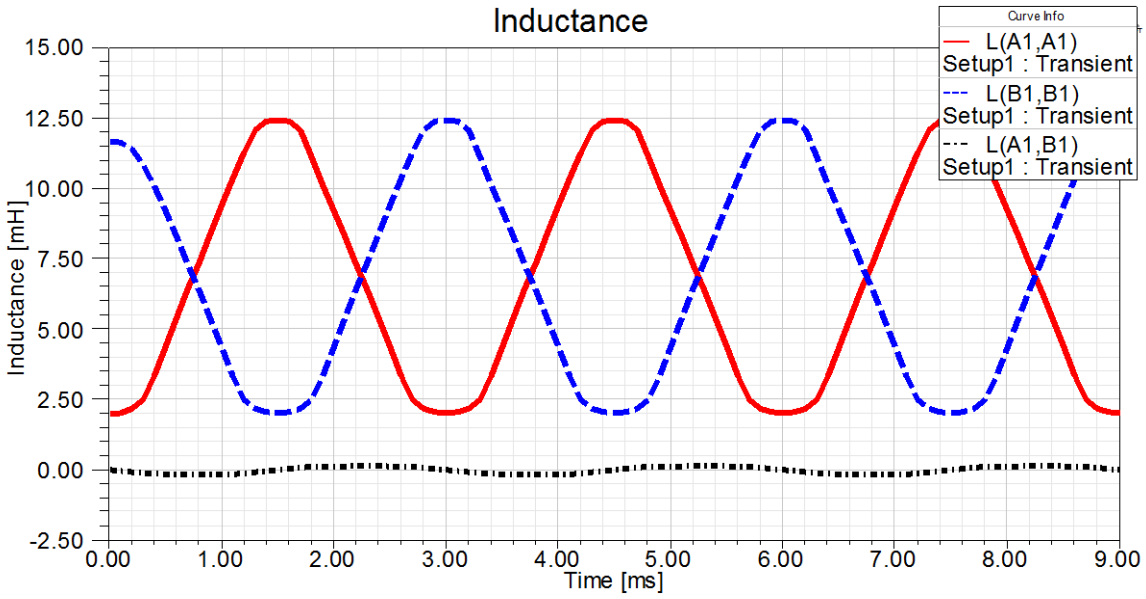

Fig 5.8 FEA simulation inductance profile of the SRM prototype with the regular rotor

The FEA simulation torque profile is shown in Fig 5.9, where the maximum and minimum values are 12.5 mN-m and -5 mN-m, respectively. Again, the machine is tested in no-load mode, and the average torque is only 7.86 mN-m.

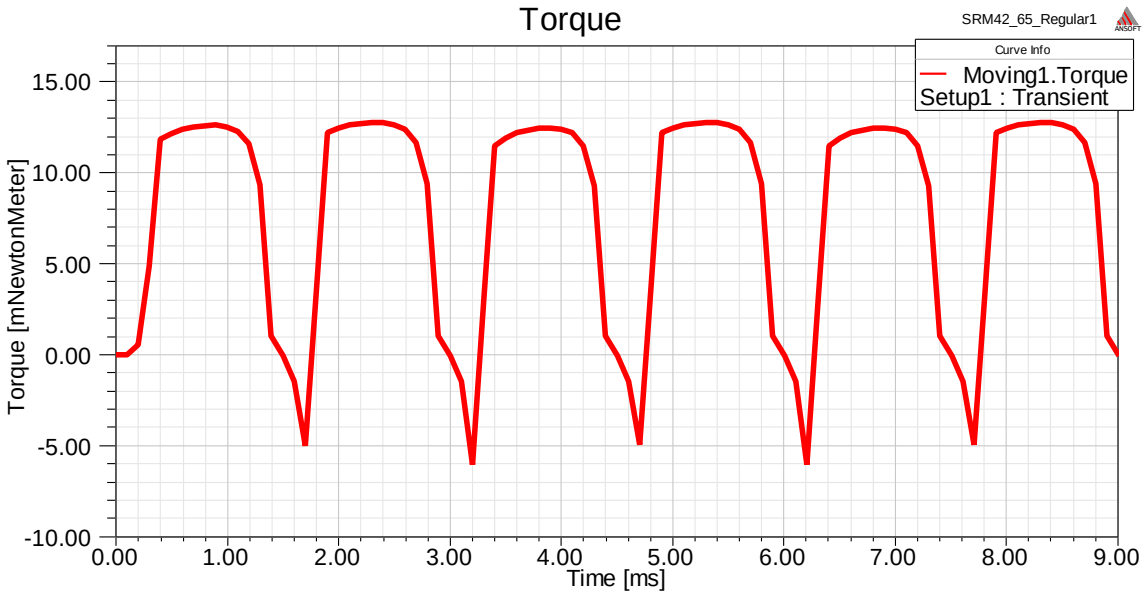

Fig 5.9 FEA simulation torque profile of the SRM prototype with the regular rotor (10 krpm)

After evaluating the performance of the SRM prototype with the regular rotor at 10,000 rpm, the SRM prototype with the enhanced rotor (with the flux bridge) is tested at 20,000 rpm (Fig. 5.10) and 50,000 rpm (Fig. 5.11) respectively. The performance of these two prototypes is compared at the end of this section.

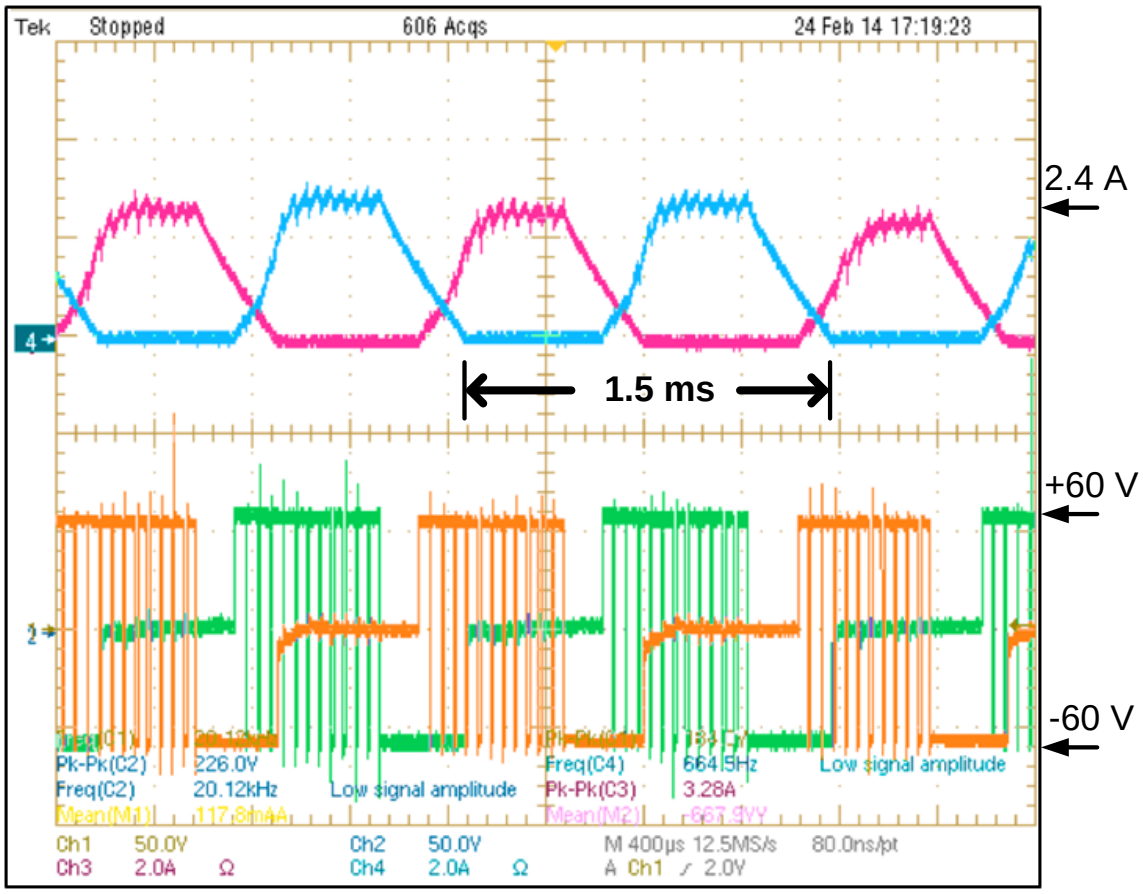

Fig 5.10 Experimental results for the SRM with the enhanced rotor at 20 krpm

When tested at 20,000 rpm, the period with respect to the fundamental frequency is $\frac{1}{\frac{20000\times 2}{60}} = 1.5ms$. In Fig 5.10, the period for a phase current waveform is 1.5 ms. This shows that the speed of the tested SRM is indeed 20,000 rpm. The current peak value is about 2.4 A (upper trace), and the DC bus voltage is about 60 V (lower trace). When the current reaches the peak value it is regulated at 2.4 A, as a current and speed dual close-

loop control is adopted. The detail of the control scheme is to be presented in Chapter 6. There is good symmetry between the two phases as the current waveform shapes are similar to each other.

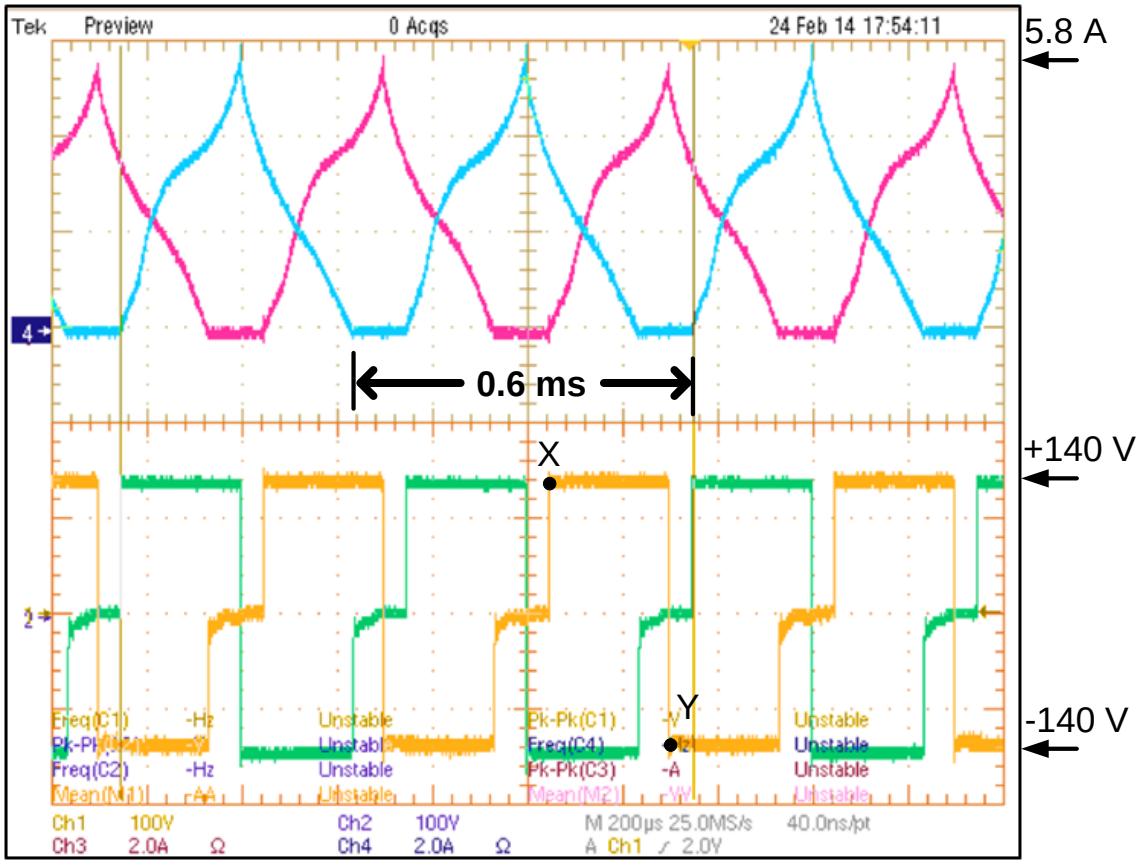

Fig 5.11 Experimental results for the SRM with the enhanced rotor at 50 krpm

When tested at 50,000 rpm, the period with respect to the fundamental frequency is $\frac{1}{\frac{50000\times 2}{60}} = 0.6ms$. In Fig 5.11, the period for a phase current waveform is 0.6 ms. This shows that the speed of the tested SRM is indeed 50,000 rpm. Here the current peak value is about 5.8 A, and there is no current regulation at 50 krpm. This is usually true for ultra high speed operations because there is not enough time within one phase current period for the current regulation to kick in. Due to the increase of the speed, the back EMF is increased, thus the DC bus voltage has to be increased to 140 V (lower trace), compared

to the 60 V used at speeds up to 20,000 rpm. At point X, the DC bus voltage is turned fully on to the phase coil. At point Y it is time to extinguish the current by applying full negative DC bus voltage to the phase coil.

Again, the FEA simulation is performed for the SRM with the enhanced rotor at 50,000 rpm, and the current and voltage profiles are shown in Fig 5.12.

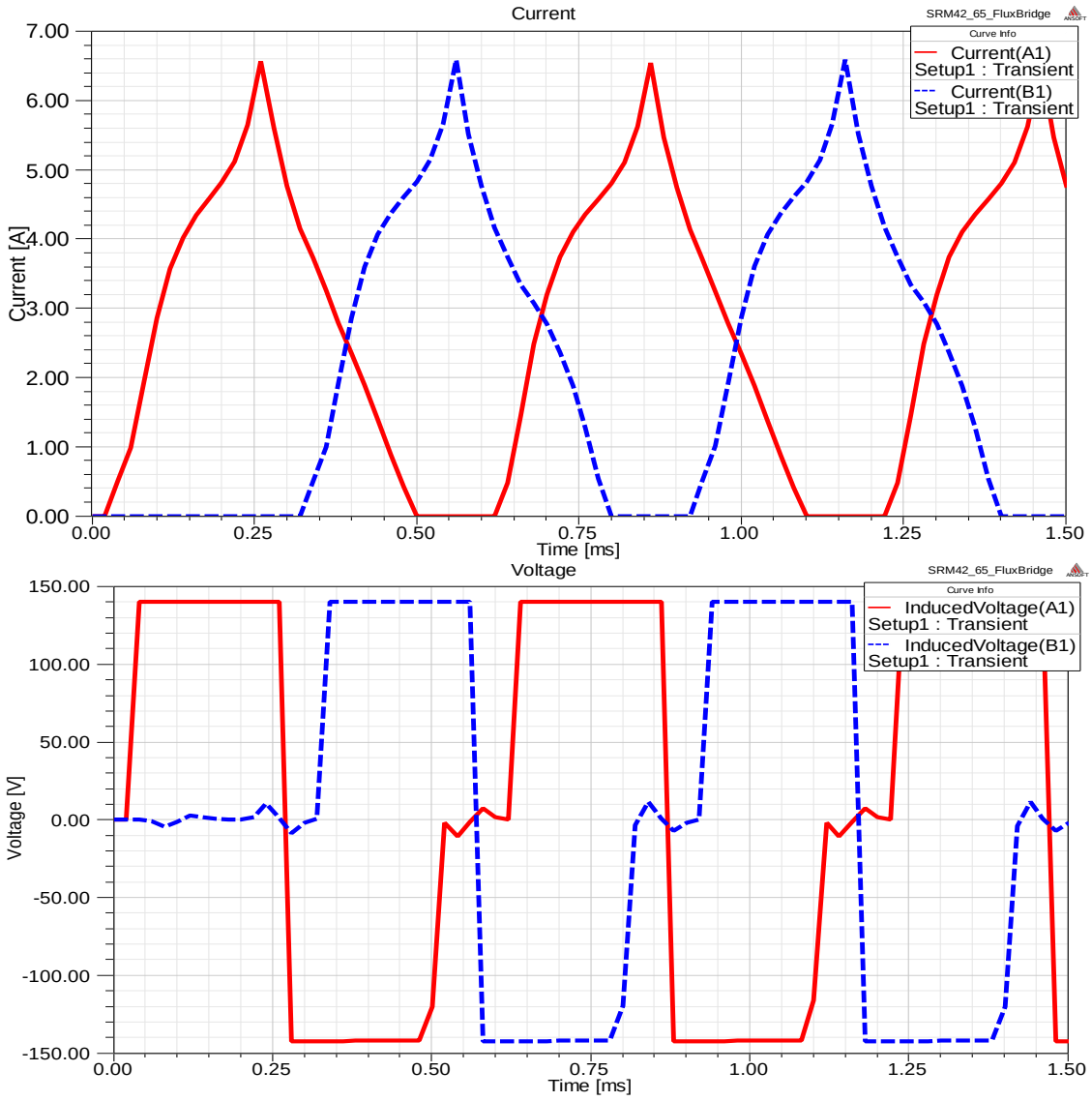

Fig 5.12 FEA simulation results for the SRM with the enhanced rotor at 50 krpm (current: top diagram, voltage: bottom diagram)

Given the same voltage profile (both 140 V and the same turn-on and turn-off timings), the current profiles of the FEA simulation (Fig 5.12) and of the experimental result (Fig 5.11) are very close to each other in terms of the shape and the peak value (5.8 A in Fig 5.11 and 6.3 A in Fig 5.12). Therefore, the FEA simulation gives sufficient confidence to predict the performance of the SRM prototype with the enhanced rotor, and it is to be used to estimate the SRM prototype torque profile at 50,000 rpm as shown in Fig 5.13.

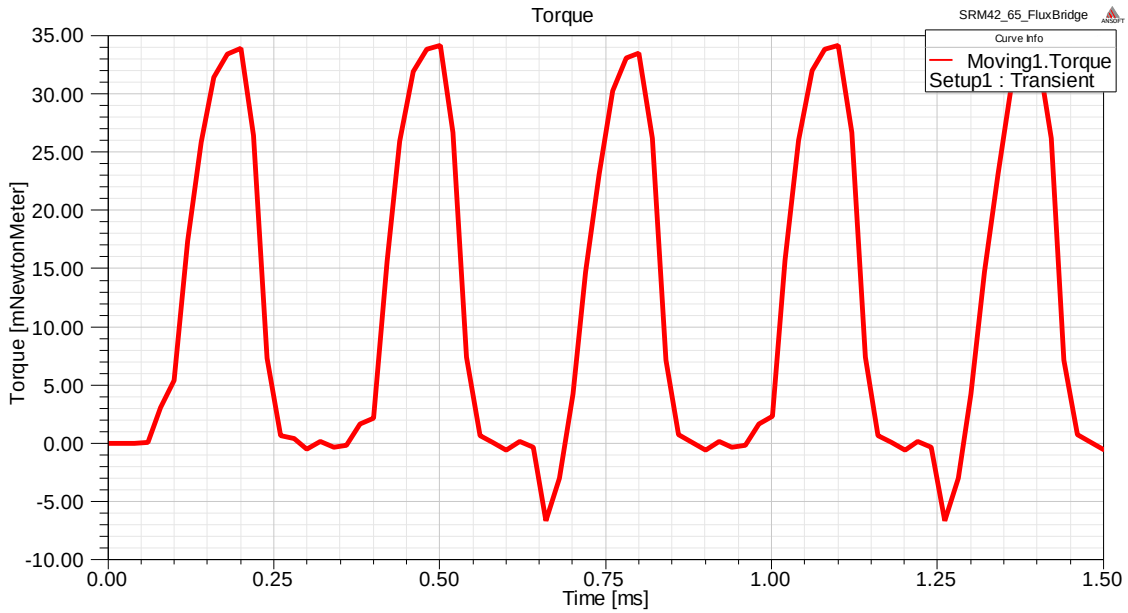

Fig 5.13 FEA simulation torque profile of the SRM prototype with the enhanced rotor

The temperature change of the motor tested at 50,000 rpm is shown in Fig 5.14. The curves with a red arrow indicate the stator coil winding temperature of Phase A and Phase B, and the curves with a yellow arrow indicate the ambient temperature as a reference. Each test only lasts 10 sec to avoid over-stressing the bearing. The temperature rise for each test is only about 2 ℃. This shows that the thermal management of the SRM prototype is done well for the no load test.

Fig 5.14 Temperature of the SRM prototype with the enhanced rotor at 50 krpm

The FEA simulation is also used for the flux density analysis as shown in Fig 5.15. It illustrates a certain rotor position when the flux density is at its peak value. The peak flux density occurs at the junction of the flux bridge and the rotor pole tip (red circle).

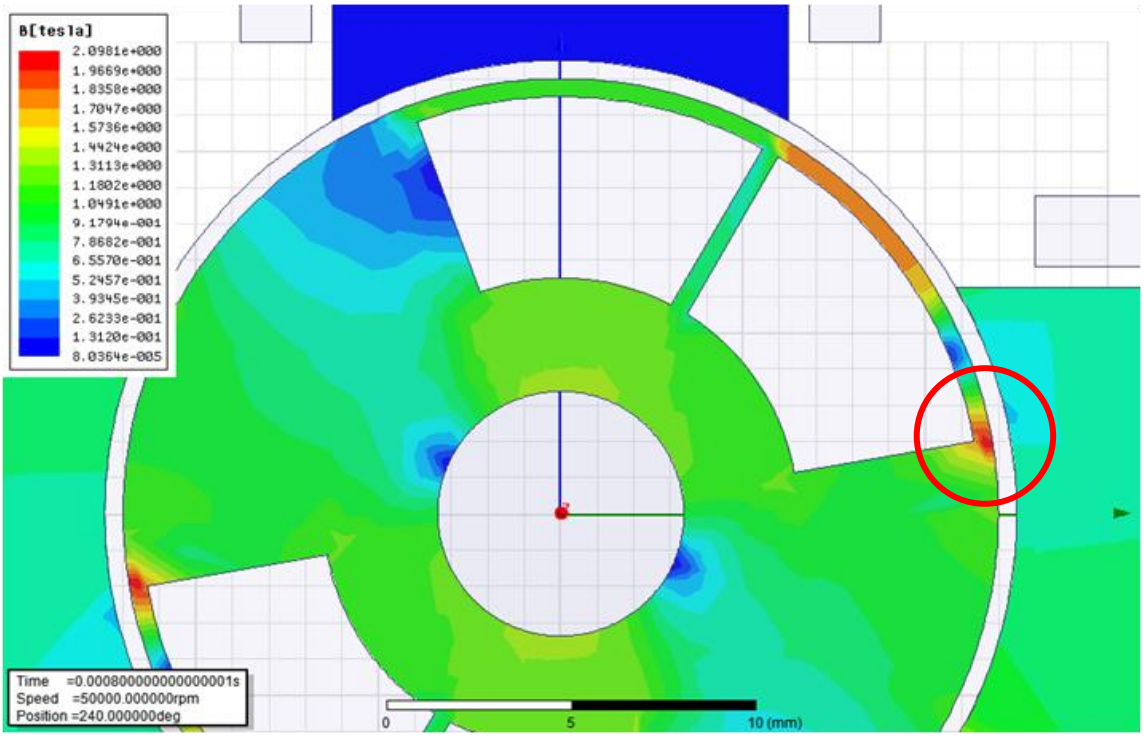

Fig 5.15 FEA simulation of the SRM prototype flux density at 50,000 rpm

Finally, the FEA simulated torque profiles of the SRM prototype (regular rotor vs. enhanced rotor) at 50,000 rpm are compared as shown in Fig 5.16. The average torque is reduced by 39% from 18.7 mN-m (the regular rotor) to 11.4 mN-m (the enhanced rotor). This can be explained by the decrease of the ratio between the maximum inductance value and the minimum inductance value.

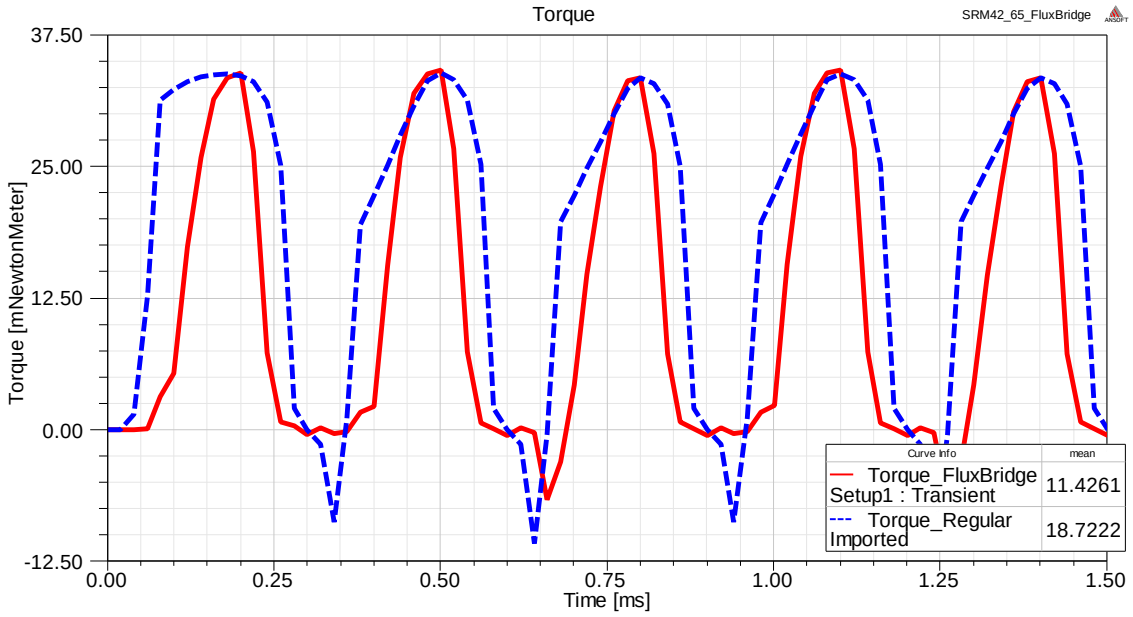

Fig 5.16 FEA simulation torque profiles of the SRM prototype (regular rotor vs. enhanced rotor) at 50,000 rpm

5. 4 SRM improved design with non-uniform air-gap

Besides the work on the rotor configuration, much research of SRM designs has focused on modifications to the symmetry of the air-gap [78, 79] and this has a significant impact on the inductance profile and on SRM performance. In this section, the SRM design with a flux bridge rotor is improved by introducing a variation in the air-gap via shaping the stator pole profile, as shown in Fig 5.17.

However, no experimental results of this non-uniform air-gap design are presented because no such prototype has been fabricated. The idea of the stator pole profile

modification is however presented below with FEA simulation results. Therefore, for the rest of this section, the *benchmark* design is chosen to be the one shown in Fig 5.1 (not the fabricated prototype), where the original air-gap length is 0.3 mm and the flux bridge thickness is 0.2 mm.

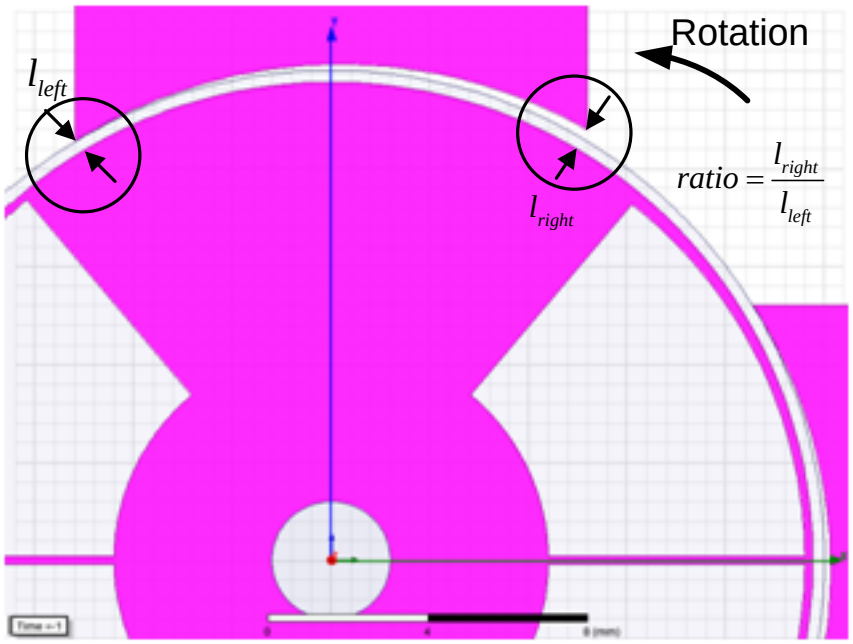

Fig 5.17 Cross section view of the non-uniform air-gap design

In Fig 5.17 the rotor rotates in the CCW direction, and the air gap length at the stator pole's right tip is changed to be double that at the stator pole's left tip (indicated by the two circles). Moreover, the air gap length decreases linearly from 0.6 mm at the right tip to 0.3 mm at the left tip. This modification is done to improve the torque profile and reduce the torque ripple as claimed in [79].

To achieve the best *improved* performance for the non-uniform air-gap design, a FEA simulation is performed to investigate the ratio between the air-gap length at the stator pole right tip and the one at the left tip. The air gap length at the left tip is held constant at 0.3 mm, while the one at the right tip is changed. The current and torque profiles for different ratio values are presented in Fig 5.18.

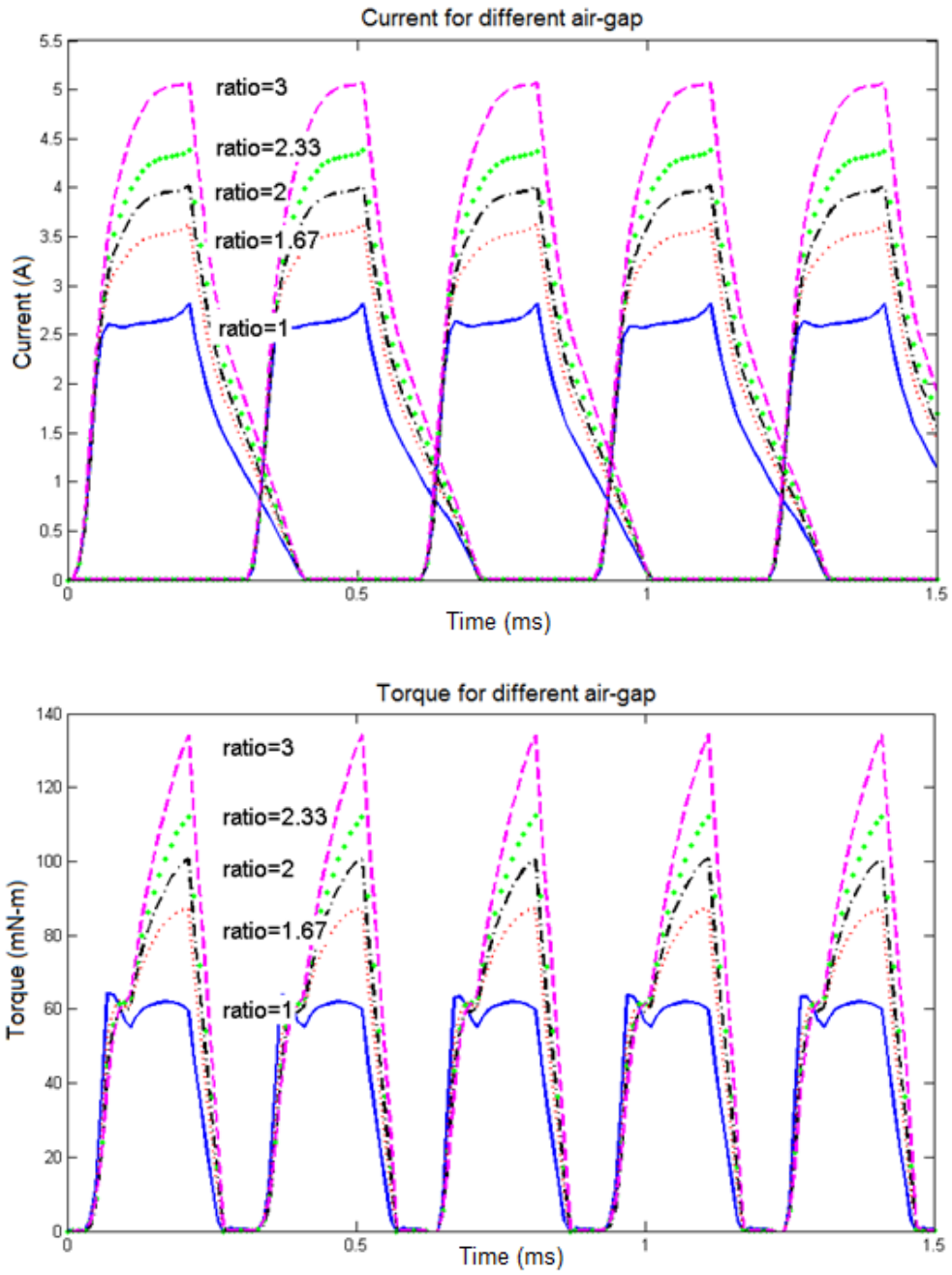

Fig 5.18 FEA simulation current (top) and torque (bottom) profiles of the non-uniform air-gap design for different ratio values

The results of Fig 5.18 show that with the increase of the ratio, both the current and the output torque increase, which comes as a consequence of a reduction in the inductance. The average torque in the bottom diagram of Fig 5.18, is 47.4 mN-m for a ratio of 2 and

57.3 mN-m for a ratio of 3, which is an increase of 29.2% and 56.1% compared to the torque of 35.7 mN-m for the benchmark ratio design. However, the current RMS values in the top diagram are 2.38 A (ratio=2) and 2.95 A (ratio=3), which are undesirable increases by 38.3% and 71.5% compared to 1.72 A for the benchmark ratio design. Higher current means higher copper and core losses, and thus lower efficiency of the machine.

As a tradeoff between the torque profile improvement and the consequent current increase, the ratio of 2 is selected for the final *non-uniform air-gap (NUAG)* design. The next step of improvement is to minimize the losses while increasing the average torque. For the high speed applications, the core losses are the dominant portion of the total losses. The core losses are determined by the fundamental frequency and the flux density. However, the flux density could be reduced by lowering the excitation voltage. Therefore, FEA simulations are performed to investigate the SRM core losses with different DC bus voltage, as shown in Table 5.1. For the benchmark design, the DC bus voltage is 250 V, as shown in the second row of Table 5.1.

Table 5.1 Core losses comparison with different DC bus voltage

	Average Torque (mN-m)	Average Core Losses (W)
250V/*Benchmark Design*	35.7	63.8
250V/*NUAG Design*	47.6	62.6
240V/*NUAG Design*	43.1	57.9
230V/*NUAG Design*	38.9	53.4
220V/*NUAG Design*	34.9	49.1

In Table 5.1, the average torque and core losses are calculated with FEA simulation. The results of the *NUAG design* with different DC bus voltages are shown under the benchmark design. For example, for the *NUAG design* with a 230 V DC bus voltage (5th row), the average core losses are reduced from 63.8 W to 53.4 W by 16.3%, while the

average torque is increased from 35.7 to 38.9 mN-m by 9.0% compared to the *benchmark design*. Therefore, for the *NUAG design*, a lower DC bus voltage can reduce the core losses while retaining or even increasing the torque output.

An additional step is carried out to include the copper losses in the investigation. The total losses, which combine the copper and core losses, are compared between the *benchmark design* with a 250 V DC bus voltage and the *NUAG design* with a 230V DC bus voltage. The result is presented in Fig 5.19, where the solid line denotes the *benchmark design* and the dashed line denotes the *NUAG design*.

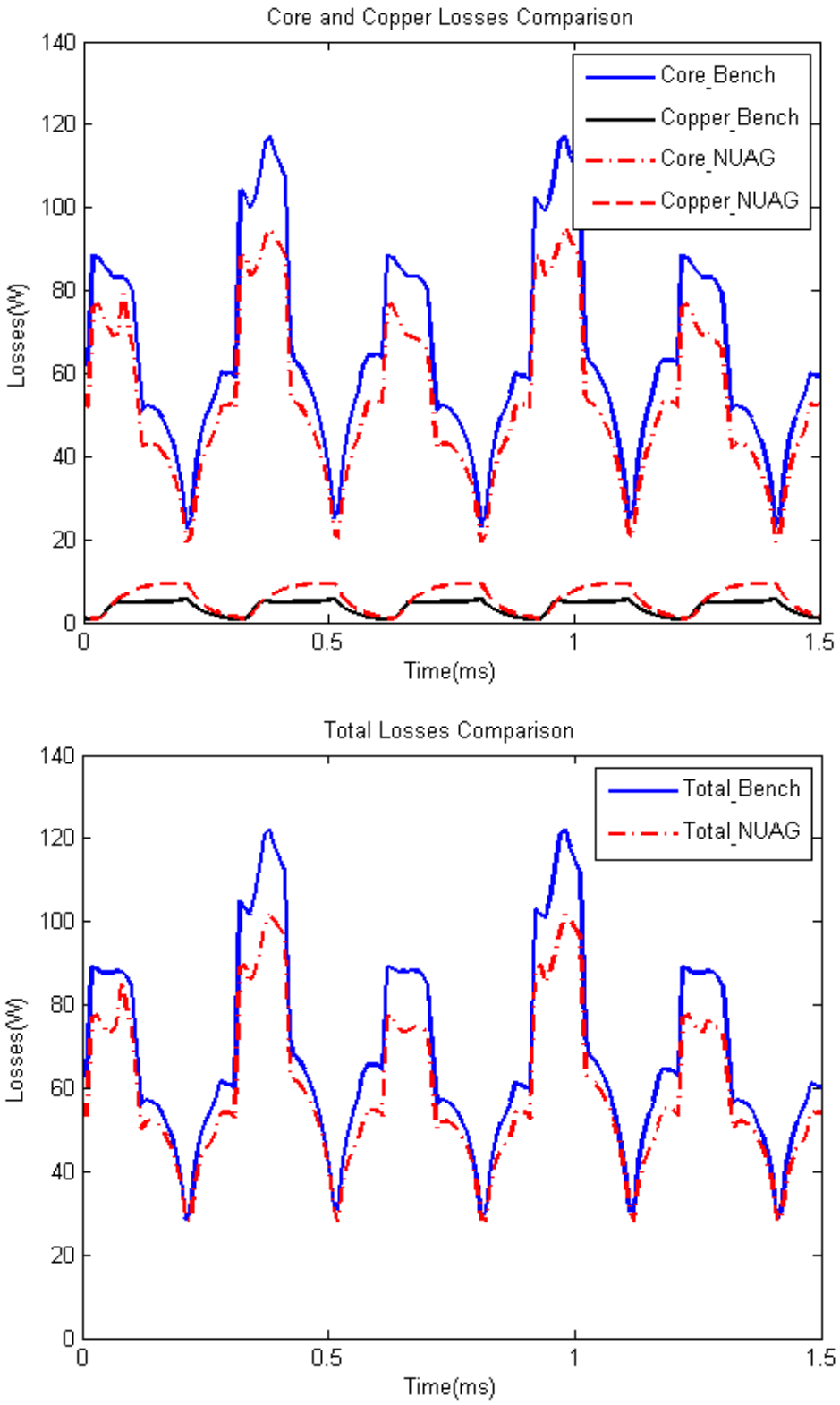

Fig 5.19 FEA simulation results for the losses comparison
(Core and copper losses: top; Total losses: bottom)

In the top diagram of Fig 5.19, the core losses are much higher than the copper losses at high speeds. In the bottom diagram of Fig 5.19, the average total losses of the *NUAG design* (59.1 W) are 12.3% lower than that of the benchmark design (67.4 W).

Therefore, the final *NUAG design* has an unsymmetrical air-gap with a ratio of 2 and a reduced DC bus voltage of 230 V. The inductance and torque profiles of the final *NUAG design* are shown in Fig 5.20. In the top diagram of Fig 5.20, the inductance sag which appears in the *benchmark design* is almost negligibly small. This is because the reduced DC bus voltage reduces the saturation level of the flux bridge support. In the bottom diagram of Fig 5.20, the torque profile is changed to have a sharp peak, but with a higher average value of 38.9 mN-m compared to 35.7 mN-m for the benchmark design.

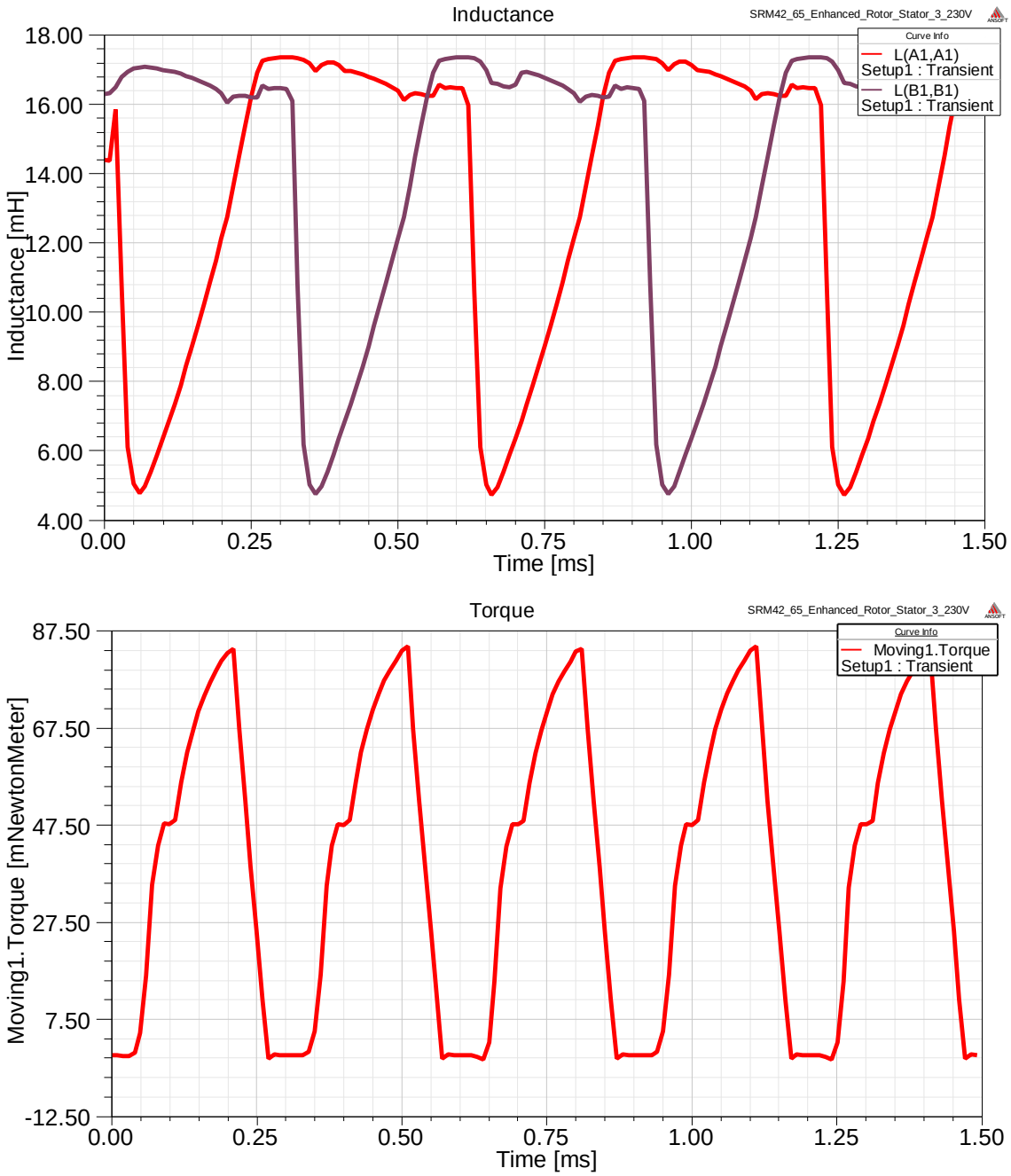

Fig 5.20 FEA simulation inductance (top) and torque (bottom) profiles of the final *NUAG design*

Again, the *NUAG design* is only presented with FEA simulation results, and no experimental results are provided for this work. However, it offers a conceptual idea about how the SRM performance can be improved by shaping the air-gap profile.

5. 5 Chapter summary

The practical considerations of the design and construction of a 50,000 rpm SRM are discussed in this chapter. First, a flux bridge topology is proposed to create a cylindrical rotor. The main motivation for building the flux bridge on the rotor is to reduce the windage losses at high speeds. The electromagnetic behavior of the flux bridge rotor design is investigated using FEA simulations. A SRM prototype is fabricated with one regular rotor and one flux bridge rotor, which is tested at 10 krpm, 20 krpm and 50 krpm. Good agreement has been achieved between the FEA simulation and the experimental results. A performance comparison between the two rotors is performed using FEA simulations. Furthermore, the flux bridge rotor design is improved with a non-uniform air-gap profile. The impact of this modification is investigated with FEA simulations, and it shows that the *NUAG design* can increase the average torque while reducing the total losses with a lower DC bus voltage. After understanding the electromagnetic behaviors of the flux-bridge rotor, the control of such a high speed SRM is investigated in the following chapter.

Chapter 6 High Speed SRM Control

6. 1 Introduction

After achieving the optimal design for the high speed SRM, the next step is to find a good control strategy to operate it at 50,000 rpm. The challenge of the high speed SRM lies in the fact that the SRM characteristics are a highly nonlinear function of both rotor position and phase current. As a result, several nonlinear control schemes, such as artificial intelligence (AI) techniques, fuzzy-neural network, and sliding mode control methods, are studied in [82]. However those nonlinear control methods are complex and computational-costly to implement.

Therefore it is desired to design a simple control method that requires less computational investment but with good performance. In particular, the design of a closed-loop speed control for a SRM at 50 krpm is studied in this chapter. A simple PI control is selected and is implemented using Matlab/Simulink, and the simulation and experimental results are presented at the end of this chapter.

6. 2 SRM control strategy

To achieve the speed close-loop control, typical dual-loop control is used to control the SRM. The outer loop is the speed control, and the inner loop is the torque control. However there are different ways to implement the inner loop torque control and they are discussed in this section.

6.2.1 Rotor position measurement

The position of the rotor is very important for the SRM control. Therefore, an encoder is mounted on the shaft to provide the position information. The encoder model is E5-

100-250-IE-S-H-G-2, which has 3 channels (A, B and index), 100 pulses per revolution, and a maximum speed of 60,000 rpm.

The index signal is necessary to control the SRM. This signal is shown in the top trace of Fig 6.1, and it resets the counter to zero every revolution. Without the index signal, the measurement error may accumulate over time, which will eventually result in a control failure. Between two adjacent index signals, the position is indicated by the number of pulses from 0 to 99. This can be read by the SRM controller, which is a DSP program in this work. As a result, the position measurement resolution is 360 ⁄100=3.6 .

First, the four aligned positions θ_a with respect to the stator poles need to be known at first. They can be measured from the pulse counter (0-99) when energizing only one phase coil at a time. This is achieved by using an extra current source power supply connected to the terminals of one phase, and leaving the other phase open circuit. Next a small DC current is applied to the connected phase. The rotor pole is attracted to be aligned with this phase stator poles and this position can be read by the DSP program. Then the rotor is rotated 180 manually by hand and the rotor pole is aligned again with the same phase stator poles, but in an opposite direction. This is the other aligned position for this particular phase. The same procedures are repeated for the other phase until finally all the four aligned positions are found.

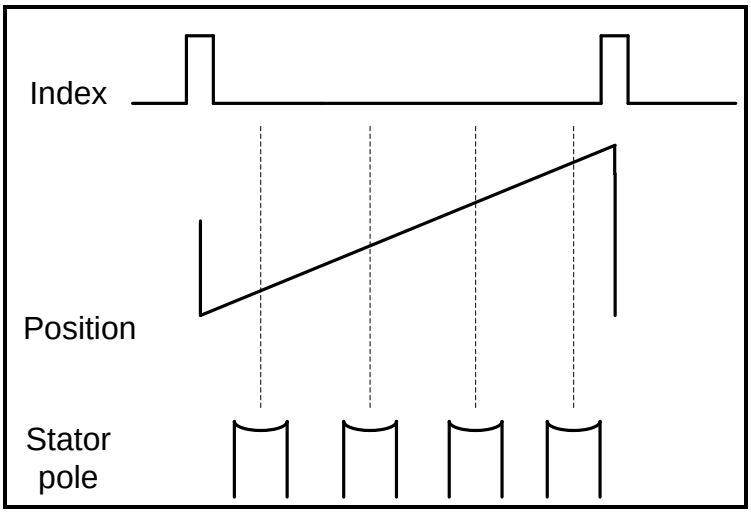

Fig 6.1 Encoder function schematic diagram

Hereafter, the initial turn-on θ_{on} and turn-off θ_{off} angles can be selected according to these four aligned positions θ_a. For example, the four aligned positions are 10, 35, 60 and 85, so the initial θ_{on} and θ_{off} can set as 95-15, 20-40, 45-65 and 70-90 for one direction of rotation, and 25-5, 50-30, 75-55, 00-80 for the opposite direction of rotation. Those θ_{on} and θ_{off} values are obtained with trial and error at first, and they can be tuned by using the SRM simulation model afterwards.

6.2.2 Torque control strategy

For the close-loop control, the outer loop speed control is used to control the SRM speed, so the output of the speed controller should adjust the torque command according to the difference or error between the speed command and the actual speed. Therefore, the inner loop is essentially a torque control loop. According to the SRM torque equation (6.1), there are two ways to control the torque. One is the current control by adjusting i, and the other is the angle control by changing $\frac{dL}{d\theta}$.

$$T = \frac{1}{2} \cdot i^2 \cdot \frac{dL}{d\theta} \tag{6.1}$$

For the angle control, because $\frac{dL}{d\theta}$ is changing at different angles, the torque can be adjusted by moving the turn-on and turn-off angles, as shown in Fig 6.2.

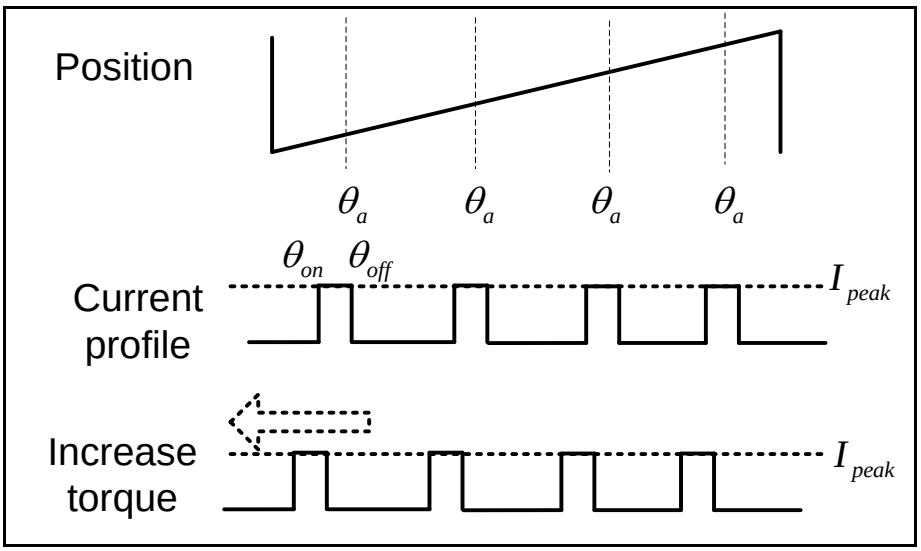

Fig 6.2 Possible SRM control strategy: angle control

In Fig 6.2, the top trace is the position reading from the encoder, where the counter increases from 0 to 99 for one revolution and resets to 0 at the next index signal. The middle trace shows the initial values of θ_{on} and θ_{off}, which are used to start the SRM from standstill. Between θ_{on} and θ_{off}, the current is regulated at a fixed peak value I_{peak}. The bottom trace shows that the torque can be increased by advancing θ_{on} and θ_{off} while the current peak value remains constant.

However, the problems of the angle control are: 1) there is a maximum torque limit for advancing the angles, and beyond this limit the SRM control loses stability, which means that the SRM may rotate in the opposite direction and the angle control fails; 2) the SRM torque is very sensitive to the angle value, but the angle measurement resolution (3.6) is

relatively large. So the angles cannot be adjusted by small steps in a smooth and continuous way, and the angle control performance therefore is very poor.

The current control therefore is chosen as the torque control scheme for the inner loop, which is shown in Fig 6.3. In the bottom trace, the SRM torque can be increased by increasing the current peak command value, while θ_{on} and θ_{off} remain constant. For the current control, there is no regulation limit, so the control scheme is always stable. In addition, the torque can be adjusted in a smooth and continuous way so its performance is better than the angle control.

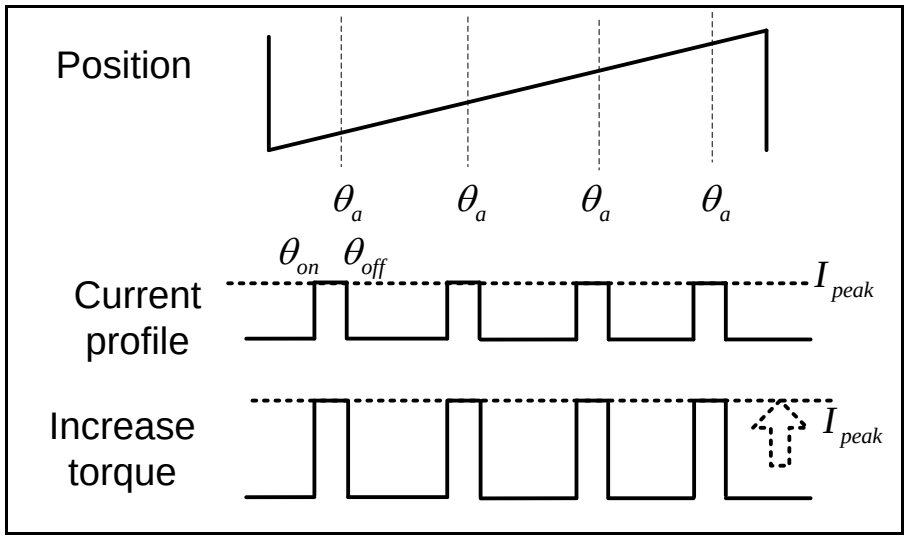

Fig 6.3 Possible SRM control strategy: current control

The output of the speed controller provides this current peak command I_{peak}, and the inner current control loop regulates the current at that peak value. The turn-on θ_{on} and turn-off θ_{off} angles remain constant.

Waveforms of the inner loop current control are shown in Fig 6.4. The three traces of Fig 6.4, from top to bottom, denote the current profile, the switching signal, and the voltage profile. At the beginning of each switching period, the instantaneous current is measured and the switching duty cycle is calculated by the current controller. The

switching frequency is fixed at 20 kHz, so the period T in the switching signal profile is 50 μs. In the switching signal profile, the duty cycle D is adjusted according to the difference between the peak current command I_{peak} and the actual current measurement. With a proper design of the current controller, the current can be regulated around the desired peak value between θ_{on} and θ_{off}. The detailed design procedure is presented in Section 6.4.

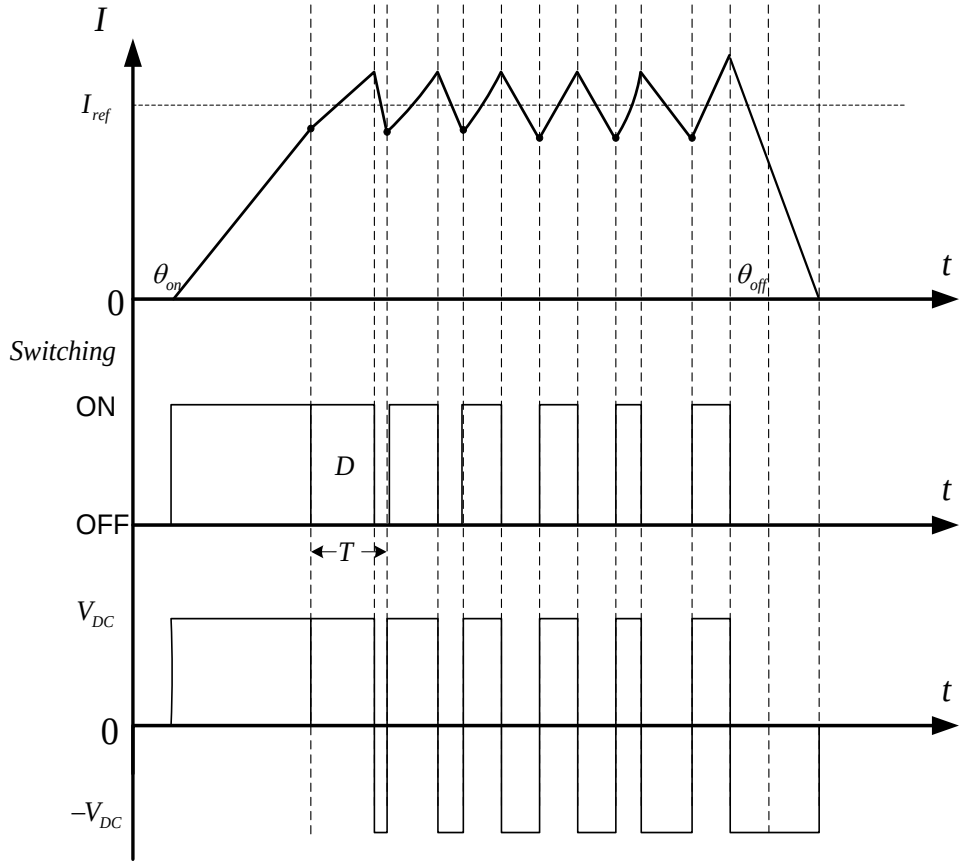

Fig 6.4 Current control profile and switching signal

6.2.3 Speed and current dual-loop control

Given the selection of current control for the inner loop control, the complete speed and current dual-loop control is shown in Fig 6.5.

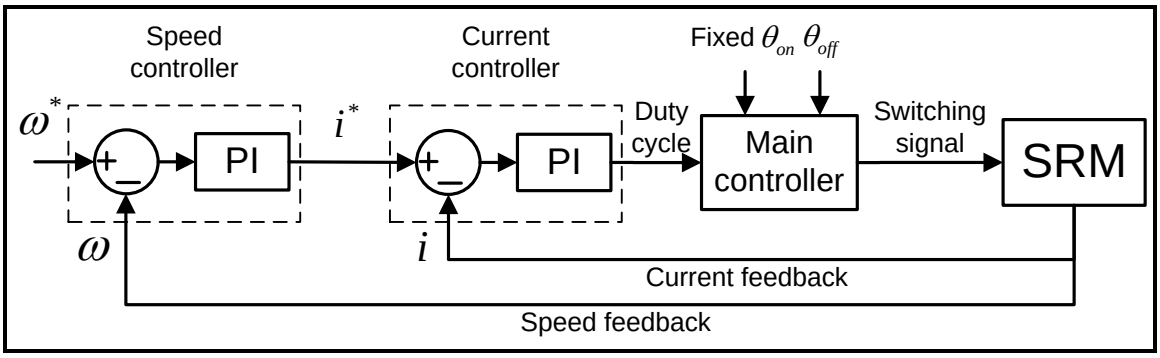

Fig 6.5 High speed SRM dual-loop control block diagram

In Fig 6.5, both the speed controller and the current controller are PI controllers. The speed feedback signal is provided by the encoder. Given the PWM switching frequency of 20 kHz, the current loop bandwidth is desired to be about 2 kHz, and the speed loop bandwidth is desired to be about 200 Hz. The main controller synthesizes the duty cycle, θ_{on} and θ_{off} , to calculate the switching signal to control the SRM.

6. 3 SRM simulation model

After constructing the dual-loop SRM control strategy, a complete SRM drive model is assembled by using MATLAB/Simulink, presented in this section. This simulation model helps tune the controller parameters (PI control coefficients), and to predict the SRM control performance. In addition, this model can be used to investigate and validate advanced control ideas, such as sensorless control, direct torque control, etc., for future work.

The block diagram of the SRM drive model is shown in Fig 6.6, which is expanded from Fig 6.5.

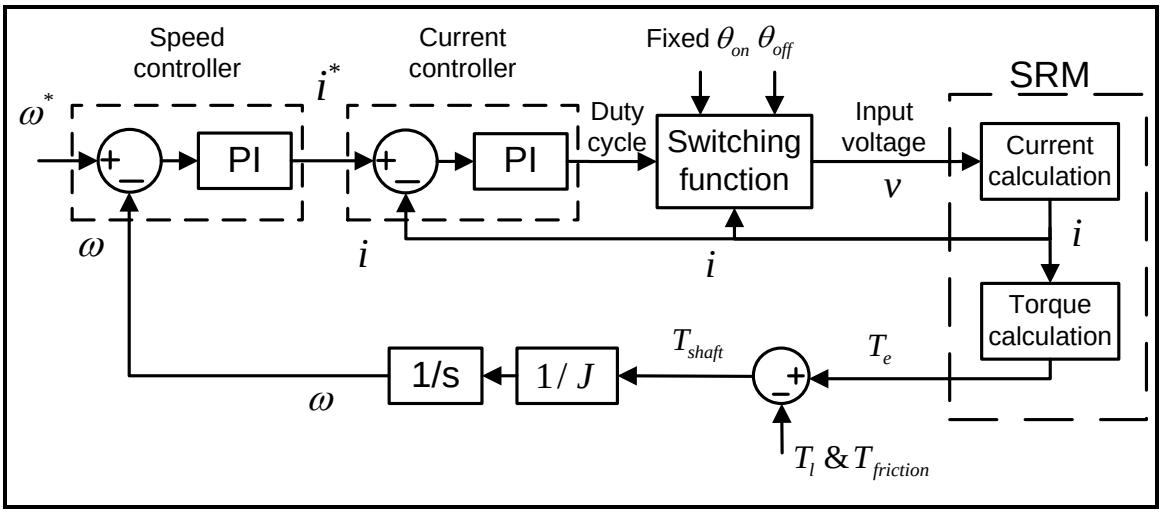

Fig 6.6 SRM simulation model block diagram

The main controller translates the duty cycle signal into the gate switching signal, and outputs this to the SRM block. The SRM block consists of a current calculation block and a torque calculation block. The output of the SRM block is the electromagnetic torque, and the torque is used to calculate the speed and to feed the speed back to the speed controller. The functions of each block are described in detail in this section.

6.3.1 Inertia constant J

In Fig 6.6, the shaft torque is used to calculate the speed ω, using the torque equation (6.2):

$$T_{shaft} - T_l - T_{friction} = J \cdot \frac{d\omega}{dt} \tag{6.2}$$

where T_{shaft} denotes the mechanical torque applied on the SRM shaft, T_l denotes the load torque, J denotes the inertia constant of the rotor, ω denotes the SRM speed in rad/s, and $T_{friction}$ denotes the friction torque. For the scope of this study, the SRM is operated in no load mode, thus $T_l = 0$.

The friction torque is simplified to be proportional to the speed as expressed in (6.3), where F is a constant.

$$T_{friction} = F \cdot \omega \tag{6.3}$$

The rotor inertia constant J is determined by the rotor mass, and it can be calculated using equation (6.4):

$$J = \int r^2 dm \tag{6.4}$$

where r denotes the radium between the rotation mass and the rotation axis, and m denotes the mass.

For the rotor with the flux bridge, the flux bridge is very thin and it can be ignored for the inertia calculation. Therefore, the flux bridge rotor is dealt with as a regular rotor, and the rotor geometric dimensions are shown in Fig 6.7.

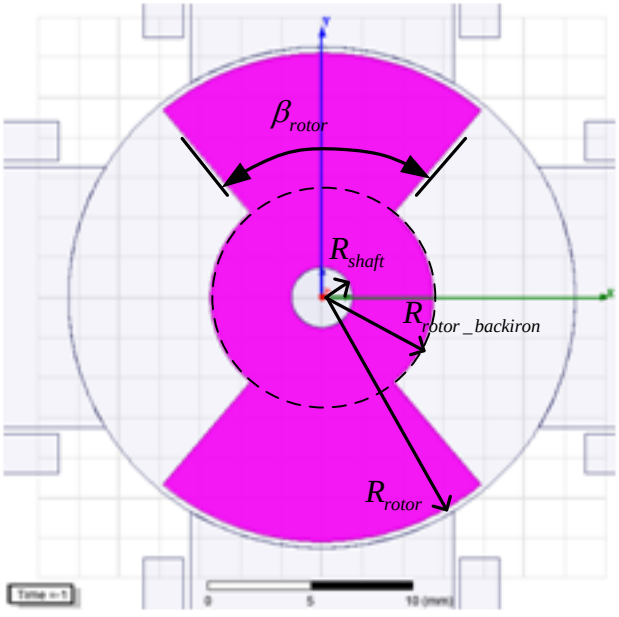

Fig 6.7 SRM rotor cross section view

Then, the rotor can be divided into three parts, a ring and two fans. The ring is the part between the radium R_{shaft} and $R_{rotor\_backiron}$. The fan is the part with a radium between $R_{rotor\_backiron}$ and R_{rotor}, and with a central angle of β_{rotor}. Therefore the inertia constant J of the rotor is calculated by equation (6.5):

$$J = \rho(\int_{R_{shaft}}^{R_{rotor\_backiron}} r^2 \cdot 2\pi r \cdot dr \cdot L + 2 \cdot \int_{R_{rotor\_backiron}}^{R_{rotor}} \int_0^{\beta_{rotor}} r^2 \cdot r \cdot d\theta \cdot dr \cdot L) \qquad (6.5)$$

where ρ denotes the rotor material density, and L denotes the rotor stack length. Substitute the values listed in Table 6.1 into (6.5), and J is calculated to be $2.5\times10^{-6} kg \cdot m^2$.

Table 6.1 Parameter values for the rotor inertia calculation

$R_{rotor\_backiron}$	6.5 mm
R_{shaft}	3.375 mm
β_{rotor}	80 °
L	20 mm
ρ	7.88×10^3 kg/m^3

6.3.2 Switching function block

The switching function block in Fig 6.6 translates the duty cycle into the SRM drive gate switching signal first, and then converts it to the input voltage and sends it to the SRM block. The duty cycle D is a signal with a value between 0 and 1. It is compared to a high frequency triangular wave, and the comparator generates 0/1 digital signal, where 0 means off and 1 means on, as shown in Fig 6.8. The carrier triangular signal frequency is equal to the PWM switching frequency, 20 kHz.

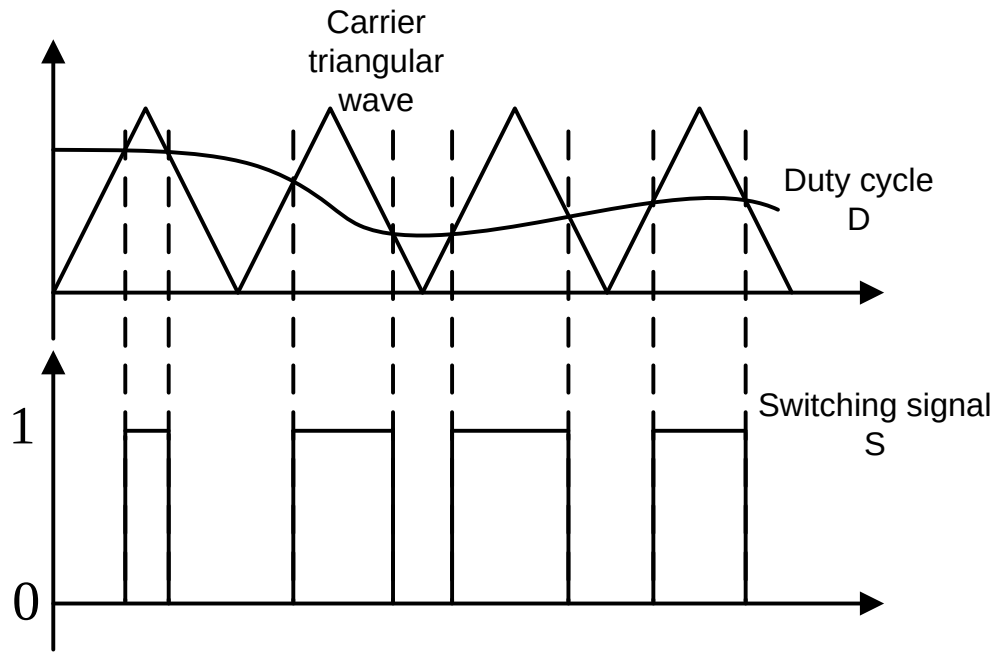

Fig 6.8 Schematic diagram of translating the duty cycle signal to the gate switching signal

Next, the switching signal is synthesized with the rotor angle signal to convert to the SRM input voltage. In particular for the rotor position, when the rotor angle is in the range of Phase A (0 - 90 º and 180 º - 270 º), Phase B switches are turned off (output switching signal remains 0 for Phase B), and vice versa. In addition, for each phase between the turn-on and turn-off angles, θ_{on} and θ_{off} , the corresponding phase switches can be turned on; otherwise they remain off.

Furthermore, the SRM inverter topology (the H-bridge topology as shown in Fig 6.9) is also taken into account for the SRM input voltage calculation. Specifically, when the current is positive, the SRM input voltage is positive DC bus voltage when the MOSFET switch is on, and the SRM input voltage is negative DC bus voltage when the MOSFET switch is off. This phenomenon is due to the conduction of the diodes as shown in Fig

6.9. The voltage across the SRM phase winding is negative DC bus voltage when the current flows through those diodes.

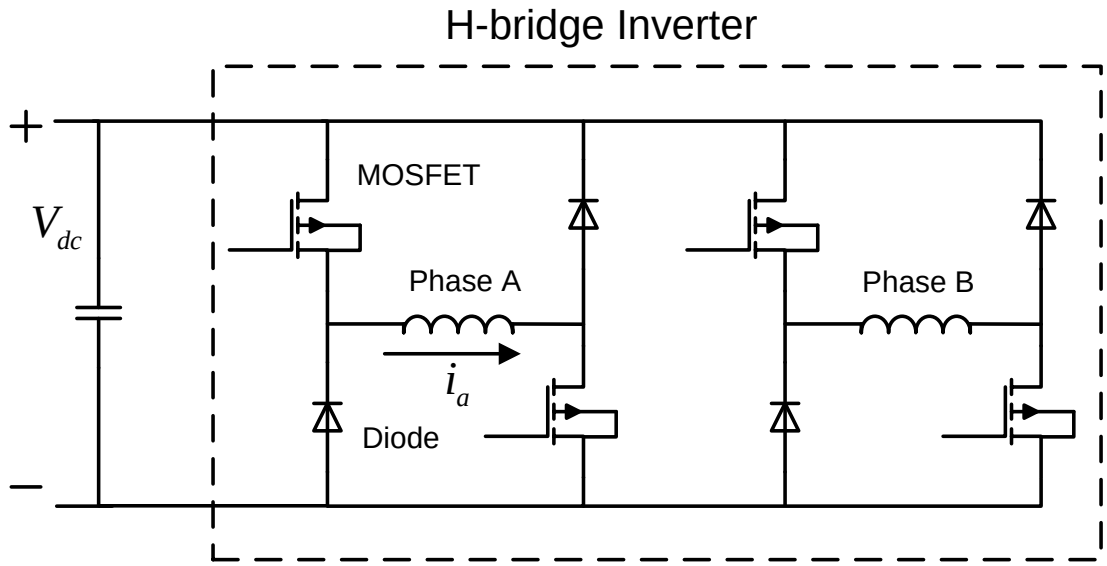

Fig 6.9 SRM H-bridge inverter circuit diagram

Therefore there are three states, 0, $+V_{DC}$ and $-V_{DC}$, for the SRM input voltage, and the logic of these three voltage states is illustrated in Fig 6.10. First, it is needed to determine whether the rotor angle θ is in the range of Phase A or Phase B. When the rotor angle is in the range of Phase A, the Phase B input voltage v_b is 0. Next if θ is out of the range between the turn-on and turn-off angle of Phase A, the Phase A input voltage v_a is 0. Then if the switching signal S_a (output of the voltage comparator) is 1, v_a should be the positive DC bus voltage $+V_{DC}$. Afterwards if S_a is 0 and the Phase A current i_a is greater than 0, the input voltage v_a should be equal to the negative DC bus voltage $-V_{DC}$; otherwise v_a should be zero.

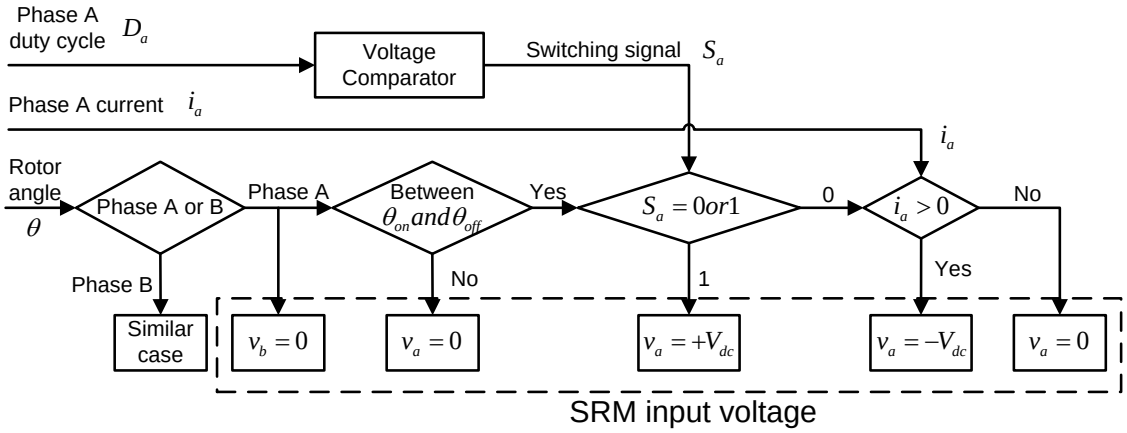

Fig 6.10 SRM input voltage logic flow chart

6.3.3 Inductance measurement

After the calculation of the SRM input voltage the next step is to calculate the current, which is executed in the current calculation block in Fig 6.6. Therefore it is needed to know the inductance profile at first. In practice, the SRM inductance is dependent on the rotor angle and the current value (saturation level). However it is not an easy task to obtain the inductance profile $L(\theta)$ because it varies with the current. The inductance profile used in the reference [49] is described as a function of the rotor position θ and the current value i, named $L(\theta, i)$. This method increases the complexity of the model, and a great amount of inductance data needs to be measured and stored.

An experimental way to measure the inductance profile $L(\theta)$ is to use an inductance meter, where a high frequency low magnitude voltage (e.g. 1V 1 kHz sinusoidal voltage) is applied to the phase winding. In this work, the 4/2 SRM prototype with the flux-bridge rotor is measured. The experimental setup of the inductance measurement is shown in Fig 6.11.

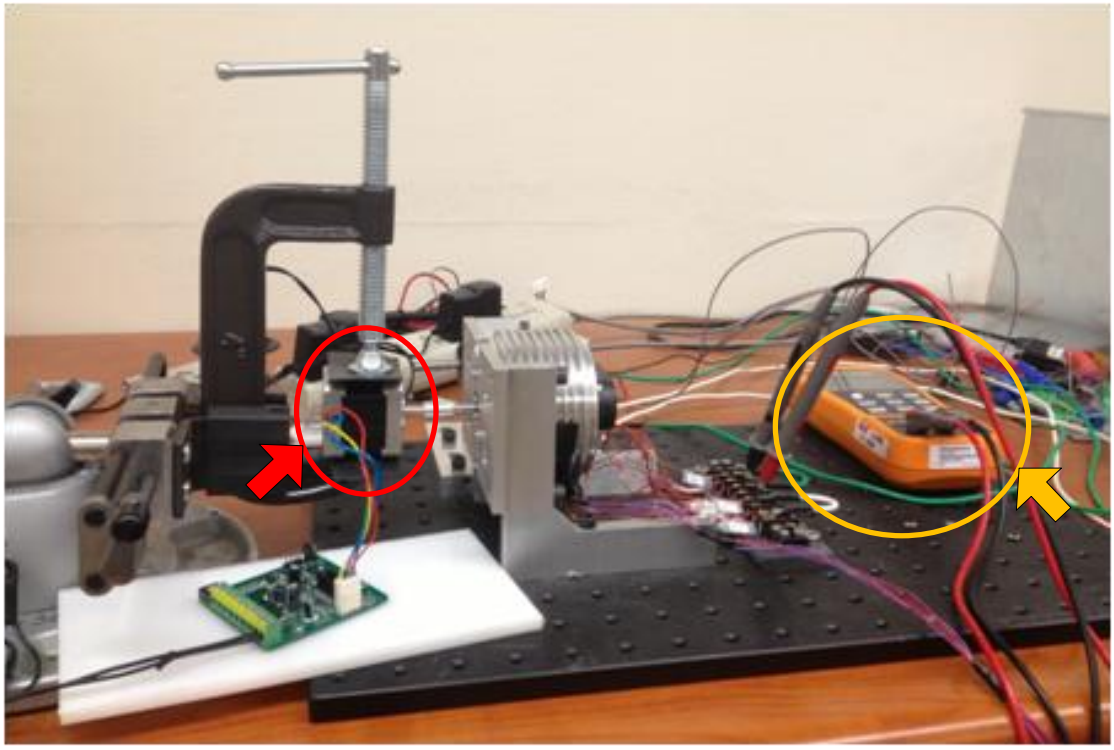

Fig 6.11 SRM prototype inductance measurement experimental setup

In Fig 6.11, a stepper motor (red circle), which is coupled with the SRM prototype shaft, is used to rotate the SRM rotor in a very slow fashion (1 rpm). An inductance meter (yellow circle) is used to measure the inductance value at different rotor angles. The output of the inductance meter probe is a high frequency low voltage (1 kHz 1 V) sinusoidal wave signal. The measured inductance values for one revolution (360) are plotted in Fig 6.12. The maximum value is 5.9 mH, and the minimum value is 5.4 mH. There is good symmetry between Phase A and Phase B. Due to the existence of the flux bridge, the upper part of the inductance profile (with the maximum value) is wider than the lower part (with the minimum value). However the current in the phase winding is very low and the SRM is very much unsaturated. Therefore it is desired to investigate the inductance profile with higher current values when the SRM is saturated with different degrees.

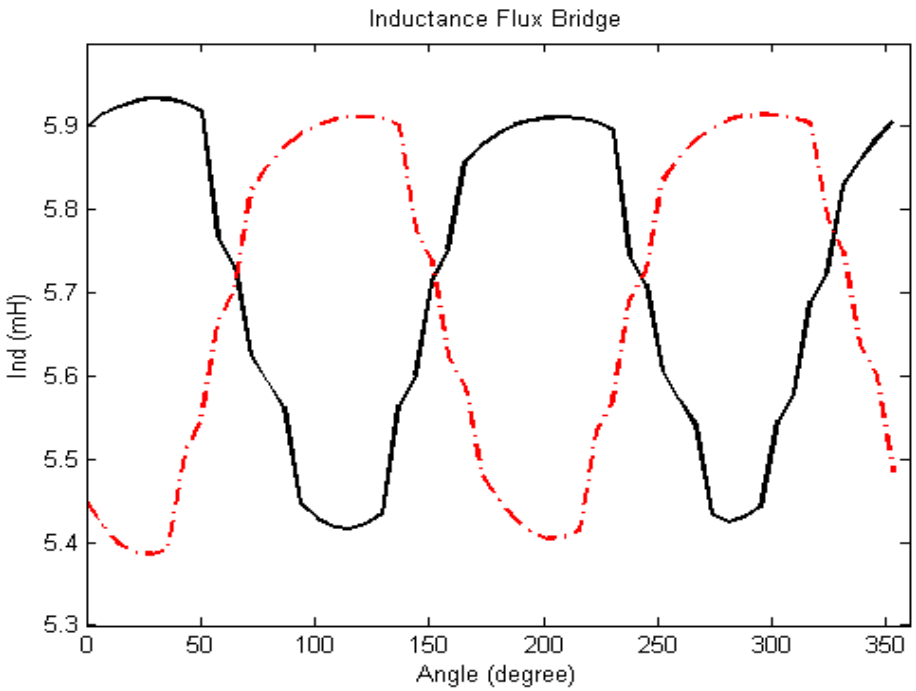

Fig 6.12 Experimental measurement of the SRM prototype inductance

The experimental measurement is validated by the FEA simulation result as shown in Fig 6.13. In the FEA simulation where a small DC current (0.01 A) is used for the excitation, the maximum inductance value is 5.64 mH and the minimum value is 5.41 mH, which are values reasonably close to the experimental measurement.

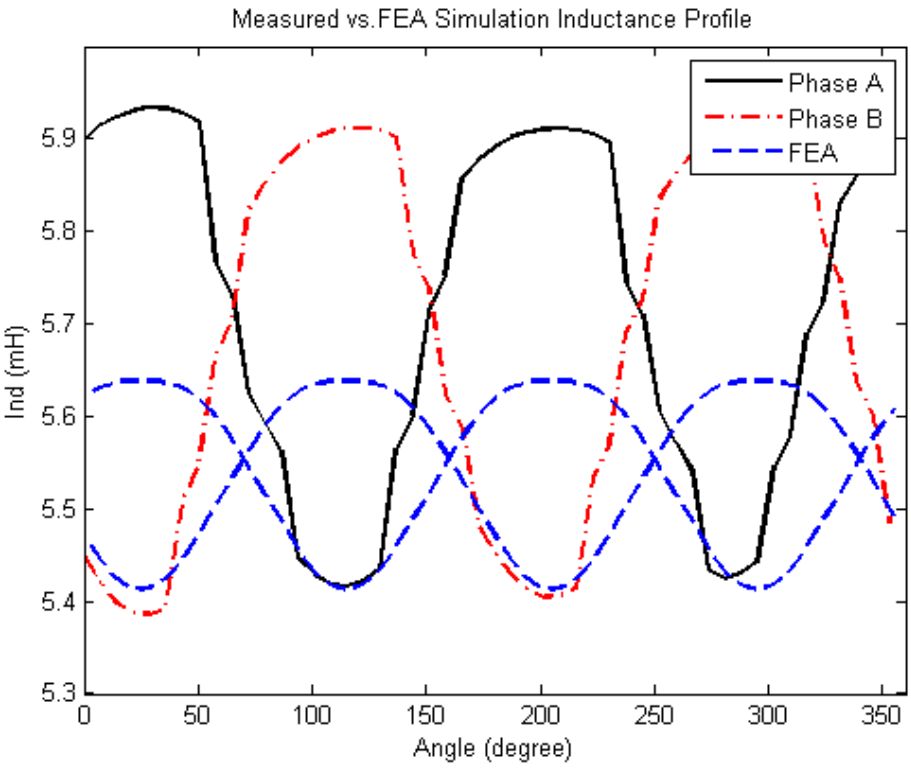

Fig 6.13 SRM inductance profile FEA simulation (excited with a small DC current)

Given the well-known accuracy in the inductance calculation, an alternative approach to obtain the inductance profile is using FEA simulation,. Particularly when describing the different saturation degrees, the FEA simulation is performed with different excitation current values. The calculated inductance profile is shown in Fig 6.14, where the different curves are labeled with their excitation current values. The inductance profile of the flux-bridge rotor is very different from the one of the regular salient-pole rotor, due to the various flux bridge saturation degrees for different current values. In the case of the 0.01 A current, the max and min inductance values are 5.6 mH and 5.4 mH, which are close to the results of Fig 6.12. In the case of the 6 A current, the max and min inductance values are 5.3 mH and 2 mH, and in the case of the 8 A current the max and min inductance values are 4.8 mH and 1.8 mH. Therefore, the SRM is highly saturated with the excitation current of 6 A, because there is no significant variation (within 10%) in the

inductance profile between the curves of 6 A and 8 A. In this section, the inductance profile of the 6 A current is used for the simulation model, and the controller design is based on this chosen inductance profile, which is to be presented in the following section. In addition, the impact of the different inductance profiles to the SRM control performance will be discussed in the following section, which is the major contribution of this chapter.

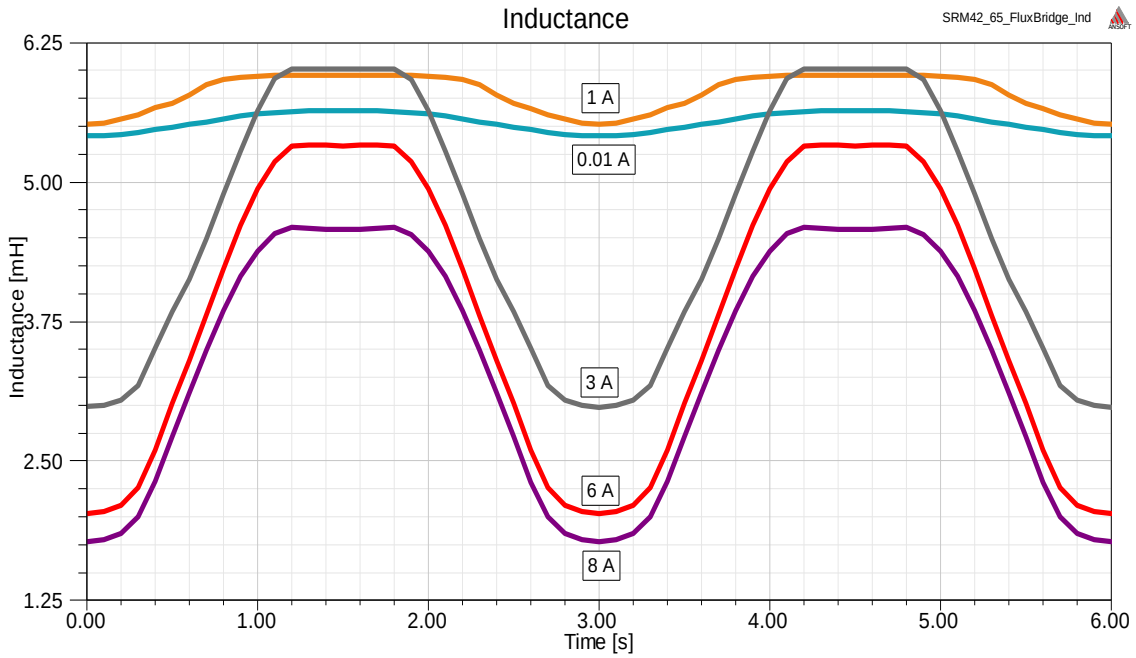

Fig 6.14 FEA simulation SRM inductance profile with different excitation current values

For the sake of simplicity, a linearized inductance profile is used in the simulation model to approximate the actual case as shown in Fig 6.15. The red and black curves indicate the FEA simulation using the 6 A current as shown in Fig 6.14, and the blue curve indicates the simplified linear inductance profile. The Phase A linearized inductance profile remains at the constant maximum value in the range between 0 º and 40 º, decreases from the maximum value to the minimum value in the range between 40 º

and 100 º, and remains at the constant minimum value in the range between 100 º and 120 º. The inductance values for the rest of the angles repeats in a symmetric way.

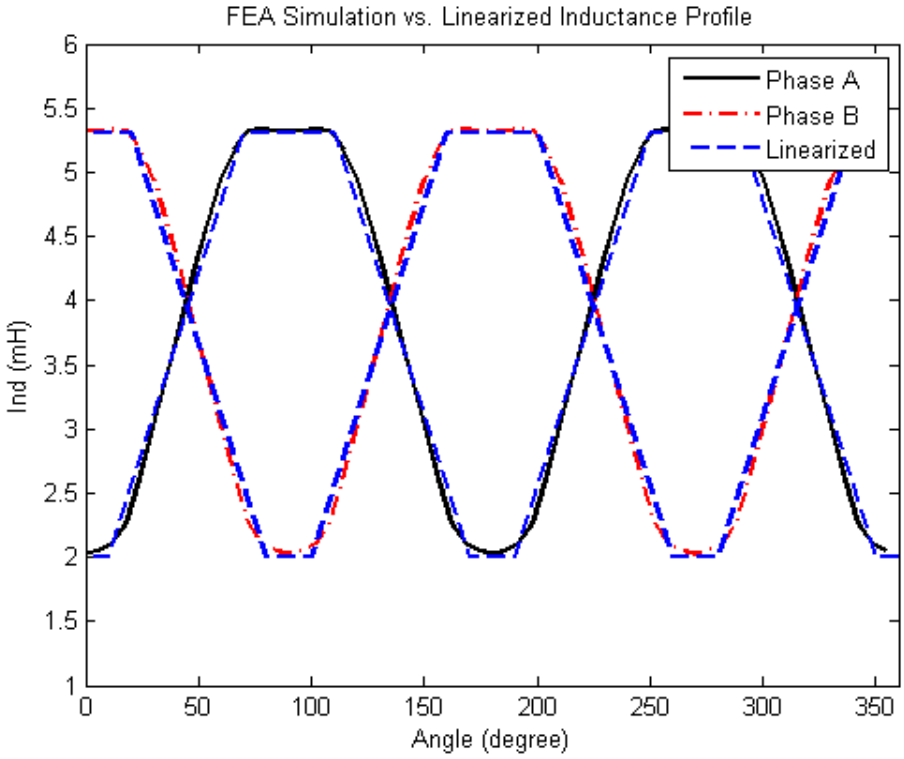

Fig 6.15 Linearized inductance profile for the SRM simulation model

6.3.4 Current calculation block

Given the inductance profile and the input voltage, the current can be calculated using the voltage equation (6.6)-(6.7):

$$v = R_s \cdot i + \frac{d\lambda(\theta)}{dt} = R_s \cdot i + \frac{d[L(\theta) \cdot i]}{dt} \tag{6.6}$$

$$v = R_s \cdot i + L(\theta) \cdot \frac{di}{dt} + \frac{dL(\theta)}{d\theta} \cdot \omega \cdot i \tag{6.7}$$

where R_s denotes the stator winding resistance, and $L(\theta)$ denotes the inductance as a function of the rotor angle.

For the sake of simplicity, $L(\theta)$ in the second term of equation (6.7) is assumed to be a constant of the average value of the maximum and the minimum inductance values. In addition, $\frac{dL(\theta)}{d\theta}$ is known according to the linear inductance profile shown in Fig 6.15. Therefore, the block diagram of the current calculation is illustrated in Fig 6.16, and the calculated current is used to calculate the SRM electromagnetic torque.

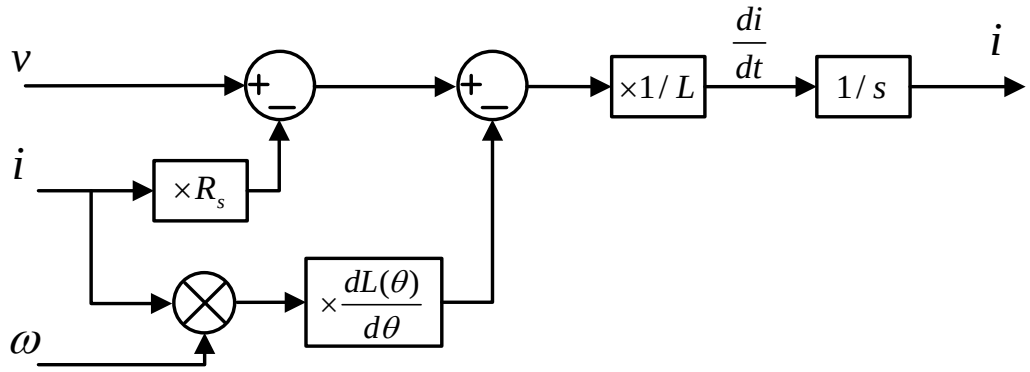

Fig 6.16 Current calculation block diagram of the SRM simulation model

6.3.5 Electromagnetic torque calculation

Given the SRM current calculation result, the SRM electromagnetic torque is calculated by using (6.8):

$$T_e = \frac{1}{2} \cdot i^2 \cdot \frac{dL(\theta)}{d\theta} \tag{6.8}$$

where $\frac{dL(\theta)}{d\theta}$ is known as a function of the rotor angle, and thus T_e can be calculated in a straightforward way.

6. 4 PI controller design

After the establishment of the SRM simulation model, the next step is to appropriately design the current and speed controllers. As concluded in Section 6.1, a classic dual-loop control is selected for the SRM control scheme. Therefore, the proportional and integral gains of those two controllers need to be carefully calculated to achieve good SRM control performance. In this section, a small signal model of the SRM drive system is built first. Then the PI controller parameters can be calculated accordingly, to satisfy the control specification. Lastly, simulation results are provided to verify the designed SRM control scheme.

6.4.1 SRM small signal model

In order to utilize classic control theorem to design the controllers, the SRM drive system needs to be described as a linear system with transfer functions. For this purpose a small signal system needs to be derived first, which can indicate the output response with respect to the input. The core idea of small signal system is to perturb the system around a steady-state operating point with small variation. The new system states and inputs are:

$$i = i_0 + \delta i \tag{6.18}$$

$$\omega = \omega_0 + \delta\omega \tag{6.19}$$

$$v = v_0 + \delta v \tag{6.20}$$

$$T_l = T_{l0} + \delta T_l \tag{6.21}$$

where the extra subscript 0 indicates steady-state values of the states and inputs, and the small signals are indicated by δ preceding the variables. Substituting the perturbed variables in the system voltage equation (6.7) and torque equation (6.2), it is seen that the steady-state terms cancel and the residual of these equations gives:

$$\frac{d\delta i}{dt} = \left(-\frac{R_s}{L} - \frac{1}{L} \cdot \frac{dL}{d\theta} \cdot \omega_0 \right) \cdot \delta i - \frac{1}{L} \cdot \frac{dL}{d\theta} \cdot i_0 \cdot \delta\omega + \frac{\delta v}{L} \tag{6.22}$$

$$\frac{d\delta\omega}{dt} = \left(-\frac{1}{J} \cdot \frac{dL}{d\theta} \cdot i_0 \right) \cdot \delta i - \frac{F}{J} \cdot \delta\omega + \frac{\delta T_l}{J} \tag{6.23}$$

It is noted that the inductance is assumed to be constant for the sake of simplification, which is the mean value of the maximum and minimum inductance values in Fig 6.14.

Next, the following substitutes are used:

$$R_{eq} = R_s + \frac{dL}{d\theta} \cdot \omega_0 \tag{6.24}$$

$$K_b = \frac{dL}{d\theta} \cdot i_0 \tag{6.25}$$

$$\delta e = \frac{dL}{d\theta} \cdot i_0 \cdot \delta\omega \tag{6.26}$$

where R_{eq} is the equivalent resistance, K_b is the emf constant, and δe is the induced emf. Now, the small signal model of the SRM can be derived based on equation (6.22) and (6.23), and its block diagram is shown in Fig 6.17.

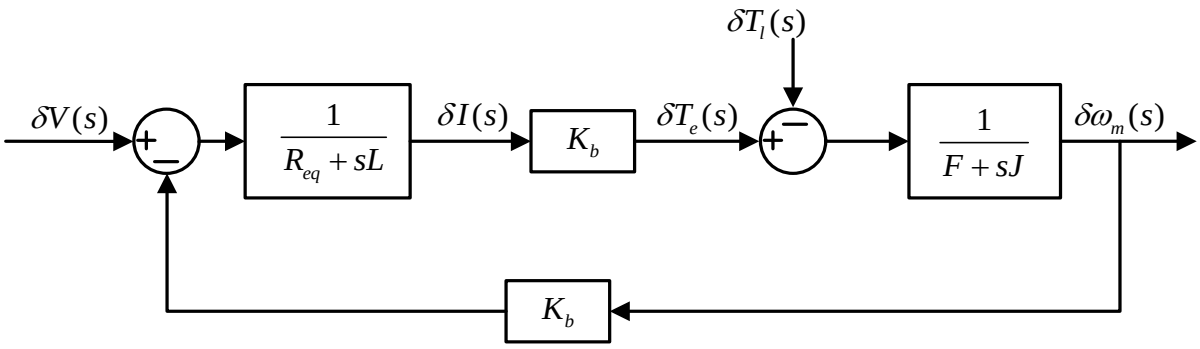

Fig 6.17 The SRM small signal model block diagram

For the sake of simplification, the back emf feedback loop is decoupled from the system which gives:

$$\delta V(s) - K_b \cdot \delta\omega(s) = \frac{\delta\omega(s)}{\frac{1}{R_{eq} + s \cdot L} \cdot K_b \cdot \frac{1}{F + s \cdot J}} \tag{6.27}$$

$$\frac{\delta V(s)}{\delta\omega(s)} = \frac{1}{K_b \cdot \frac{1}{R_{eq} + s \cdot L} \cdot \frac{1}{F + s \cdot J}} + K_b = \frac{(R_{eq} + s \cdot L) \cdot (F + s \cdot J) + K_b{}^2}{K_b} \tag{6.28}$$

$$T_l = \delta T_l = 0 \tag{6.29}$$

where in (6.23) the load torque T_l is assumed to be zero.

Then, the SRM block diagram is cast in a two-stage transfer function as shown in Fig 6.18, which is very similar to a DC machine model.

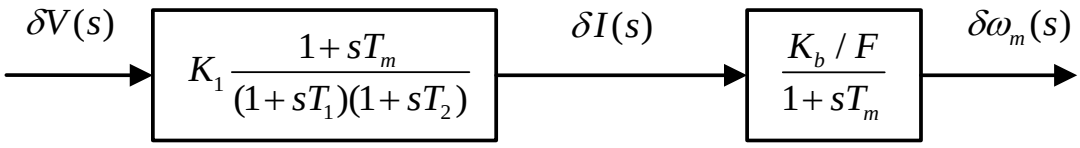

Fig 6.18 The SRM block diagram in a two-stage transfer function

where

$$K_1 = \frac{F}{K_b{}^2 + R_{eq} \cdot F} \tag{6.30}$$

$$T_m = \frac{J}{F} \tag{6.31}$$

$$-\frac{1}{T_1}, -\frac{1}{T_2} = -\frac{1}{2}\left[\frac{F}{J} + \frac{R_{eq}}{L}\right] \pm \sqrt{\frac{1}{4} \cdot \left(\frac{F}{J} + \frac{R_{eq}}{L}\right)^2 - \frac{K_b{}^2 + R_{eq} \cdot F}{JL}} \tag{6.32}$$

Now the SRM model can be described by a few transfer functions, so the complete SRM drive system can be rewritten as shown in Fig 6.19.

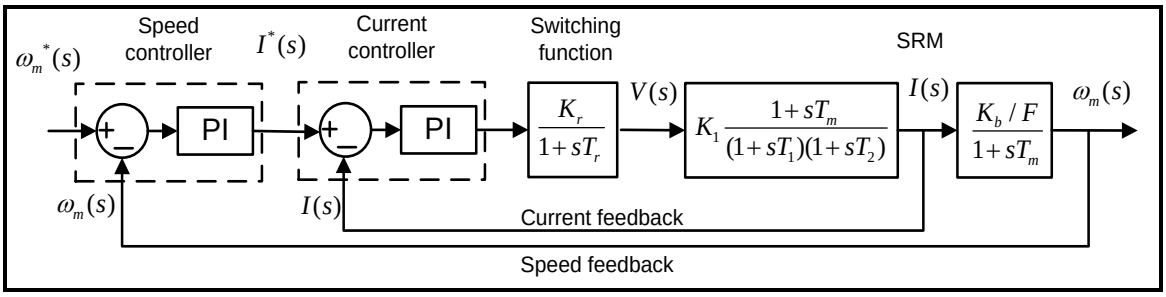

Fig 6.19 The SRM small signal system described using transfer functions

where the switching function block in Fig 6.24 is modeled as a gain with a first-order lag, and the gain is given by:

$$K_r = \frac{V_{dc}}{V_{cm}} \tag{6.33}$$

where V_{cm} is the maximum control voltage. In this work, $V_{cm} = 1$ as the control signal is the duty cycle *D* and is limited between 0 and 1. The time constant of the switching function block, T_r, assuming PWM control of the converter with a switching frequency of f_c, is given by:

$$T_r = \frac{1}{2 f_c} \tag{6.34}$$

Given that f_c = 20 kHz and the desired the current loop bandwidth is 2 kHz, the switching frequency of the converter is 10 times greater than the current control loop bandwidth. Therefore, the switching function block can be simplified as a gain K_r.

6.4.2 Current controller design

First, the design of the current PI controller is investigated. The block diagram of the current control loop is shown in Fig 6.20.

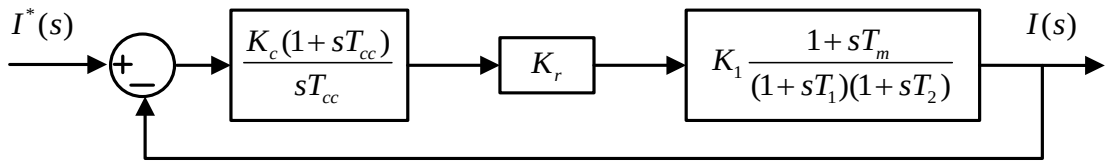

Fig 6.20 The SRM current control loop block diagram

where the PI controller is described as a transfer function of equation (6.35):

$$G_c(s) = K_c + \frac{K_c}{s \cdot T_{cc}} \tag{6.35}$$

where K_c is the proportional gain, and T_{cc} is the current controller time constant.

Since the mechanical time constant of the system, T_m, is large, $(1+s \cdot T_m)$ can be approximated as sT_m. With this approximation the current loop becomes a second-order system. The approximated system is given below:

$$\frac{I(s)}{I^*(s)} = \frac{K_c K_r K_1 T_m (1+sT_{cc})}{T_c(1+sT_1)\cdot(1+sT_2) + H_c K_c K_r K_1 T_m (1+sT_{cc})} \tag{6.36}$$

And the characteristics equation of the current loop is given as:

$$s^2 + \left(\frac{T_1 + T_2 + H_c K_c K_r K_1 T_m}{T_1 T_2}\right)\cdot s + \frac{H_c K_c K_r K_1 T_m + T_{cc}}{T_{cc} T_1 T_2} \tag{6.37}$$

Since it is a second-order equation, the natural frequency (bandwidth), ω_n, and the damping ratio, ζ, of a second-order system can be specified for the desired system performance. Furthermore they can be used to calculate the current controller gain and time constant. Given below are the equations which specify the damping (6.38) and the natural frequency (6.39):

$$2\zeta\omega_n = \frac{T_1 + T_2 + H_c K_c K_r K_1 T_m}{T_1 T_2} \tag{6.38}$$

$$\omega_n{}^2 = \frac{H_c K_c K_r K_1 T_m + T_{cc}}{T_{cc} T_1 T_2} \tag{6.39}$$

For a given natural frequency and damping ratio (here $\omega_n = 2000$ and $\zeta = 0.707$), the gain K_c and the time constant T_{cc} can be solved by equation (6.40) and (6.41).

$$K_c = \frac{2\zeta\omega_n T_1 T_2 - T_1 - T_2}{H_c K_r K_1 T_m} \tag{6.40}$$

$$T_{cc} = \frac{H_c K_c K_r K_1 T_m}{T_1 T_2 \omega_n{}^2 - 1} \tag{6.41}$$

And the calculation results are:

$$K_c = 0.4032$$

$$T_{cc} = 9.57 \times 10^{-5}$$

The values of the parameters used in this calculation are listed in Table 6.2.

Table 6.2 Parameter values used for
the current control loop parameter calculation

R_s	$0.6\,\Omega$
$L_{\max}$	2 mH
$L_{\min}$	5.3 mH
$dL/d\theta$	$0.0032\,H/rad$
ω_0	50 krpm
i_0	5 A
F	1×10^{-7}
K_1	0.0115
T_m	25

T_1, T_2	1.44, 0.0011
V_{dc}	150 V
V_{cm}	1 V
K_r	150

Given the calculated parameter values and the transfer function (6.36), the current control loop response in frequency domain can be demonstrated using the Bode plot of Fig 6.21. The upper diagram of Fig 6.21 is the magnitude and the lower diagram is the phase shift. It can be observed that the current control loop bandwidth is 12.56 krad/s, or 2 kHz, and there is no sharp peak in the magnitude diagram. The magnitude at low frequency is flat at constant 0, and the phase shift at high frequency is at a constant value above -100 º. These are great gain margins and phase margins for the current control loop, so it is very stable.

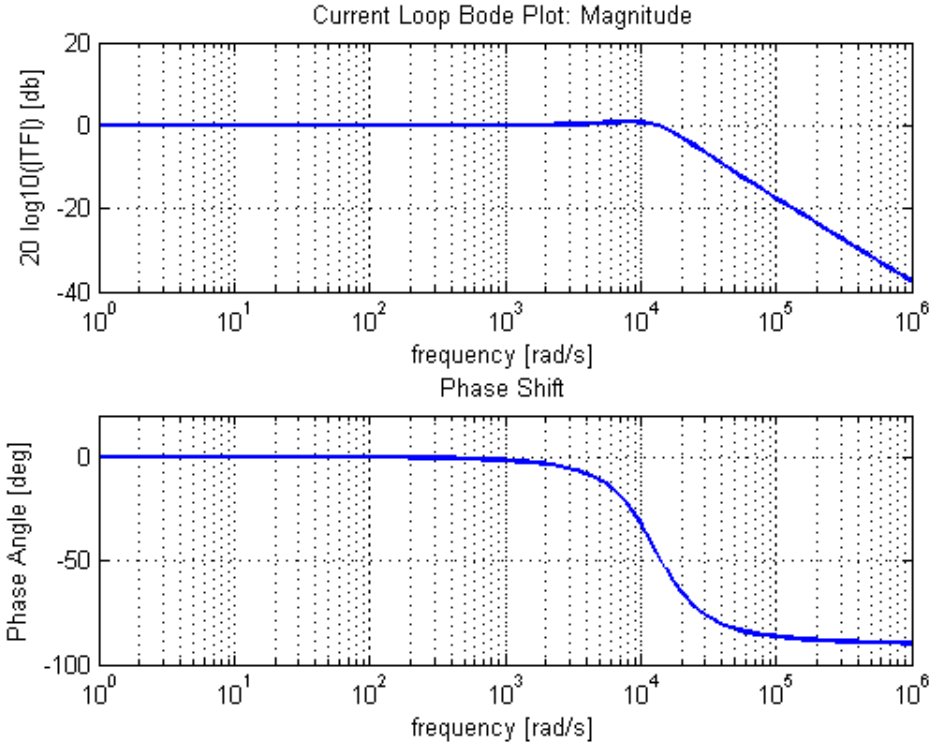

Fig 6.21 The Bode plot of the SRM current control loop

The performance of the current control loop can be further testified by the simulation results in Fig 6.22 and Fig 6.23, showing the SRM response to a step change of the current reference value (from 3 A to 3.5 A). In Fig 6.22, the SRM current is regulated at the reference value, and in Fig 6.23 the current follows the reference value change in a very fast fashion.

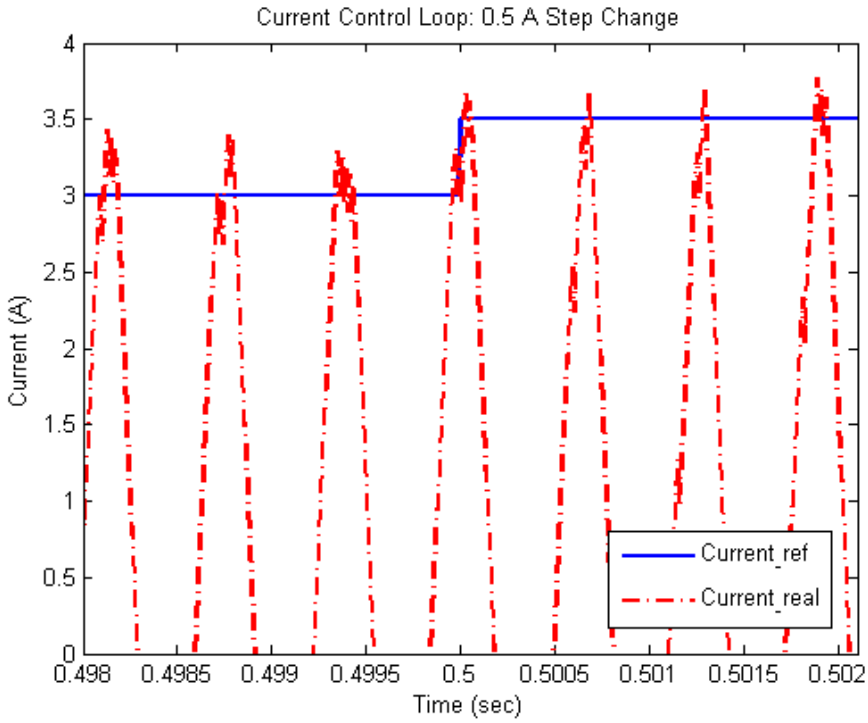

Fig 6.22 The SRM response to a current reference value step change

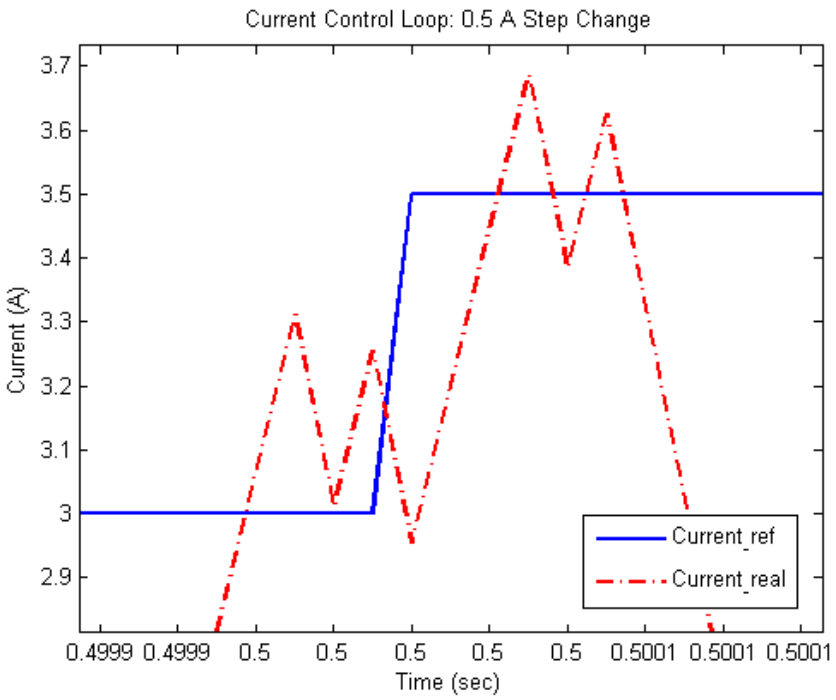

Fig 6.23 The SRM response to a current reference value step change (zoomed in)

6.4.3 Speed controller design

After the design of the current controller, the next step is to design the speed controller. To simplify the problem, it is assumed that the delay of the current loop is negligible due to the fact that usually the response speed of the current loop is at least ten times faster than the response speed of the speed loop. Therefore the current loop gain is approximated as unity and its time delay is neglected. In addition the delay of the speed feedback is neglected in the simulation model, and it is usually true in practice as well. As a result the speed control loop is reduced to a second-order system. The block diagram of the approximated speed loop is shown in Fig 6.24.

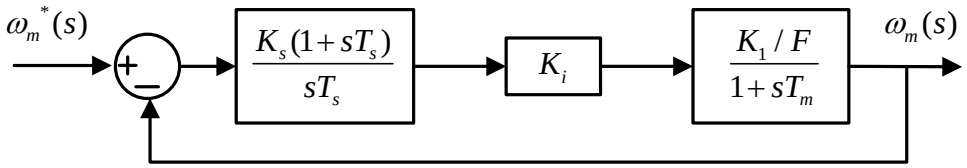

Fig 6.24 The SRM speed control loop block diagram

where the speed controller is described as a transfer function of (6.42), and $K_i = 1$ in Fig 6.24

$$G_s(s) = K_s + \frac{K_s}{s \cdot T_s} \tag{6.42}$$

Then, as T_m is large compared to other time constants, $1 + sT_m$ is approximated to be sT_m. Therefore, the speed control loop transfer function is derived as:

$$\frac{\omega_m(s)}{\omega_m^*(s)} = \frac{K_2 \cdot K_s \cdot (s + \frac{1}{T_s})}{s^2 + K_2 K_s \cdot s + \frac{K_2 K_s}{T_s}} \tag{6.43}$$

where

$$K_2 = \frac{K_b}{F \cdot T_m} \tag{6.44}$$

This is a second-order system, so the appropriate PI coefficients, K_s and T_s, can be calculated using the specified speed control loop bandwidth ω_{n_speed} and damping ratio ζ_{speed}. The calculation equations are given as:

$$2\zeta_{speed}\omega_{n\_speed} = K_2 K_s \tag{6.45}$$

$$\omega_{n\_speed}^{\ 2} = \frac{K_2 K_s}{T_s} \tag{6.46}$$

$$K_s = \frac{K_2}{2\zeta_{speed}\omega_{n\_speed}} \tag{6.47}$$

$$T_s = \frac{K_2 K_s}{\omega_{n\_speed}^{\ 2}} \tag{6.48}$$

Given $\omega_{n\_speed} = 200$, $\zeta_{speed} = 0.707$ and $K_2 = 1146$, the speed controller gains are calculated to be:

$$K_s = 0.3877$$

$$T_s = 0.0011$$

Given the calculated PI coefficients and the transfer function (6.43), the speed control loop response in frequency domain can be demonstrated using the Bode plot of Fig 6.25. The upper diagram of Fig 6.25 is the magnitude and the lower diagram is the phase shift. It can be observed that the speed control loop bandwidth is 1.256 krad/s, or 200 Hz, and there is no sharp peak in the magnitude diagram. The magnitude at low frequency is flat at constant 0, and the phase shift at high frequency is at a constant value above -100°. These are great gain margins and phase margins for the speed control loop, so it is very stable.

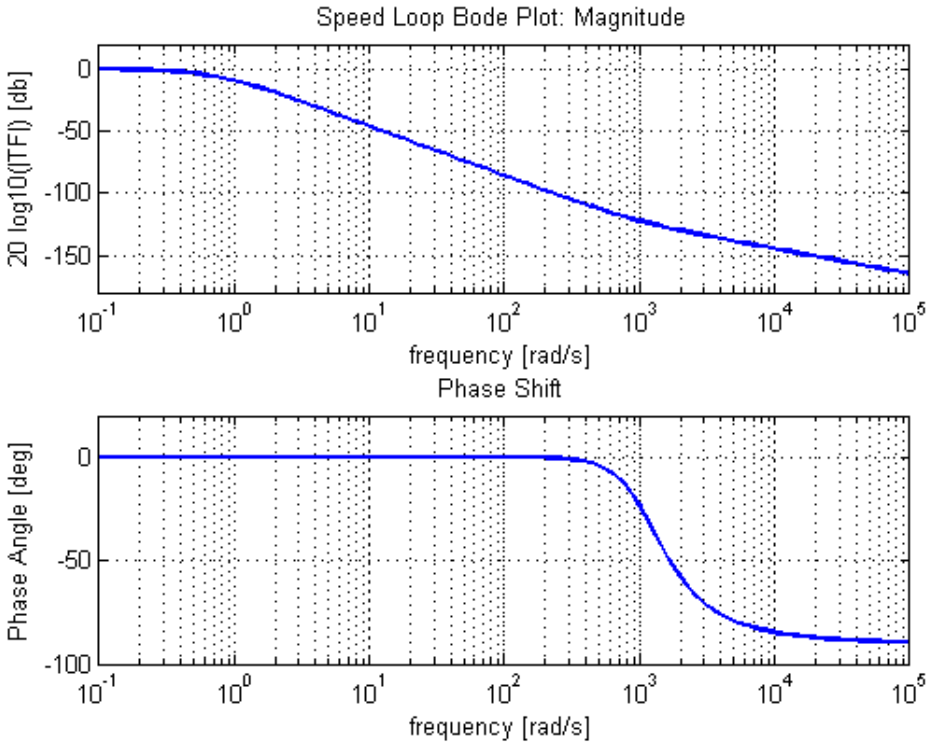

Fig 6.25 The Bode plot of the SRM speed control loop

The performance of the SRM speed control loop can be further testified by the simulation results of Fig 6.26 and Fig 6.27, showing the response to a step change of the speed reference value (from 50 krpm to 52.5 krpm). In Fig 6.26, the speed is regulated at the reference value with almost zero steady state error, and in Fig 6.27 the speed transient overshoot and damping phenomenon is very small.

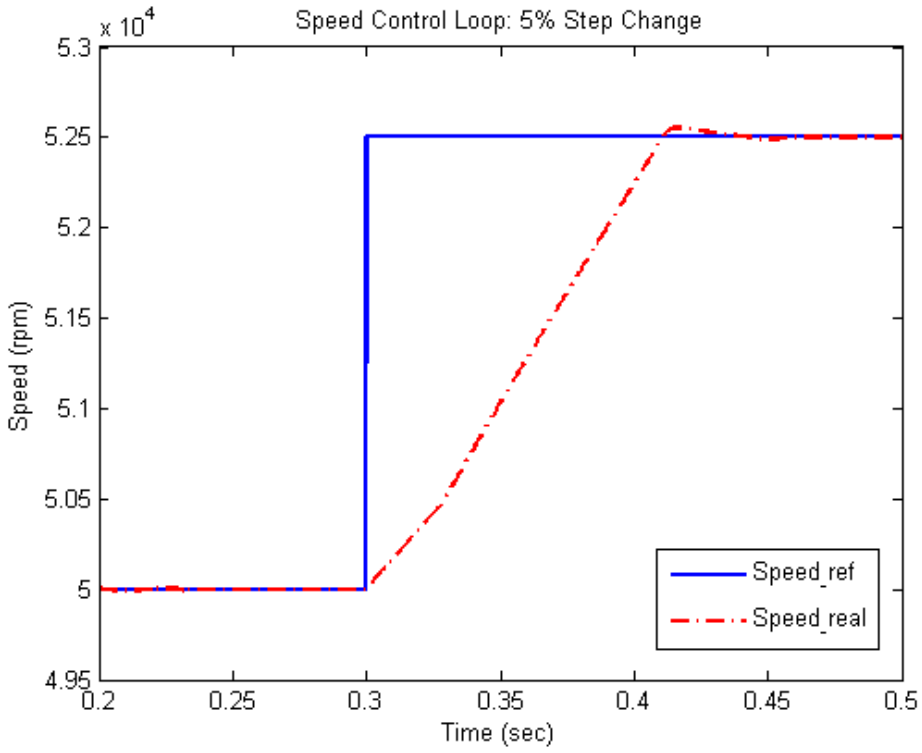

Fig 6.26 The SRM response to a speed reference value step change

6. 5 SRM control simulation performance

Following the design of the current and speed controllers, a SRM drive system simulation model is built using Malab/Simulink, as shown in Fig 6.27.

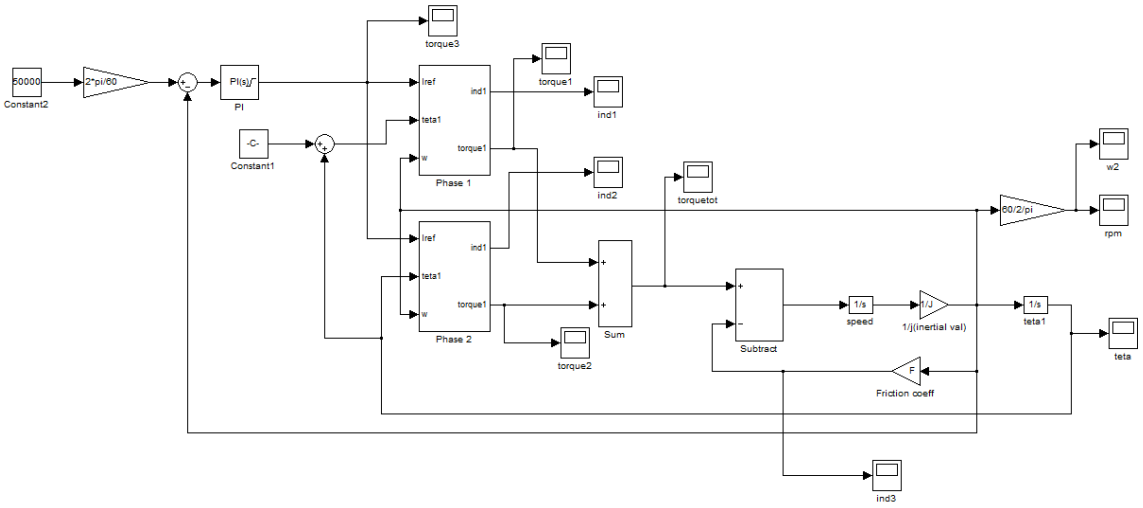

Fig 6.27 SRM drive system simulation model in Matlab/Simulink

In each phase block of Fig 6.27, the simulation blocks including the current controller, the current calculation block, and the torque calculation block, are shown in Fig 6.28.

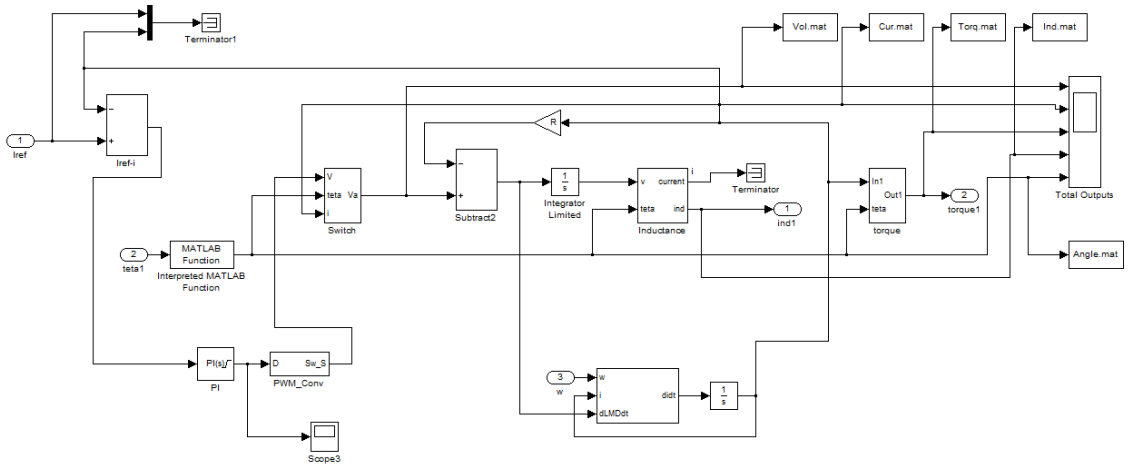

Fig 6.28 Detailed blocks in each phase block of the SRM simulation model

First the simulation results of the SRM Matlab/Simulink model at 50,000 rpm in steady state are presented in Fig 6.29. The five traces in Fig 6.29, from top to bottom, are the SRM phase A voltage, current, torque, inductance (both phases) and rotor angle (both phases) waveforms respectively. When the rotor moves passing θ_{on} (rotor angle trace),

the inductance starts to increase with a slope of $\frac{dL}{d\theta}$ (inductance trace). At the same time, the Phase A switch turns on and a positive DC but voltage (voltage trace) is applied to the phase winding, so the current starts to increase (current trace). Between θ_{on} and θ_{off}, the voltage switches between $\pm 150V$ (voltage trace), and the current is regulated to be around 1 A (current trace). As a result, the torque (torque trace) is controlled to be around $1\times10^{-3} N*m$. After the rotor passing θ_{off}, the voltage remains at negative DC bus voltage (voltage trace) until the current drops to zero (current trace).

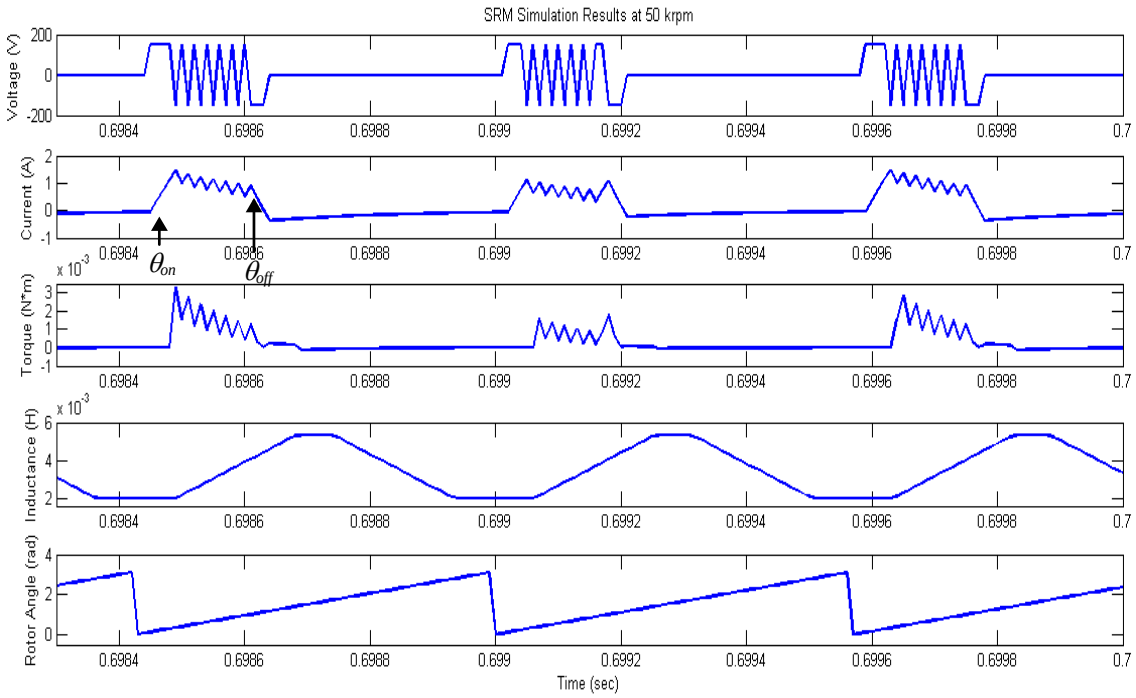

Fig 6.29 The SRM simulation results at 50,000 rpm using Matlab/Simulink

The SRM speed of the simulation model at 50,000 rpm in steady state is shown in Fig 6.30. The steady state error is almost zero, and the transient behavior when the speed reaches 50,000 rpm is very good.

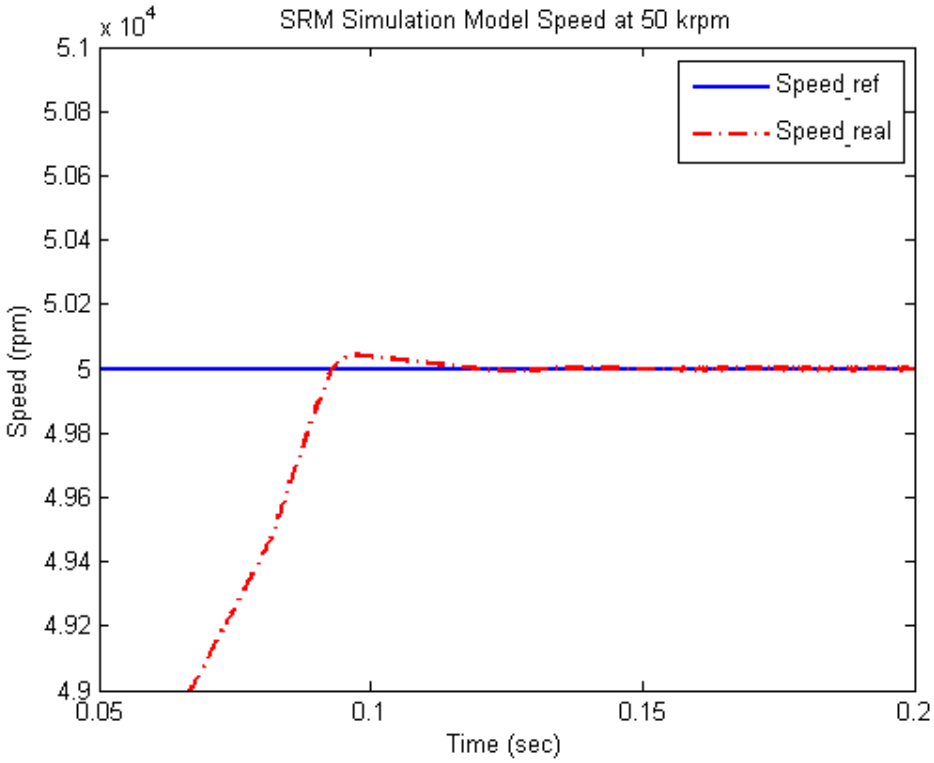

Fig 6.30 The SRM speed of the simulation model at 50,000 rpm (steady state)

Next a speed reference value step change, from 50,000 rpm to 52,500 rpm, is applied to the simulation model at 0.3 sec. The SRM speed profile is shown previously in Fig 6.26. Particular interest is paid on the SRM transient behavior between 0.4 sec and 0.5 sec (Fig 6.31), when the speed passes the final speed of 52,500 rpm and swings around that value. Moreover the current and torque profiles during the step change transient are shown in Fig 6.32. In the top trace of Fig 6.32, a smooth change of the current peak value, from 5 A to 1.8 A, can be observed. As a result, a smooth change of the torque value is also observed in the bottom trace of Fig 6.32. Both profiles indicate small overshoot and fast damping response of the transient when the speed approaches the reference value.

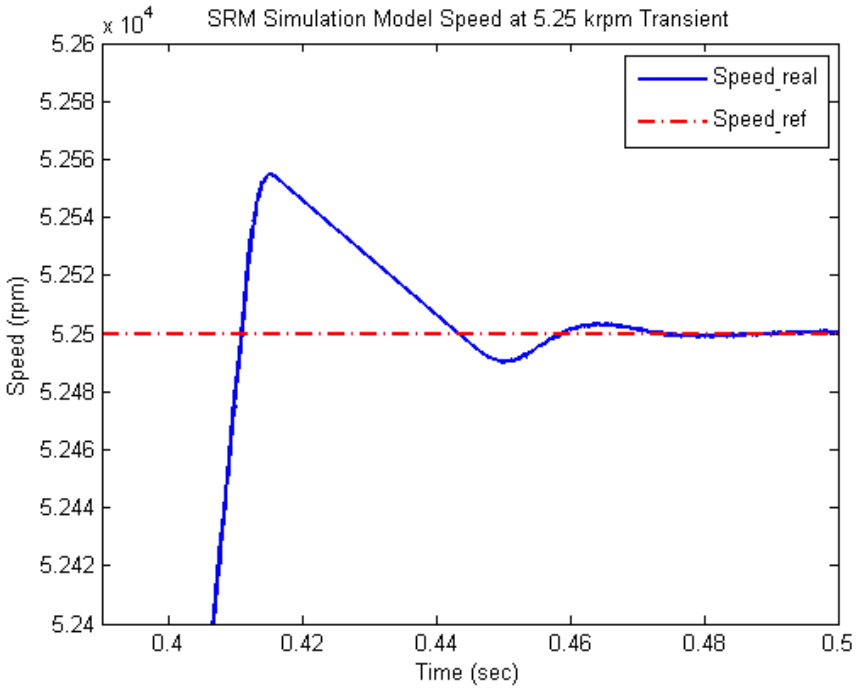

Fig 6.31 The SRM simulation speed during the speed step change from 50 krpm to 52.5 krpm

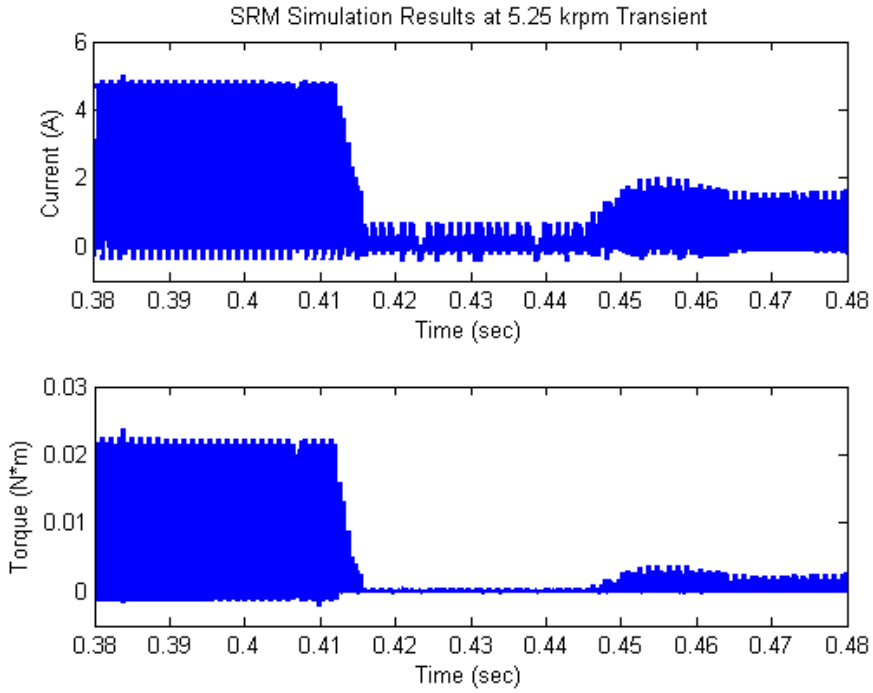

Fig 6.32 The SRM current and torque simulation results during the speed step change from 50 krpm to 52.5 krpm

Furthermore the SRM control performance is examined by applying a load torque step change to the model. It is to test the control stability in the case of load torque disturbance, and the simulation results are presented in Fig 6.33 and 6.34. The load torque used in the simulation model is friction torque, which is proportional to the rotation speed with a constant coefficient $F=1\times10^{-7}$. In the bottom trace of Fig 6.33, the load torque at 50 krpm steady state is 0.5×10^{-3} N-m. At 0.3 second, the load torque is changed to 1×10^{-3} N-m, and the speed oscillation is shown in the top trace of Fig 6.33. It can be observed that the speed damping is very small, and the peak value of the speed sag is less than 0.1% of the reference speed. The SRM speed returns to the reference value of 50 krpm in about 0.03 sec, and the transient current and torque profiles are shown in Fig 6.34.

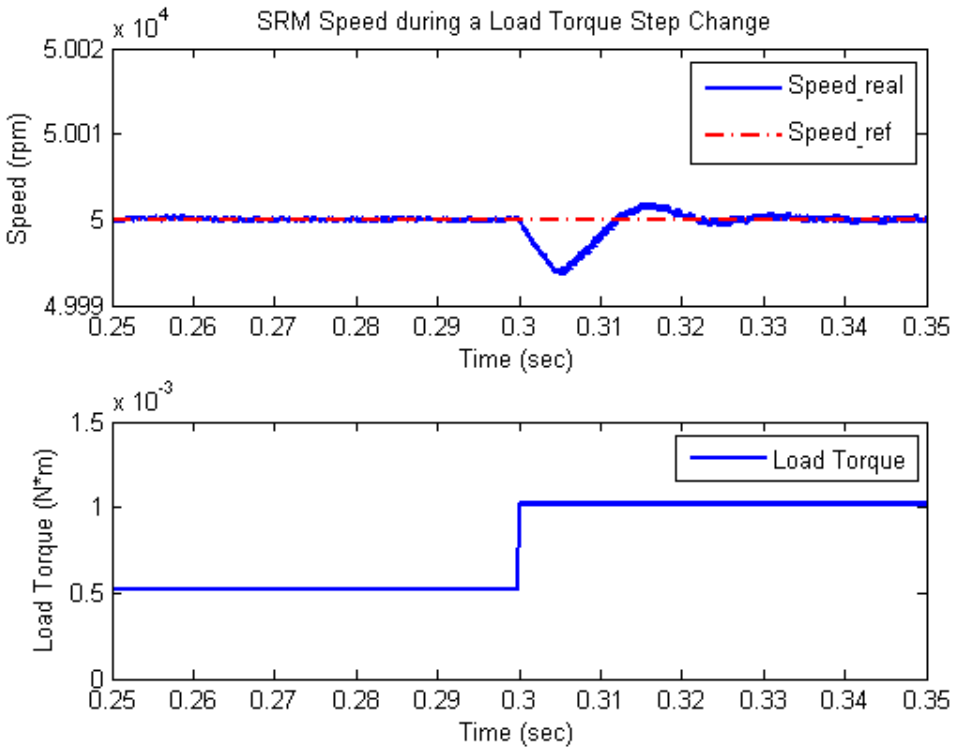

Fig 6.33 The SRM speed during a load torque step change

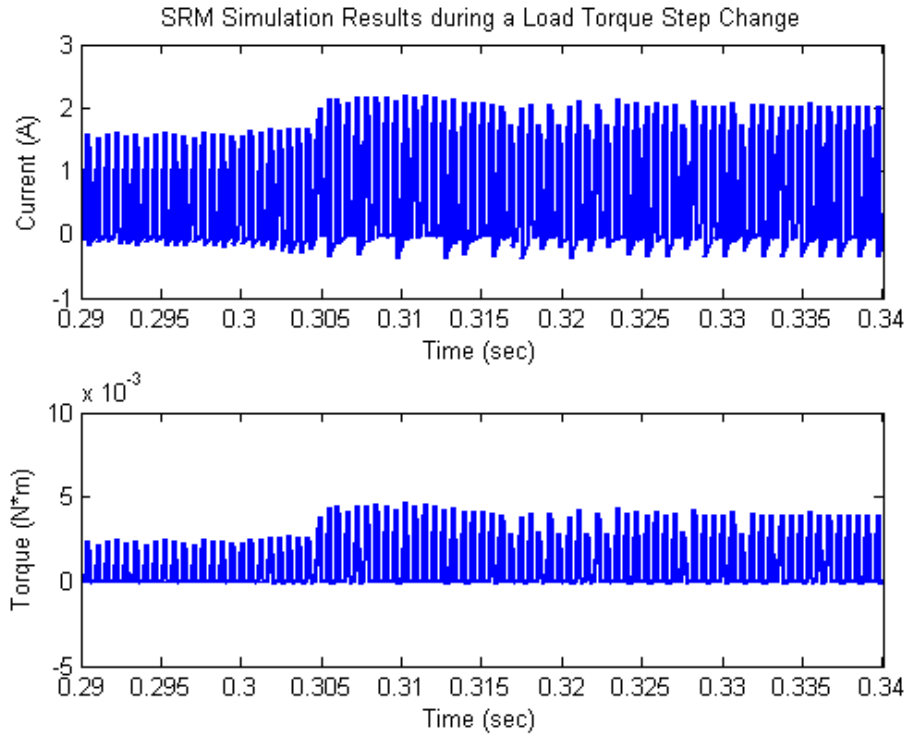

Fig 6.34 The SRM current and torque profiles during a load torque step change

The simulation results of the speed and load torque step change both show great performance of the SRM control. However the used control parameters are designed based on a particular inductance profile, the one in Fig 6.14 using a constant excitation current of 6 A. The comparison of the simulation using different inductance profiles is presented as follows, where the control parameters remain the same as calculated in Section 6.4.

First the inductance profile of 1 A current in Fig 6.14 is used to compare with the benchmark model using the inductance profile of 6 A current, as shown in Fig 6.35.

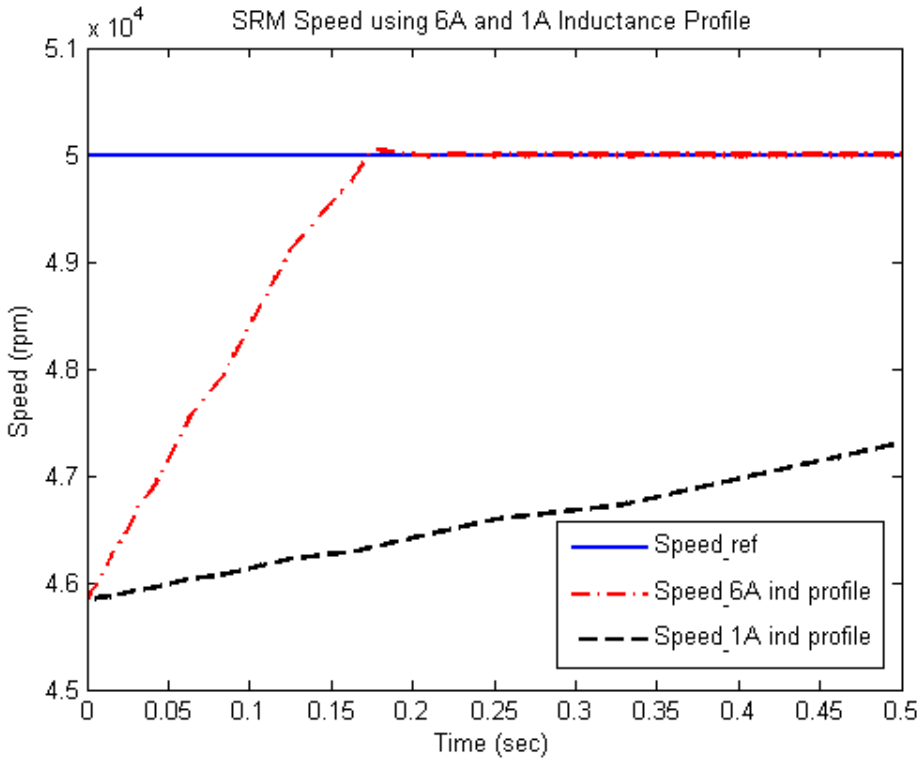

Fig 6.35 The SRM speed comparison of using different inductance profiles (1 A and 6 A current)

In Fig 6.14 the maximum and minimum inductance values of the 1 A current inductance profile are 6 mH and 5.5 mH, and the ones in the 6 A current inductance profile are 5.3 mH and 2 mH. Due to the significant difference between the maximum and minimum inductance values, the $dL/d\theta$ value and the SRM torque are greatly reduced for the 1 A current inductance profile. That explains why the speed increases much more slowly than the 6 A inductance profile curve in Fig 6.35. Therefore, the inductance profile of 1 A current should not be used for SRM control design, because it cannot describe the SRM behavior during acceleration transient (when the SRM current is relatively high).

Next the inductance profiles of 3 A and 8 A current in Fig 6.14 are used to compare with the benchmark model using the 6 A current inductance profile, as shown in Fig 6.36.

It can be observed that the curves of different inductance profiles are very close to each other, and the SRM speed can follow the reference value change in a fast fashion. This indicates that the control parameters calculated in Section 6.4 (using 6 A current inductance profile) can work very well in the cases of a moderate current value (3 A) and a very high current value (8 A).

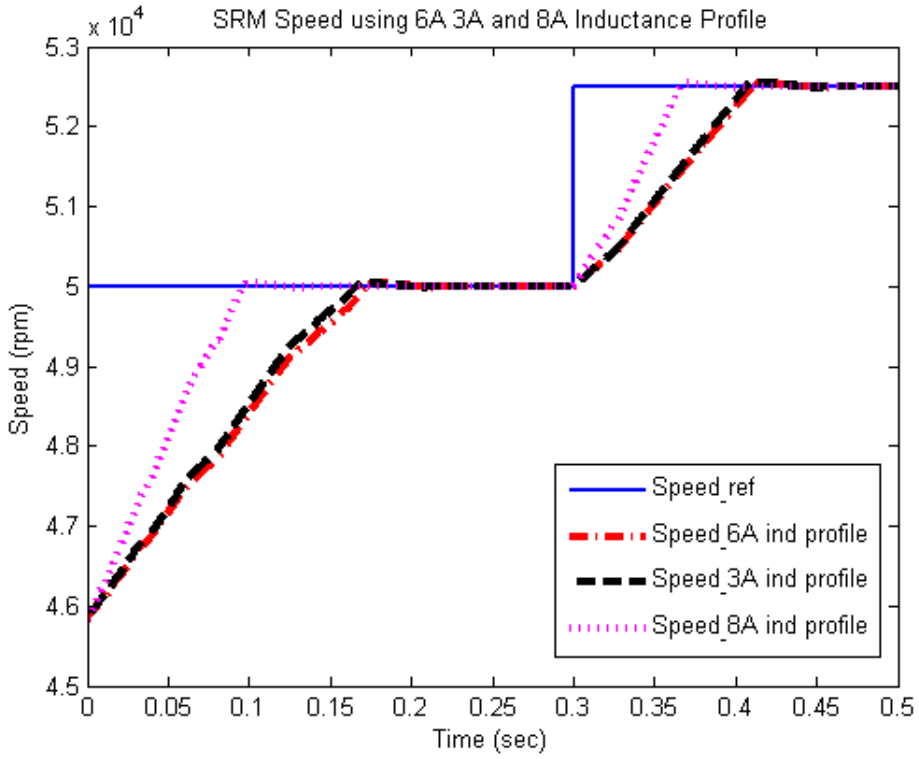

Fig 6.36 The SRM speed comparison of using different inductance profiles (3 A and 8 A current)

Although in Fig 6.14 the maximum and minimum inductance values for the 3 A, 6 A and 8 A inductance profiles are different with each other, the $dL/d\theta$ values are approximated the same because their $dL/d\theta$ slopes are in parallel with each other in Fig 6.14. Therefore the control design method used in Section 6.4 is very sensitive to the $dL/d\theta$ value of the inductance profile. For the inductance profile selection, it is suggested to first performing FEA simulations using different constant current values as

shown in Fig 6.14, and selecting the inductance profile which has an appropriate $dL/d\theta$ slope to design the SRM control parameters.

6. 6 SRM control experimental results

After the examination of the SRM speed-and-current dual-loop control performance in simulation, the designed control scheme is implemented in hardware with power electronics circuits and a DSP controller. The calculated control parameters are used, and the SRM prototype is tested at different speeds. The experimental work is presented in this section.

First the SRM drive circuit diagram is shown in Fig 6.37. A single phase AC voltage source is used for the power supply (voltage adjustable). A fuse is connected between the power supply and the rectifier. A single-phase diode bridge is used for the rectifier, and it follows with a choke inductor and the DC bus capacitor. The choke inductor is used to limit the rush current to protect the capacitor. Next the DC bus is connected with a H-bridge inverter. The asymmetric H-bridge inverter topology is the most common topology for the SRM drive. In the inverter, MOSFET is chosen as the switching device due to the relatively high switching frequency (20 kHz). For the 4/2 SRM prototype, two identical H-bridge inverters are built for Phase A and Phase B. Each of the H-bridge inverters consists of two MOSFET switches and two diodes. The phase winding is connected between the two arms of each H-bridge inverter.

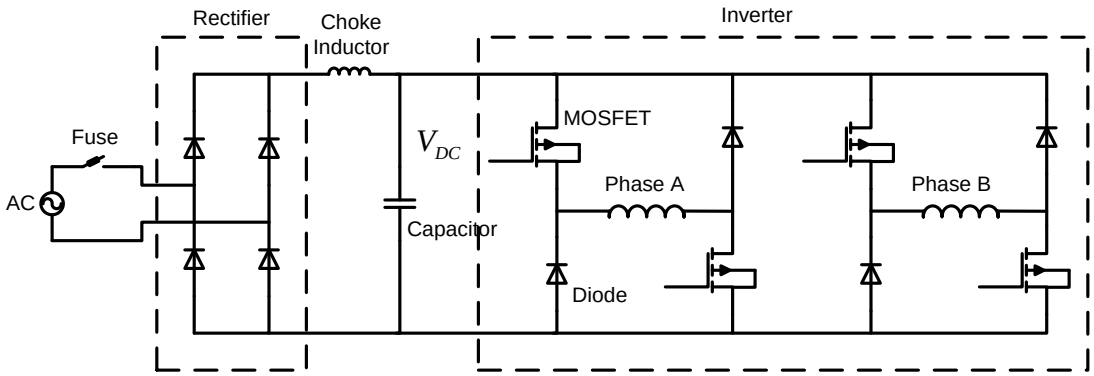

Fig 6.37 SRM drive circuit diagram

The rating of the components in the circuit diagram is listed in Table 6.3. For experimental purpose, the component ratings are selected with great margins.

Table 6.3 Circuit diagram component rating

Component	Power Rating	Part Name
AC Power Supply	Input 120V (AC), Output 0-140V (AC), 10 A, 1.4 kVA	Variable autotransformer Type 3PN1010
Fuse	Fast burn 10 A	BUS AGC 10
Rectifier	600 V, 25 A, 3 phase	RU E62320 26MT60
Choke inductor	10 mH, Max DC current 12.5 A	C-59U
Capacitor	400 V, 1500 uF	ECE-T2GP152FA
MOSFET	500 V, 44 A	FDH44N50
Diode	600 V, 30 A	STTH3006W

Secondly, the control architecture used for the SRM inverter is shown in Fig 6.38, which includes a DSP kit, a FPGA interface board, a MOSFET driver board, and a sensor board. The DSP kit, the FPGA interface board, and the sensor board are shared for both Phase A and Phase B. Two identical MOSFET driver boards are used to each phase respectively.

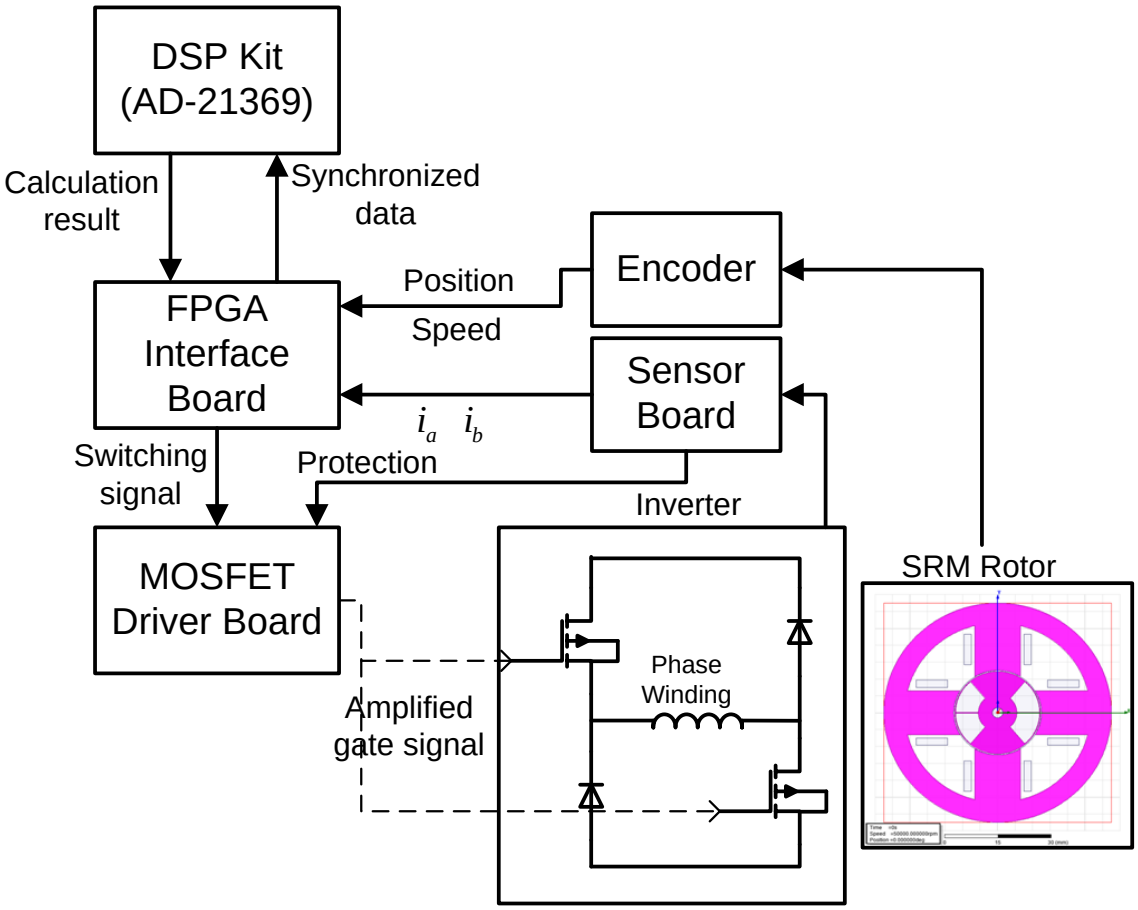

Fig. 6.38 Control architecture of the SRM inverter

- The DSP kit is a commercial ADSP-21369 evaluation board from Analog Devices©. It serves as the main processor, similar to the switching function block in Fig 6.6. The DSP program will be explained in Fig 6.39.
- Directly mated with the DSP kit is an interface board using Xilinx Spartan-3 FPGA, which handles routine tasks such as translating the duty cycle signal from the DSP board into actual gate signal, translating pulses from the speed encoder into the position and speed values, and translating serial current measurement data from the sensor board into synchronized parallel signal for the DSP board to process.

- The MOSFET driver board amplifies the switching signals from the FPGA interface board and outputs the gate signal to control the MOSFET switches.
- Both phases current is measured by the sensor board and converted into serial digital signals, which are then sent to the FPGA interface board via optical fiber links. The sensor board has over current protection, which can turn off the MOSFET driver board automatically if the current measurement exceeds the protection threshold value (13 A).
- The encoder is mounted on the SRM shaft, and it provides the SRM rotor position and speed information to the FPGA interface board.

Next the block diagram of the DSP program used to control the SRM drive switches is shown in Fig 6.39.

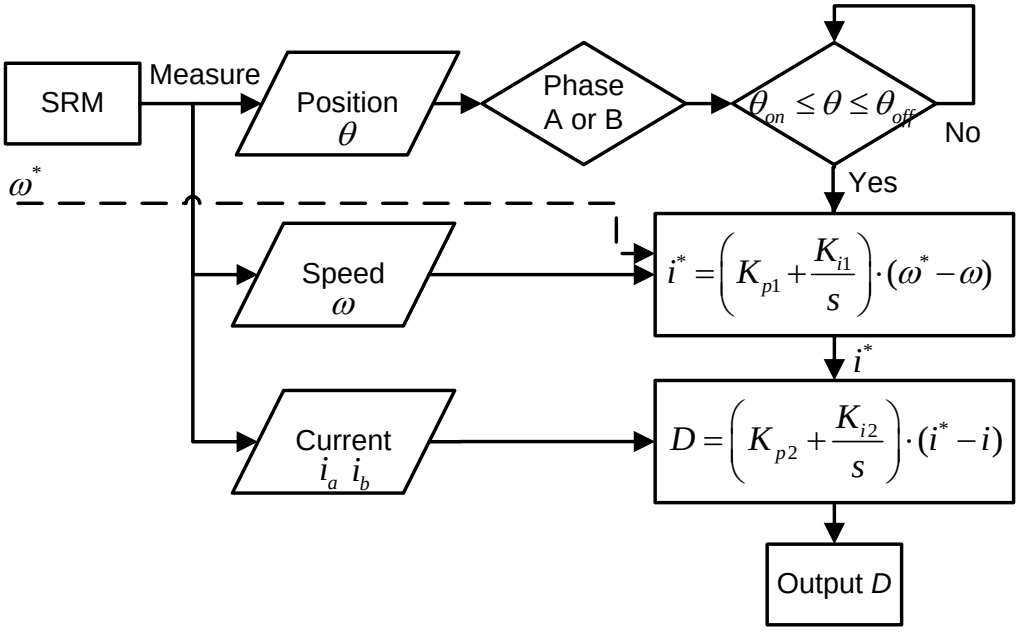

Fig 6.39 DSP program block diagram

The SRM measurement signals, rotor position θ, SRM speed ω, and phase current i, are sampled with their respective frequencies and sent to the DSP program as input. The DSP program first determines which phase to be turned on based on the position θ. For a particular phase, and if $\theta_{on} \le \theta \le \theta_{off}$, the speed PI controller calculates the current reference value i^* based on the actual speed ω and the speed reference value ω^*. Then the current PI controller calculates the switching duty cycle *D* based on the actual current value i and the current reference value i^*. The output of the DSP program is the duty cycle *D*. In addition, the speed reference value ω^* can be changed in the code so that the SRM can operate at different speeds.

Then the SRM drive system experimental setup is shown in Fig 6.40, and the hardware layout is labeled with their respective name.

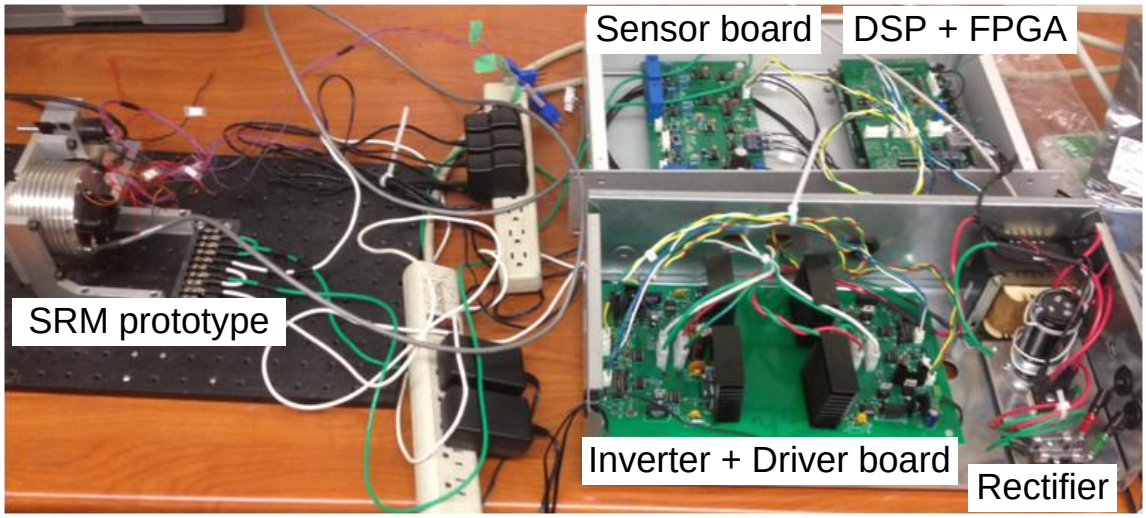

Fig 6.40 SRM drive system experimental setup

Finally the SRM prototype is tested at different speeds, e.g. 20 krpm and 50 krpm. The experimental result of the 50 krpm test is shown in Fig 6.41, which are the current and voltage waveforms.

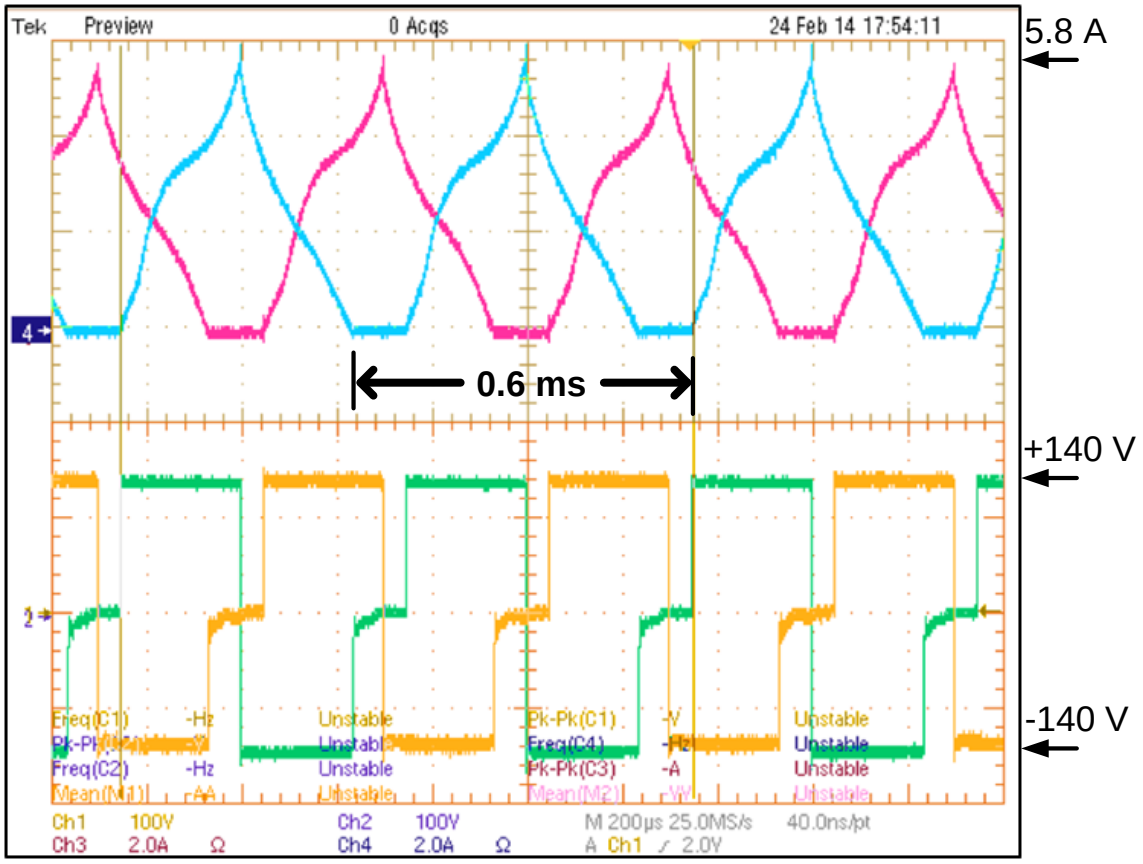

Fig 6.41 Experimental result of the SRM prototype at 50 krpm

As explain in Fig 5.11, the fundamental frequency of 50 krpm is 0.6 ms, and it is denoted in Fig 6.41, which means the speed of the tested SRM is 50,000 rpm. It can be observed that the peak current value is about 5.8 A, so the inductance profile used in the SRM control design, which is calculated by the FEA simulation with a constant 6 A current excitation, is appropriate. In addition, it can be observed in Fig 6.41 that there is good similarity in each fundamental cycle. Therefore the steady state of the SRM at 50 krpm is very smooth, and the control performance is very great. Such phenomenon can also be found in the 20 krpm test result of Fig 5.10, so the designed SRM control work very well at different speeds.

6. 7 Chapter summary

In this chapter the high speed SRM control is investigated for the fabricated SRM prototype at 50 krpm. To achieve simple and robust control performance, a speed-and-current dual-loop control is selected for the control strategy. At first the control architecture is developed with function blocks. Next, a small signal system is used to describe the SRM control with transfer functions. Then the small signal system is broken down into the current control loop and the speed control loop. The characteristic functions of each control loop are derived, so that the close-loop control bandwidth and damping ratio can be specified based on the desired control performance. In this way, the current and speed controller parameters can be calculated accordingly. Afterwards the designed SRM drive system is implemented using Matlab/Simulink and the control performance is testified in simulation. In particular, simulations are performed for cases of a 50 krpm steady state, a transient of speed reference value step change and a transient of load torque step change. In addition, the inductance profile selection suggestions are provided for the SRM control design, where the $dL/d\theta$ value is the key consideration. Finally the developed SRM control is built in hardware with power electronics circuits and a DSP program. The experimental results are presented to show the great performance of the designed control scheme.

CHAPTER 7 SRM Optimization with overlapped excitation current profile

7. 1 Introduction

The research of high torque density machines is another interest of this dissertation, and the research effort in this area is mainly driven by the increasing need for energy-efficient automation. Nowadays, permanent magnet synchronous machines (PMSMs) are the most common option for this application. However, the main issues of the high torque density PM machine are the temperature rise and the resulting magnet property decay problem.

In recent years the rise in permanent magnet prices has driven the machine design research towards PM-free machines, such as IM, synchronous reluctance machine (SynRM), SRM, and flux switched machine (FSM). The concerns about the PM cost and the performance improvement of the PM-free machines are making those machines more and more attractive for the high torque applications. However compared to SRMs, the problems of IMs include: poor fault tolerant capacity, the shoot through problem of the drives, and higher rotor losses (difficult to dissipate the heat) [21]. In addition, the rotors of SynRMs and FSMs are both more complex compared to the SRM rotor, which leads to higher manufactory cost.

For the automation and traction applications, the torque density and the torque ripple are the main two specifications for a SRM design. However much research has been carried out in Prof. Emadi's group at McMaster University on SRMs with a power rating of around 3kW [84-86]. Robust performance in the presence of high temperature, safe operation, high efficiency, a long constant power region, and a rugged structure, contribute to their suitability for this high impact application. In addition key technologies including sensorless operation and closed-loop torque and speed control have been developed. A novel SRM topology which has higher rotor pole numbers than

the stator has been proposed in [61, 84], and it helps to reduce the torque ripple and increase the efficiency [62].

A torque density of 45 Nm/*l* is achieved by Japanese companies for the SRM design in [62, 87-89], where the SRM torque, efficiency, operating speed-torque region are competitive with PM machines. The SRM shaft output power is compared with PM machines over the entire speed range as shown in Fig 7.1. At high speeds (6000 – 10,000 rpm), the output power of a SRM can be enhanced to 1.6 times that of a IPMSM, thus higher torque density is achieved.

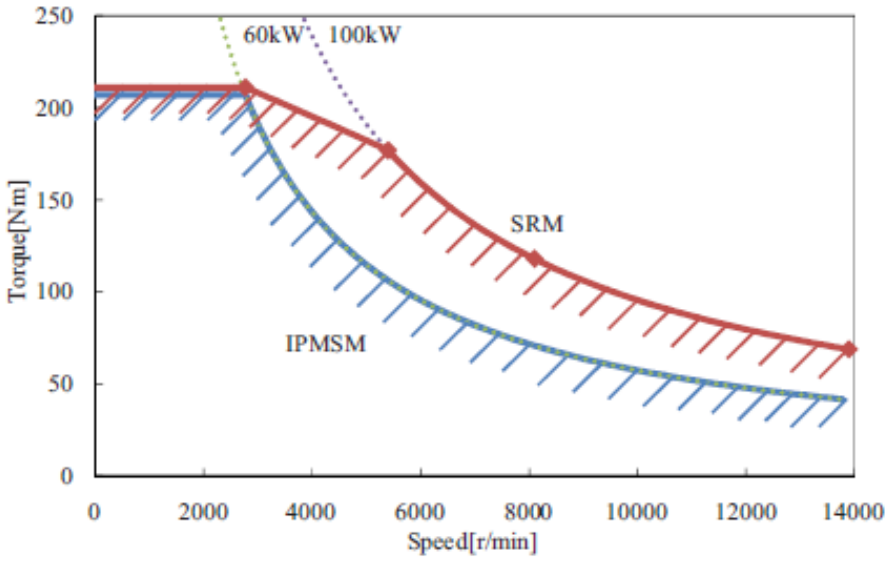

Fig 7.1 High torque density SRM and IPMSM torque-speed characteristics [89]

Moreover the SRM efficiency compared to the PM machine is shown in Fig 7.2, where the SRM has a few percent better efficiency in the low torque high speed region and the low speed high torque region (region A and C), but the SRM efficiency is inferior to that of the IPMSM in the middle speed region (region B).

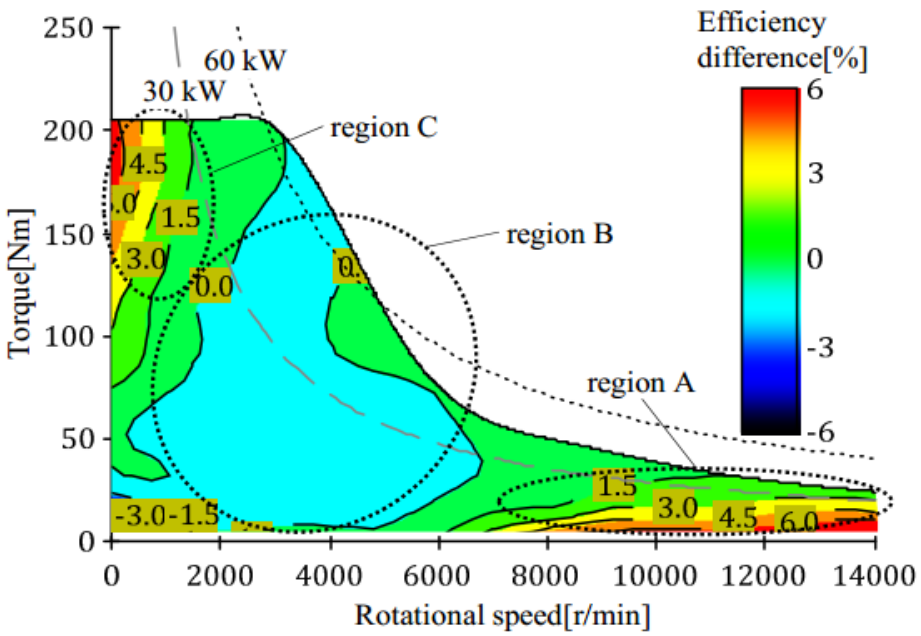

Fig 7.2 High torque density SRM and IPMSM efficiency comparison [63]

Therefore, the SRM is selected for the high torque density application in this dissertation. The most common SRM configuration for this application is 6/4 or 12/8. To minimize the torque ripple, the configuration of 12/8 is chosen in this work. This chapter serves as a continuation of Chapter 3, and particularly focuses on the high torque applications.

In Chapter 3, the typical SRM excitation current profile is described as shown in the upper diagram of Fig 7.3. The current of each phase is turned on at the unaligned position, and the phase current is reduced to zero at the aligned position. In this way only positive torque is generated so that the SRM is operated in the most efficient way. For two adjacent phases in the switching sequence, the aligned position of one phase corresponds to the unaligned position of the next phase, so there is no overlap in the current profile. The SRM design method presented in Chapters 3 and 4 is based on this non-overlapped current profile, which is usually true for the high speed applications but is not valid for the high torque machine design.

Specifically this control strategy (non-overlapped current profile) compromises output power for efficiency as the conduction time of the current is limited to the time interval between the unaligned and the aligned positions. To increase the output power and the torque density value, the conduction time of the current has to be increased. As shown in the bottom diagram of Fig 7.3, the current profile needs to have some overlap between two adjacent phases. In this chapter the SRM design and optimization with the overlapped excitation current is investigated.

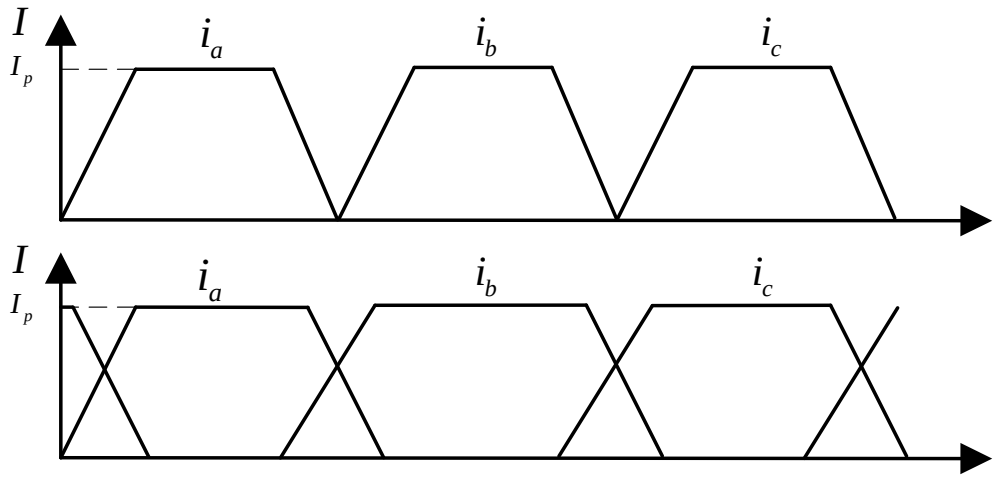

Fig 7.3 Non-overlapped current profile and overlapped current profile

7. 2 SRM design with overlapped excitation current profile

First, the different overlapped current profiles are simplified and sorted into three categories: *advanced turning-on*, *delayed turning-off*, and *combined situation*, as shown in Fig 7.4 (b), (c) and (d). Fig 7.4 (a) indicates the inductance profiles for phase A and B, and the SRM is excited in the sequence of phase A, B and C; the aligned position of phase A corresponds to the unaligned position of phase B, so $\theta_{a\_A} = \theta_{u\_B}$ and similarly $\theta_{u\_C} = \theta_{a\_B}$.

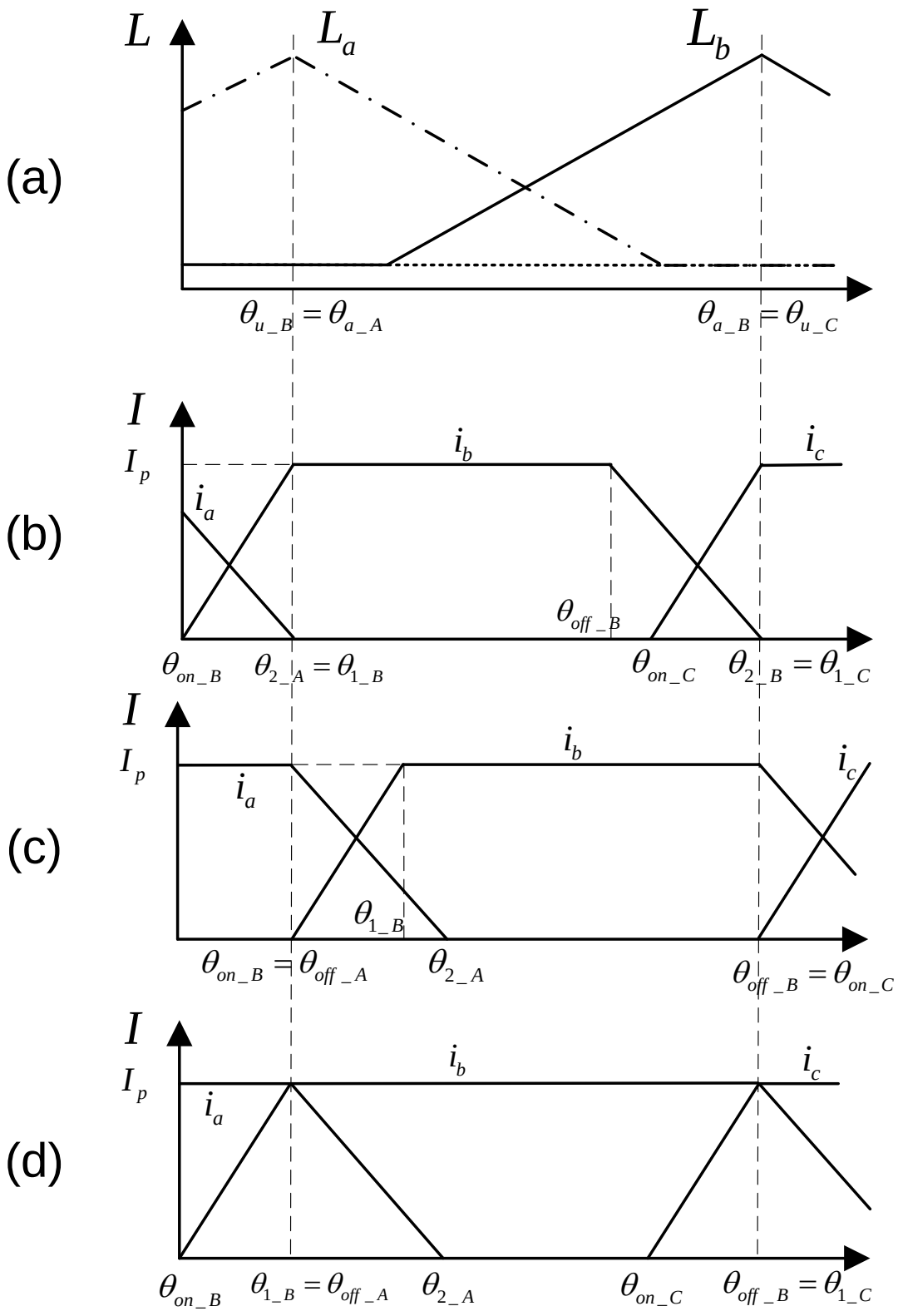

Fig 7.4 Different cases for overlapped current profiles

The case of *advanced turning-on* is shown in diagram (b), where the phase B current is turned on before its unaligned position θ_{u_B}. Recall that the non-overlapped current profile in Chapter 3 is characterized as $\theta_{on\_B} = \theta_{u\_B}$ and $\theta_{2\_B} = \theta_{a\_B}$. However in diagram (b), $\theta_{on\_B} < \theta_{u\_B}$, and for the sake of simplicity, θ_{1_B} is set to be equal to θ_{u_B}. Recall again that in Chapter 3 θ_{on} and θ_{off} are defiend to represent the current turning-on and turning-off positions, θ_1 denotes the position when the current reaches I_P, and θ_2 denotes the position when the current drops to zero. Therefore in diagram (b), the phase B current is turned on before θ_{u_B}, and the phase B current reaches the peak value of I_P at θ_{u_B}. Similarly, the phase C current is turned on before θ_{u_C}, and the phase C current reaches I_P at θ_{u_C} ($\theta_{u\_C} = \theta_{a\_B}$). In the FEA simulation, for the period between θ_{u_B} and θ_{a_B}, both the phase B and phase C current profiles need to be specified.

The case of *delayed turning-off* is shown in diagram (c), where phase B current is turned on at its unaligned position θ_{u_B}, and is turned off at its aligned position θ_{a_B}. So compared to Chapter 3, $\theta_{off\_B} = \theta_{a\_B}$ and $\theta_{2\_B} > \theta_{a\_B}$, which shows how the turning off of the phase B current is delayed. Similarly the phase A current is turned off at θ_{a_A} ($\theta_{a\_A} = \theta_{u\_B}$), and the phase A current drops to zero at θ_{2_A}. In the FEA simulation for the period between θ_{u_B} and θ_{a_B}, both the phase A and phase B current profiles need to be specified.

Finally the case of *combined situation* is shown in diagram (d). The phase B current is turned on before its unaligned position θ_{u_B}, and is turned off at its aligned position θ_{u_B}. So compared to Chapter 3 $\theta_{on\_B} < \theta_{u\_B}$ and $\theta_{2\_B} > \theta_{a\_B}$, which indicate the in-advance turning-on and the delayed turning-off of the phase B current. Similarly the phase A

current is turned off at θ_{a_A} ($\theta_{a\_A} = \theta_{u\_B}$), and the phase A current drops to zero after θ_{a_A}; the phase C current is turned on before θ_{u_C} ($\theta_{u\_C} = \theta_{a\_B}$), and the phase C current reaches I_P at θ_{u_C}. In the FEA simulation, for the period between θ_{u_B} and θ_{a_B}, all the three phases current profiles need to be specified.

Next the FEA simulation is performed for these three cases, and the calculated average torque is listed in Table 7.1. It is known that only the current between θ_u and θ_a can produce positive torque, otherwise the current may produce negative torque. Therefore an increase of the current conduction time does not always result in an increase of average torque. For example, the average torque of Case 3 is negative.

Table 7.1 Average torque of different overlapped current cases

	Average torque
Case 1	0.63 N-m
Case 2	0.16 N-m
Case 3	-0.35 N-m

In Table 7.1, Case 1 (*advanced turning-on*) has the highest average torque value, and thus it is chosen as the overlapped current profile in this chapter, for the purpose of the maximizing the torque density.

Particularly the overlapped current profile of the *advanced turning-on* case is plotted again in Fig 7.5, where the phase B current is turned on before the phase B unaligned position θ_{u_B}, and the phase B current i_b is increased to I_p at θ_{u_B}. Then i_b is maintained at I_p until θ_{off_B}, and i_b drops to zero at the phase B aligned position θ_{a_B}. Similarly for phase C, the current is turned on at θ_{on_C} before θ_{u_C} ($\theta_{u\_C} = \theta_{a\_B}$), and the current i_c

increases to I_p at θ_{u_C} . Therefore $\theta_{u\_B} = \theta_{a\_A} = \theta_{1\_B} = \theta_{2\_A}$, and $\theta_{a\_B} = \theta_{u\_C} = \theta_{2\_B} = \theta_{1\_C}$.

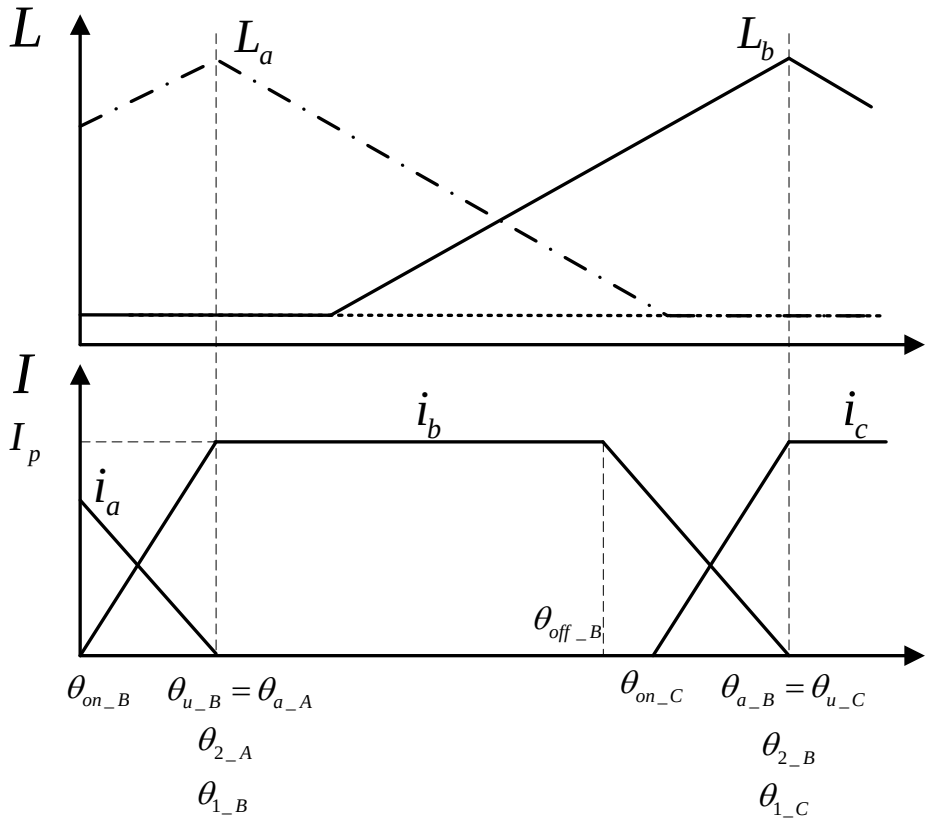

Fig 7.5 The *advanced turning-on* overlapped current profile

Given the symmetry of each phase, only the current profile between θ_{u_B} and θ_{a_B} (Fig 7.5) needs to be considered for the SRM performance estimation. Hence in the FEA simulation, when the rotor moves from θ_{u_B} to θ_{a_B}, the phase B and phase C current profiles need to be specified. Therefore the key problem is to calculate the position θ_{off_B} and θ_{on_C}, which is determined by the phase B and phase C flux linkage. The calculation of these two positions are presented as follows.

To investigate the flux linkage change with the overlapped current profile (*advanced turning-on*), a schematic overlapped current profile is fed into the FEA simulation first as

shown in Fig 7.6. The FEA simulation model is the 12/8 SRM of Chapter 3. In Fig 7.6, the timing of 0 sec indicates the unaligned position of phase B, θ_{u_B}, and the timing of 1.25 ms indicates the aligned position θ_{a_B}. The phase B current is maintained at the peak value of 10 A until at 0.5 ms (θ_{off_B}) when it drops to zero at θ_{a_B}. On the other hand, the phase C current is turned on at 0.75 ms (θ_{on_C}), and its current reaches the peak value at θ_{a_B}. The phase A current is zero between θ_{u_B} and θ_{a_B}.

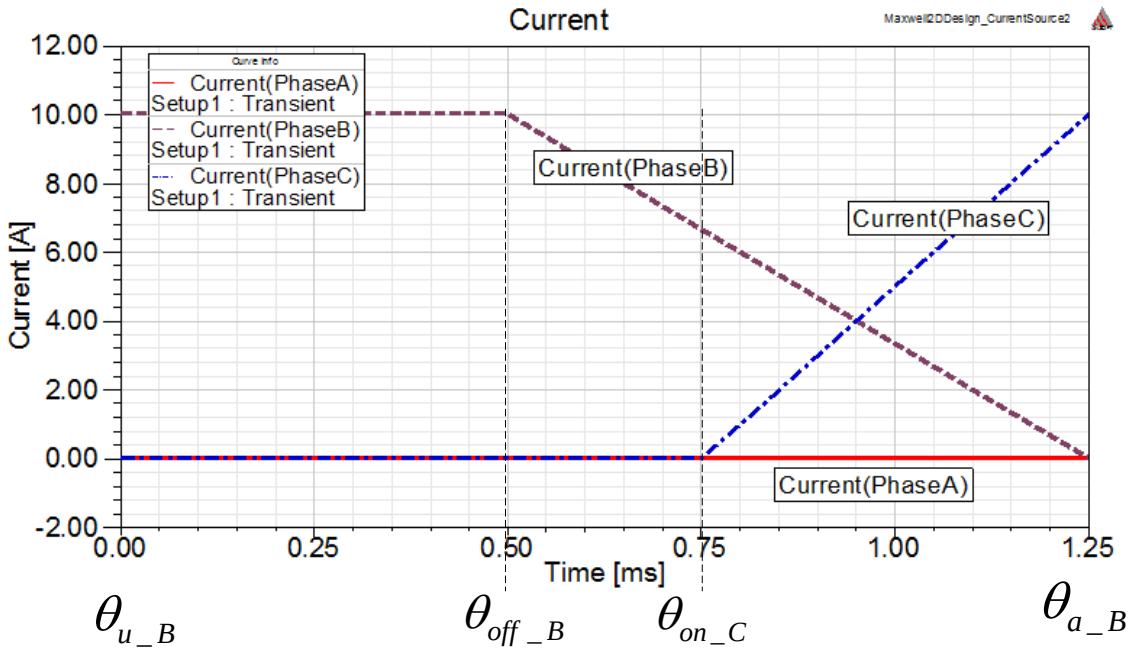

Fig 7.6 FEA simulation overlapped current profile (schematic)

Then the calculated flux linkage is shown in Fig 7.7. It can be observed that the value of phase B flux linkage is changed from 0.135 Wb-tunrs (0 ms) to -0.08 Wb-turns (1.25 ms), where 0.135 Wb-turns equals the phase C flux linkage value at 1.25 ms, and -0.08 Wb-turns equals to the phase A flux linkage value at 0 ms. In other words, the flux linkage values of phase A, B and C at 1.25 ms correspond to the ones of phase C, A and B at 0 ms, which is highlighted by the horizontal dash lines in Fig 7.7. This phenomenon can be understood that when given the symmetry of each phase (one phase's aligned

position corresponds to the next phase's unaligned position), the flux linkages of the three phases are changing periodically between the different positions. From θ_{u_B} to θ_{a_B}, i_b changes from I_p to zero and i_c changes from zero to I_p, so $\lambda_{C\_final} = \lambda_{B\_0}$. It is important to calculate the final flux linkage values (at 1.25 ms) if their initial values (at 0 ms) are known, as it can be concluded that $\lambda_{A\_final} = \lambda_{C\_0}$, $\lambda_{B\_final} = \lambda_{A\_0}$, and $\lambda_{C\_final} = \lambda_{B\_0}$.

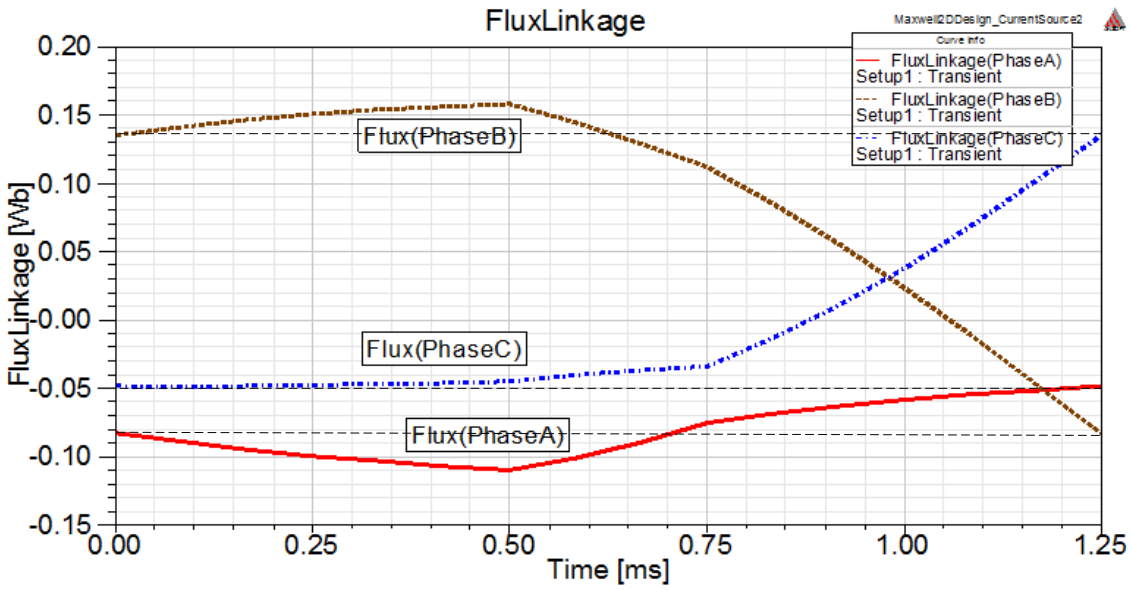

Fig 7.7 FEA simulation flux linkage using the overlapped current profile

After knowing the flux linkage final values (equal to the initial values with a change of the phase sequence), it is needed to know how the flux linkages are varying specifically between θ_{u_B} and θ_{a_B}. For the sake of generality, a current-fed FEA simulation with a constant phase B current ($i_b = I_p, i_a = i_c = 0$) is performed and the calculated flux linkages are shown in Fig 7.8.

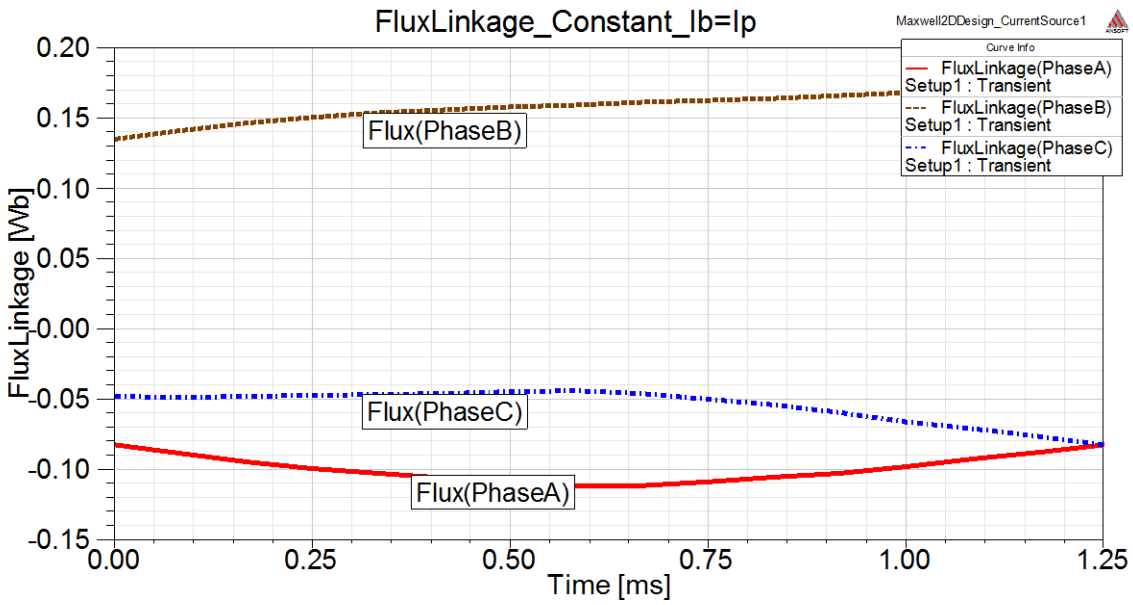

Fig 7.8 FEA simulation flux linkage using the constant current profile

In Fig 7.8, the phase B flux linkage increases from 0.135 Wb-tunrs at 0 sec to 0.17 Wb-turns at 1.25 ms. Now the flux linkages of Fig 7.7 and Fig 7.8 are plotted together (Fig 7.9). In Fig 7.9, the flux linkage of the overlapped current profile (called *OCP*) in Fig 7.7 is indicated by the subscript 1, and the flux linkage of the constant current profile (called *CCP*) in Fig 7.8 is indicated by subscript 2.

The reason for studying the flux linkage change is to investigate the relationship between the flux linkage and the current profile. Similar to the method presented in Chapter 3, it is needed to specify the overlapped excitation current profile based on the *CCP* FEA simulation results (Fig 7.8). Specifically, the overlapped current profile is specified by the two positions, θ_{off_B} and θ_{on_C}. Therefore the calculation of θ_{off_B} and θ_{on_C} based on the flux linkage of the *CCP* FEA simulation is to be presented next.

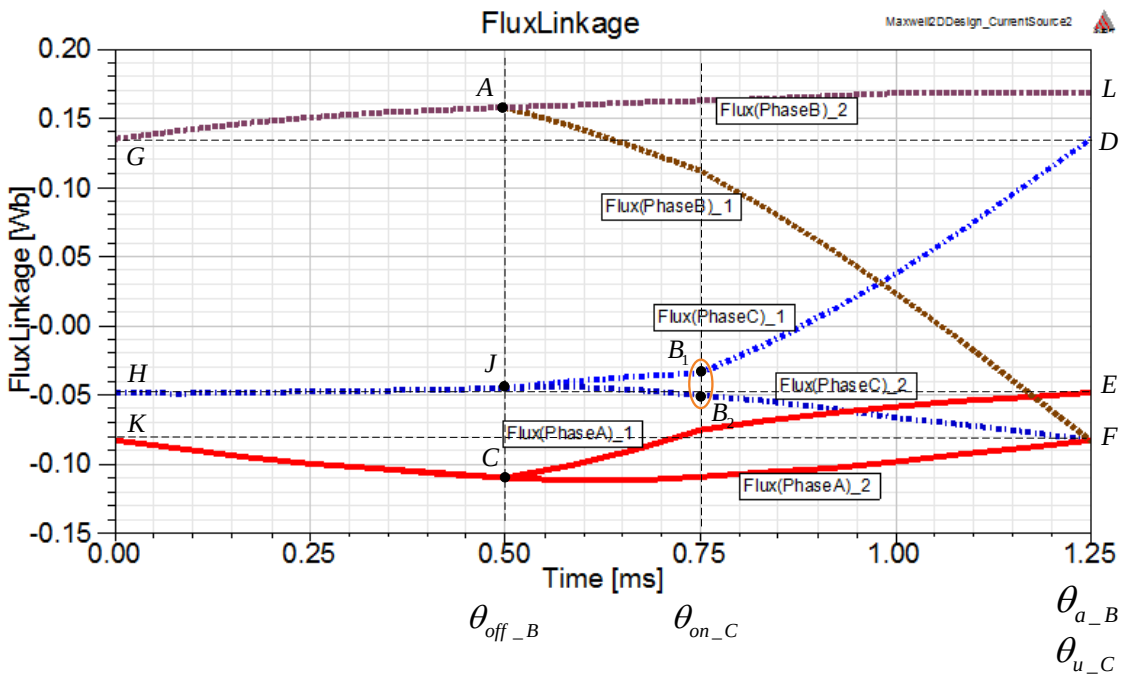

Fig 7.9 FEA simulation flux linkage using *OCP* and *CCP*

1). Between 0 ms to 0.6 ms, the flux linkages of *OCP* and *CCP* are overlapping each other (line *GA* for phase B, line *HJ* for phase C, and line *KC* for phase A)

2). At 0.6 ms (θ_{off_B}) when the phase B current turns off, the phase B flux linkage of *OCP* (Flux(PhaseB)_1) starts to drop from point A to point F at 1.25 ms.

- Point A is specified as the crossing point of the *CCP phase B* flux linkage (*GL*) and the timing of θ_{off_B}.
- Recall that $\lambda_{B\_final} = \lambda_{A\_0}$, so point F is specified as the initial value of the *CCP phase A* flux linkage.
- Therefore, point A and F can be specified by the *CCP* flux linkage profile (phase A and B) and the timing of θ_{off_B}. Furthermore, the *OCP* phase B flux linkage (line *GAF*) can be specified by the *CCP* flux linkage profile (line *GAL* and point K) and the timing of θ_{off_B}.

3). Between 0.6 ms (θ_{off_B}) to 0.75 ms (θ_{on_C}), the *OCP* phase C flux linkage (Flux(PhaseC)_1) changes from point J to point B_1, and the *CCP* flux linkage (Flux(PhaseC)_2) changes from point J to point B_2. However, because point B_1 is very close to point B_2, we assume that point B_1 = point B_2 for the rest of this chapter, and they are both called as point B.

4). At 0.75 ms (θ_{on_C}) when the phase C current turns on, the *OCP* phase C flux linkage (Flux(PhaseC)_1) starts to increase from point B to point D at 1.25 ms.

- Point B is specified as the crossing point of the *CCP phase C* flux linkage (*HF*) and the timing of θ_{on_C}.
- Recall that $\lambda_{C\_final} = \lambda_{B\_0}$, so point D is specified as the initial value of the *CCP phase B* flux linkage.
- Therefore, point B and D can be specified by the *CCP* flux linkage profile (phase B and C) and the timing of θ_{on_C}. Furthermore, the *OCP* phase C flux linkage (line *HBD*) can be specified by the *CCP* flux linkage profile (line *HBF* and point G) and the timing of θ_{on_C}.

After understanding the relationship between the *CCP* and *OCP* flux linkage profiles, now the timing of θ_{off_B} and θ_{on_C} can be calculated based on the *CCP* flux linkage profile as presented below.

7.2.1 The calculation of θ_{off_B}

The phase B flux linkages using *CCP* and *OCP* are plotted in Fig 7.10 separately. From point A to point F, it is known that the phase B flux linkage drops from $\lambda_{B\_OCP}(\theta_{off\_B})$ to $\lambda_{B\_OCP}(\theta_{a\_B})$, where $\lambda_{B\_OCP}(\theta_{off\_B})$ denotes the *OCP* phase B flux linkage at position θ_{off_B}. It is also known that $\lambda_{B\_OCP}(\theta_{off\_B}) = \lambda_{B\_CCP}(\theta_{off\_B})$ and

$\lambda_{B\_OCP}(\theta_{a\_B}) = \lambda_{A\_CCP}(\theta_{u\_B})$. So the phase B flux linkage drop actually is from $\lambda_{B\_CCP}(\theta_{off\_B})$ to $\lambda_{A\_CCP}(\theta_{u\_B})$, which are both known in the *CCP* flux linkage profile of Fig 7.6.

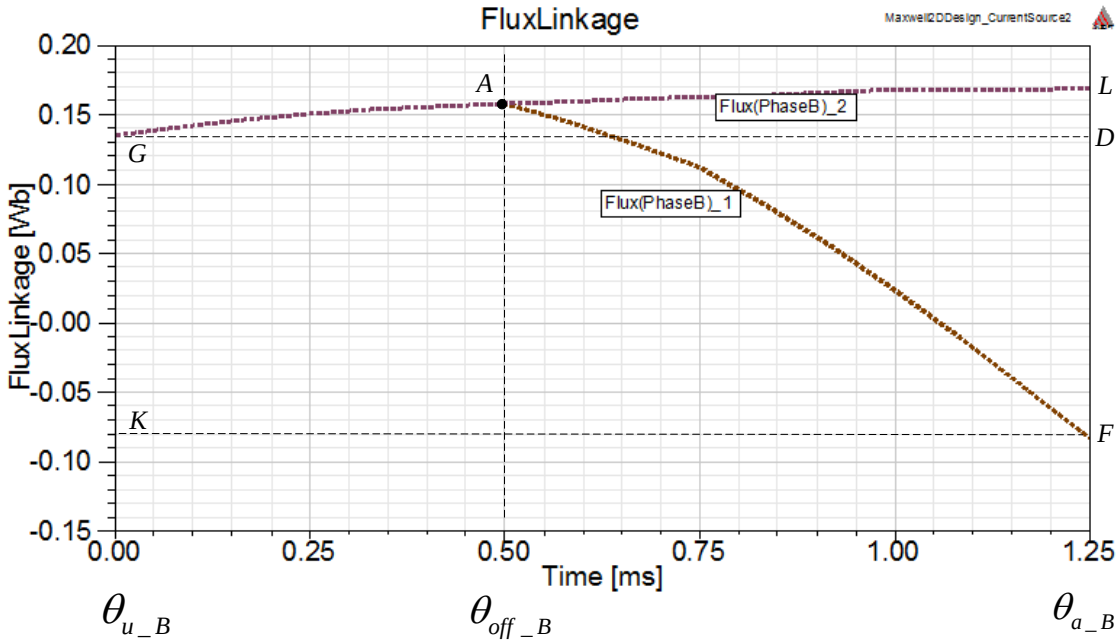

Fig 7.10 FEA simulation phase B flux linkage using *OCP* and *CCP*

On the other hand, the angle between point A and point F is the one between θ_{off_B} and θ_{a_B}, and the corresponding time interval Δt can be calculated as:

$$\Delta t = \frac{\theta_{a\_B} - \theta_{off\_B}}{\omega_r} \tag{7.1}$$

Recall the voltage equation of (7.2) and ignore the phase resistance R, we have:

$$V_{DC} = R \cdot i + \frac{d\lambda}{dt} \tag{7.2}$$

$$\lambda = \int V_{DC} \cdot dt = V_{DC} \cdot \Delta t \tag{7.3}$$

Thus the time interval Δt can also be calculated by using the flux linkage as:

$$\Delta t = \frac{\Delta\lambda}{V_{DC}} = \frac{\lambda_{B\_CCP}(\theta_{off\_B}) - \lambda_{A\_CCP}(\theta_{u\_B})}{V_{DC}} \tag{7.4}$$

Substitute (7.4) into (7.1), it gives:

$$\frac{\theta_{a\_B} - \theta_{off\_B}}{\omega_r} = \frac{\lambda_{B\_CCP}(\theta_{off\_B}) - \lambda_{A\_CCP}(\theta_{u\_B})}{V_{DC}} \tag{7.5}$$

$$\theta_{off\_B} = \theta_{a\_B} - \left[\frac{\omega_r}{V_{DC}} \cdot \left(\lambda_{B\_CCP}(\theta_{off\_B}) - \lambda_{A\_CCP}(\theta_{u\_B})\right)\right] \tag{7.6}$$

In (7.6) when trying to calculate θ_{off_B}, only $\lambda_{B\_CCP}(\theta_{off\_B})$ is unknown, as $\lambda_{A\_CCP}(\theta_{u\_B})$ is known in the *CCP* flux linkage profile. However $\lambda_{B\_CCP}(\theta_{off\_B})$ can be estimated in an iterative way which is similar with Chapter 3, and the new calculation flow chart is shown in Fig 7.11.

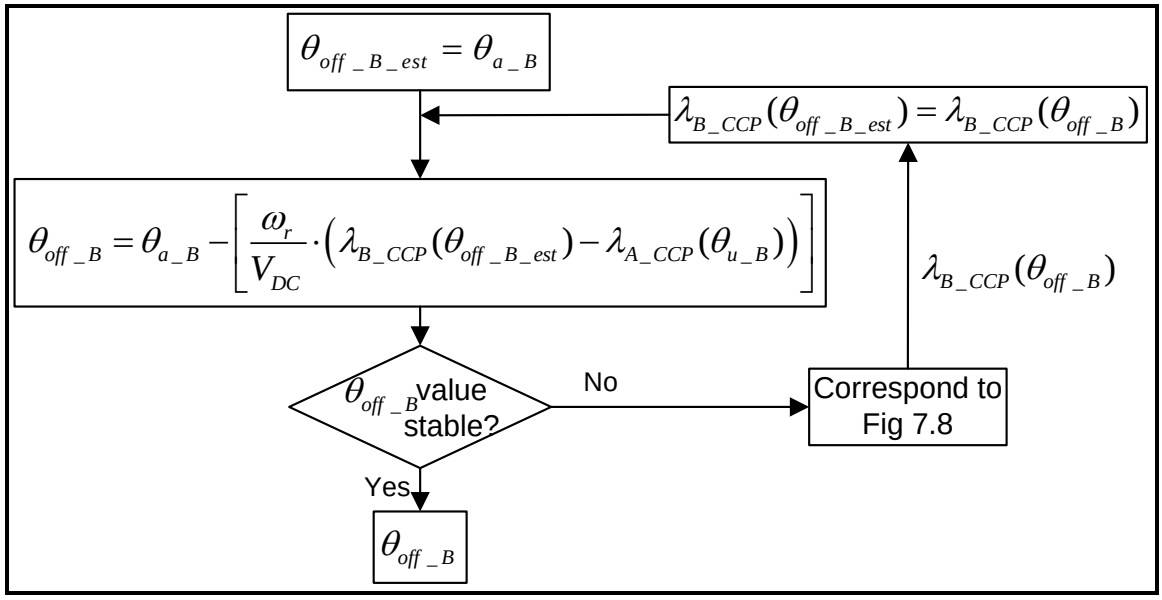

Fig 7.11 θ_{off_B} calculation flow chart

In Fig 7.11 θ_{off_B} is estimated to be θ_{a_B} at first, and $\lambda_{B\_CCP}(\theta_{off\_B\_est}) = \lambda_{B\_CCP}(\theta_{a\_B})$, so θ_{off_B} is calculated by (7.6). Then $\lambda_{B\_CCP}(\theta_{off\_B})$ is found from the corresponding

value of θ_{off_B} in Fig 7.8, and $\lambda_{B\_CCP}(\theta_{off\_B\_est})$ is replaced by the new $\lambda_{B\_CCP}(\theta_{off\_B})$ value. This process is repeated until the value of θ_{off_B} converges to a stable value.

7.2.2 The calculation of θ_{on_C}

The phase C flux linkage using *CCP* and *OCP* are plotted in Fig 7.12 again. From point B to point D, it is known that the phase C flux linkage increases from $\lambda_{C\_OCP}(\theta_{on\_C})$ to $\lambda_{C\_OCP}(\theta_{a\_B})$. It is also known that $\lambda_{C\_OCP}(\theta_{on\_C}) = \lambda_{C\_CCP}(\theta_{on\_C})$ and $\lambda_{C\_OCP}(\theta_{a\_B}) = \lambda_{B\_CCP}(\theta_{u\_B})$. So the incremental phase C flux linkage is actually from $\lambda_{C\_CCP}(\theta_{on\_C})$ to $\lambda_{B\_CCP}(\theta_{u\_B})$, which are both known in the *CCP* flux linkage profile of Fig 7.6.

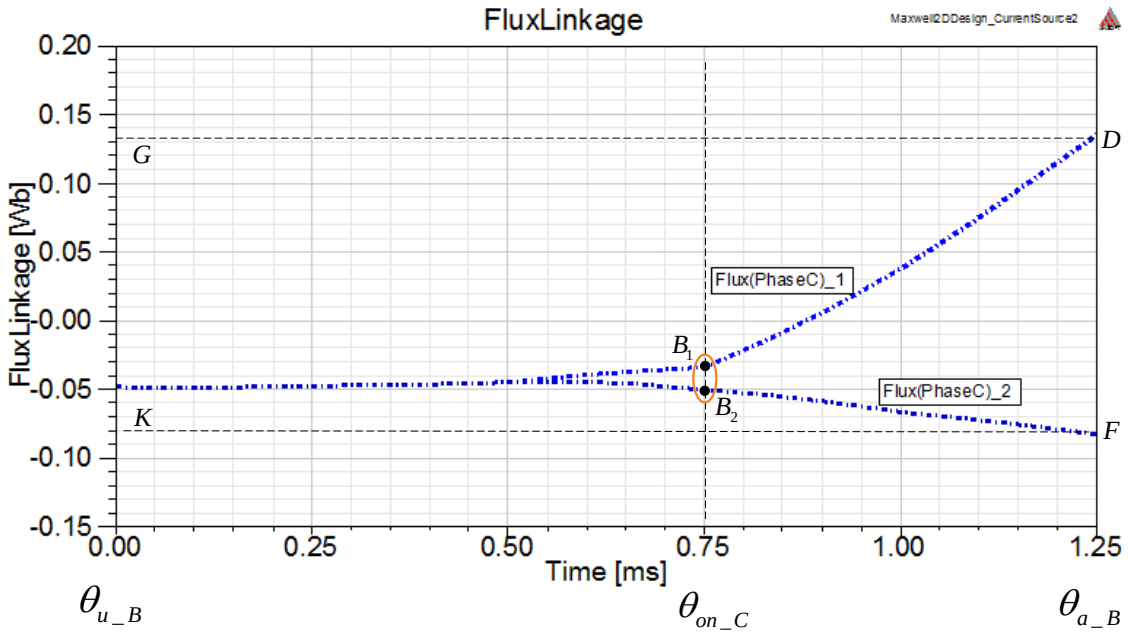

Fig 7.12 FEA simulation phase C flux linkage using *OCP* and *CCP*

On the other hand, the angle between point B and point D is the one between θ_{on_C} and θ_{a_B}, and the corresponding time interval Δt can be calculated as:

$$\Delta t = \frac{\theta_{a\_B} - \theta_{on\_C}}{\omega_r} \tag{7.7}$$

Again, the time interval Δt can also be calculated by using the flux linkage as:

$$\Delta t = \frac{\Delta\lambda}{V_{DC}} = \frac{\lambda_{B\_CCP}(\theta_{u\_B}) - \lambda_{C\_CCP}(\theta_{on\_C})}{V_{DC}} \tag{7.8}$$

Substitute (7.8) into (7.7), we have:

$$\frac{\theta_{a\_B} - \theta_{on\_C}}{\omega_r} = \frac{\lambda_{B\_CCP}(\theta_{u\_B}) - \lambda_{C\_CCP}(\theta_{on\_C})}{V_{DC}} \tag{7.9}$$

$$\theta_{on\_C} = \theta_{a\_B} - \left[\frac{\omega_r}{V_{DC}} \cdot \left(\lambda_{B\_CCP}(\theta_{u\_B}) - \lambda_{C\_CCP}(\theta_{on\_C})\right)\right] \tag{7.10}$$

In (7.10) when trying to calculate θ_{on_C}, only $\lambda_{C\_CCP}(\theta_{on\_C})$ is unknown, as $\lambda_{B\_CCP}(\theta_{u\_B})$ is known in the *CCP* flux linkage profile. However $\lambda_{C\_CCP}(\theta_{on\_C})$ can be estimated in a similar iterative way, and the new calculation flow chart is shown in Fig 7.13.

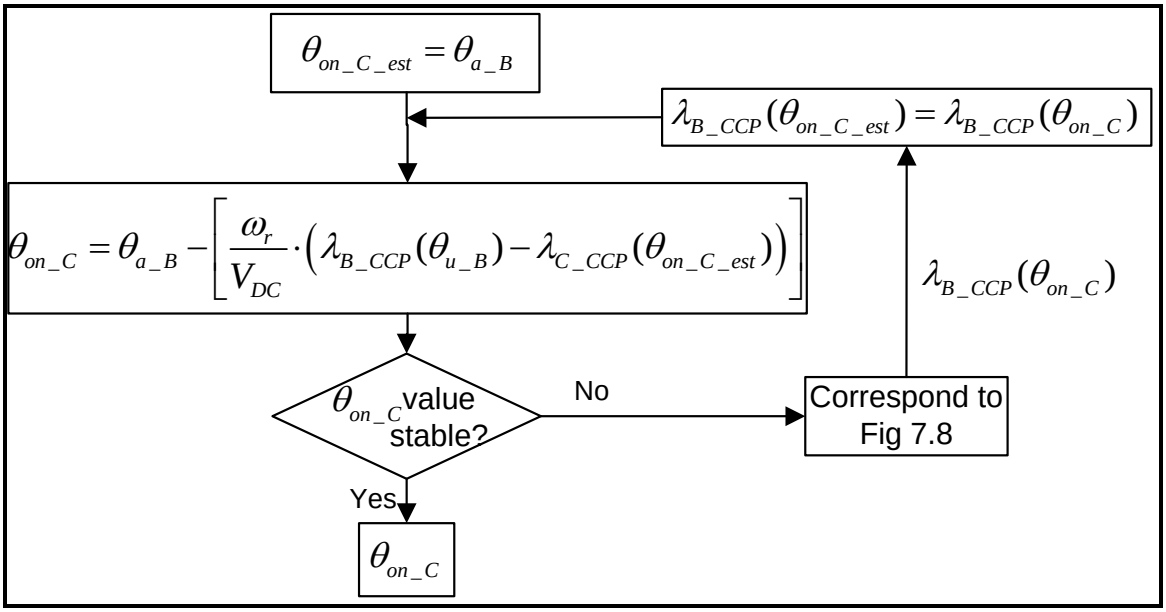

Fig 7.13 θ_{on_C} calculation flow chart

In Fig 7.13, θ_{on_C} is estimated to be θ_{a_B} at first, $\lambda_{B\_CCP}(\theta_{on\_C\_est}) = \lambda_{B\_CCP}(\theta_{a\_B})$, and θ_{on_C} is calculated by (7.10). Then $\lambda_{B\_CCP}(\theta_{on\_C})$ is found from the corresponding value of θ_{on_C} in Fig 7.8, and $\lambda_{B\_CCP}(\theta_{on\_C\_est})$ is replaced by the new $\lambda_{B\_CCP}(\theta_{on\_C})$ value. This process is repeated until the value of θ_{on_C} converges to a stable value.

7.2.3 θ_{off_B} and θ_{on_C} calculation example

To illustrate the detail of the θ_{off_B} and θ_{on_C} calculation process, an example of the 12/8 SRM is demonstrated here.

First a *CCP* FEA simulation is performed with $i_b = I_p = 10A$ and $i_a = i_c = 0$. Now compare the overlapped current profile to the non-overlapped one (Chapter 3). Due to the increase of the current conduction time, the current peak value is increased from 5 A to 10 A. As a result both the increase of the current conduction time and the current peak value contribute to the increase of the output torque.

The calculated flux linkage is shown in Fig 7.14 and Fig 7.15. From θ_{u_B} (0°) to θ_{a_B} (15°), the phase B flux linkage increase from 0.135 Wb-turns to 0.17 Wb-turns, and $\lambda_{A\_CCP}(\theta_{u\_B}) = -0.085Wb - turnrs$, $\lambda_{B\_CCP}(\theta_{u\_B}) = 0.135Wb - turns$.

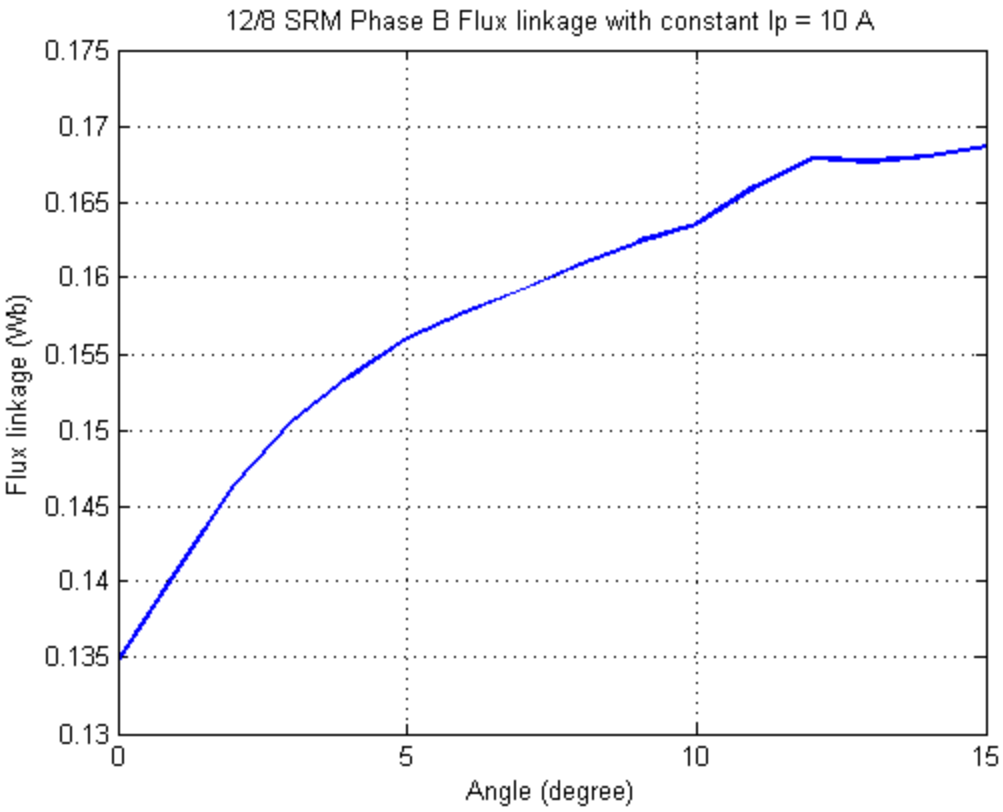

Fig 7.14 FEA simulation phase B flux linkage using *CCP* ($i_b = I_p, i_a = i_c = 0$)

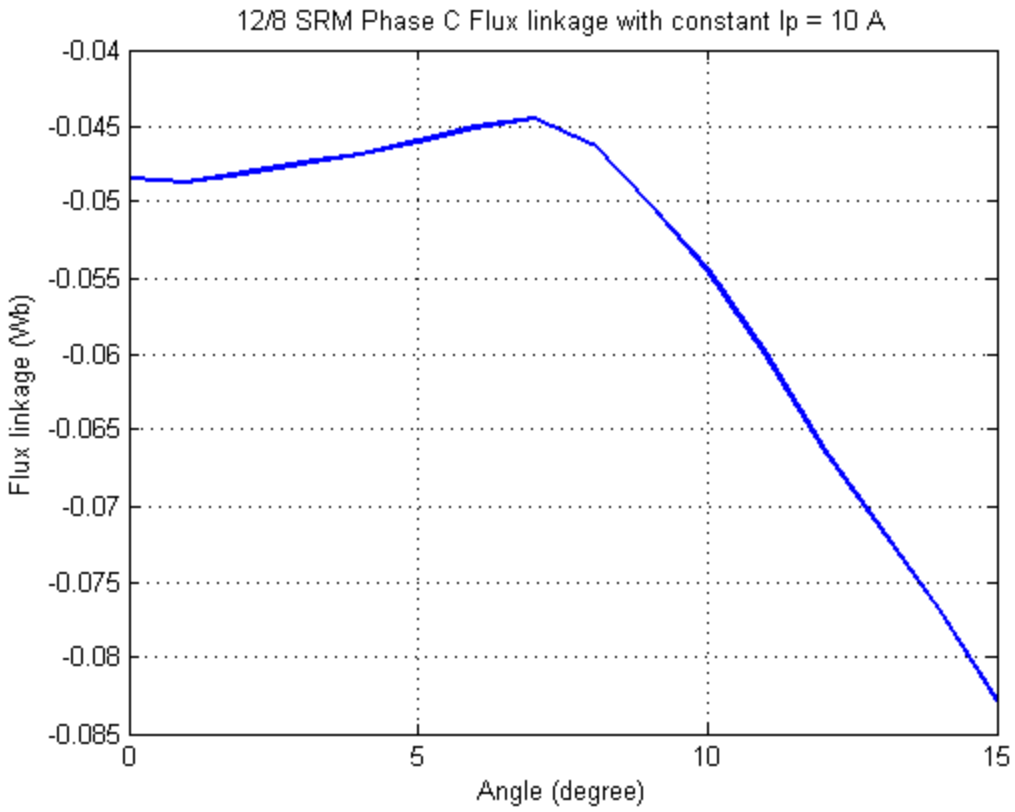

Fig 7.15 FEA simulation phase B flux linkage using *CCP* ($i_b = I_p, i_a = i_c = 0$)

Next based on these calculated flux linkages, the timing of θ_{off_B} is calculated as shown in Fig 7.16, and the timing of θ_{on_C} is calculated as shown in Fig 7.17, where the speed $\omega_r = 2000rpm$ and the DC bus voltage $V_{dc} = 350V$.

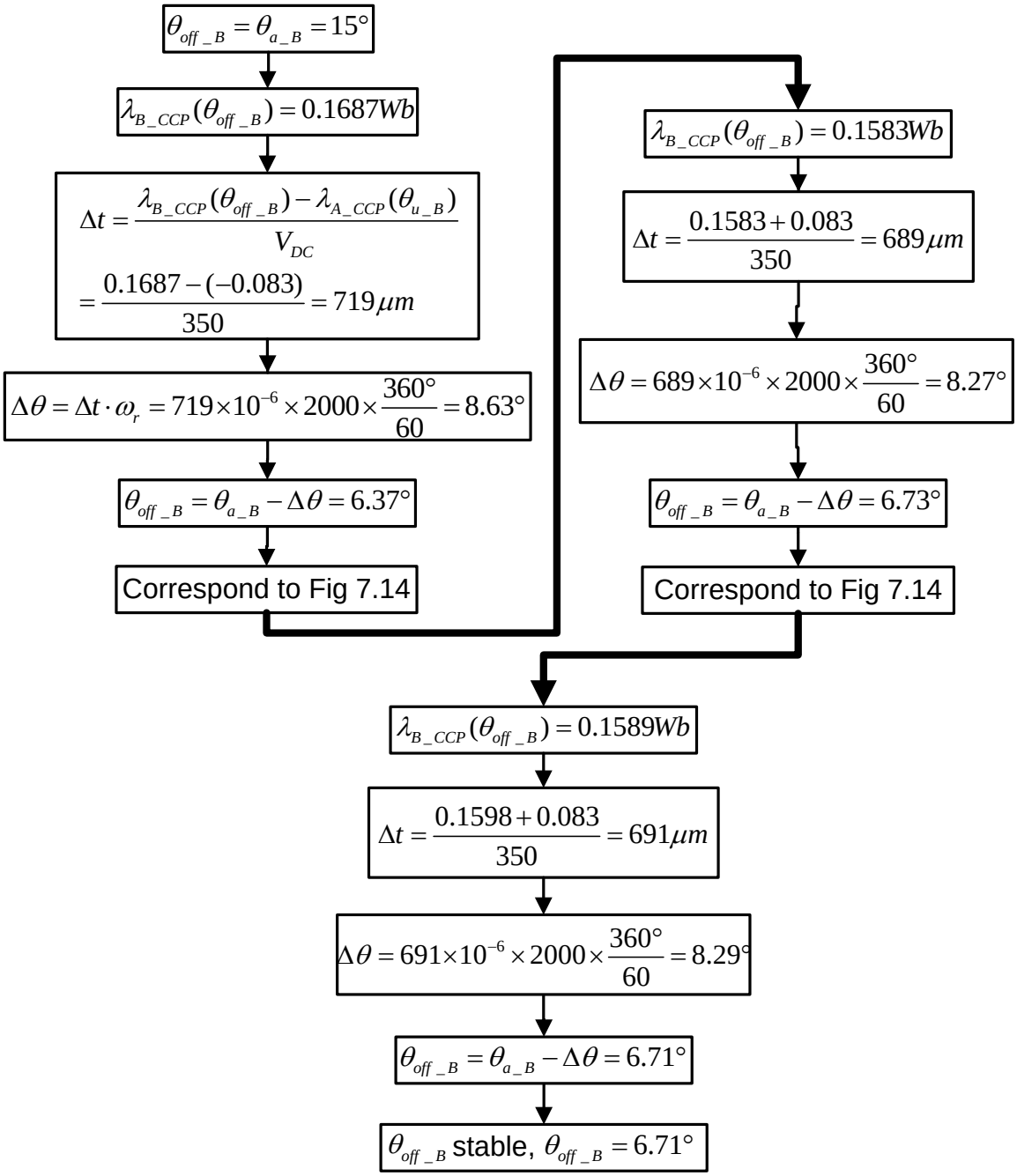

Fig 7.16 θ_{off_B} calculation flow chart (2000 rpm, 350 V DC bus)

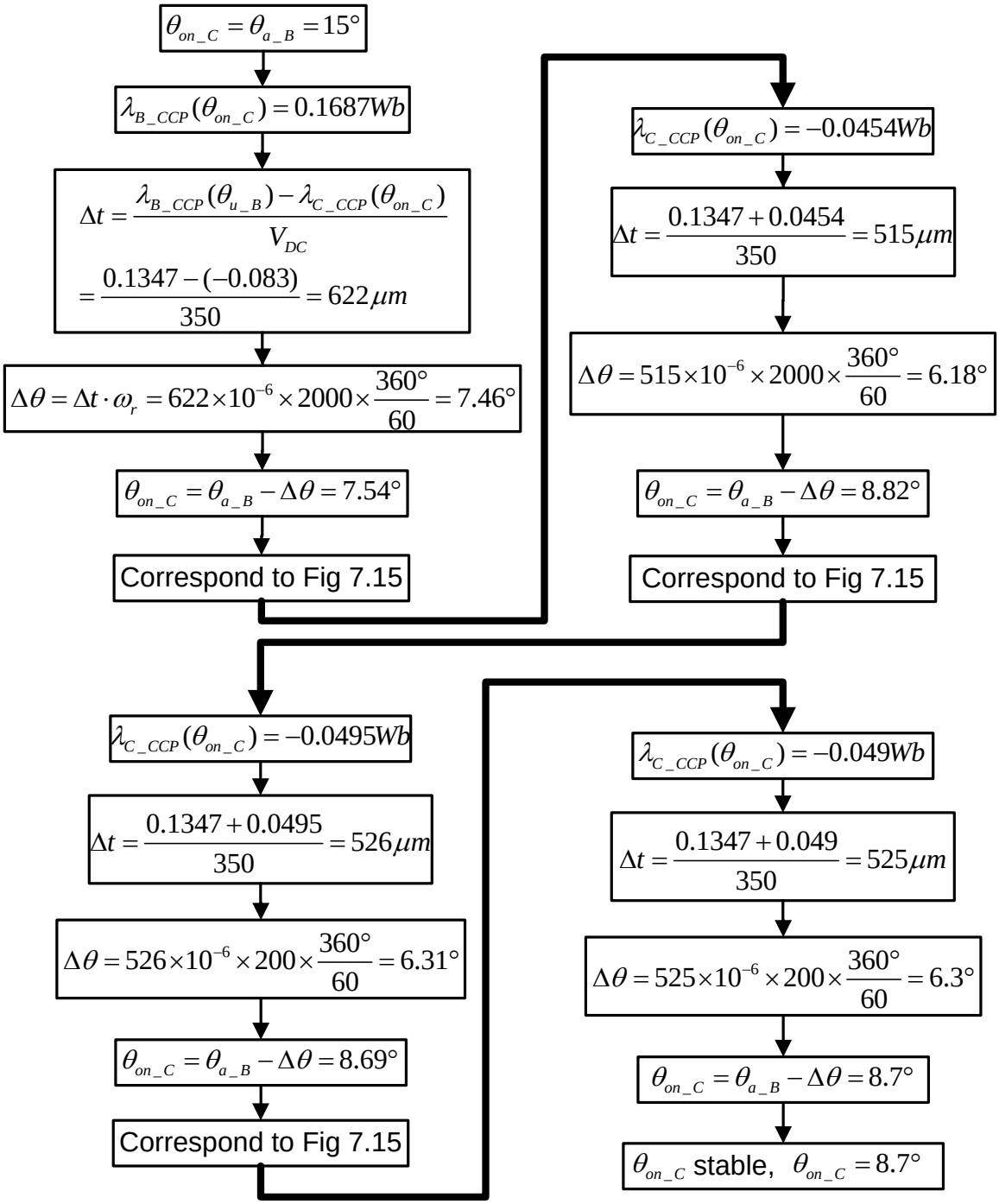

Fig 7.17 θ_{on_C} calculation flow chart (2000 rpm, 350 V DC bus)

Then given the results of θ_{off_B} (6.71 º = 0.55 ms) and θ_{on_C} (8.7 º = 0.725 ms), the overlapped current profile is specified as shown in Fig 7.18. The phase B current is

constant at 10 A from θ_{u_B} (0 sec) to θ_{off_B} (0.55 ms), and then decreases linearly from 10 A at θ_{off_B} (0.55 ms) to 0 at θ_{a_B} (1.25 ms). On the other hand, the phase C current increases from 0 at θ_{on_C} (0.725 ms) to 10 A at θ_{a_B} (1.25 ms); otherwise it is constant at 0. The phase A current is constant at 0 from θ_{u_B} (0 sec) to θ_{a_B} (1.25 ms).

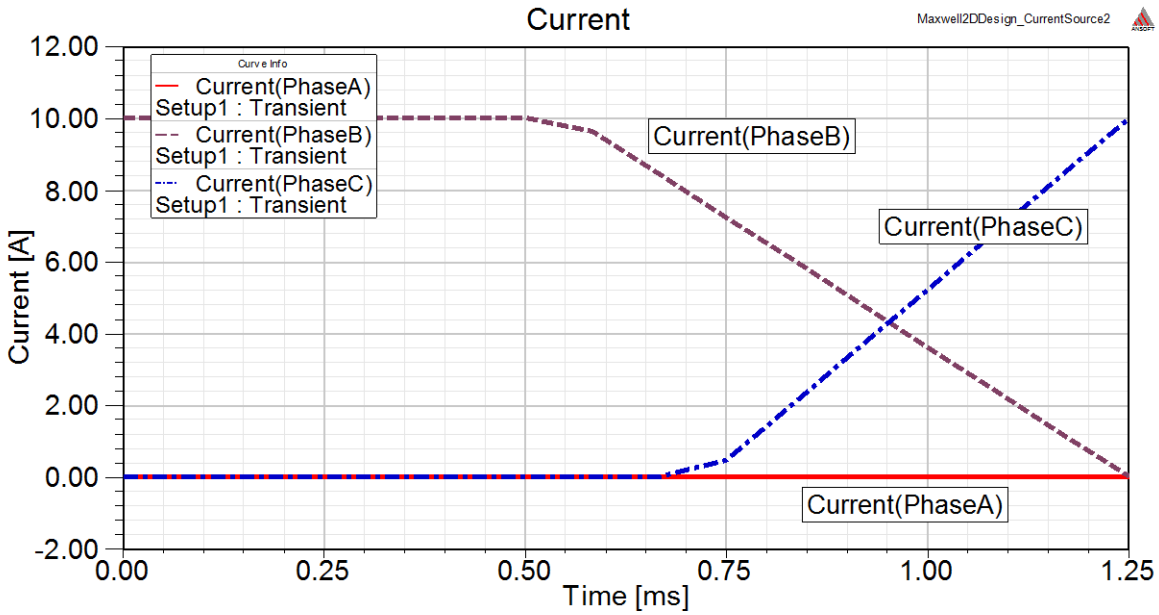

Fig 7.18 Specified overlapped current profile by the calculated θ_{off_B} and θ_{on_C}

Finally, another FEA simulation is performed using the overlapped current profile of Fig 7.18 and the calculated torque profile is shown in Fig 7.19. Due to the extension of the current conduction time, negative torque is observed in Fig 7.19 (blue circle). However comparing Fig 7.19 to the result of Chapter 3 (Fig 3.9), the average torque is increased from 0.15 N-m to 0.63 N-m, by a factor of 4.2. Therefore an increased torque density is achieved, and such a design method can be used for the high torque density SRM design, which is to be presented in the following section.

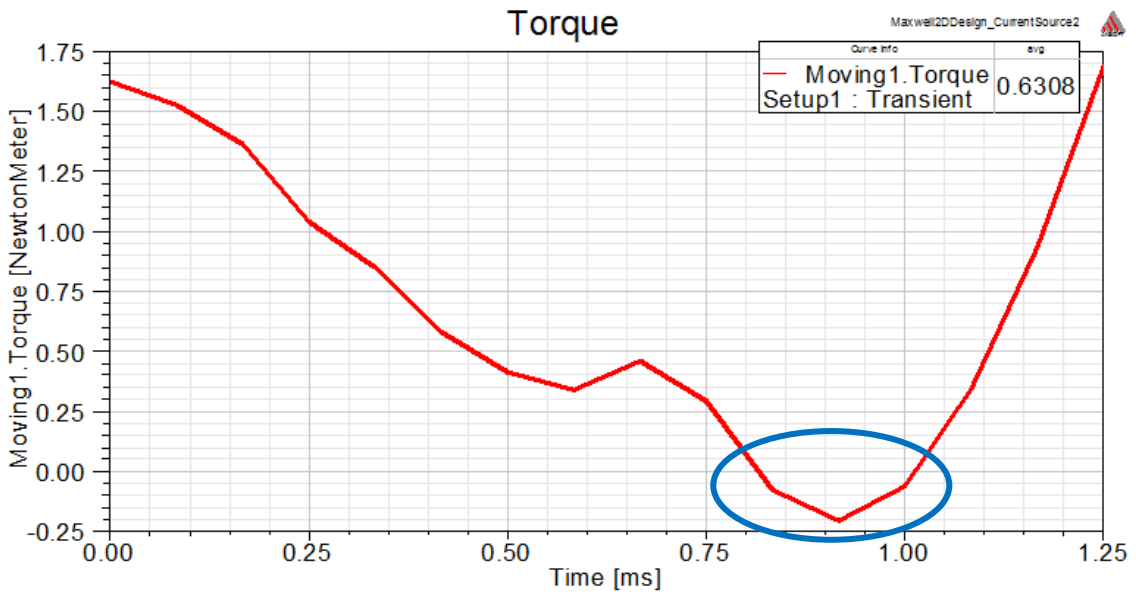

Fig 7.19 FEA simulation torque profile using overlapped current profile

7. 3 12/8 SRM design with overlapped current profile

In Chapter 3, a 12/8 SRM rotor design and optimization is presented using the method with a non-overlapped current profile. However to achieve the maximum torque density, the design method with the overlapped current profile is used in this section and a complete 12/8 SRM design (including the stator) is demonstrated.

First of all, similar to the complete 4/2 SRM design in Chapter 4, the target 12/8 SRM cross section view is shown in Fig 7.20. Again the 12/8 SRM laminations are described by 7 geometric variables, which are the stator and rotor diameters D_s and D_r, the stator and rotor pole angles β_s and β_r, the stator and rotor back iron thicknesses b_{sy} and b_{ry}, and the shaft diameter D_{sh}. D_s is fixed at 177 mm and the other parameters are the optimization variables.

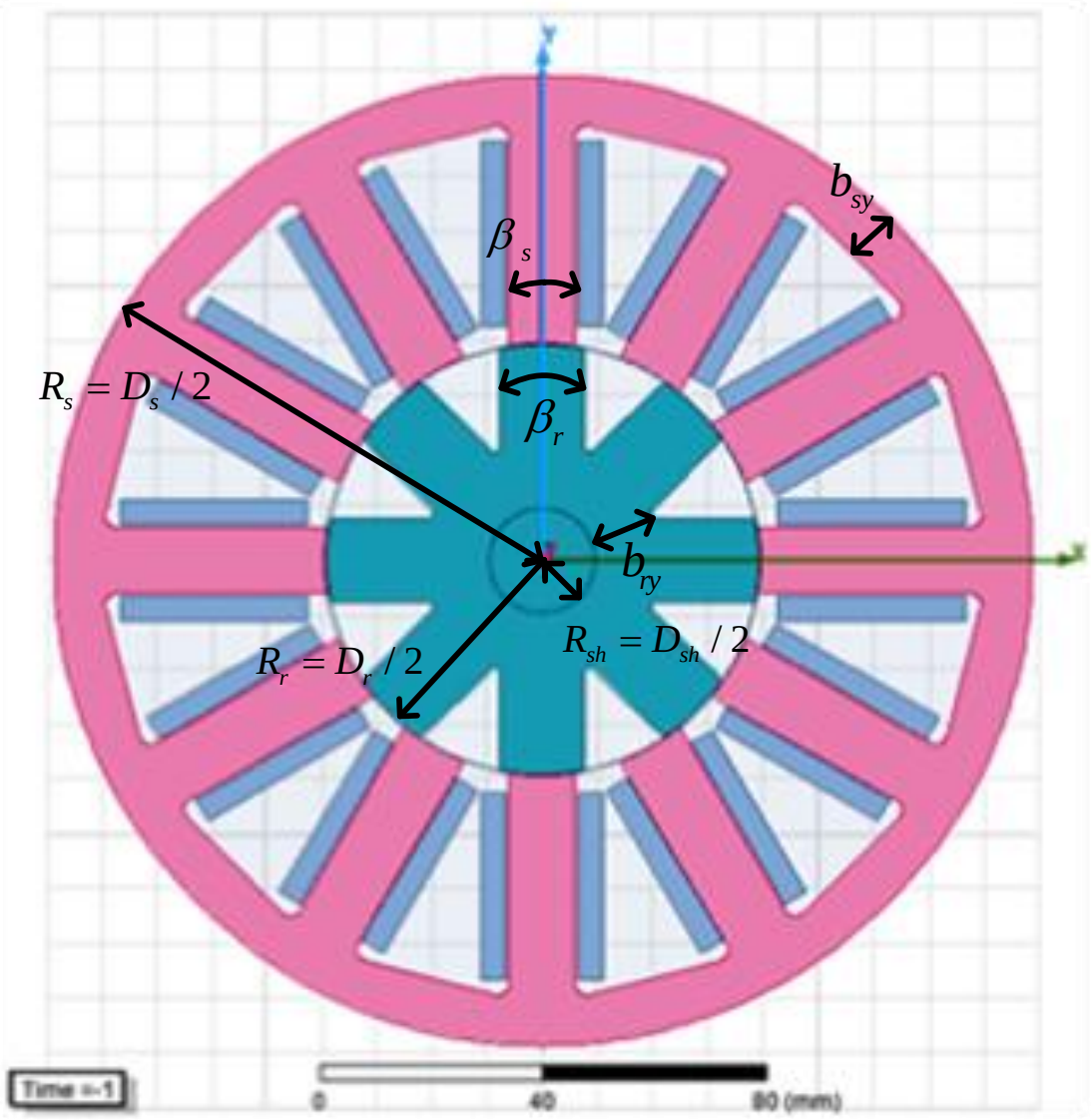

Fig 7.20 12/8 SRM lamination cross section view

Next, the initial design's variable values are listed in Table 7.2.

Table 7.2 Initial 12/8 SRM geometric variable values

D_r	β_s	β_r	b_{sy}	b_{ry}	D_{sh}
38 mm	20 º	25 º	8 mm	14 mm	9 mm

Then, as before b_{sy} b_{ry} and D_{sh} are excluded from the optimization process, as their impact on the torque is very small. Their values are fixed as shown in Table 7.2, and the optimization of the other geometric variables is investigated as follows.

- The number of turns for the coil winding per phase N_{ph}

The generic method to calculate N_{ph} is based on the magnetic circuit shown in Fig 7.21, where R_s, R_r, R_g, R_y indicate the flux path reluctance elements in the stator pole, rotor pole, air-gap and the back iron, and the total flux for one phase is $N_{ph}I_P$.

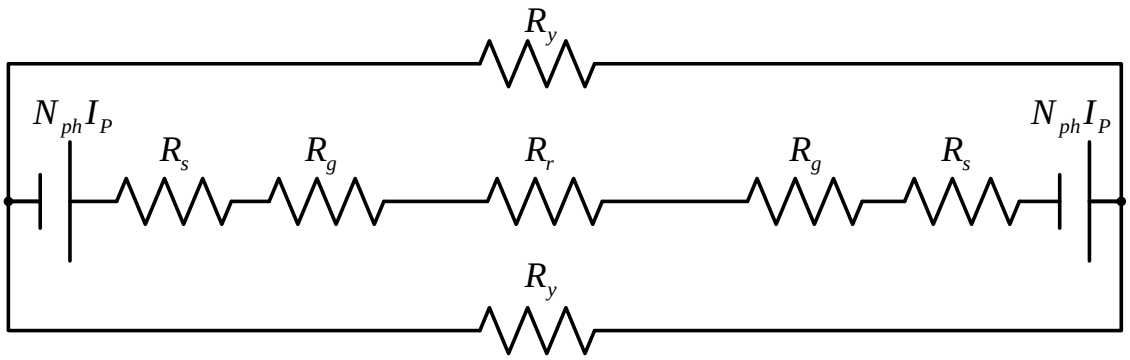

Fig 7.21 Magnetic circuit of the 12/8 SRM lamination

Similar to Chapter 4, N_{ph} is calculated to be 110 for the 12/8 SRM design, because the air-gap length is increased from 0.3 mm of the 4/2 SRM to 0.5 mm of the 12/8 SRM.

- Current-fed FEA simulation current peak value I_P

Again, the value of I_P is calculated using (7.11). In addition, $J_c = 5A/mm^2$, $Ff = 0.3$, and the detail of A_s calculation can be found in Table 7.3.

$$I_p = \frac{J_c \cdot A_s \cdot Ff}{N_{ph}}$$	(7.11)

Finally, the 12/8 SRM lamination geometry variable optimization is carried out by way of sweeping the design space, and the flow chart is shown in Fig 7.22. Particularly D_r is swept from 70 mm to 100 mm with steps of 6 mm, β_s is swept from 15 º to 24 º with steps of 3 º, and β_r is swept from 25 º to 34 º with steps of 3 º. For each design candidate, the FEA simulation with the overlapped current profile (*advanced turning-on*) is used.

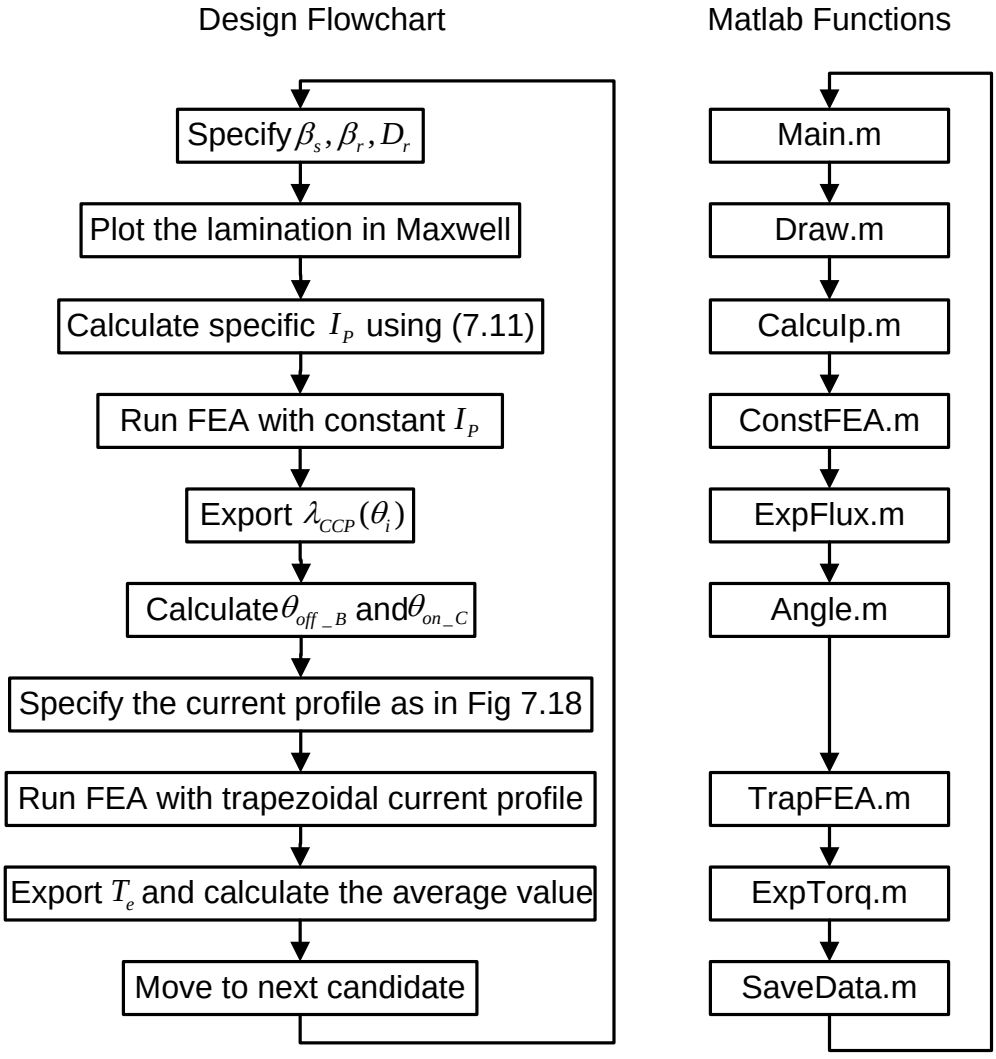

Fig 7.22 The 12/8 SRM design flow chart (overlapped current profile)

The optimization results are illustrated as in Fig 7.23, where the X and Y axes denote β_r and β_s respectively, the different layers denote different values of D_r, and the Z axis denotes the torque. The optimal design in terms of highest torque is identified by the circle in Fig 7.24, which is β_r = 25 º, β_s = 15 º, and D_r = 82 mm.

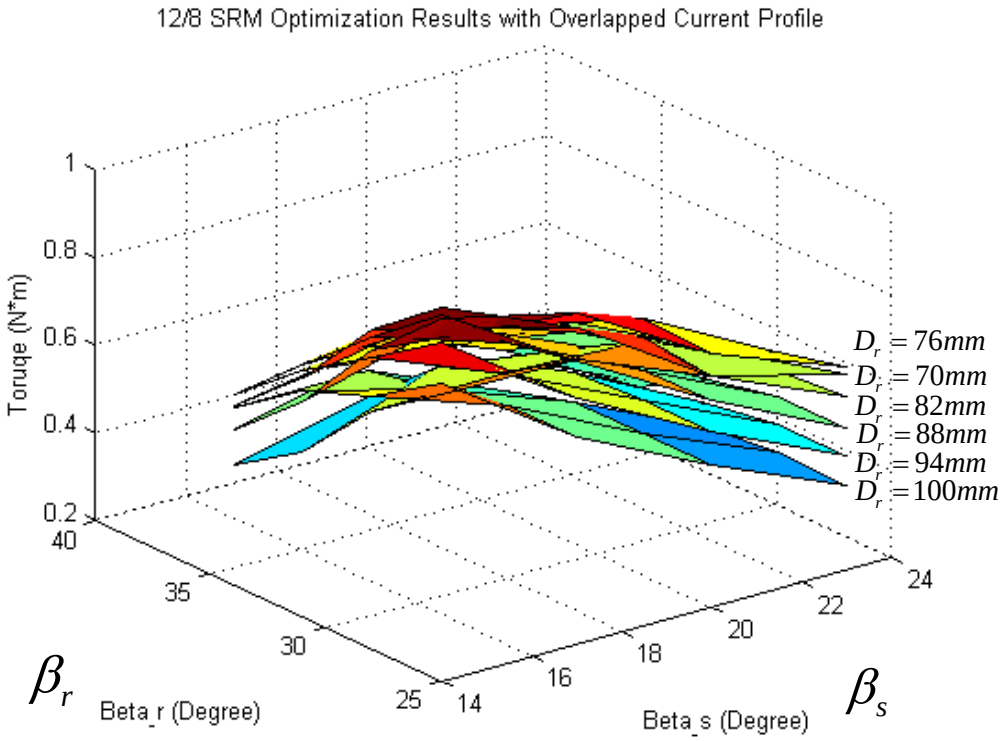

Fig 7.23 12/8 SRM optimization result with overlapped current profile

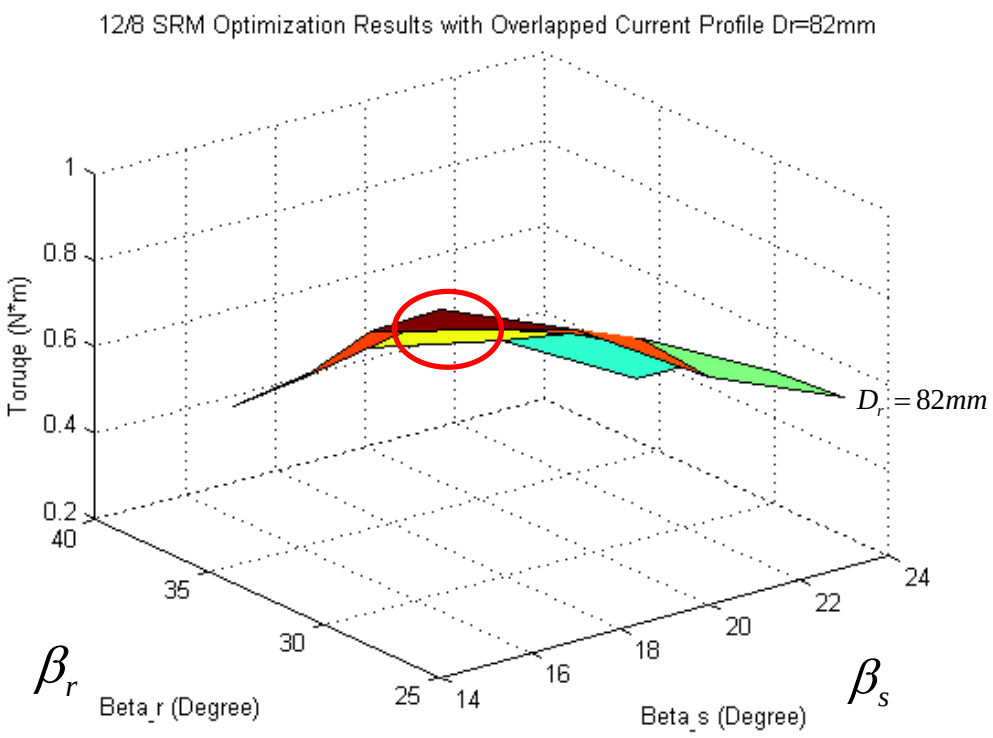

Fig 7.24 12/8 SRM optimization result with overlapped current profile ($D_r = 82mm$)

The optimization result of Fig 7.23 (12/8 SRM) is very different from the one in Fig 4.5 (4/2 SRM), and a convex shape can be observed for each layer. This can be explained as a synthesized result from the change of the inductance profile and the current profile. The change of β_s and β_r values influence the inductance profile. On the other hand, the change of β_s has impacts on the stator coiling winding area and furthermore on the current profile. For example, the optimal design is found at the corner of the layer $D_r = 82mm$ (Fig 7.24). With the minimum value of β_s = 15 º, the value of I_p can be maximized; and with the value of β_r = 25 º and D_r = 82 mm, the inductance profile is optimized. Therefore this design (β_r = 25 º, β_s = 15 º, and D_r = 82 mm) outperforms other candidates with the highest average torque of 0.97 N-m.

7. 4 Chapter Summary

In this chapter, the SRM design method with current-fed FEA simulation is improved to consider the case of an overlapped current profile for high torque density applications. First different overlapped current profile cases are characterized into three categories, and the *advanced turning-on* case is selected for this work. Next the calculation of the overlapped current profile based on the flux linkage is presented, where the flux linkage is calculated in a constant-current-fed FEA simulation. Then the design of a complete 12/8 SRM is investigated using the method with the overlapped current profile. The SRM optimization process of Chapter 3 is repeated, and the design space is a 3D space (D_r, β_s and β_r). Finally the optimal design is found when β_r = 25 º, β_s = 15 º, and D_r = 82 mm. An average torque of 0.97 N-m is achieved with the optimal design and the torque density increased by a factor of 6 comparing to the result in Chapter 3.

Table 7.3 12/8 SRM stator coil area calculation

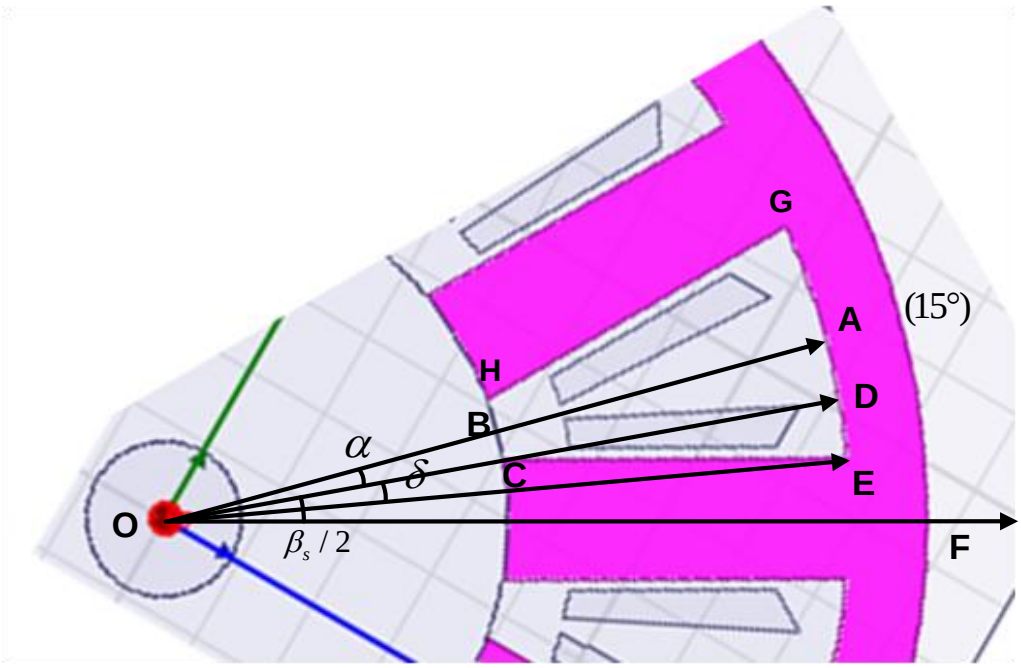

$\alpha = \pi/12 - \beta_s/2$	(7.12)
$S_{ABCD} = \alpha \cdot (AO^2 - BO^2) = \alpha \cdot ((D_s/2 - b_{sy})^2 - (D_r/2)^2)$	(7.13)
$y_E = y_C = D_r/2 \cdot \sin\frac{\beta_s}{2}$	(7.14)
$x_E = \sqrt{(D_s/2 - b_{sy})^2 - y_E{}^2}$	(7.15)
$\angle EOF = \arctan(y_E / x_E)$	(7.16)
$\delta = \pi/12 - \angle EOF$	(7.17)
$S_{DOE} = \delta \cdot (D_s/2 - b_{sy})^2$	(7.18)
$S_{COE} = (x_E - x_C) \cdot y_C / 2 = (x_E - D_r/2 \cdot \cos\frac{\beta_s}{2}) \cdot D_r/2 \cdot \sin\frac{\beta_s}{2} / 2$	(7.19)
$S_{CDE} = S_{ODE} - S_{OCE}$	(7.20)
$A_s = S_{GHCE} = 2 \cdot (S_{ABCD} + S_{CDE})$	(7.21)

CHAPTER 8 Conclusion, contribution and recommendions for future work

8. 1 Summary

This dissertation has proposed a method for the electromagnetic design and optimization of Switched Reluctance Machine (SRM), which is applicable to different SRM topologies for different applications, e.g. high speed and high torque applications. A current-fed FEA simulation approach has been used for the calculation of the SRM design performance, and the proposed design method has been verified by the experimental results of a SRM prototype.

Chapter one has introduced the background of electric machine, with the focus on the high speed applications and the comparison between SRM and other types of electric machines. In general, the interest in ultra high speed machines mainly comes from spindle and drilling industry, including micro-machinery spindles, printed circuit board drillings, and dental drilling tools. The up-to-date development of ultra high speed machine research has been summarized and categorized with respect to the applications. Next the traditional electric machine design approach has been summaried with the breakdown of the electromagnetic, thermal, and mechanical aspects. However, the traditional design method is strongly based on the heuristic selection of the parameter values and the empirical equations, and does not reflect the modern advances in materials, power electronics, etc. In particular, the design of ultra high speed machines has many differences compared to a regular speed electric machine design. The specific challenges include the mechanical design of the rotor, the lamination material selection, the power electronics design for the high frequency operation, and the type of bearings attached to the machine.

Then the respective characteristics of different machine types are outlined. Induction machines (IM) and permanent magnet (PM) machines are the two types of electric machines which are most widely used. From a conventional perspective, the SRM is

usually considered as a low cost and low performance motor. However, in the recent decade, SRM efficiency has improved to a level that is comparable to the PM motor when the magnetic steel, machine design, and control method issues are addressed. As a result, the SRM offers an alternative option in areas which have been dominated by PM machines and IMs in the past, due to its advantages such as robust rotor and reliable performance. However, not enough attention has been paid to the SRM study compared to the well developed research in IM and PM machine.

Chapter two has presented a comprehensive review of previous work on the ultra high speed SRM design, to justify the need and novelty of the proposed research. The focus of the high speed SRM design in the literature is on the rotor structure, and in particular, a rotor sleeve is a common option due to the high windage losses considerations. Based on the literature survey, the target SRM design specification is set as 50,000 rpm and 1 kW. However, the problem of the conventional SRM design methods is that there is no appropriate tool available to estimate the SRM performance. Those methods of what either have significant estimation errors or are not widely applicable to different SRM topologies, thus finite element analysis (FEA) simulation has to be used in this work. The focus of the research effort is on the development of a generic SRM performance estimation approach. It aims to pursue an automatic and rapid SRM design and optimization approach which is based on electromagnetic fundamentals and takes the SRM control into considerations.

Chapter three has proposed a novel SRM design method using current-fed FEA simulation. The new method can firstly calculate the SRM excitation current profile by using a constant-current-fed FEA simulation, and then calculates the SRM performance with a second current-fed FEA simulation. The SRM design and optimization is achieved by running an automatic Matlab-Maxwell coupled simulation program, without the tedious modeling of a particular SRM. Hence it is portable to any SRM configuration and

any dimension. The proposed excitation current profile calculation approach is verified with FEA simulation results, and good accuracy is achieved. At the end, this method is used to design a 12/8 SRM rotor, and an optimal design is found to have the highest torque.

Chapter four has presented the design of a complete 4/2 SRM, and the geometric variables are optimized to achieve the highest torque. First, the SRM lamination is described using 7 geometric variables. Next, the calculation of the b_{sy}, b_{ry}, D_{sh} and N_{ph} values is introduced, and the design space is reduced to a 3D space (D_r, β_s and β_r). Then the SRM design optimization is carried out by sweeping the design space, and the current-fed FEA simulation is used. The optimal design in terms of highest torque is found to be β_r = 77 º, β_s = 45 º, and D_r = 22 mm. At the end, the sensitivity analysis of the SRM performance to the geometric variables is presented to indentify that the stator pole angle β_s is the most influencing variable.

Chapter five has investigated the practical considerations of the design and construction of a 50,000 rpm SRM. First, a flux bridge topology is proposed to create a cylindrical rotor. The main motivation of building the flux bridge on the rotor is to reduce the windage losses at high speeds. The electromagnetic behavior of the flux bridge rotor design is investigated using FEA simulations. A SRM prototype is fabricated with one regular rotor and one flux bridge rotor, and it is tested at 10 krpm, 20 krpm and 50 krpm. Good agreement has been achieved between the FEA simulation and the experimental results. The performance comparison between one rotor with a flux bridge and one without a flux bridge is performed using FEA simulations. Furthermore, the flux bridge rotor design is improved with a non-uniform air-gap (*NUAG*) profile. The impact of this modification is investigated with FEA simulations, and it shows that the *NUAG design*

can increase the average torque while reducing the total losses with a lower DC bus voltage.

Chapter six has presented the study of the high speed SRM control for the fabricated SRM prototype at 50 krpm. To achieve simple and robust control performance, a speed-and-current dual-loop control is selected for the control strategy. At first, the control architecture is developed with function blocks. Next, a small signal system is used to describe the SRM control with transfer functions. Then, the small signal system is broken down into the current control loop and the speed control loop. The characteristic functions of each control loop are derived, so that the close-loop control bandwidth and damping ratio can be specified based on the desired control performance. In this way, the current and speed controller parameters can be calculated accordingly. Afterwards, the designed SRM drive system is implemented using Matlab/Simulink, and the control performance is testified in simulation. In particular, simulations are performed for cases of 50 krpm steady state, speed reference value step change and load torque step change. In addition, the inductance profile selection suggestions are provided for the SRM control design, where the $dL/d\theta$ value is the key consideration. Finally, the developed SRM control is build in hardware with power electronics circuits and DSP program. The experimental results are presented to show the great performance of the designed control scheme.

Chapter seven has discussed the improvement of the proposed SRM design method with current-fed FEA simulation to consider the case of overlapped current profile, for the high torque density applications. First of all, different overlapped current profile cases are characterized into three categories, and the *advanced turning-on* case is selected for this work. Next, the calculation of the overlapped current profile based on the flux linkage is presented, where the flux linkage is calculated in a constant-current-fed FEA simulation. Then, the design of a complete 12/8 SRM is investigated, using the method

with the overlapped current profile. The SRM optimization process is similar with the one presented in Chapter 3, and the design space is a 3D space (D_r , β_s and β_r). Finally, the optimal design is found to be β_r = 25 º, β_s = 15 º, and D_r = 82 mm. An average torque of 0.97 N*m is achieved with the optimal design, and the torque density increased by a factor of 6 comparing to the result in Chapter 3.

8. 2 Conclusion and contributions

The main contributions of this research are outlined as follows:

1. A comprehensive literature survey of the high speed electric machine development and the traditional SRM design methods has been presented. The high speed electric machine research has been summarized with the focus on the comparison between SRM and other types of machines. It provides the motivation and the application of high speed SRM research, and justifies the design specification of a 50,000 rpm 1 kW SRM designed in this work. In addition, the review of the traditional SRM design methods points out the drawbacks and limitations of the previous SRM design work, and concludes the challenge and objective of this dissertation.
2. A novel SRM electromagnetic design and optimization method has been developed, which uses the current-fed FEA simulation as the SRM performance estimation tool. This method serves as the main innovation of this research work. First, the proposed method can be applicable to any SRM topologies and dimensions, and no detailed modeling of a specific SRM configuration is required in advance. Therefore, an automatic SRM design and optimization approach is developed. Secondly, good accuracy of the SRM electromagnetic analysis, e.g. flux density, torque, and current calculation, has been achieved due to the

utilization of FEA simulation. This contribution is particularly significant when considering the poor accuracy of conventional SRM analytical analysis methods, where many assumptions and approximations are used. Last, the proposed design method takes the typical SRM control strategy into account, where the excitation current profile is characterized as a trapezoid. This method adopts the flux linkage of the first FEA simulation result to specify the excitation current profile for the second FEA simulation, so the calculated SRM performance in FEA simulation agrees with the case in practical operation.

3. The proposed SRM design and optimization method has been used for a 12/8 SRM rotor design and a complete 4/2 SRM design. In those two cases, there is no overlap in the current profile between two adjacent phases. Those design examples are to validate the applicability of the proposed method to different SRM configurations and dimensions. Detailed design steps have been presented for both design cases, and the selection of the parametric design variables are also discussed. The optimization results have been demonstrated using multi-dimension diagrams, where the optimal design with the highest torque can be easily identified. The FEA simulation results have been compared to the experimental results of a fabricated SRM prototype, and good agreement has been observed between each other.
4. A novel sensitivity analysis of the optimal 4/2 SRM design has been performed and presented. This study provides useful insight into how the optimal SRM design performance will be affected by the variation of geometric parameters. It has been concluded that the stator pole angle has the most significant impact to the SRM torque, and the influences of the stator and rotor back-iron thickness are very small. This result can help rule out some design variables in the optimization so

that the design space dimension can be minimized and the optimization time can be significantly reduced.

5. A new rotor configuration with a flux bridge has been proposed for an ultra high speed SRM design. The primary motivation of this rotor topology is to reduce the windgae losses and the acoustic noise at a high speed of 50,000 rpm. However, care must be taken for the flux bridge design, and the impact of different flux bridge thickness to the SRM performance has been studied. Meanwhile, the manufacturing difficulty and the mechanical stress should also be considered when fabricating the flux-bridge rotor. As a result, two SRM prototypes have been built, and the two rotors are a regular rotor without a flux bridge and a flux-bridge rotor. The prototypes are tested at different speeds (10,000 rpm, 20,000 rpm and 50,000 rpm) respectively, and the experimental results show good agreement with the FEA simulation results.
6. Detailed high speed SRM control design procedures have been developed. To test the fabricated SRM prototype, hardware such as power electronics circuit, DSP controller, and accessory sensor board have been built. A simple and robust control strategy is needed for the high speed operation, thus the speed-and-current dual-loop control scheme is selected. A complete SRM drive system has been developed in Matlab/Simulink, and the design steps of the current and speed controllers have been presented. In particular, the choice of the inductance profile in the SRM simulation model has been discussed, where the $dL/d\theta$ value is the key factor. The developed SRM control method is featured with simple implementation and robust performance. It is evaluated in the simulation first, and then is implemented in the SRM drive hardware. The experimental results show good control performance which indicates the success of the SRM control design.

7. An improvement of the proposed SRM design method has been presented to consider the case of overlapped excitation current profile. Such improvement has expanded the applicability of the proposed method to high torque applications, where overlapped current profile is more likely to happen. The selection between different overlapped current profiles for this work has been investigated. The SRM performance calculation and dimension optimization procedures are very similar with the method presented in Chapter three, where the non-overlapped current profile is used. Comparing with the non-overlapped current profile, the method with overlapped current profile has increased the average torque of the optimal design by a factor of six, which is a significant improvement for the high torque density applications.

The research work presented in this dissertation has resulted in several publications, which are listed as follows:

Journal papers:

J1: **J. Dang**, Jose Restrepo, J. Rhett Mayor, Semidey Andrew, Ronald Harley, Thomas Habetler, "Practical considerations for the design and construction of a high speed SRM with a flux-bridge rotor", IEEE Transactions on Industry Applications, 2015, accepted

Conference papers:

C1: **J. Dang**, S. Haghbin, Y. Du, C. Bednar, H. Liles, J. Restrepo, J.R. Mayor, Ronald Harley, and Thomas Habetler, "Electromagnetic design considerations for a 50,000 rpm 1kW Switched Reluctance Machine using a flux bridge", IEEE International Electric Machines and Drives Conference (IEMDC), Chicago IL, May 2013, pp. 325-331

C2: **J. Dang**, Ronald G. Harley, "Sensorless control scheme for ultra high speed switched reluctance machine", 2013 IEEE Energy Conversion Congress & Expo (ECCE), Denver CO, Sep 2013, pp. 3830-3836

C3: **J. Dang**, Jose Restrepo, J. Rhett Mayor, Semidey Andrew, Ronald Harley, Thomas Habetler, "Practical considerations for the design and construction of a high speed SRM with a flux-bridge rotor", IEEE Energy Conversion Congress & Expo (ECCE), Pittsburgh PA, Sep 2014, pp. 3842-3849.

C4: **J. Dang**, J. Rhett Mayor, Jose Restrepo, Andrew Semidey, Ronald Harley, and Thomas Habetler, "Switched reluctance machine optimization using current-fed FEA simulation", IEEE International Electric Machines and Drives Conference (IEMDC), Coeur d'Alene ID, May 2015, published

C5: **J. Dang**, J. Rhett Mayor, Jose Restrepo, Andrew Semidey, Ronald Harley, and Thomas Habetler, "High speed SRM control considering the inductance profile of a flux-bridge rotor", IEEE International Electric Machines and Drives Conference (IEMDC), Coeur d'Alene ID, May 2015, published

Additional papers (not included in this dissertation):

J2: **J. Dang**, J. Seuss, L. Suneja, and Ronald G. Harley, "SOC feedback control for wind and ESS hybrid power system frequency regulation", IEEE Journal of Emerging and Selected Topics in Power Electronics, vol. 2, issue 1, pp. 79-86.

C6: **J. Dang**, Ronald G. Harley, "Islanded microgrids black start procedures with wind power integration", 2013 IEEE Power & Energy Society General Meeting (PES), July 2013, pp. 1-5

8. 3 Recommendations for future work

Although this work has made contributions to different areas of SRM design and optimization, there are future improvements which may pave the way for more in-depth research in the future.

1. The SRM design for 500 krpm or beyond

   The highest speed of SRM in the literature is 150 krpm, and the speed record of any electric machine is 1 million rpm, which is a PM machine. The 50 krpm SRM

design and prototype implementation presented in this work provide a solid foundation, and in particular, the proposed SRM electromagnetic design and optimization method can be portable to an SRM design of higher speeds. However, there is some gap between the design of a 50 krpm SRM and one of 500 krpm.

First of all, a more in-depth mechanical design should be performed for the 500 krpm SRM, especially for the rotor. With the increase of the speed by a factor of ten, the fundamental frequency in the machine core will increase by a factor of ten. Considering the saturation of the lamination material, the core area of the 500 krpm SRM should be reduced to one tenth of the 50 krpm SRM. As a result, the size for the 500 krpm SRM design will be significantly reduced. Sophisticated manufacturing will be required to fabricate a much smaller machine. In particular, care should be taken to deal with mechanical issues such as the balancing of the shaft, viscous air drag, rotor natural frequency and rotor stress for the operation speed of 500 krpm or higher. Such study has been investigated in [29] for the design of a 750 krpm SRM, which may provide some useful insight for the future work.

Secondly, there are some challenges that need to be addressed for the existing power electronics hardware before the test of a 500 krpm SRM prototype.

- Switching device frequency limit: the fundamental switching frequency at 500 krpm is 166.7 kHz for a 4/2 SRM. A typical control strategy for the operation of 500 krpm is a single switch operation per revolution, which can be observed in the experimental result of 50 krpm. The maximum frequency suggested for the MOSFET in use is 1 MHz, so the switching device in the existing power electronics should be able to handle the required switching frequency.
- Winding inductance: the current increase or decrease rate is determined by the winding inductance, which is further determined by the number of turns N_{ph} in the stator coil. However, higher current changing rates are required for the

higher speed operation, and the value of N_{ph} may have be adjusted. FEA simulations should be used to investigate this problem.

- Power electronics voltage rating: the DC bus voltage for the test at 50 krpm is 140 V, and it is expected to increase significantly for higher speeds. However, the maximum voltage that the existing power electronics can handle is 250 V. It is possible that new power electronic components may be needed for high speed operation.
- Encoder: the encoder is necessary to provide the position information to achieve the closed-loop speed control. However, the maximum speed of the encoder in use now is 70 krpm. Position sensorless control is a possible solution but the stability of the sensorless control needs to be evaluated at first.
- Bearings: ball bearings are currently in use for the 50 krpm SRM prototype. However, air bearing or magnetic bearing are recommended in the literature for higher speeds in the literature, so it is suggested to replace the ball bearings with more suitable bearings for higher speed operation.

2. Sensorless control

For good control of a SRM, knowledge of the rotor position is required. A position sensor mounted on the shaft can be used to provide the rotor position information, like the encoder used at present in the 50 krpm SRM, but any such sensor may lead to reliability problems when it has to rotate at the ultra high speed itself. First, an encoder for a speed as high as 500 krpm is not available commercially to the best of the author's knowledge. Secondly, mounting the encoder on the machine shaft may bring mechanical stress and balancing problems to the shaft and the bearing.

Much research has been done in an effort to eliminate these position sensors to achieve sensorless control [90]. First, most SRM sensorless control techniques utilize the relationship between the flux linkage, the rotor position, and the phase current,

which requires a large memory space to store a look-up table. Secondly, intelligent algorithms like neural networks and fuzzy logic have the drawback of intensive computational requirement which makes them not suitable for high speed applications. Such approaches may not be suitable due to the difficulty in processing the data fast enough at 500 krpm or beyond. Thirdly, observer-based approaches which utilize model-based estimators to estimate the rotor position have the limitation of high parameter sensitivity. Dependency upon an accurate mathematical model of the SRM is considered as the main issue in this approach. As a result, a method called current-waveform monitoring due to its simple implementation and robust performance has been used in [91]. In particular, the current gradient sensorless control presented in [91] is suggested by the author. This method only requires the knowledge of the phase current to operate, and no prior knowledge of the SRM parameters are required, which allows this scheme to be implemented at low cost. However, the sensorless control stability is the most important concern for this implementation.

3. Evolutionary optimization techniques

Although a complete SRM design and optimization method is presented in this dissertation, the focus of the research effort is on the SRM design side, in particular the SRM performance calculation approach. For the optimization algorithm used in this work, a simple one-by-one sweep method is used. This method can provide a credible optimization result throughout the whole design space, but the number of considered design candidates is relatively small, and the number of optimization variables is small too. However, more design variables and more optimization objectives are expected to be included, so an advanced optimization technique is needed with a significant increase of computational effort. Instead of sweeping the whole design space, relatively few FEA samples can be selected, as the path S_1, S_2, …

S_n shown in Fig 8.1, with the aid of optimization tools to achieve a saving of computational costs.

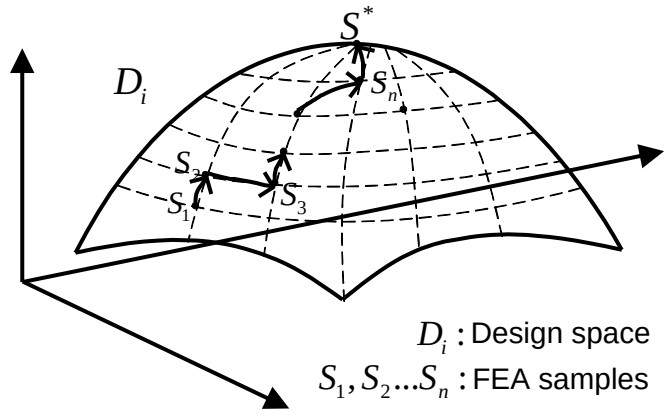

Fig 8.1 FEA sampling by advanced optimization techniques

Then, such optimization tools should reach a global optimal point with minimum computational effort. A few papers present an analytical model to predict the optimal point, while others focus on the numerical techniques. The numerical searching methods are broadly classified into two categories: the deterministic algorithms and the stochastic algorithms. For the former, the algorithm finds the optimas deterministically; and for the latter, the algorithm finds the optimal in the complete design space via stochastic methods.

If the gradient is available in the simplified specific motor model, the deterministic method is utilized. However, the stochastic method is more generally implemented to explore the complete solution space for the global optima. In particular, genetic algorithm (GA) and particle swarm optimization (PSO) have been widely applied to design optimization of other electric machines.

Aside from GA and PSO techniques, there is a shift towards a variety of differential evolution (DE) algorithms. DE has only recently been applied to machine design optimization, including spoke-type ferrite magnet machines, fractional-slot

concentrated winding (FSCW) surface PM machine, SMPM/IPMSM fractional slot/ integer slot machines.

4. Electromagnetic-thermal-mechanical integrated design

Various optimization techniques with different objectives have been carried out for machine design in the literature. Typical design objectives include high efficiency, low cost, high torque, low torque ripple, low harmonics losses, small weight of active materials, etc. Some papers focus on the electromagnetic model, while a few are extended to the mechanical model, like thermal designs. In pursuit of this goal, the future work should establish and verify parametric performance estimators for the electromagnetic performance, the spatial-temporal thermal response and the rotor mechanical (structural) response of machine design candidates to enable the evaluation of the thermo-electromechanical performance of candidate designs. Furthermore, the research effort should aim to assess computational intelligence solutions to the multi-variable multi-objective optimization functions through numerical evolutionary optimization techniques, and identify the approaches that enhance exploration of the full-domain design space.

The architecture of the conventional machine design performance assessment is a sequential physics solution strategy. It first estimates electromagnetic performance and thermal and mechanical performance independently. And then the overall performance metric is consolidated based on the application-specific design requirements into the objective function, and the computational intelligence engine explores the full-domain design space until the optimality is satisfied.

Alternatively, a parallel physics solution approach can be pursued that utilizes an integrated electromagnetic-thermo mechanical (ETM) performance estimator that directly solves the combined electromagnetic and thermal response of the design candidate to the governing transport equations (Maxwell and Fourier) on a

parametrically generated mesh. Figure 8.2 indicates the flow chart of such a SRM ETM integrated design. Each design candidate that is described as a set of independent variables is the input of the integrated ET module. In the module, the electromagnetic estimator solves the Maxwell equation to calculate the magnetic field B and the electric field E. The thermo estimator solves the Fourier heat equation to calculate the temperature T. In addition, the rotor mechanical response module solves the rotor lamination deflection δ. All the estimators work on the same parametric mesh. Afterwards, the design performance is evaluated by an objective function where the variables include the weight or volume, the efficiency, the temperature and the rotor deflection. In order to investigate a large design space without terminating the search exploration due to the violation of physics limitation, soft constraints are utilized in a way of penalty function. The design space Di sampling is guided by a numerical evolutionary optimization tool, and the response surface method is used to predict the entire Di response. Different intelligent algorithms (GA, PSO, and DE) are compared for the numerical optimization based on a performance criterion, which is defined by the algorithm converging capability and computational costs.

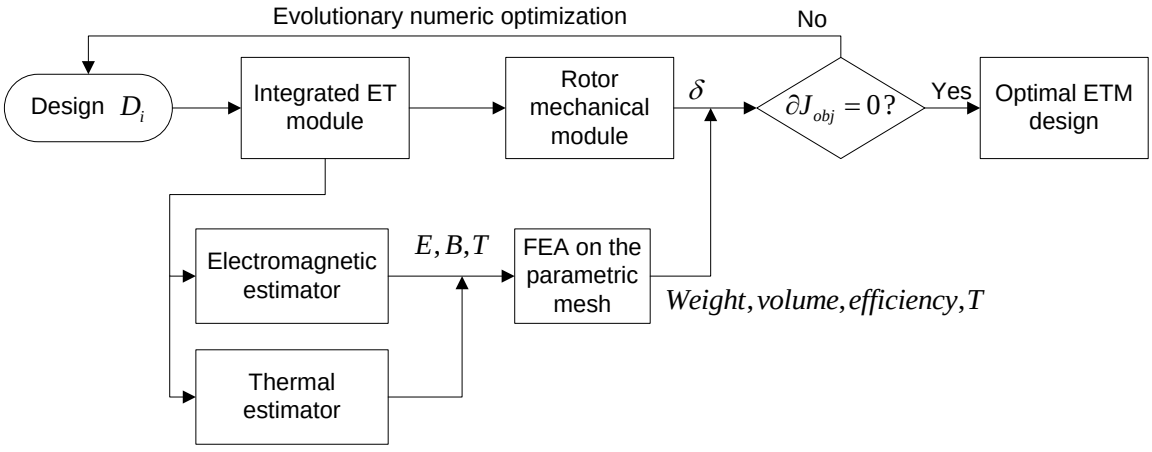

Fig 8.2 Integrated SRM ETM design flow chart

APPENDIX A

12/8 SRM ROTOR DESIGN AND OPTIMIZATION CODE

1. Main function (Main.m in Fig 3.25)

```
clc
clear all

iMaxwell = actxserver('AnsoftMaxwell.MaxwellScriptInterface');
Desktop = iMaxwell.GetAppDesktop();
Desktop.RestoreWindow
Project = Desktop.SetActiveProject('SRM_Andrew1');
Design = Project.SetActiveDesign('Maxwell2DDesign_Drawing');
Editor = Design.SetActiveEditor('3D Modeler');
DefinitionManager = Project.GetDefinitionManager();


% Define geometry parameter
R_rotor = 39/1000;
Beta_r = 23;
HH = 18;

for HH = 14:2:22
for Beta_r = 20:1:24


Draw

% run 'Constant current simulation'
ConstFEA

% run 'flux data processing'
ExpFlux

% run 'current increase time calculation'
Angle_increase

% run 'current decrease time calculation'
Angle_decrease

% run 'trapezoidal current fed simulation'
TrapFEA

% run 'torque data processing'
ExpTorq

% after one interation, delete the rotor and redraw one
SaveData

      end
end
```

2. Draw the lamination in Maxwell (Draw.m)

```
% Define geometry parameter
L1=R_rotor*cos(Beta_r/2*pi/180);
H1=R_rotor*sin(Beta_r/2*pi/180);
L1_N=-L1;
H1_N=-H1;

% Convert the geometry parameter to the string
Beta_r_str=strcat(num2str(Beta_r),'deg');
R_rotor_str=strcat(num2str(R_rotor),'m');
L1_str=strcat(num2str(L1),'m');
L1_N_str=strcat(num2str(L1_N),'m');
H1_str=strcat(num2str(H1),'m');
H1_N_str=strcat(num2str(H1_N),'m');
HH_str=strcat(num2str(HH),'mm');


invoke(Design,             'ChangeProperty',             {'NAME:AllTabs',
{'NAME:LocalVariableTab', {'NAME:PropServers', ...
'LocalVariables'},    {'NAME:ChangedProps',    {'NAME:HH',    'Value:=',
HH_str}}}});
invoke(Design,             'ChangeProperty',             {'NAME:AllTabs',
{'NAME:LocalVariableTab', {'NAME:PropServers', ...
'LocalVariables'},   {'NAME:ChangedProps',   {'NAME:Beta_r',   'Value:=',
Beta_r_str}}}});
invoke(Design,             'ChangeProperty',             {'NAME:AllTabs',
{'NAME:LocalVariableTab', {'NAME:PropServers', ...
'LocalVariables'},   {'NAME:ChangedProps',   {'NAME:R_rotor',   'Value:=',
R_rotor_str}}}});
invoke(Design,             'ChangeProperty',             {'NAME:AllTabs',
{'NAME:LocalVariableTab', {'NAME:PropServers', ...
'LocalVariables'},    {'NAME:ChangedProps',    {'NAME:L1',    'Value:=',
L1_str}}}});
invoke(Design,             'ChangeProperty',             {'NAME:AllTabs',
{'NAME:LocalVariableTab', {'NAME:PropServers', ...
'LocalVariables'},    {'NAME:ChangedProps',    {'NAME:H1',    'Value:=',
H1_str}}}});
invoke(Design,             'ChangeProperty',             {'NAME:AllTabs',
{'NAME:LocalVariableTab', {'NAME:PropServers', ...
'LocalVariables'},    {'NAME:ChangedProps',    {'NAME:L1_N',    'Value:=',
L1_N_str}}}});
invoke(Design,             'ChangeProperty',             {'NAME:AllTabs',
{'NAME:LocalVariableTab', {'NAME:PropServers', ...
'LocalVariables'},    {'NAME:ChangedProps',    {'NAME:H1_N',    'Value:=',
H1_N_str}}}});


invoke(Editor,       'CreatePolyline',       {'NAME:PolylineParameters',
'IsPolylineCovered:=', true, 'IsPolylineClosed:=', ...
  false, {'NAME:PolylinePoints', ...
  {'NAME:PLPoint', 'X:=', L1, 'Y:=', H1, 'Z:=', '0mm'}, ...
  {'NAME:PLPoint', 'X:=', L1, 'Y:=', H1_N, 'Z:=', '0mm'}}, ...
  {'NAME:PolylineSegments', {'NAME:PLSegment', 'SegmentType:=', ...
```

```
  'AngularArc', 'StartIndex:=', 0, 'NoOfPoints:=', 3, 'NoOfSegments:=',
'0', 'ArcAngle:=', ...
  '-Beta_r',     'ArcCenterX:=',     '0mm',     'ArcCenterY:=',     '0mm',
'ArcCenterZ:=', '0mm', 'ArcPlane:=', ...
  'XY'}},     {'NAME:PolylineXSection',     'XSectionType:=',     'None',
'XSectionOrient:=', ...
  'Auto',    'XSectionWidth:=',    '0mm',    'XSectionTopWidth:=',    '0mm',
'XSectionHeight:=', ...
  '0mm',     'XSectionNumSegments:=',     '0',     'XSectionBendType:=',
'Corner'}}, {'NAME:Attributes', 'Name:=', ...
  'Polyline3',    'Flags:=',    '',    'Color:=',    '(132    132    193)',
'Transparency:=', 0, 'PartCoordinateSystem:=', ...
  'Global',     'UDMId:=',     '',     'MaterialValue:=',     '"vacuum"',
'SolveInside:=', true});
invoke(Editor,  'DuplicateMirror',  {'NAME:Selections',  'Selections:=',
'Polyline3', 'NewPartsModelFlag:=', ...
  'Model'},                          {'NAME:DuplicateToMirrorParameters',
'DuplicateMirrorBaseX:=', '0mm', 'DuplicateMirrorBaseY:=', ...
  '0mm',  'DuplicateMirrorBaseZ:=',  '0mm',  'DuplicateMirrorNormalX:=',
'1mm', 'DuplicateMirrorNormalY:=', ...
  '0mm',     'DuplicateMirrorNormalZ:=',     '0mm'},     {'NAME:Options',
'DuplicateAssignments:=', false});

invoke(Editor,       'CreatePolyline',       {'NAME:PolylineParameters',
'IsPolylineCovered:=', true, 'IsPolylineClosed:=', ...
  false, {'NAME:PolylinePoints', ...
{'NAME:PLPoint', 'X:=', L1_N, 'Y:=', H1, 'Z:=', '0mm'},...
{'NAME:PLPoint', 'X:=', L1,  'Y:=', H1, 'Z:=', '0mm'}}, ...
{'NAME:PolylineSegments', {'NAME:PLSegment', 'SegmentType:=',  ...
  'Line',       'StartIndex:=',       0,       'NoOfPoints:=',       2}},
{'NAME:PolylineXSection', 'XSectionType:=', ...
  'None',   'XSectionOrient:=',   'Auto',   'XSectionWidth:=',   '0mm',
'XSectionTopWidth:=', ...
  '0mm',   'XSectionHeight:=',   '0mm',   'XSectionNumSegments:=',   '0',
'XSectionBendType:=', ...
  'Corner'}}, {'NAME:Attributes', 'Name:=', 'Polyline4', 'Flags:=', '',
'Color:=', ...
  '(132  132  193)',  'Transparency:=',  0,  'PartCoordinateSystem:=',
'Global', 'UDMId:=', ...
  '', 'MaterialValue:=', '"vacuum"', 'SolveInside:=', true});
invoke(Editor,       'CreatePolyline',       {'NAME:PolylineParameters',
'IsPolylineCovered:=', true, 'IsPolylineClosed:=', ...
  false, {'NAME:PolylinePoints', ...
{'NAME:PLPoint', 'X:=', L1_N, 'Y:=', H1_N, 'Z:=', '0mm'}, ...
{'NAME:PLPoint', 'X:=', L1, 'Y:=', H1_N, 'Z:=', '0mm'}}, ...
{'NAME:PolylineSegments', {'NAME:PLSegment', 'SegmentType:=',  ...
  'Line',       'StartIndex:=',       0,       'NoOfPoints:=',       2}},
{'NAME:PolylineXSection', 'XSectionType:=', ...
  'None',   'XSectionOrient:=',   'Auto',   'XSectionWidth:=',   '0mm',
'XSectionTopWidth:=', ...
  '0mm',   'XSectionHeight:=',   '0mm',   'XSectionNumSegments:=',   '0',
'XSectionBendType:=',...
  'Corner'}}, {'NAME:Attributes', 'Name:=', 'Polyline5', 'Flags:=', '',
'Color:=', ...
  '(132  132  193)',  'Transparency:=',  0,  'PartCoordinateSystem:=',
'Global', 'UDMId:=',  ...
```

```
  '', 'MaterialValue:=', '"vacuum"', 'SolveInside:=', true});

invoke(Editor, 'Unite', {'NAME:Selections', 'Selections:=', ...
  'Polyline3,Polyline3_1,Polyline4,Polyline5'},
{'NAME:UniteParameters', 'KeepOriginals:=', false});
invoke(Editor,    'CoverLines',    {'NAME:Selections',    'Selections:=',
'Polyline3', 'NewPartsModelFlag:=', 'Model'});

invoke(Editor,         'DuplicateAroundAxis',         {'NAME:Selections',
'Selections:=', 'Polyline3', 'NewPartsModelFlag:=', ...
  'Model'},                       {'NAME:DuplicateAroundAxisParameters',
'CreateNewObjects:=', true, 'WhichAxis:=', ...
  'Z',  'AngleStr:=',  '45deg',  'NumClones:=',  '4'},  {'NAME:Options',
'DuplicateAssignments:=', false});
invoke(Editor, 'Unite', {'NAME:Selections', 'Selections:=', ...
  'Polyline3_2,Polyline3_3,Polyline3_4,Polyline3'},
{'NAME:UniteParameters', 'KeepOriginals:=', false});

invoke(Editor, 'CreateCircle', {'NAME:CircleParameters', 'IsCovered:=',
true, 'XCenter:=',...
  '0mm',  'YCenter:=',  '0mm',  'ZCenter:=',  '0mm',  'Radius:=',  'R1',
'WhichAxis:=', ...
  'Z', 'NumSegments:=', '0'}, {'NAME:Attributes', 'Name:=', 'Circle4',
'Flags:=',...
  '',    'Color:=',    '(132    132    193)',    'Transparency:=',    0,
'PartCoordinateSystem:=', ...
  'Global',     'UDMId:=',     '',     'MaterialValue:=',     '"vacuum"',
'SolveInside:=', true});

invoke(Editor,     'Unite',     {'NAME:Selections',     'Selections:=',
'Circle4,Polyline3_2'}, {'NAME:UniteParameters', 'KeepOriginals:=', ...
  false});

invoke(Editor, 'CreateCircle', {'NAME:CircleParameters', 'IsCovered:=',
true, 'XCenter:=', ...
  '0mm', 'YCenter:=', '0mm', 'ZCenter:=', '0mm', 'Radius:=', 'R_shaft',
'WhichAxis:=', ...
  'Z', 'NumSegments:=', '0'}, {'NAME:Attributes', 'Name:=', 'Circle5',
'Flags:=',  ...
  '',    'Color:=',    '(132    132    193)',    'Transparency:=',    0,
'PartCoordinateSystem:=', ...
  'Global',     'UDMId:=',     '',     'MaterialValue:=',     '"vacuum"',
'SolveInside:=', true});

invoke(Editor, 'Copy', {'NAME:Selections', 'Selections:=', 'Circle5'});
invoke(Editor, 'Paste');

invoke(Editor,   'Subtract',   {'NAME:Selections',   'Blank   Parts:=',
'Circle4', 'Tool Parts:=',  ...
  'Circle5'}, {'NAME:SubtractParameters', 'KeepOriginals:=', false});

invoke(Editor,            'ChangeProperty',            {'NAME:AllTabs',
{'NAME:Geometry3DAttributeTab', {'NAME:PropServers',...
  'Circle4'},    {'NAME:ChangedProps',    {'NAME:Material',    'Value:=',
'"steel_1008"'}}}});
```

```
invoke(Editor,            'ChangeProperty',            {'NAME:AllTabs',
{'NAME:Geometry3DAttributeTab', {'NAME:PropServers',...
  'Circle4'},     {'NAME:ChangedProps',     {'NAME:Name',     'Value:=',
'Rotor'}}}});

invoke(Editor,            'ChangeProperty',            {'NAME:AllTabs',
{'NAME:Geometry3DAttributeTab', {'NAME:PropServers',  ...
  'Circle6'},     {'NAME:ChangedProps',     {'NAME:Name',     'Value:=',
'Shaft'}}}});

invoke(Editor, 'CreateCircle', {'NAME:CircleParameters', 'IsCovered:=',
true, 'XCenter:=', ...
  '0mm', 'YCenter:=', '0mm', 'ZCenter:=', '0mm', 'Radius:=', '39.35mm',
'WhichAxis:=', ...
  'Z', 'NumSegments:=', '0'}, {'NAME:Attributes', 'Name:=', 'Circle6',
'Flags:=', ...
  '',    'Color:=',    '(132    132    193)',    'Transparency:=',    0,
'PartCoordinateSystem:=', ...
  'Global',     'UDMId:=',     '',     'MaterialValue:=',     '"vacuum"',
'SolveInside:=', true});

invoke(Editor,            'ChangeProperty',            {'NAME:AllTabs',
{'NAME:Geometry3DAttributeTab', {'NAME:PropServers', ...
  'Circle6'},     {'NAME:ChangedProps',     {'NAME:Name',     'Value:=',
'Inner'}}}});
```

3. Constant current fed FEA simulation setup (ConstFEA.m)

```
iMaxwell = actxserver('AnsoftMaxwell.MaxwellScriptInterface');
Desktop = iMaxwell.GetAppDesktop();
Desktop.RestoreWindow
Project = Desktop.SetActiveProject('SRM_Andrew1');
Design = Project.SetActiveDesign('Maxwell2DDesign_Drawing');
Editor = Design.SetActiveEditor('3D Modeler');
DefinitionManager = Project.GetDefinitionManager();

Module = Design.GetModule('ModelSetup');

invoke(Design,  'ChangeProperty',  {'NAME:AllTabs',  {'NAME:Maxwell2D',
{'NAME:PropServers', ...
  'BoundarySetup:PhaseB'},     {'NAME:ChangedProps',     {'NAME:Current',
'Value:=', 'Ip'}}}} );

invoke(Module,  'AssignBand',  {'NAME:Data',  'Move  Type:=',  'Rotate',
'Coordinate System:=', ...
  'Global', 'Axis:=', 'Z', 'Is Positive:=', true, 'InitPos:=', '0deg',
'HasRotateLimit:=', ...
  false, 'NonCylindrical:=', false, 'Consider Mechanical Transient:=',
false, 'Angular Velocity:=', ...
  '2000rpm', 'Objects:=', {'Inner'}} );

invoke(Project, 'Save');
invoke(Design, 'AnalyzeAll');
```

4. Extract flux linkage calculation result (ExpFlux.m)

```
Module = Design.GetModule('ReportSetup');
invoke(Module,              'ExportToFile',              'FluxLinkage',
'\\ad.gatech.edu\ecefs$\users\students\jdang3\Profile\Desktop\Opt_test_
12_8\Sweep_result\Flux.tab');

fid = fopen('Sweep_result\Flux.tab', 'r');
FF = textscan(fid, '%f%f%f%f', 21, 'headerlines', 1);

% First column is time
Time = FF{1,1};

% Column 2 to 4 are phase A B C flux, here phase B flux is needed
Flux_B = FF{1,2};
```

5. Calculate current increase time (Angle_increase.m)

```
% load Flux_Ip
w = 2000;
wr = 2*pi*(w/60);
Vdc = 350;

if Time(2) >= 1000
    Time = Time/1000;
end

Time_step = Time(2)*1e-6;
Theta_step = Time_step*wr;

Flux = Flux_B'
Theta = Time*1e-6*wr;

Theta_on = 0;  % Timing
Theta_1_est = Theta_on;

% dfdtheta_Theta_mid1 = dfdtheta(1);
Flux_theta1 = Flux(1);

for i = 1:50
    Time_increase = Flux_theta1/Vdc;
    Theta_increase = Time_increase*wr;
    Theta_1 = Theta_on + Theta_increase;
    Flux_theta1 = interp1(Theta, Flux, Theta_1);
end
```

6. Calculate current decrease time (Angle_decrease.m)

```
% load Flux_Ip
w = 2000;
wr = 2*pi*(w/60);
Vdc = 350;

if Time(2) >= 1000
    Time = Time/1000;
end

Time_step = Time(2)*1e-6;
Theta_step = Time_step*wr;

Flux = Flux_B';
Theta = Time*1e-6*wr;

Theta_2 = Theta(length(Theta));  % Timing
Flux_theta2 = Flux(length(Flux));

Theta_off_est = Theta_2;
Flux_theta_off = Flux_theta2;


for i = 1:20
    Time_decrease = Flux_theta_off/Vdc;
    Theta_decrease = Time_decrease*wr;
    Theta_off = Theta_2 - Theta_decrease;
    Flux_theta_off = interp1(Theta, Flux, Theta_off);
end
```

7. Trapezoidal current profile fed FEA simulation setup (TrapFEA.m)

```
Module = Design.GetModule('ModelSetup');

Time_increase_str = strcat(num2str(Time_increase));
Time_decrease_str = strcat(num2str(Time_decrease));

invoke(Design,             'ChangeProperty',            {'NAME:AllTabs',
{'NAME:LocalVariableTab', {'NAME:PropServers', ...
'LocalVariables'},      {'NAME:ChangedProps',      {'NAME:Time_increase',
'Value:=', Time_increase_str}}}});
invoke(Design,             'ChangeProperty',            {'NAME:AllTabs',
{'NAME:LocalVariableTab', {'NAME:PropServers', ...
'LocalVariables'},      {'NAME:ChangedProps',      {'NAME:Time_decrease',
'Value:=', Time_decrease_str}}}});

invoke(Design,             'ChangeProperty',            {'NAME:AllTabs',
{'NAME:LocalVariableTab', {'NAME:PropServers', ...
  'LocalVariables'},     {'NAME:ChangedProps',     {'NAME:Time_increase',
'Value:=', ...
```

```
  Time_increase},  {'NAME:Time_decrease',  'Value:=',  Time_decrease}}}}
);

invoke(Design,  'ChangeProperty',  {'NAME:AllTabs',  {'NAME:Maxwell2D',
{'NAME:PropServers', ...
  'BoundarySetup:PhaseB'},    {'NAME:ChangedProps',    {'NAME:Current',
'Value:=', ...
  'Ip*time/(Time_increase)*(time  <=  Time_increase)  +  Ip*((time  >
Time_increase)&&(time    <=    (Tstop-Time_decrease)))+    Ip*(Tstop-
time)/Time_decrease*(((Tstop-Time_decrease)  <  time)&&(time  <=  Tstop))'
}}}} );

invoke(Project, 'Save');
invoke(Design, 'AnalyzeAll');
```

8. Extract torque calculation result (ExpTorq.m)

```
Module = Design.GetModule('ReportSetup');
invoke(Module,                'ExportToFile',                'Torque',
'//ad.gatech.edu/ecefs$/users/students/jdang3/Profile/Desktop/Opt_test_
12_8/Sweep_result/Torque.tab');

fid = fopen('Sweep_result\Torque.tab', 'r');
FF = textscan(fid, '%f%f', 21, 'headerlines', 1);

Torque = FF{1,2};
torque = mean(Torque)*1e-3
```

9. After one iteration, delete the lamination (SaveData.m)

```
invoke(Editor, 'Delete', {'NAME:Selections', 'Selections:=', 'Rotor'});
invoke(Editor, 'Delete', {'NAME:Selections', 'Selections:=', 'Inner'});
invoke(Editor, 'Delete', {'NAME:Selections', 'Selections:=', 'Shaft'});
```

APPENDIX B

4/2 SRM DESIGN AND OPTIMIZATION CODE

1. Main function (Main.m in Fig 4.4)

```
clc
clear all

iMaxwell = actxserver('AnsoftMaxwell.MaxwellScriptInterface');
Desktop = iMaxwell.GetAppDesktop();
Desktop.RestoreWindow
Project = Desktop.SetActiveProject('SRM_Andrew1');
Design = Project.SetActiveDesign('Maxwell2DDesign_Drawing_4_2');
Editor = Design.SetActiveEditor('3D Modeler');
DefinitionManager = Project.GetDefinitionManager();

% Define geometry parameter
R_shaft = 3.374;
N = 70;

for R_stator_in = 10:0.2:12;
        bsy = 4.5;
        R_rotor = R_stator_in - 0.5;
        H_tooth = 32.5 - R_stator_in - bsy;
        bry = 6.5;

for Beta_s = 40:1:50
for Beta_r = 72:1:82;


Slot_Area

Jc = 5; %Current density (A/mm2)
FF = 0.5; % Filling Facotr
Ip = SA*Jc*FF/2/N;


Draw

% run 'Constant current simulation'
ConstIp

% run 'flux data processing'
ExpFlux

% run 'current increase time calculation'
Angle_increase

% run 'current decrease time calculation'
Angle_decrease

% run 'trapezoidal current fed simulation'
TrapFEA
```

```
% run 'torque data processing'
ExpTorq

% after one interation, delete the rotor and redraw one
SaveData


            end
        end
    end
```

2. Slot Area Calculation (Slot_Area.m)

```
% R1: stator back iron & stator pole
R1    =    sqrt((R_stator_in*sin(Beta_s/2*pi/180))^2    +    (H_tooth    +
R_stator_in*cos(Beta_s/2*pi/180))^2);
R1_angle     =     atan((R_stator_in*sin(Beta_s/2*pi/180))/(H_tooth     +
R_stator_in*cos(Beta_s/2*pi/180)));

% Ring Area
RA = (R1^2 - R_stator_in^2)*pi/360*(90 - Beta_s);

% Fan-sector Area
FA_R1 = R1^2*pi/360*(Beta_s/2 - R1_angle/pi*180);
Triangle = H_tooth*R_stator_in*sin(Beta_s/2*pi/180)/2;
FA = FA_R1 - Triangle;

% Slot Area
SA = RA + FA*2;
```

3. Draw the lamination in Maxwell (Draw.m)

```
% Convert the geometry parameter to the string
R_s_in_str = strcat(num2str(R_stator_in),'mm');
R_r_str = strcat(num2str(R_rotor),'mm');
R_shaft_str = strcat(num2str(R_shaft),'mm');
H_tooth_str = strcat(num2str(H_tooth),'mm');
Beta_s_str = strcat(num2str(Beta_s),'deg');
Beta_r_str = strcat(num2str(Beta_r),'deg');
N_str = strcat(num2str(N));
Ip_str = strcat(num2str(Ip),'A');
R_backiron_str = strcat(num2str(bry),'mm');

invoke(        Design,        'ChangeProperty',        {'NAME:AllTabs',
{'NAME:LocalVariableTab', {'NAME:PropServers', ...
  'LocalVariables'},  {'NAME:ChangedProps',  {'NAME:R_rotor',  'Value:=',
R_r_str}}}});
invoke(        Design,        'ChangeProperty',        {'NAME:AllTabs',
{'NAME:LocalVariableTab', {'NAME:PropServers', ...
```

```
  'LocalVariables'},  {'NAME:ChangedProps',  {'NAME:R_s_in',  'Value:=',
R_s_in_str}}}});
invoke(        Design,        'ChangeProperty',        {'NAME:AllTabs',
{'NAME:LocalVariableTab', {'NAME:PropServers', ...
  'LocalVariables'},  {'NAME:ChangedProps',  {'NAME:R_shaft',  'Value:=',
R_shaft_str}}}});
invoke(        Design,        'ChangeProperty',        {'NAME:AllTabs',
{'NAME:LocalVariableTab', {'NAME:PropServers', ...
  'LocalVariables'},  {'NAME:ChangedProps',  {'NAME:H_tooth',  'Value:=',
H_tooth_str}}}});
invoke(        Design,        'ChangeProperty',        {'NAME:AllTabs',
{'NAME:LocalVariableTab', {'NAME:PropServers', ...
  'LocalVariables'},  {'NAME:ChangedProps',  {'NAME:Beta_r',  'Value:=',
Beta_r_str}}}});
invoke(        Design,        'ChangeProperty',        {'NAME:AllTabs',
{'NAME:LocalVariableTab', {'NAME:PropServers', ...
  'LocalVariables'},  {'NAME:ChangedProps',  {'NAME:Beta_s',  'Value:=',
Beta_s_str}}}});
invoke(        Design,        'ChangeProperty',        {'NAME:AllTabs',
{'NAME:LocalVariableTab', {'NAME:PropServers', ...
  'LocalVariables'},   {'NAME:ChangedProps',   {'NAME:Ip',   'Value:=',
Ip_str}}}});
invoke(        Design,        'ChangeProperty',        {'NAME:AllTabs',
{'NAME:LocalVariableTab', {'NAME:PropServers', ...
  'LocalVariables'},      {'NAME:ChangedProps',      {'NAME:R_backiron',
'Value:=', R_backiron_str}}}});

% Stator
invoke(      Editor,      'CreateCircle',      {'NAME:CircleParameters',
'IsCovered:=', true, 'XCenter:=', ...
  '0mm', 'YCenter:=', '0mm', 'ZCenter:=', '0mm', 'Radius:=', '32.5mm',
'WhichAxis:=', ...
  'Z', 'NumSegments:=', '0'}, {'NAME:Attributes', 'Name:=', 'Circle1',
'Flags:=', ...
  '',    'Color:=',    '(132    132    193)',    'Transparency:=',    0,
'PartCoordinateSystem:=', ...
  'Global',     'UDMId:=',     '',     'MaterialValue:=',     '"vacuum"',
'SolveInside:=', true});

invoke(      Editor,      'CreateCircle',      {'NAME:CircleParameters',
'IsCovered:=', true, 'XCenter:=', ...
  '0mm', 'YCenter:=', '0mm', 'ZCenter:=', '0mm', 'Radius:=', 'R_s_in',
'WhichAxis:=', ...
  'Z', 'NumSegments:=', '0'}, {'NAME:Attributes', 'Name:=', 'Circle2',
'Flags:=', ...
  '',    'Color:=',    '(132    132    193)',    'Transparency:=',    0,
'PartCoordinateSystem:=', ...
  'Global',     'UDMId:=',     '',     'MaterialValue:=',     '"vacuum"',
'SolveInside:=', true});
invoke(   Editor,   'Subtract',   {'NAME:Selections',   'Blank   Parts:=',
'Circle1', 'Tool Parts:=', ...
  'Circle2'}, {'NAME:SubtractParameters', 'KeepOriginals:=', false});
invoke(    Editor,    'Copy',    {'NAME:Selections',    'Selections:=',
'Circle1'});
invoke( Editor, 'Paste');
```

```
invoke(        Editor,        'ChangeProperty',        {'NAME:AllTabs',
{'NAME:Geometry3DAttributeTab', {'NAME:PropServers', ...
  'Circle3'},     {'NAME:ChangedProps',     {'NAME:Name',     'Value:=',
'Outer'}}}});
invoke(        Editor,        'ChangeProperty',        {'NAME:AllTabs',
{'NAME:Geometry3DAttributeTab', {'NAME:PropServers', ...
  'Circle1'},    {'NAME:ChangedProps',    {'NAME:Material',    'Value:=',
'"steel_1008"'}}}});


invoke(    Editor,    'CreatePolyline',    {'NAME:PolylineParameters',
'IsPolylineCovered:=', true, 'IsPolylineClosed:=', ...
  false, {'NAME:PolylinePoints', {'NAME:PLPoint', ...
  'X:=', 'L1', 'Y:=', 'H1', 'Z:=', '0mm'}, {'NAME:PLPoint', ...
  'X:=',  'LL1',  'Y:=','H1',  'Z:=',  '0mm'}},  {'NAME:PolylineSegments',
{'NAME:PLSegment', 'SegmentType:=', ...
  'Line',       'StartIndex:=',       0,       'NoOfPoints:=',       2}},
{'NAME:PolylineXSection', 'XSectionType:=', ...
  'None',    'XSectionOrient:=',    'Auto',    'XSectionWidth:=',    '0mm',
'XSectionTopWidth:=', ...
  '0mm',   'XSectionHeight:=',   '0mm',   'XSectionNumSegments:=',   '0',
'XSectionBendType:=', ...
  'Corner'}}, {'NAME:Attributes', 'Name:=', 'Polyline2', 'Flags:=', '',
'Color:=', ...
  '(132  132  193)',  'Transparency:=',  0,  'PartCoordinateSystem:=',
'Global', 'UDMId:=', ...
  '', 'MaterialValue:=', '"vacuum"', 'SolveInside:=', true});
invoke( Editor, 'DuplicateMirror', {'NAME:Selections', 'Selections:=',
'Polyline2', 'NewPartsModelFlag:=', ...
  'Model'},                          {'NAME:DuplicateToMirrorParameters',
'DuplicateMirrorBaseX:=', '0mm', 'DuplicateMirrorBaseY:=', ...
  '0mm',  'DuplicateMirrorBaseZ:=',  '0mm',  'DuplicateMirrorNormalX:=',
'0mm', 'DuplicateMirrorNormalY:=', ...
  '1mm',     'DuplicateMirrorNormalZ:=',     '0mm'},     {'NAME:Options',
'DuplicateAssignments:=', false});
invoke(    Editor,    'Rotate',    {'NAME:Selections',    'Selections:=',
'Polyline2_1', 'NewPartsModelFlag:=', ...
  'Model'},      {'NAME:RotateParameters',      'RotateAxis:=',      'Z',
'RotateAngle:=', '90deg'});
invoke(    Editor,    'CreatePolyline',    {'NAME:PolylineParameters',
'IsPolylineCovered:=', true, 'IsPolylineClosed:=', ...
  false, {'NAME:PolylinePoints', {'NAME:PLPoint', ...
  'X:=', 'H1', 'Y:=', 'L1', 'Z:=', '0mm'}, {'NAME:PLPoint', ...
  'X:=', 'L1_mid', 'Y:=', 'L1_mid', 'Z:=', '0mm'}, {'NAME:PLPoint', ...
  'X:=',  'L1',  'Y:=',  'H1',  'Z:=',  '0mm'}},  {'NAME:PolylineSegments',
{'NAME:PLSegment', 'SegmentType:=', ...
  'AngularArc', 'StartIndex:=', 0, 'NoOfPoints:=', 3, 'NoOfSegments:=',
'0', 'ArcAngle:=', ...
  'Ang_s_in',    'ArcCenterX:=',    '0mm',    'ArcCenterY:=',    '0mm',
'ArcCenterZ:=', '0mm', 'ArcPlane:=', ...
  'XY'}},     {'NAME:PolylineXSection',     'XSectionType:=',     'None',
'XSectionOrient:=', ...
  'Auto',   'XSectionWidth:=',   '0mm',   'XSectionTopWidth:=',   '0mm',
'XSectionHeight:=', ...
  '0mm',     'XSectionNumSegments:=',     '0',     'XSectionBendType:=',
'Corner'}}, {'NAME:Attributes', 'Name:=', ...
```

```
  'Polyline3',    'Flags:=',    '',    'Color:=',    '(132    132    193)',
'Transparency:=', 0, 'PartCoordinateSystem:=', ...
  'Global',     'UDMId:=',     '',     'MaterialValue:=',     '"vacuum"',
'SolveInside:=', true});
invoke(     Editor,     'CreatePolyline',     {'NAME:PolylineParameters',
'IsPolylineCovered:=', true, 'IsPolylineClosed:=', ...
  false, {'NAME:PolylinePoints', {'NAME:PLPoint', ...
  'X:=', 'H1', 'Y:=', 'LL1', 'Z:=', '0mm'}, {'NAME:PLPoint', ...
  'X:=', 'LL1_mid', 'Y:=', 'LL1_mid', 'Z:=', '0mm'}, {'NAME:PLPoint',
...
  'X:=', 'LL1', 'Y:=','H1', 'Z:=', '0mm'}}, {'NAME:PolylineSegments',
{'NAME:PLSegment', 'SegmentType:=', ...
  'AngularArc', 'StartIndex:=', 0, 'NoOfPoints:=', 3, 'NoOfSegments:=',
'0', 'ArcAngle:=', ...
  'Ang_s_out',    'ArcCenterX:=',    '0mm',    'ArcCenterY:=',    '0mm',
'ArcCenterZ:=', ...
  '0mm',      'ArcPlane:=',      'XY'}},      {'NAME:PolylineXSection',
'XSectionType:=', 'None', 'XSectionOrient:=', ...
  'Auto',   'XSectionWidth:=',   '0mm',   'XSectionTopWidth:=',   '0mm',
'XSectionHeight:=', ...
  '0mm',     'XSectionNumSegments:=',     '0',     'XSectionBendType:=',
'Corner'}}, {'NAME:Attributes', 'Name:=', ...
  'Polyline4',    'Flags:=',    '',    'Color:=',    '(132    132    193)',
'Transparency:=', 0, 'PartCoordinateSystem:=', ...
  'Global',     'UDMId:=',     '',     'MaterialValue:=',     '"vacuum"',
'SolveInside:=', true});
invoke( Editor, 'Unite', {'NAME:Selections', 'Selections:=', ...
  'Polyline2,Polyline2_1,Polyline3,Polyline4'},
{'NAME:UniteParameters', 'KeepOriginals:=', false});
invoke(   Editor,   'CoverLines',   {'NAME:Selections',   'Selections:=',
'Polyline2', 'NewPartsModelFlag:=', ...
  'Model'});
invoke(        Editor,        'ChangeProperty',        {'NAME:AllTabs',
{'NAME:Geometry3DAttributeTab', {'NAME:PropServers', ...
  'Polyline2'},   {'NAME:ChangedProps',   {'NAME:Material',   'Value:=',
'"copper"'}, {'NAME:Material', 'Value:=', ...
  '"steel_1008"'}}}});
invoke( Editor, 'DuplicateMirror', {'NAME:Selections', 'Selections:=',
'Polyline2', 'NewPartsModelFlag:=', ...
  'Model'},                          {'NAME:DuplicateToMirrorParameters',
'DuplicateMirrorBaseX:=', '0mm', 'DuplicateMirrorBaseY:=', ...
  '0mm',  'DuplicateMirrorBaseZ:=',  '0mm',  'DuplicateMirrorNormalX:=',
'0mm', 'DuplicateMirrorNormalY:=', ...
  '1mm',     'DuplicateMirrorNormalZ:=',     '0mm'},     {'NAME:Options',
'DuplicateAssignments:=', false});
invoke( Editor, 'DuplicateMirror', {'NAME:Selections', 'Selections:=',
...
  'Polyline2_2,Polyline2',       'NewPartsModelFlag:=',       'Model'},
{'NAME:DuplicateToMirrorParameters', 'DuplicateMirrorBaseX:=', ...
  '0mm',   'DuplicateMirrorBaseY:=',   '0mm',   'DuplicateMirrorBaseZ:=',
'0mm', 'DuplicateMirrorNormalX:=', ...
  '1mm', 'DuplicateMirrorNormalY:=', '0mm', 'DuplicateMirrorNormalZ:=',
'0mm'}, {'NAME:Options', 'DuplicateAssignments:=', false});
invoke(   Editor,   'Subtract',   {'NAME:Selections',   'Blank   Parts:=',
'Circle1', 'Tool Parts:=', ...
```

```
  'Polyline2,Polyline2_2,Polyline2_2_1,Polyline2_3'},
{'NAME:SubtractParameters', 'KeepOriginals:=', false});
invoke(        Editor,        'ChangeProperty',        {'NAME:AllTabs',
{'NAME:Geometry3DAttributeTab', {'NAME:PropServers', ...
  'Circle1'},     {'NAME:ChangedProps',     {'NAME:Name',     'Value:=',
'Stator'}}}});

%Inner
invoke(      Editor,      'CreateCircle',      {'NAME:CircleParameters',
'IsCovered:=', true, 'XCenter:=', ...
  '0mm', 'YCenter:=', '0mm', 'ZCenter:=', '0mm', 'Radius:=', 'R_s_in',
'WhichAxis:=', ...
  'Z', 'NumSegments:=', '0'}, {'NAME:Attributes', 'Name:=', 'Circle5',
'Flags:=', ...
  '',    'Color:=',    '(132    132    193)',    'Transparency:=',    0,
'PartCoordinateSystem:=', ...
  'Global',     'UDMId:=',     '',     'MaterialValue:=',     '"vacuum"',
'SolveInside:=', true});
invoke(        Editor,        'ChangeProperty',        {'NAME:AllTabs',
{'NAME:Geometry3DAttributeTab', {'NAME:PropServers', ...
  'Circle5'},     {'NAME:ChangedProps',     {'NAME:Name',     'Value:=',
'Inner'}}}});

%Rotor
invoke(      Editor,      'CreateCircle',      {'NAME:CircleParameters',
'IsCovered:=', true, 'XCenter:=', ...
  '0mm', 'YCenter:=', '0mm', 'ZCenter:=', '0mm', 'Radius:=', 'R_rotor',
'WhichAxis:=', ...
  'Z', 'NumSegments:=', '0'}, {'NAME:Attributes', 'Name:=', 'Circle5',
'Flags:=', ...
  '',    'Color:=',    '(132    132    193)',    'Transparency:=',    0,
'PartCoordinateSystem:=', ...
  'Global',     'UDMId:=',     '',     'MaterialValue:=',     '"vacuum"',
'SolveInside:=', true});
invoke(      Editor,      'CreateCircle',      {'NAME:CircleParameters',
'IsCovered:=', true, 'XCenter:=', ...
  '0mm', 'YCenter:=', '0mm', 'ZCenter:=', '0mm', 'Radius:=', 'R_shaft',
'WhichAxis:=', ...
  'Z', 'NumSegments:=', '0'}, {'NAME:Attributes', 'Name:=', 'Circle6',
'Flags:=', ...
  '',    'Color:=',    '(132    132    193)',    'Transparency:=',    0,
'PartCoordinateSystem:=', ...
  'Global',     'UDMId:=',     '',     'MaterialValue:=',     '"vacuum"',
'SolveInside:=', true});
invoke(  Editor,  'Subtract',  {'NAME:Selections',  'Blank  Parts:=',
'Circle5', 'Tool Parts:=', ...
  'Circle6'}, {'NAME:SubtractParameters', 'KeepOriginals:=', false});

invoke(    Editor,    'CreatePolyline',    {'NAME:PolylineParameters',
'IsPolylineCovered:=', true, 'IsPolylineClosed:=', ...
  false, {'NAME:PolylinePoints', {'NAME:PLPoint', ...
  'X:=', 'L2', 'Y:=', 'H2', 'Z:=', '0mm'}, {'NAME:PLPoint', ...
  'X:=', 'L3', 'Y:=', 'H3', 'Z:=', '0mm'}}, ...
  {'NAME:PolylineSegments', {'NAME:PLSegment', 'SegmentType:=', ...
  'Line',       'StartIndex:=',       0,       'NoOfPoints:=',       2}},
{'NAME:PolylineXSection', 'XSectionType:=', ...
```

```
  'None',   'XSectionOrient:=',   'Auto',   'XSectionWidth:=',   '0mm',
'XSectionTopWidth:=', ...
  '0mm',   'XSectionHeight:=',   '0mm',   'XSectionNumSegments:=',   '0',
'XSectionBendType:=', ...
  'Corner'}}, {'NAME:Attributes', 'Name:=', 'Polyline5', 'Flags:=', '',
'Color:=', ...
  '(132  132  193)',  'Transparency:=',  0,  'PartCoordinateSystem:=',
'Global', 'UDMId:=', ...
  '', 'MaterialValue:=', '"vacuum"', 'SolveInside:=', true});
invoke( Editor, 'DuplicateMirror', {'NAME:Selections', 'Selections:=',
'Polyline5', 'NewPartsModelFlag:=', ...
  'Model'},                        {'NAME:DuplicateToMirrorParameters',
'DuplicateMirrorBaseX:=', '0mm', 'DuplicateMirrorBaseY:=', ...
  '0mm',  'DuplicateMirrorBaseZ:=',  '0mm',  'DuplicateMirrorNormalX:=',
'0mm', 'DuplicateMirrorNormalY:=', ...
  '1mm',    'DuplicateMirrorNormalZ:=',    '0mm'},    {'NAME:Options',
'DuplicateAssignments:=',  false});
invoke(    Editor,    'CreatePolyline',    {'NAME:PolylineParameters',
'IsPolylineCovered:=', true, 'IsPolylineClosed:=', ...
  false, {'NAME:PolylinePoints', {'NAME:PLPoint', ...
  'X:=', 'L2', 'Y:=', 'H2', 'Z:=', '0mm'}, {'NAME:PLPoint', ...
  'X:=',  'R_backiron',  'Y:=',  '0mm',  'Z:=',  '0mm'},  {'NAME:PLPoint',
...
  'X:=', 'L2', 'Y:=', 'H2_N', 'Z:=', '0mm'}}, ...
  {'NAME:PolylineSegments', {'NAME:PLSegment', 'SegmentType:=', ...
  'AngularArc', 'StartIndex:=', 0, 'NoOfPoints:=', 3, 'NoOfSegments:=',
'0', 'ArcAngle:=', ...
  'Ang_r',    'ArcCenterX:=',    '0mm',    'ArcCenterY:=',    '0mm',
'ArcCenterZ:=', '0mm', 'ArcPlane:=', ...
  'XY'}},    {'NAME:PolylineXSection',    'XSectionType:=',    'None',
'XSectionOrient:=', ...
  'Auto',   'XSectionWidth:=',   '0mm',   'XSectionTopWidth:=',   '0mm',
'XSectionHeight:=', ...
  '0mm',    'XSectionNumSegments:=',    '0',    'XSectionBendType:=',
'Corner'}}, {'NAME:Attributes', 'Name:=', ...
  'Polyline6',   'Flags:=',   '',   'Color:=',   '(132   132   193)',
'Transparency:=', 0, 'PartCoordinateSystem:=', ...
  'Global',    'UDMId:=',    '',    'MaterialValue:=',    '"vacuum"',
'SolveInside:=', true});
invoke(    Editor,    'CreatePolyline',    {'NAME:PolylineParameters',
'IsPolylineCovered:=', true, 'IsPolylineClosed:=', ...
  false, {'NAME:PolylinePoints', {'NAME:PLPoint', ...
  'X:=', 'L3', 'Y:=', 'H3', 'Z:=', '0mm'}, {'NAME:PLPoint', ...
  'X:=', 'R_rotor', 'Y:=', '0mm', 'Z:=', '0mm'}, {'NAME:PLPoint', ...
  'X:=', 'L3', 'Y:=', 'H3_N', 'Z:=', '0mm'}}, ...
  {'NAME:PolylineSegments', {'NAME:PLSegment', 'SegmentType:=', ...
  'AngularArc', 'StartIndex:=', 0, 'NoOfPoints:=', 3, 'NoOfSegments:=',
'0', 'ArcAngle:=', ...
  'Ang_r',    'ArcCenterX:=',    '0mm',    'ArcCenterY:=',    '0mm',
'ArcCenterZ:=', '0mm', 'ArcPlane:=', ...
  'XY'}},    {'NAME:PolylineXSection',    'XSectionType:=',    'None',
'XSectionOrient:=', ...
  'Auto',   'XSectionWidth:=',   '0mm',   'XSectionTopWidth:=',   '0mm',
'XSectionHeight:=', ...
  '0mm',    'XSectionNumSegments:=',    '0',    'XSectionBendType:=',
'Corner'}}, {'NAME:Attributes', 'Name:=', ...
```

```
  'Polyline7',    'Flags:=',    '',    'Color:=',    '(132    132    193)',
'Transparency:=', 0, 'PartCoordinateSystem:=', ...
  'Global',     'UDMId:=',     '',     'MaterialValue:=',     '"vacuum"',
'SolveInside:=',  true});
invoke( Editor, 'Unite', {'NAME:Selections', 'Selections:=', ...
  'Polyline5,Polyline5_1,Polyline6,Polyline7'},
{'NAME:UniteParameters', 'KeepOriginals:=', false});
invoke(   Editor,   'CoverLines',   {'NAME:Selections',   'Selections:=',
'Polyline5', 'NewPartsModelFlag:=', 'Model'});
invoke( Editor, 'DuplicateMirror', {'NAME:Selections', 'Selections:=',
'Polyline5', 'NewPartsModelFlag:=', ...
  'Model'},                          {'NAME:DuplicateToMirrorParameters',
'DuplicateMirrorBaseX:=', '0mm', 'DuplicateMirrorBaseY:=', ...
  '0mm',  'DuplicateMirrorBaseZ:=',  '0mm',  'DuplicateMirrorNormalX:=',
'-1mm', 'DuplicateMirrorNormalY:=', ...
  '0mm',     'DuplicateMirrorNormalZ:=',     '0mm'},     {'NAME:Options',
'DuplicateAssignments:=', false});
invoke(   Editor,   'Subtract',   {'NAME:Selections',   'Blank   Parts:=',
'Circle5', 'Tool Parts:=', ...
  'Polyline5,Polyline5_2'},                  {'NAME:SubtractParameters',
'KeepOriginals:=', false});
invoke(        Editor,        'ChangeProperty',        {'NAME:AllTabs',
{'NAME:Geometry3DAttributeTab', {'NAME:PropServers', ...
  'Circle5'},    {'NAME:ChangedProps',    {'NAME:Material',    'Value:=',
'"steel_1008"'}}}});
invoke(        Editor,        'ChangeProperty',        {'NAME:AllTabs',
{'NAME:Geometry3DAttributeTab', {'NAME:PropServers', ...
  'Circle5'},     {'NAME:ChangedProps',     {'NAME:Name',     'Value:=',
'Rotor'}}}});

%Shaft
invoke(      Editor,      'CreateCircle',      {'NAME:CircleParameters',
'IsCovered:=', true, 'XCenter:=', ...
  '0mm', 'YCenter:=', '0mm', 'ZCenter:=', '0mm', 'Radius:=', 'R_shaft',
'WhichAxis:=', ...
  'Z', 'NumSegments:=', '0'}, {'NAME:Attributes', 'Name:=', 'Circle7',
'Flags:=', ...
  '',    'Color:=',    '(132    132    193)',    'Transparency:=',    0,
'PartCoordinateSystem:=', ...
  'Global',     'UDMId:=',     '',     'MaterialValue:=',     '"vacuum"',
'SolveInside:=', true});
invoke(        Editor,        'ChangeProperty',        {'NAME:AllTabs',
{'NAME:Geometry3DAttributeTab', {'NAME:PropServers', ...
  'Circle7'},     {'NAME:ChangedProps',     {'NAME:Name',     'Value:=',
'Shaft'}}}});

%Winding Phase A
invoke(     Editor,     'CreatePolyline',     {'NAME:PolylineParameters',
'IsPolylineCovered:=', true, 'IsPolylineClosed:=', ...
  true, {'NAME:PolylinePoints', {'NAME:PLPoint', ...
  'X:=', 'P1_X', 'Y:=', 'P1_Y', 'Z:=', '0mm'}, {'NAME:PLPoint', ...
  'X:=', 'P2_X', 'Y:=', 'P1_Y', 'Z:=', '0mm'}, {'NAME:PLPoint', ...
  'X:=', 'P3_X', 'Y:=', 'P3_Y', 'Z:=', '0mm'}, {'NAME:PLPoint', ...
  'X:=', 'P4_X', 'Y:=', 'P4_Y', 'Z:=', '0mm'}, {'NAME:PLPoint', ...
  'X:=',       'P1_X',       'Y:=',       'P1_Y',       'Z:=',       '0mm'}},
{'NAME:PolylineSegments', {'NAME:PLSegment', 'SegmentType:=', ...
```

```
  'Line',  'StartIndex:=',  0,  'NoOfPoints:=',  2},  {'NAME:PLSegment',
'SegmentType:=', ...
  'Line',  'StartIndex:=',  1,  'NoOfPoints:=',  2},  {'NAME:PLSegment',
'SegmentType:=', ...
  'Line',  'StartIndex:=',  2,  'NoOfPoints:=',  2},  {'NAME:PLSegment',
'SegmentType:=', ...
  'Line',       'StartIndex:=',       3,       'NoOfPoints:=',       2}},
{'NAME:PolylineXSection', 'XSectionType:=', ...
  'None',   'XSectionOrient:=',   'Auto',   'XSectionWidth:=',   '0mm',
'XSectionTopWidth:=', ...
  '0mm',   'XSectionHeight:=',   '0mm',   'XSectionNumSegments:=',   '0',
'XSectionBendType:=', ...
  'Corner'}}, {'NAME:Attributes', 'Name:=', 'Polyline8', 'Flags:=', '',
'Color:=', ...
  '(132  132  193)',  'Transparency:=',  0,  'PartCoordinateSystem:=',
'Global', 'UDMId:=', ...
  '', 'MaterialValue:=', '"vacuum"', 'SolveInside:=', true});

invoke(        Editor,        'ChangeProperty',        {'NAME:AllTabs',
{'NAME:Geometry3DAttributeTab', {'NAME:PropServers', ...
  'Polyline8'},   {'NAME:ChangedProps',   {'NAME:Material',   'Value:=',
'"copper"'}}}});
invoke(        Editor,        'ChangeProperty',        {'NAME:AllTabs',
{'NAME:Geometry3DAttributeTab', {'NAME:PropServers', ...
  'Polyline8'},    {'NAME:ChangedProps',    {'NAME:Name',    'Value:=',
'PhaseA1'}}}});
invoke( Editor, 'DuplicateMirror', {'NAME:Selections', 'Selections:=',
'PhaseA1', 'NewPartsModelFlag:=', ...
  'Model'},                        {'NAME:DuplicateToMirrorParameters',
'DuplicateMirrorBaseX:=', '0mm', 'DuplicateMirrorBaseY:=', ...
  '0mm',  'DuplicateMirrorBaseZ:=',  '0mm',  'DuplicateMirrorNormalX:=',
'0mm', 'DuplicateMirrorNormalY:=', ...
  '1mm',    'DuplicateMirrorNormalZ:=',    '0mm'},    {'NAME:Options',
'DuplicateAssignments:=', false});
invoke( Editor, 'DuplicateMirror', {'NAME:Selections', 'Selections:=',
'PhaseA1,PhaseA1_1', 'NewPartsModelFlag:=', ...
  'Model'},                        {'NAME:DuplicateToMirrorParameters',
'DuplicateMirrorBaseX:=', '0mm', 'DuplicateMirrorBaseY:=', ...
  '0mm',  'DuplicateMirrorBaseZ:=',  '0mm',  'DuplicateMirrorNormalX:=',
'1mm', 'DuplicateMirrorNormalY:=', ...
  '0mm',    'DuplicateMirrorNormalZ:=',    '0mm'},    {'NAME:Options',
'DuplicateAssignments:=', false});
invoke(        Editor,        'ChangeProperty',        {'NAME:AllTabs',
{'NAME:Geometry3DAttributeTab', {'NAME:PropServers', ...
  'PhaseA1_1_1'},   {'NAME:ChangedProps',   {'NAME:Name',   'Value:=',
'PhaseA2'}}}});
invoke(        Editor,        'ChangeProperty',        {'NAME:AllTabs',
{'NAME:Geometry3DAttributeTab', {'NAME:PropServers', ...
  'PhaseA1_2'},    {'NAME:ChangedProps',    {'NAME:Name',    'Value:=',
'PhaseA2_1'}}}});

%Phase B
invoke(     Editor,     'DuplicateAroundAxis',     {'NAME:Selections',
'Selections:=', 'PhaseA1', 'NewPartsModelFlag:=', ...
  'Model'},                       {'NAME:DuplicateAroundAxisParameters',
'CreateNewObjects:=', true, 'WhichAxis:=', ...
```

```
  'Z',  'AngleStr:=',  '90deg',  'NumClones:=',  '2'},  {'NAME:Options',
'DuplicateAssignments:=', false});
invoke(        Editor,        'ChangeProperty',        {'NAME:AllTabs',
{'NAME:Geometry3DAttributeTab', {'NAME:PropServers', ...
  'PhaseA1_2'},    {'NAME:ChangedProps',    {'NAME:Name',    'Value:=',
'PhaseB1'}}}});
invoke( Editor, 'DuplicateMirror', {'NAME:Selections', 'Selections:=',
'PhaseB1', 'NewPartsModelFlag:=', ...
  'Model'},                        {'NAME:DuplicateToMirrorParameters',
'DuplicateMirrorBaseX:=', '0mm', 'DuplicateMirrorBaseY:=', ...
  '0mm',  'DuplicateMirrorBaseZ:=',  '0mm',  'DuplicateMirrorNormalX:=',
'-1mm', 'DuplicateMirrorNormalY:=', ...
  '0mm',    'DuplicateMirrorNormalZ:=',    '0mm'},    {'NAME:Options',
'DuplicateAssignments:=', false});
invoke( Editor, 'DuplicateMirror', {'NAME:Selections', 'Selections:=',
'PhaseB1_1,PhaseB1', 'NewPartsModelFlag:=', ...
  'Model'},                        {'NAME:DuplicateToMirrorParameters',
'DuplicateMirrorBaseX:=', '0mm', 'DuplicateMirrorBaseY:=', ...
  '0mm',  'DuplicateMirrorBaseZ:=',  '0mm',  'DuplicateMirrorNormalX:=',
'0mm', 'DuplicateMirrorNormalY:=', ...
  '1mm',    'DuplicateMirrorNormalZ:=',    '0mm'},    {'NAME:Options',
'DuplicateAssignments:=', false});
invoke(        Editor,        'ChangeProperty',        {'NAME:AllTabs',
{'NAME:Geometry3DAttributeTab', {'NAME:PropServers', ...
  'PhaseB1_1_1'},    {'NAME:ChangedProps',    {'NAME:Name',    'Value:=',
'PhaseB2'}}}});
invoke(        Editor,        'ChangeProperty',        {'NAME:AllTabs',
{'NAME:Geometry3DAttributeTab', {'NAME:PropServers', ...
  'PhaseB1_2'},    {'NAME:ChangedProps',    {'NAME:Name',    'Value:=',
'PhaseB2_1'}}}});

%Winding Setup
Module = Design.GetModule('BoundarySetup');
invoke(    Module,    'AssignCoil',    {'NAME:PhaseA1',    'Objects:=',
{'PhaseA1'}, 'ParentBndID:=', ...
  'PhaseA',   'Conductor   number:=',   N_str,   'Winding:=',   'PhaseA',
'PolarityType:=', 'Positive'});
invoke(    Module,    'AssignCoil',    {'NAME:PhaseA1_1',    'Objects:=',
{'PhaseA1_1'}, 'ParentBndID:=', ...
  'PhaseA',   'Conductor   number:=',   N_str,   'Winding:=',   'PhaseA',
'PolarityType:=', 'Negative'});
invoke(    Module,    'AssignCoil',    {'NAME:PhaseA2_1',    'Objects:=',
{'PhaseA2_1'}, 'ParentBndID:=', ...
  'PhaseA',   'Conductor   number:=',   N_str,   'Winding:=',   'PhaseA',
'PolarityType:=', 'Positive'});
invoke(    Module,    'AssignCoil',    {'NAME:PhaseA2',    'Objects:=',
{'PhaseA2'}, 'ParentBndID:=', ...
  'PhaseA',   'Conductor   number:=',   N_str,   'Winding:=',   'PhaseA',
'PolarityType:=', 'Negative'});
invoke(    Module,    'AssignCoil',    {'NAME:PhaseB1',    'Objects:=',
{'PhaseB1'}, 'ParentBndID:=', ...
  'PhaseB',   'Conductor   number:=',   N_str,   'Winding:=',   'PhaseB',
'PolarityType:=', 'Positive'});
invoke(    Module,    'AssignCoil',    {'NAME:PhaseB1_1',    'Objects:=',
{'PhaseB1_1'}, 'ParentBndID:=', ...
```

```
  'PhaseB',  'Conductor  number:=',  N_str,  'Winding:=',  'PhaseB',
'PolarityType:=', 'Negative'});
invoke(   Module,   'AssignCoil',   {'NAME:PhaseB2_1',   'Objects:=',
{'PhaseB2_1'}, 'ParentBndID:=', ...
  'PhaseB',  'Conductor  number:=',  N_str,  'Winding:=',  'PhaseB',
'PolarityType:=', 'Positive'});
invoke(   Module,   'AssignCoil',   {'NAME:PhaseB2',   'Objects:=',
{'PhaseB2'}, 'ParentBndID:=', ...
  'PhaseB',  'Conductor  number:=',  N_str,  'Winding:=',  'PhaseB',
'PolarityType:=', 'Negative'});

%Motion Setup
Module = Design.GetModule('ModelSetup');
invoke( Module, 'AssignBand', {'NAME:Data', 'Move Type:=', 'Rotate',
'Coordinate System:=', ...
  'Global', 'Axis:=', 'Z', 'Is Positive:=', true, 'InitPos:=', '0deg',
'HasRotateLimit:=', ...
  false, 'NonCylindrical:=', false, 'Consider Mechanical Transient:=',
false, 'Angular Velocity:=', ...
  '10000rpm', 'Objects:=', {'Inner'}});

%Mesh Setup
Module = Design.GetModule('MeshSetup');
invoke( Module, 'AssignLengthOp', {'NAME:Length1', 'RefineInside:=',
false, 'Enabled:=', ...
  true, 'Objects:=', {'Rotor', 'Stator'}, 'RestrictElem:=', false,
'NumMaxElem:=', ...
  '1000', 'RestrictLength:=', true, 'MaxLength:=', '3mm'});
```

4. Constant current fed FEA simulation setup (ConstFEA.m)

```
Module = Design.GetModule('ModelSetup');

invoke(Design, 'ChangeProperty', {'NAME:AllTabs', {'NAME:Maxwell2D',
{'NAME:PropServers', ...
  'BoundarySetup:PhaseA'}, {'NAME:ChangedProps', {'NAME:Current',
'Value:=', Ip_str}}}});

invoke(Project, 'Save');
invoke(Design, 'AnalyzeAll');
```

5. Extract flux linkage calculation result (ExpFlux.m)

```
Module = Design.GetModule('ReportSetup');
invoke(Module,              'ExportToFile',              'FluxLinkage',
'//ad.gatech.edu/ecefs$/users/students/jdang3/Profile/Desktop/Opt_test_
4_2/Sweep_result/Flux.tab');
```

```
fid = fopen('Sweep_result\Flux.tab', 'r');
FF = textscan(fid, '%f%f%f%f', 16, 'headerlines', 1);

% First column is time
Time = FF{1,1};

% Column 2 to 3 are phase A B flux, here phase A flux is needed
Flux_A = FF{1,2};
```

6. Calculate current increase time (Angle_increase.m)

```
% load Flux_Ip
w = 10000;
wr = 2*pi*(w/60);
Vdc = 100;

if Time(2) >= 1000
    Time = Time/1000;
end

Time_step = Time(2)*1e-6;
Theta_step = Time_step*wr;

Flux = Flux_A;
Theta = Time*1e-6*wr;

Theta_on = 0;  % Timing
Theta_1_est = Theta_on;

% dfdtheta_Theta_mid1 = dfdtheta(1);
Flux_theta1 = Flux(1);

for i = 1:50
    Time_increase = Flux_theta1/Vdc;
    Theta_increase = Time_increase*wr;
    Theta_1 = Theta_on + Theta_increase;
    Flux_theta1 = interp1(Theta, Flux, Theta_1);
end
```

7. Calculate current decrease time (Angle_decrease.m)

```
% load Flux_Ip
w = 10000;
wr = 2*pi*(w/60);
Vdc = 100;

if Time(2) >= 1000
    Time = Time/1000;
```

```
end

Time_step = Time(2)*1e-6;
Theta_step = Time_step*wr;

Flux = Flux_A;
Theta = Time*1e-6*wr;

Theta_2 = Theta(length(Theta));  % Timing
Flux_theta2 = Flux(length(Flux));

Theta_off_est = Theta_2;
Flux_theta_off = Flux_theta2;


for i = 1:20
    Time_decrease = Flux_theta_off/Vdc;
    Theta_decrease = Time_decrease*wr;
    Theta_off = Theta_2 - Theta_decrease;
    Flux_theta_off = interp1(Theta, Flux, Theta_off);
end
```

8. Trapezoidal current profile fed FEA simulation setup (TrapFEA.m)

```
Module = Design.GetModule('ModelSetup');

Time_increase_str = strcat(num2str(Time_increase));
Time_decrease_str = strcat(num2str(Time_decrease));

invoke(Design,             'ChangeProperty',             {'NAME:AllTabs',
{'NAME:LocalVariableTab', {'NAME:PropServers', ...
'LocalVariables'},      {'NAME:ChangedProps',      {'NAME:Time_increase',
'Value:=', Time_increase_str}}}});
invoke(Design,             'ChangeProperty',             {'NAME:AllTabs',
{'NAME:LocalVariableTab', {'NAME:PropServers', ...
'LocalVariables'},      {'NAME:ChangedProps',      {'NAME:Time_decrease',
'Value:=', Time_decrease_str}}}});

invoke(Design,             'ChangeProperty',             {'NAME:AllTabs',
{'NAME:LocalVariableTab', {'NAME:PropServers', ...
  'LocalVariables'},     {'NAME:ChangedProps',     {'NAME:Time_increase',
'Value:=', ...
  Time_increase},  {'NAME:Time_decrease',  'Value:=',  Time_decrease}}}
);

invoke(Design,  'ChangeProperty',  {'NAME:AllTabs',  {'NAME:Maxwell2D',
{'NAME:PropServers', ...
  'BoundarySetup:PhaseA'},     {'NAME:ChangedProps',     {'NAME:Current',
'Value:=', ...
  'Ip*time/(Time_increase)*(time  <=  Time_increase)  +  Ip*((time  >
Time_increase)&&(time     <=     (Tstop-Time_decrease)))+     Ip*(Tstop-
time)/Time_decrease*(((Tstop-Time_decrease)  <  time)&&(time  <=  Tstop))'
}}}} );
```

```
invoke(Project, 'Save');
invoke(Design, 'AnalyzeAll');
```

9. Extract torque calculation result (ExpTorq.m)

```
Module = Design.GetModule('ReportSetup');
invoke(Module,                'ExportToFile',                'Torque',
'//ad.gatech.edu/ecefs$/users/students/jdang3/Profile/Desktop/Opt_test_
4_2/Sweep_result/Torque.tab');

fid = fopen('Sweep_result\Torque.tab', 'r');
FF = textscan(fid, '%f%f', 16, 'headerlines', 1);

Torque = FF{1,2};

torque = mean(Torque)*1e-3
```

10. After one iteration, delete the lamination (SaveData.m)

```
invoke(Editor, 'Delete', {'NAME:Selections', 'Selections:=', 'Rotor'});
invoke(Editor,     'Delete',     {'NAME:Selections',     'Selections:=',
'Stator'});
invoke(Editor, 'Delete', {'NAME:Selections', 'Selections:=', 'Inner'});
invoke(Editor, 'Delete', {'NAME:Selections', 'Selections:=', 'Outer'});
invoke(Editor, 'Delete', {'NAME:Selections', 'Selections:=', 'Shaft'});
invoke(Editor,     'Delete',     {'NAME:Selections',     'Selections:=',
'PhaseB2_1'});
invoke(Editor,     'Delete',     {'NAME:Selections',     'Selections:=',
'PhaseB2'});
invoke(Editor,     'Delete',     {'NAME:Selections',     'Selections:=',
'PhaseB1_1'});
invoke(Editor,     'Delete',     {'NAME:Selections',     'Selections:=',
'PhaseB1'});
invoke(Editor,     'Delete',     {'NAME:Selections',     'Selections:=',
'PhaseA2_1'});
invoke(Editor,     'Delete',     {'NAME:Selections',     'Selections:=',
'PhaseA2'});
invoke(Editor,     'Delete',     {'NAME:Selections',     'Selections:=',
'PhaseA1_1'});
invoke(Editor,     'Delete',     {'NAME:Selections',     'Selections:=',
'PhaseA1'});
```

APPENDIX C

12/8 SRM DESIGN AND OPTIMIZATION CODE

1. Main function (Main.m in Fig 7.22)

```
clc
clear all

iMaxwell = actxserver('AnsoftMaxwell.MaxwellScriptInterface');
Desktop = iMaxwell.GetAppDesktop();
Desktop.RestoreWindow
Project = Desktop.SetActiveProject('SRM_Andrew1');
Design = Project.SetActiveDesign('Maxwell2DDesign_Drawing');
Editor = Design.SetActiveEditor('3D Modeler');
DefinitionManager = Project.GetDefinitionManager();

% Geometry Parameter
R_shaft = 9;
N = 100;

for R_stator_in = 35:3:50
    R_rotor = R_stator_in - 0.5;
    H_tooth = 88.65 - R_stator_in - 8.65;

    for Beta_s = 15:3:24

        for Beta_r = 25:3:34


Draw

Slot_Area

ff = 0.3;
Jc = 5;
Ip = Jc*SA*ff/N;
Ip_str = strcat(num2str(Ip),'A');

% run 'Constant current simulation'
ConstFEA

% run 'flux data processing'
ExpFlux

% run 'current increase time calculation'
Angle_increase

% run 'current decrease time calculation'
Angle_decrease

% run 'trapezoidal current fed simulation'
TrapFEA
```

```
% run 'torque data processing'
ExpTorq

% after one interation, delete the lamination and redraw one
SaveData


        end
    end
end
```

2. Slot Area Calculation (Slot_Area.m)

```
% Slot Area Calculation
% R1: stator back iron & stator pole
R1    =    sqrt((R_stator_in*sin(Beta_s/2*pi/180))^2    +    (H_tooth    +
R_stator_in*cos(Beta_s/2*pi/180))^2);
R1_angle     =     atan((R_stator_in*sin(Beta_s/2*pi/180))/(H_tooth     +
R_stator_in*cos(Beta_s/2*pi/180)));

% Ring Area
RA = (R1^2 - R_stator_in^2)*pi/360*(30 - Beta_s);

% Fan-sector Area
FA_R1 = R1^2*pi/360*(Beta_s/2 - R1_angle/pi*180);
Triangle = H_tooth*R_stator_in*sin(Beta_s/2*pi/180)/2;
FA = FA_R1 - Triangle;

% Slot Area
SA = RA + FA*2;
```

3. Draw the lamination in Maxwell (Draw.m)

```
% Convert the geometry parameter to the string
R_s_in_str = strcat(num2str(R_stator_in),'mm');
R_r_str = strcat(num2str(R_rotor),'mm');
R_shaft_str = strcat(num2str(R_shaft),'mm');
H_tooth_str = strcat(num2str(H_tooth),'mm');
Beta_s_str = strcat(num2str(Beta_s),'deg');
Beta_r_str = strcat(num2str(Beta_r),'deg');
N_str = strcat(num2str(N));

invoke(        Design,        'ChangeProperty',        {'NAME:AllTabs',
{'NAME:LocalVariableTab', {'NAME:PropServers', ...
  'LocalVariables'},  {'NAME:ChangedProps',  {'NAME:R_rotor',  'Value:=',
R_r_str}}}});
invoke(        Design,        'ChangeProperty',        {'NAME:AllTabs',
{'NAME:LocalVariableTab', {'NAME:PropServers', ...
  'LocalVariables'},  {'NAME:ChangedProps',  {'NAME:R_s_in',  'Value:=',
R_s_in_str}}}});
```

```
invoke(        Design,        'ChangeProperty',        {'NAME:AllTabs',
{'NAME:LocalVariableTab', {'NAME:PropServers', ...
  'LocalVariables'}, {'NAME:ChangedProps', {'NAME:R_shaft', 'Value:=',
R_shaft_str}}}});
invoke(        Design,        'ChangeProperty',        {'NAME:AllTabs',
{'NAME:LocalVariableTab', {'NAME:PropServers', ...
  'LocalVariables'}, {'NAME:ChangedProps', {'NAME:H_tooth', 'Value:=',
H_tooth_str}}}});
invoke(        Design,        'ChangeProperty',        {'NAME:AllTabs',
{'NAME:LocalVariableTab', {'NAME:PropServers', ...
  'LocalVariables'}, {'NAME:ChangedProps', {'NAME:Beta_r', 'Value:=',
Beta_r_str}}}});
invoke(        Design,        'ChangeProperty',        {'NAME:AllTabs',
{'NAME:LocalVariableTab', {'NAME:PropServers', ...
  'LocalVariables'}, {'NAME:ChangedProps', {'NAME:Beta_s', 'Value:=',
Beta_s_str}}}});

% Stator
invoke(      Editor,      'CreateCircle',      {'NAME:CircleParameters',
'IsCovered:=', true, 'XCenter:=', ...
  '0mm', 'YCenter:=', '0mm', 'ZCenter:=', '0mm', 'Radius:=', '88.65mm',
'WhichAxis:=', ...
  'Z', 'NumSegments:=', '0'}, {'NAME:Attributes', 'Name:=', 'Circle1',
'Flags:=', ...
  '',    'Color:=',    '(132    132    193)',    'Transparency:=',    0,
'PartCoordinateSystem:=', ...
  'Global',     'UDMId:=',     '',     'MaterialValue:=',     '"vacuum"',
'SolveInside:=', true});

invoke(      Editor,      'CreateCircle',      {'NAME:CircleParameters',
'IsCovered:=', true, 'XCenter:=', ...
  '0mm', 'YCenter:=', '0mm', 'ZCenter:=', '0mm', 'Radius:=', 'R_s_in',
'WhichAxis:=', ...
  'Z', 'NumSegments:=', '0'}, {'NAME:Attributes', 'Name:=', 'Circle2',
'Flags:=', ...
  '',    'Color:=',    '(132    132    193)',    'Transparency:=',    0,
'PartCoordinateSystem:=', ...
  'Global',     'UDMId:=',     '',     'MaterialValue:=',     '"vacuum"',
'SolveInside:=', true});
invoke(  Editor,  'Subtract',  {'NAME:Selections',  'Blank  Parts:=',
'Circle1', 'Tool Parts:=', ...
  'Circle2'}, {'NAME:SubtractParameters', 'KeepOriginals:=', false});
invoke(    Editor,    'Copy',    {'NAME:Selections',    'Selections:=',
'Circle1'});
invoke( Editor, 'Paste');
invoke(        Editor,        'ChangeProperty',        {'NAME:AllTabs',
{'NAME:Geometry3DAttributeTab', {'NAME:PropServers', ...
  'Circle3'},     {'NAME:ChangedProps',     {'NAME:Name',     'Value:=',
'Outer'}}}});
invoke(        Editor,        'ChangeProperty',        {'NAME:AllTabs',
{'NAME:Geometry3DAttributeTab', {'NAME:PropServers', ...
  'Circle1'},    {'NAME:ChangedProps',    {'NAME:Material',    'Value:=',
'"steel_1008"'}}}});

invoke(    Editor,    'CreatePolyline',    {'NAME:PolylineParameters',
'IsPolylineCovered:=', true, 'IsPolylineClosed:=', ...
```

```
  false, {'NAME:PolylinePoints', {'NAME:PLPoint', ...
  'X:=', 'L1', 'Y:=', 'H1', 'Z:=', '0mm'}, {'NAME:PLPoint', ...
  'X:=', 'LL1', 'Y:=','H1', 'Z:=', '0mm'}}, {'NAME:PolylineSegments',
{'NAME:PLSegment', 'SegmentType:=', ...
  'Line', 'StartIndex:=', 0, 'NoOfPoints:=', 2}},
{'NAME:PolylineXSection', 'XSectionType:=', ...
  'None', 'XSectionOrient:=', 'Auto', 'XSectionWidth:=', '0mm',
'XSectionTopWidth:=', ...
  '0mm', 'XSectionHeight:=', '0mm', 'XSectionNumSegments:=', '0',
'XSectionBendType:=', ...
  'Corner'}}, {'NAME:Attributes', 'Name:=', 'Polyline2', 'Flags:=', '',
'Color:=', ...
  '(132 132 193)', 'Transparency:=', 0, 'PartCoordinateSystem:=',
'Global', 'UDMId:=', ...
  '', 'MaterialValue:=', '"vacuum"', 'SolveInside:=', true});
invoke( Editor, 'DuplicateMirror', {'NAME:Selections', 'Selections:=',
'Polyline2', 'NewPartsModelFlag:=', ...
  'Model'}, {'NAME:DuplicateToMirrorParameters',
'DuplicateMirrorBaseX:=', '0mm', 'DuplicateMirrorBaseY:=', ...
  '0mm', 'DuplicateMirrorBaseZ:=', '0mm', 'DuplicateMirrorNormalX:=',
'0mm', 'DuplicateMirrorNormalY:=', ...
  '1mm', 'DuplicateMirrorNormalZ:=', '0mm'}, {'NAME:Options',
'DuplicateAssignments:=', false});
invoke( Editor, 'Rotate', {'NAME:Selections', 'Selections:=',
'Polyline2_1', 'NewPartsModelFlag:=', ...
  'Model'}, {'NAME:RotateParameters', 'RotateAxis:=', 'Z',
'RotateAngle:=', '30deg'});
invoke( Editor, 'CreatePolyline', {'NAME:PolylineParameters',
'IsPolylineCovered:=', true, 'IsPolylineClosed:=', ...
  false, {'NAME:PolylinePoints', {'NAME:PLPoint', ...
  'X:=', 'H1', 'Y:=', 'L1', 'Z:=', '0mm'}, {'NAME:PLPoint', ...
  'X:=', 'L1_mid', 'Y:=', 'L1_mid', 'Z:=', '0mm'}, {'NAME:PLPoint', ...
  'X:=', 'L1', 'Y:=', 'H1', 'Z:=', '0mm'}}, {'NAME:PolylineSegments',
{'NAME:PLSegment', 'SegmentType:=', ...
  'AngularArc', 'StartIndex:=', 0, 'NoOfPoints:=', 3, 'NoOfSegments:=',
'0', 'ArcAngle:=', ...
  'Ang_s_in', 'ArcCenterX:=', '0mm', 'ArcCenterY:=', '0mm',
'ArcCenterZ:=', '0mm', 'ArcPlane:=', ...
  'XY'}}, {'NAME:PolylineXSection', 'XSectionType:=', 'None',
'XSectionOrient:=', ...
  'Auto', 'XSectionWidth:=', '0mm', 'XSectionTopWidth:=', '0mm',
'XSectionHeight:=', ...
  '0mm', 'XSectionNumSegments:=', '0', 'XSectionBendType:=',
'Corner'}}, {'NAME:Attributes', 'Name:=', ...
  'Polyline3', 'Flags:=', '', 'Color:=', '(132 132 193)',
'Transparency:=', 0, 'PartCoordinateSystem:=', ...
  'Global', 'UDMId:=', '', 'MaterialValue:=', '"vacuum"',
'SolveInside:=', true});
invoke( Editor, 'CreatePolyline', {'NAME:PolylineParameters',
'IsPolylineCovered:=', true, 'IsPolylineClosed:=', ...
  false, {'NAME:PolylinePoints', {'NAME:PLPoint', ...
  'X:=', 'H1', 'Y:=', 'LL1', 'Z:=', '0mm'}, {'NAME:PLPoint', ...
  'X:=', 'LL1_mid', 'Y:=', 'LL1_mid', 'Z:=', '0mm'}, {'NAME:PLPoint',
...
  'X:=', 'LL1', 'Y:=','H1', 'Z:=', '0mm'}}, {'NAME:PolylineSegments',
{'NAME:PLSegment', 'SegmentType:=', ...
```

```
  'AngularArc', 'StartIndex:=', 0, 'NoOfPoints:=', 3, 'NoOfSegments:=',
'0', 'ArcAngle:=', ...
  'Ang_s_out',    'ArcCenterX:=',    '0mm',    'ArcCenterY:=',    '0mm',
'ArcCenterZ:=', ...
  '0mm',      'ArcPlane:=',      'XY'}},      {'NAME:PolylineXSection',
'XSectionType:=', 'None', 'XSectionOrient:=', ...
  'Auto',   'XSectionWidth:=',   '0mm',   'XSectionTopWidth:=',   '0mm',
'XSectionHeight:=', ...
  '0mm',     'XSectionNumSegments:=',     '0',     'XSectionBendType:=',
'Corner'}}, {'NAME:Attributes', 'Name:=', ...
  'Polyline4',    'Flags:=',    '',    'Color:=',    '(132    132    193)',
'Transparency:=', 0, 'PartCoordinateSystem:=', ...
  'Global',     'UDMId:=',     '',     'MaterialValue:=',     '"vacuum"',
'SolveInside:=', true});
invoke(    Editor,    'Rotate',    {'NAME:Selections',    'Selections:=',
'Polyline3', 'NewPartsModelFlag:=', ...
  'Model'},      {'NAME:RotateParameters',      'RotateAxis:=',      'Z',
'RotateAngle:=', '-60deg'});
invoke(    Editor,    'Rotate',    {'NAME:Selections',    'Selections:=',
'Polyline4', 'NewPartsModelFlag:=', ...
  'Model'},      {'NAME:RotateParameters',      'RotateAxis:=',      'Z',
'RotateAngle:=', '-60deg'});
invoke( Editor, 'Unite', {'NAME:Selections', 'Selections:=', ...
  'Polyline2,Polyline2_1,Polyline3,Polyline4'},
{'NAME:UniteParameters', 'KeepOriginals:=', false});
invoke(   Editor,   'CoverLines',   {'NAME:Selections',   'Selections:=',
'Polyline2', 'NewPartsModelFlag:=', ...
  'Model'});
invoke(         Editor,         'ChangeProperty',         {'NAME:AllTabs',
{'NAME:Geometry3DAttributeTab', {'NAME:PropServers', ...
  'Polyline2'},    {'NAME:ChangedProps',    {'NAME:Material',    'Value:=',
'"copper"'}, {'NAME:Material', 'Value:=', ...
  '"steel_1008"'}}}});
invoke(      Editor,      'DuplicateAroundAxis',      {'NAME:Selections',
'Selections:=', 'Polyline2', 'NewPartsModelFlag:=', ...
  'Model'},                      {'NAME:DuplicateAroundAxisParameters',
'CreateNewObjects:=', true, 'WhichAxis:=', ...
  'Z',  'AngleStr:=',  '30deg',  'NumClones:=',  '12'},  {'NAME:Options',
'DuplicateAssignments:=', ...
  false});
invoke(   Editor,   'Subtract',   {'NAME:Selections',   'Blank   Parts:=',
'Circle1', 'Tool Parts:=', ...

'Polyline2,Polyline2_2,Polyline2_3,Polyline2_4,Polyline2_5,Polyline2_6,
Polyline2_7,Polyline2_8,Polyline2_9,Polyline2_10,Polyline2_11,Polyline2
_12'}, ...
  {'NAME:SubtractParameters', 'KeepOriginals:=', false});
invoke(         Editor,         'ChangeProperty',         {'NAME:AllTabs',
{'NAME:Geometry3DAttributeTab', {'NAME:PropServers', ...
  'Circle1'},     {'NAME:ChangedProps',     {'NAME:Name',     'Value:=',
'Stator'}}}});

%Inner
invoke(      Editor,      'CreateCircle',      {'NAME:CircleParameters',
'IsCovered:=', true, 'XCenter:=', ...
```

```
  '0mm', 'YCenter:=', '0mm', 'ZCenter:=', '0mm', 'Radius:=', 'R_s_in',
'WhichAxis:=', ...
  'Z', 'NumSegments:=', '0'}, {'NAME:Attributes', 'Name:=', 'Circle5',
'Flags:=', ...
  '',    'Color:=',    '(132    132    193)',    'Transparency:=',    0,
'PartCoordinateSystem:=', ...
  'Global',     'UDMId:=',     '',     'MaterialValue:=',     '"vacuum"',
'SolveInside:=', true});
invoke(        Editor,        'ChangeProperty',        {'NAME:AllTabs',
{'NAME:Geometry3DAttributeTab', {'NAME:PropServers', ...
  'Circle5'},     {'NAME:ChangedProps',     {'NAME:Name',     'Value:=',
'Inner'}}}});

%Rotor
invoke(Editor,       'CreatePolyline',       {'NAME:PolylineParameters',
'IsPolylineCovered:=', true, 'IsPolylineClosed:=', ...
  false, {'NAME:PolylinePoints', ...
  {'NAME:PLPoint', 'X:=', 'H3', 'Y:=', 'L3', 'Z:=', '0mm'}, ...
  {'NAME:PLPoint', 'X:=', 'H3', 'Y:=', 'L3_N', 'Z:=', '0mm'}}, ...
  {'NAME:PolylineSegments', {'NAME:PLSegment', 'SegmentType:=', ...
  'AngularArc', 'StartIndex:=', 0, 'NoOfPoints:=', 3, 'NoOfSegments:=',
'0', 'ArcAngle:=', ...
  '-Beta_r',     'ArcCenterX:=',     '0mm',     'ArcCenterY:=',     '0mm',
'ArcCenterZ:=', '0mm', 'ArcPlane:=', ...
  'XY'}},     {'NAME:PolylineXSection',     'XSectionType:=',     'None',
'XSectionOrient:=', ...
  'Auto',    'XSectionWidth:=',    '0mm',    'XSectionTopWidth:=',    '0mm',
'XSectionHeight:=', ...
  '0mm',     'XSectionNumSegments:=',     '0',     'XSectionBendType:=',
'Corner'}}, {'NAME:Attributes', 'Name:=', ...
  'Polyline5',    'Flags:=',    '',    'Color:=',    '(132    132    193)',
'Transparency:=', 0, 'PartCoordinateSystem:=', ...
  'Global',     'UDMId:=',     '',     'MaterialValue:=',     '"vacuum"',
'SolveInside:=', true});
invoke(Editor,  'DuplicateMirror',  {'NAME:Selections',  'Selections:=',
'Polyline5', 'NewPartsModelFlag:=', ...
  'Model'},                          {'NAME:DuplicateToMirrorParameters',
'DuplicateMirrorBaseX:=', '0mm', 'DuplicateMirrorBaseY:=', ...
  '0mm',  'DuplicateMirrorBaseZ:=',  '0mm',  'DuplicateMirrorNormalX:=',
'1mm', 'DuplicateMirrorNormalY:=', ...
  '0mm',     'DuplicateMirrorNormalZ:=',     '0mm'},     {'NAME:Options',
'DuplicateAssignments:=', false});
invoke(Editor,       'CreatePolyline',       {'NAME:PolylineParameters',
'IsPolylineCovered:=', true, 'IsPolylineClosed:=', ...
  false, {'NAME:PolylinePoints', ...
{'NAME:PLPoint', 'X:=', 'H3_N', 'Y:=', 'L3', 'Z:=', '0mm'},...
{'NAME:PLPoint', 'X:=', 'H3',   'Y:=', 'L3', 'Z:=', '0mm'}}, ...
{'NAME:PolylineSegments', {'NAME:PLSegment', 'SegmentType:=',  ...
  'Line',       'StartIndex:=',       0,       'NoOfPoints:=',       2}},
{'NAME:PolylineXSection', 'XSectionType:=', ...
  'None',    'XSectionOrient:=',    'Auto',    'XSectionWidth:=',    '0mm',
'XSectionTopWidth:=', ...
  '0mm',   'XSectionHeight:=',   '0mm',   'XSectionNumSegments:=',   '0',
'XSectionBendType:=', ...
  'Corner'}}, {'NAME:Attributes', 'Name:=', 'Polyline6', 'Flags:=', '',
'Color:=', ...
```

```
  '(132  132  193)',  'Transparency:=',  0,  'PartCoordinateSystem:=',
'Global', 'UDMId:=', ...
  '', 'MaterialValue:=', '"vacuum"', 'SolveInside:=', true});
invoke(Editor,       'CreatePolyline',       {'NAME:PolylineParameters',
'IsPolylineCovered:=', true, 'IsPolylineClosed:=', ...
  false, {'NAME:PolylinePoints', ...
{'NAME:PLPoint', 'X:=', 'H3_N', 'Y:=', 'L3_N',   'Z:=', '0mm'}, ...
{'NAME:PLPoint', 'X:=', 'H3',   'Y:=', 'L3_N', 'Z:=', '0mm'}}, ...
{'NAME:PolylineSegments', {'NAME:PLSegment', 'SegmentType:=',  ...
  'Line',       'StartIndex:=',       0,       'NoOfPoints:=',       2}},
{'NAME:PolylineXSection', 'XSectionType:=', ...
  'None',   'XSectionOrient:=',   'Auto',   'XSectionWidth:=',   '0mm',
'XSectionTopWidth:=', ...
  '0mm',   'XSectionHeight:=',   '0mm',   'XSectionNumSegments:=',   '0',
'XSectionBendType:=',...
  'Corner'}}, {'NAME:Attributes', 'Name:=', 'Polyline7', 'Flags:=', '',
'Color:=', ...
  '(132  132  193)',  'Transparency:=',  0,  'PartCoordinateSystem:=',
'Global', 'UDMId:=',  ...
  '', 'MaterialValue:=', '"vacuum"', 'SolveInside:=', true});
invoke(Editor, 'Unite', {'NAME:Selections', 'Selections:=', ...
  'Polyline5,Polyline5_1,Polyline6,Polyline7'},
{'NAME:UniteParameters', 'KeepOriginals:=', false});
invoke(Editor,    'CoverLines',    {'NAME:Selections',    'Selections:=',
'Polyline5', 'NewPartsModelFlag:=', 'Model'});
invoke(Editor,        'DuplicateAroundAxis',        {'NAME:Selections',
'Selections:=', 'Polyline5', 'NewPartsModelFlag:=', ...
  'Model'},                       {'NAME:DuplicateAroundAxisParameters',
'CreateNewObjects:=', true, 'WhichAxis:=', ...
  'Z',  'AngleStr:=',  '45deg',  'NumClones:=',  '4'},  {'NAME:Options',
'DuplicateAssignments:=', false});
invoke(Editor, 'Unite', {'NAME:Selections', 'Selections:=', ...
  'Polyline5,Polyline5_2,Polyline5_3,Polyline5_4'},
{'NAME:UniteParameters', 'KeepOriginals:=', false});
invoke(Editor, 'CreateCircle', {'NAME:CircleParameters', 'IsCovered:=',
true, 'XCenter:=',...
  '0mm',    'YCenter:=',    '0mm',    'ZCenter:=',    '0mm',    'Radius:=',
'R_backiron', 'WhichAxis:=', ...
  'Z', 'NumSegments:=', '0'}, {'NAME:Attributes', 'Name:=', 'Circle6',
'Flags:=',...
  '',    'Color:=',    '(132    132    193)',    'Transparency:=',    0,
'PartCoordinateSystem:=', ...
  'Global',     'UDMId:=',     '',     'MaterialValue:=',     '"vacuum"',
'SolveInside:=', true});
invoke(Editor,     'Unite',     {'NAME:Selections',     'Selections:=',
'Circle6,Polyline5'}, {'NAME:UniteParameters', 'KeepOriginals:=', ...
  false});
invoke(Editor, 'CreateCircle', {'NAME:CircleParameters', 'IsCovered:=',
true, 'XCenter:=', ...
  '0mm', 'YCenter:=', '0mm', 'ZCenter:=', '0mm', 'Radius:=', 'R_shaft',
'WhichAxis:=', ...
  'Z',    'NumSegments:=',    '0'},    {'NAME:Attributes',    'Name:=',
'Circle6_1', 'Flags:=',  ...
  '',    'Color:=',    '(132    132    193)',    'Transparency:=',    0,
'PartCoordinateSystem:=', ...
```

```
  'Global',     'UDMId:=',     '',     'MaterialValue:=',     '"vacuum"',
'SolveInside:=', true});
invoke(Editor,   'Subtract',   {'NAME:Selections',   'Blank   Parts:=',
'Circle6', 'Tool Parts:=',  ...
  'Circle6_1'}, {'NAME:SubtractParameters', 'KeepOriginals:=', false});
invoke(        Editor,        'ChangeProperty',        {'NAME:AllTabs',
{'NAME:Geometry3DAttributeTab', {'NAME:PropServers', ...
  'Circle6'},     {'NAME:ChangedProps',     {'NAME:Name',     'Value:=',
'Rotor'}}}});
invoke(        Editor,        'ChangeProperty',        {'NAME:AllTabs',
{'NAME:Geometry3DAttributeTab', {'NAME:PropServers', ...
  'Rotor'},    {'NAME:ChangedProps',    {'NAME:Material',    'Value:=',
'"steel_1008"'}}}});

%Shaft
invoke(      Editor,      'CreateCircle',      {'NAME:CircleParameters',
'IsCovered:=', true, 'XCenter:=', ...
  '0mm', 'YCenter:=', '0mm', 'ZCenter:=', '0mm', 'Radius:=', 'R_shaft',
'WhichAxis:=', ...
  'Z', 'NumSegments:=', '0'}, {'NAME:Attributes', 'Name:=', 'Circle7',
'Flags:=', ...
  '',    'Color:=',    '(132    132    193)',    'Transparency:=',    0,
'PartCoordinateSystem:=', ...
  'Global',     'UDMId:=',     '',     'MaterialValue:=',     '"vacuum"',
'SolveInside:=', true});
invoke(        Editor,        'ChangeProperty',        {'NAME:AllTabs',
{'NAME:Geometry3DAttributeTab', {'NAME:PropServers', ...
  'Circle7'},     {'NAME:ChangedProps',     {'NAME:Name',     'Value:=',
'Shaft'}}}});

%Winding Phase A
invoke(    Editor,    'CreatePolyline',    {'NAME:PolylineParameters',
'IsPolylineCovered:=', true, 'IsPolylineClosed:=', ...
  true, {'NAME:PolylinePoints', {'NAME:PLPoint', ...
  'X:=', 'P1_X', 'Y:=', 'P1_Y', 'Z:=', '0mm'}, {'NAME:PLPoint', ...
  'X:=', 'P2_X', 'Y:=', 'P1_Y', 'Z:=', '0mm'}, {'NAME:PLPoint', ...
  'X:=', 'P3_X', 'Y:=', 'P3_Y', 'Z:=', '0mm'}, {'NAME:PLPoint', ...
  'X:=', 'P4_X', 'Y:=', 'P4_Y', 'Z:=', '0mm'}, {'NAME:PLPoint', ...
  'X:=',      'P1_X',      'Y:=',      'P1_Y',      'Z:=',      '0mm'}},
{'NAME:PolylineSegments', {'NAME:PLSegment', 'SegmentType:=', ...
  'Line',  'StartIndex:=',  0,  'NoOfPoints:=',  2},  {'NAME:PLSegment',
'SegmentType:=', ...
  'Line',  'StartIndex:=',  1,  'NoOfPoints:=',  2},  {'NAME:PLSegment',
'SegmentType:=', ...
  'Line',  'StartIndex:=',  2,  'NoOfPoints:=',  2},  {'NAME:PLSegment',
'SegmentType:=', ...
  'Line',      'StartIndex:=',      3,      'NoOfPoints:=',      2}},
{'NAME:PolylineXSection', 'XSectionType:=', ...
  'None',   'XSectionOrient:=',   'Auto',   'XSectionWidth:=',   '0mm',
'XSectionTopWidth:=', ...
  '0mm',   'XSectionHeight:=',   '0mm',   'XSectionNumSegments:=',   '0',
'XSectionBendType:=', ...
  'Corner'}}, {'NAME:Attributes', 'Name:=', 'Polyline8', 'Flags:=', '',
'Color:=', ...
  '(132   132   193)',   'Transparency:=',   0,   'PartCoordinateSystem:=',
'Global', 'UDMId:=', ...
```

```
  '', 'MaterialValue:=', '"vacuum"', 'SolveInside:=', true});

invoke(        Editor,        'ChangeProperty',        {'NAME:AllTabs',
{'NAME:Geometry3DAttributeTab', {'NAME:PropServers', ...
  'Polyline8'},   {'NAME:ChangedProps',   {'NAME:Material',   'Value:=',
'"copper"'}}}}});
invoke(        Editor,        'ChangeProperty',        {'NAME:AllTabs',
{'NAME:Geometry3DAttributeTab', {'NAME:PropServers', ...
  'Polyline8'},    {'NAME:ChangedProps',    {'NAME:Name',    'Value:=',
'PhaseA'}}}});
invoke( Editor, 'DuplicateMirror', {'NAME:Selections', 'Selections:=',
'PhaseA', 'NewPartsModelFlag:=', ...
  'Model'},                        {'NAME:DuplicateToMirrorParameters',
'DuplicateMirrorBaseX:=', '0mm', 'DuplicateMirrorBaseY:=', ...
  '0mm',  'DuplicateMirrorBaseZ:=',  '0mm',  'DuplicateMirrorNormalX:=',
'0mm', 'DuplicateMirrorNormalY:=', ...
  '1mm',    'DuplicateMirrorNormalZ:=',    '0mm'},    {'NAME:Options',
'DuplicateAssignments:=', false});
invoke(     Editor,     'DuplicateAroundAxis',     {'NAME:Selections',
'Selections:=', 'PhaseA,PhaseA_1', 'NewPartsModelFlag:=', ...
  'Model'},                       {'NAME:DuplicateAroundAxisParameters',
'CreateNewObjects:=', true, 'WhichAxis:=', ...
  'Z',  'AngleStr:=',  '90deg',  'NumClones:=',  '4'},  {'NAME:Options',
'DuplicateAssignments:=', ...
  false});
invoke(        Editor,        'ChangeProperty',        {'NAME:AllTabs',
{'NAME:Geometry3DAttributeTab', {'NAME:PropServers', ...
  'PhaseA_1_1'},    {'NAME:ChangedProps',    {'NAME:Name',    'Value:=',
'PhaseA2_1'}}}});
invoke(        Editor,        'ChangeProperty',        {'NAME:AllTabs',
{'NAME:Geometry3DAttributeTab', {'NAME:PropServers', ...
  'PhaseA_1_2'},    {'NAME:ChangedProps',    {'NAME:Name',    'Value:=',
'PhaseA3_1'}}}});
invoke(        Editor,        'ChangeProperty',        {'NAME:AllTabs',
{'NAME:Geometry3DAttributeTab', {'NAME:PropServers', ...
  'PhaseA_1_3'},    {'NAME:ChangedProps',    {'NAME:Name',    'Value:=',
'PhaseA4_1'}}}});

%Phase B
invoke(     Editor,     'DuplicateAroundAxis',     {'NAME:Selections',
'Selections:=', 'PhaseA,PhaseA_1', 'NewPartsModelFlag:=', ...
  'Model'},                       {'NAME:DuplicateAroundAxisParameters',
'CreateNewObjects:=', true, 'WhichAxis:=', ...
  'Z',  'AngleStr:=',  '60deg',  'NumClones:=',  '2'},  {'NAME:Options',
'DuplicateAssignments:=', false});
invoke(        Editor,        'ChangeProperty',        {'NAME:AllTabs',
{'NAME:Geometry3DAttributeTab', {'NAME:PropServers', ...
  'PhaseA_5'},    {'NAME:ChangedProps',    {'NAME:Name',    'Value:=',
'PhaseB'}}}});
invoke(        Editor,        'ChangeProperty',        {'NAME:AllTabs',
{'NAME:Geometry3DAttributeTab', {'NAME:PropServers', ...
  'PhaseA_1_1'},    {'NAME:ChangedProps',    {'NAME:Name',    'Value:=',
'PhaseB_1'}}}});
invoke(     Editor,     'DuplicateAroundAxis',     {'NAME:Selections',
'Selections:=', 'PhaseB,PhaseB_1', 'NewPartsModelFlag:=', ...
```

```
  'Model'},                          {'NAME:DuplicateAroundAxisParameters',
'CreateNewObjects:=', true, 'WhichAxis:=', ...
  'Z',  'AngleStr:=',  '90deg',  'NumClones:=',  '4'},  {'NAME:Options',
'DuplicateAssignments:=', ...
  false});
invoke(         Editor,         'ChangeProperty',         {'NAME:AllTabs',
{'NAME:Geometry3DAttributeTab', {'NAME:PropServers', ...
  'PhaseB_1_1'},    {'NAME:ChangedProps',    {'NAME:Name',    'Value:=',
'PhaseB2_1'}}}});
invoke(         Editor,         'ChangeProperty',         {'NAME:AllTabs',
{'NAME:Geometry3DAttributeTab', {'NAME:PropServers', ...
  'PhaseB_1_2'},    {'NAME:ChangedProps',    {'NAME:Name',    'Value:=',
'PhaseB3_1'}}}});
invoke(         Editor,         'ChangeProperty',         {'NAME:AllTabs',
{'NAME:Geometry3DAttributeTab', {'NAME:PropServers', ...
  'PhaseB_1_3'},    {'NAME:ChangedProps',    {'NAME:Name',    'Value:=',
'PhaseB4_1'}}}});

%Phase C
invoke(     Editor,      'DuplicateAroundAxis',      {'NAME:Selections',
'Selections:=', 'PhaseB,PhaseB_1', 'NewPartsModelFlag:=', ...
  'Model'},                          {'NAME:DuplicateAroundAxisParameters',
'CreateNewObjects:=', true, 'WhichAxis:=', ...
  'Z',  'AngleStr:=',  '60deg',  'NumClones:=',  '2'},  {'NAME:Options',
'DuplicateAssignments:=', false});
invoke(         Editor,         'ChangeProperty',         {'NAME:AllTabs',
{'NAME:Geometry3DAttributeTab', {'NAME:PropServers', ...
  'PhaseB_5'},     {'NAME:ChangedProps',     {'NAME:Name',     'Value:=',
'PhaseC'}}}});
invoke(         Editor,         'ChangeProperty',         {'NAME:AllTabs',
{'NAME:Geometry3DAttributeTab', {'NAME:PropServers', ...
  'PhaseB_1_1'},    {'NAME:ChangedProps',    {'NAME:Name',    'Value:=',
'PhaseC_1'}}}});
invoke(     Editor,      'DuplicateAroundAxis',      {'NAME:Selections',
'Selections:=', 'PhaseC,PhaseC_1', 'NewPartsModelFlag:=', ...
  'Model'},                          {'NAME:DuplicateAroundAxisParameters',
'CreateNewObjects:=', true, 'WhichAxis:=', ...
  'Z',  'AngleStr:=',  '90deg',  'NumClones:=',  '4'},  {'NAME:Options',
'DuplicateAssignments:=', ...
  false});
invoke(         Editor,         'ChangeProperty',         {'NAME:AllTabs',
{'NAME:Geometry3DAttributeTab', {'NAME:PropServers', ...
  'PhaseC_1_1'},    {'NAME:ChangedProps',    {'NAME:Name',    'Value:=',
'PhaseC2_1'}}}});
invoke(         Editor,         'ChangeProperty',         {'NAME:AllTabs',
{'NAME:Geometry3DAttributeTab', {'NAME:PropServers', ...
  'PhaseC_1_2'},    {'NAME:ChangedProps',    {'NAME:Name',    'Value:=',
'PhaseC3_1'}}}});
invoke(         Editor,         'ChangeProperty',         {'NAME:AllTabs',
{'NAME:Geometry3DAttributeTab', {'NAME:PropServers', ...
  'PhaseC_1_3'},    {'NAME:ChangedProps',    {'NAME:Name',    'Value:=',
'PhaseC4_1'}}}});

%Winding Setup
Module = Design.GetModule('BoundarySetup');
```

```
invoke(    Module,    'AssignCoil',    {'NAME:PhaseA1',    'Objects:=',
{'PhaseA_1'}, 'ParentBndID:=', ...
  'PhaseA',   'Conductor   number:=',   N_str,   'Winding:=',   'PhaseA',
'PolarityType:=', 'Positive'});
invoke(    Module,    'AssignCoil',    {'NAME:PhaseA1_1',    'Objects:=',
{'PhaseA'}, 'ParentBndID:=', ...
  'PhaseA',   'Conductor   number:=',   N_str,   'Winding:=',   'PhaseA',
'PolarityType:=', 'Negative'});
invoke(    Module,    'AssignCoil',    {'NAME:PhaseA2_1',    'Objects:=',
{'PhaseA2_1'}, 'ParentBndID:=', ...
  'PhaseA',   'Conductor   number:=',   N_str,   'Winding:=',   'PhaseA',
'PolarityType:=', 'Positive'});
invoke(    Module,    'AssignCoil',    {'NAME:PhaseA2',    'Objects:=',
{'PhaseA_2'}, 'ParentBndID:=', ...
  'PhaseA',   'Conductor   number:=',   N_str,   'Winding:=',   'PhaseA',
'PolarityType:=', 'Negative'});
invoke(    Module,    'AssignCoil',    {'NAME:PhaseA3_1',    'Objects:=',
{'PhaseA3_1'}, 'ParentBndID:=', ...
  'PhaseA',   'Conductor   number:=',   N_str,   'Winding:=',   'PhaseA',
'PolarityType:=', 'Positive'});
invoke(    Module,    'AssignCoil',    {'NAME:PhaseA3',    'Objects:=',
{'PhaseA_3'}, 'ParentBndID:=', ...
  'PhaseA',   'Conductor   number:=',   N_str,   'Winding:=',   'PhaseA',
'PolarityType:=', 'Negative'});
invoke(    Module,    'AssignCoil',    {'NAME:PhaseA4_1',    'Objects:=',
{'PhaseA4_1'}, 'ParentBndID:=', ...
  'PhaseA',   'Conductor   number:=',   N_str,   'Winding:=',   'PhaseA',
'PolarityType:=', 'Positive'});
invoke(    Module,    'AssignCoil',    {'NAME:PhaseA4',    'Objects:=',
{'PhaseA_4'}, 'ParentBndID:=', ...
  'PhaseA',   'Conductor   number:=',   N_str,   'Winding:=',   'PhaseA',
'PolarityType:=', 'Negative'});

invoke(    Module,    'AssignCoil',    {'NAME:PhaseB1',    'Objects:=',
{'PhaseB_1'}, 'ParentBndID:=', ...
  'PhaseB',   'Conductor   number:=',   N_str,   'Winding:=',   'PhaseB',
'PolarityType:=', 'Positive'});
invoke(    Module,    'AssignCoil',    {'NAME:PhaseB1_1',    'Objects:=',
{'PhaseB'}, 'ParentBndID:=', ...
  'PhaseB',   'Conductor   number:=',   N_str,   'Winding:=',   'PhaseB',
'PolarityType:=', 'Negative'});
invoke(    Module,    'AssignCoil',    {'NAME:PhaseB2_1',    'Objects:=',
{'PhaseB2_1'}, 'ParentBndID:=', ...
  'PhaseB',   'Conductor   number:=',   N_str,   'Winding:=',   'PhaseB',
'PolarityType:=', 'Positive'});
invoke(    Module,    'AssignCoil',    {'NAME:PhaseB2',    'Objects:=',
{'PhaseB_2'}, 'ParentBndID:=', ...
  'PhaseB',   'Conductor   number:=',   N_str,   'Winding:=',   'PhaseB',
'PolarityType:=', 'Negative'});
invoke(    Module,    'AssignCoil',    {'NAME:PhaseB3_1',    'Objects:=',
{'PhaseB3_1'}, 'ParentBndID:=', ...
  'PhaseB',   'Conductor   number:=',   N_str,   'Winding:=',   'PhaseB',
'PolarityType:=', 'Positive'});
invoke(    Module,    'AssignCoil',    {'NAME:PhaseB3',    'Objects:=',
{'PhaseB_3'}, 'ParentBndID:=', ...
```

```
  'PhaseB',   'Conductor   number:=',   N_str,   'Winding:=',   'PhaseB',
'PolarityType:=', 'Negative'});
invoke(    Module,    'AssignCoil',    {'NAME:PhaseB4_1',    'Objects:=',
{'PhaseB4_1'}, 'ParentBndID:=', ...
  'PhaseB',   'Conductor   number:=',   N_str,   'Winding:=',   'PhaseB',
'PolarityType:=', 'Positive'});
invoke(    Module,    'AssignCoil',     {'NAME:PhaseB4',    'Objects:=',
{'PhaseB_4'}, 'ParentBndID:=', ...
  'PhaseB',   'Conductor   number:=',   N_str,   'Winding:=',   'PhaseB',
'PolarityType:=', 'Negative'});

invoke(    Module,    'AssignCoil',     {'NAME:PhaseC1',    'Objects:=',
{'PhaseC_1'}, 'ParentBndID:=', ...
  'PhaseC',   'Conductor   number:=',   N_str,   'Winding:=',   'PhaseC',
'PolarityType:=', 'Positive'});
invoke(    Module,    'AssignCoil',    {'NAME:PhaseC1_1',    'Objects:=',
{'PhaseC'}, 'ParentBndID:=', ...
  'PhaseC',   'Conductor   number:=',   N_str,   'Winding:=',   'PhaseC',
'PolarityType:=', 'Negative'});
invoke(    Module,    'AssignCoil',    {'NAME:PhaseC2_1',    'Objects:=',
{'PhaseC2_1'}, 'ParentBndID:=', ...
  'PhaseC',   'Conductor   number:=',   N_str,   'Winding:=',   'PhaseC',
'PolarityType:=', 'Positive'});
invoke(    Module,    'AssignCoil',     {'NAME:PhaseC2',    'Objects:=',
{'PhaseC_2'}, 'ParentBndID:=', ...
  'PhaseC',   'Conductor   number:=',   N_str,   'Winding:=',   'PhaseC',
'PolarityType:=', 'Negative'});
invoke(    Module,    'AssignCoil',    {'NAME:PhaseC3_1',    'Objects:=',
{'PhaseC3_1'}, 'ParentBndID:=', ...
  'PhaseC',   'Conductor   number:=',   N_str,   'Winding:=',   'PhaseC',
'PolarityType:=', 'Positive'});
invoke(    Module,    'AssignCoil',     {'NAME:PhaseC3',    'Objects:=',
{'PhaseC_3'}, 'ParentBndID:=', ...
  'PhaseC',   'Conductor   number:=',   N_str,   'Winding:=',   'PhaseC',
'PolarityType:=', 'Negative'});
invoke(    Module,    'AssignCoil',    {'NAME:PhaseC4_1',    'Objects:=',
{'PhaseC4_1'}, 'ParentBndID:=', ...
  'PhaseC',   'Conductor   number:=',   N_str,   'Winding:=',   'PhaseC',
'PolarityType:=', 'Positive'});
invoke(    Module,    'AssignCoil',     {'NAME:PhaseC4',    'Objects:=',
{'PhaseC_4'}, 'ParentBndID:=', ...
  'PhaseC',   'Conductor   number:=',   N_str,   'Winding:=',   'PhaseC',
'PolarityType:=', 'Negative'});

%Motion Setup
Module = Design.GetModule('ModelSetup');
invoke(  Module,  'AssignBand',  {'NAME:Data',  'Move  Type:=',  'Rotate',
'Coordinate System:=', ...
  'Global', 'Axis:=', 'Z', 'Is Positive:=', true, 'InitPos:=', '0deg',
'HasRotateLimit:=', ...
  false, 'NonCylindrical:=', false, 'Consider Mechanical Transient:=',
false, 'Angular Velocity:=', ...
  '2000rpm', 'Objects:=', {'Inner'}});

%Mesh Setup
Module = Design.GetModule('MeshSetup');
```

```
invoke( Module, 'AssignLengthOp', {'NAME:Length1', 'RefineInside:=',
false, 'Enabled:=', ...
  true, 'Objects:=', {'Rotor', 'Stator'}, 'RestrictElem:=', false,
'NumMaxElem:=', ...
  '1000', 'RestrictLength:=', true, 'MaxLength:=', '3mm'});
```

4. Constant current fed FEA simulation setup (ConstFEA.m)

```
Module = Design.GetModule('ModelSetup');

invoke( Design, 'ChangeProperty', {'NAME:AllTabs',
{'NAME:LocalVariableTab', {'NAME:PropServers', ...
  'LocalVariables'}, {'NAME:ChangedProps', {'NAME:Ip', 'Value:=',
Ip_str}}}});

invoke(Design, 'ChangeProperty', {'NAME:AllTabs', {'NAME:Maxwell2D',
{'NAME:PropServers', ...
  'BoundarySetup:PhaseB'}, {'NAME:ChangedProps', {'NAME:Current',
'Value:=', 'Ip'}}}} );

invoke(Design, 'ChangeProperty', {'NAME:AllTabs', {'NAME:Maxwell2D',
{'NAME:PropServers', ...
  'BoundarySetup:PhaseC'}, {'NAME:ChangedProps', {'NAME:Current',
'Value:=', 0}}}} );

invoke(Project, 'Save');
invoke(Design, 'AnalyzeAll');
```

5. Extract flux linkage calculation result (ExpFlux.m)

```
Module = Design.GetModule('ReportSetup');
invoke(Module, 'ExportToFile', 'FluxLinkage',
'\\ad.gatech.edu\ecefs$\users\students\jdang3\Profile\Desktop\Opt_test_
12_8 _Overlap\Sweep_result\Flux.tab');

fid = fopen('Sweep_result\Flux.tab', 'r');
FF = textscan(fid, '%f%f%f%f', 16, 'headerlines', 1);

% First column is time
Time = FF{1,1};

% Column 2 to 4 are phase A B C flux, here phase B flux is needed
Flux_A = FF{1,2};
Flux_B = FF{1,3};
Flux_C = FF{1,4};
```

6. Calculate current increase time (Angle_increase.m)

```
% load Flux_Ip
w = 2000;
wr = 2*pi*(w/60);
Vdc = 350;

if Time(2) >= 1000
    Time = Time/1000;
end

Time_step = Time(2)*1e-6;
Theta_step = Time_step*wr;

Inc = [];
for i = 1:16
    Inc(i)   =   Flux_C(i)/Vdc   -   Time(i)/1e6   -   (Flux_B(1)/Vdc   -
Time(16)/1e6);
end

Time_increase = (Time(16) - interp1(Inc, Time, 0))/1e6;
```

7. Calculate current decrease time (Angle_decrease.m)

```
% load Flux_Ip
w = 2000;
wr = 2*pi*(w/60);
Vdc = 350;

if Time(2) >= 1000
    Time = Time/1000;
end

Time_step = Time(2)*1e-6;
Theta_step = Time_step*wr;

Dec = [];
for i = 1:16
    Dec(i)   =   Flux_B(i)/Vdc   +   Time(i)/1e6   -   (Flux_A(1)/Vdc   +
Time(16)/1e6);
end

Time_decrease = interp1(Dec, Time, 0)/1e6;
```

8. Trapezoidal current profile fed FEA simulation setup (TrapFEA.m)

```
Module = Design.GetModule('ModelSetup');
```

```
Time_increase_str = strcat(num2str(Time_increase));
Time_decrease_str = strcat(num2str(Time_decrease));

invoke(Design,            'ChangeProperty',            {'NAME:AllTabs',
{'NAME:LocalVariableTab', {'NAME:PropServers', ...
'LocalVariables'},      {'NAME:ChangedProps',      {'NAME:Time_increase',
'Value:=', Time_increase_str}}}});
invoke(Design,            'ChangeProperty',            {'NAME:AllTabs',
{'NAME:LocalVariableTab', {'NAME:PropServers', ...
'LocalVariables'},      {'NAME:ChangedProps',      {'NAME:Time_decrease',
'Value:=', Time_decrease_str}}}});

invoke(Design,            'ChangeProperty',            {'NAME:AllTabs',
{'NAME:LocalVariableTab', {'NAME:PropServers', ...
  'LocalVariables'},     {'NAME:ChangedProps',     {'NAME:Time_increase',
'Value:=', ...
  Time_increase},  {'NAME:Time_decrease',  'Value:=',  Time_decrease}}}}
);

invoke(Design,  'ChangeProperty',  {'NAME:AllTabs',  {'NAME:Maxwell2D',
{'NAME:PropServers', ...
  'BoundarySetup:PhaseB'},     {'NAME:ChangedProps',     {'NAME:Current',
'Value:=', ...
  'Ip*(time     <=     Time_decrease)     +     Ip*(Tstop-time)/(Tstop-
Time_decrease)*((Time_decrease < time)&&(time <= Tstop))' }}}} );

invoke(Design,  'ChangeProperty',  {'NAME:AllTabs',  {'NAME:Maxwell2D',
{'NAME:PropServers', ...
  'BoundarySetup:PhaseC'},     {'NAME:ChangedProps',     {'NAME:Current',
'Value:=', ...
  'Ip*(Time_increase - (Tstop - time))/Time_increase*(time >= (Tstop -
Time_increase))' }}}} );

invoke(Project, 'Save');
invoke(Design, 'AnalyzeAll');
```

9. Extract torque calculation result (ExpTorq.m)

```
Module = Design.GetModule('ReportSetup');
invoke(Module,                'ExportToFile',                'Torque',
'\\ad.gatech.edu\ecefs$\users\students\jdang3\Profile\Desktop\Opt_test_
12_8 _Overlap/Sweep_result/Torque.tab');

fid = fopen('Sweep_result\Torque.tab', 'r');
FF = textscan(fid, '%f%f', 16, 'headerlines', 1);

Torque = FF{1,2};

torque = mean(Torque)
```

10. After one iteration, delete the lamination (SaveData.m)

```
invoke(Editor, 'Delete', {'NAME:Selections', 'Selections:=', 'Rotor'});
invoke(Editor,     'Delete',     {'NAME:Selections',     'Selections:=',
'Stator'});
invoke(Editor, 'Delete', {'NAME:Selections', 'Selections:=', 'Inner'});
invoke(Editor, 'Delete', {'NAME:Selections', 'Selections:=', 'Outer'});
invoke(Editor, 'Delete', {'NAME:Selections', 'Selections:=', 'Shaft'});
invoke(Editor,     'Delete',     {'NAME:Selections',     'Selections:=',
'PhaseA'});
invoke(Editor,     'Delete',     {'NAME:Selections',     'Selections:=',
'PhaseA_1'});
invoke(Editor,     'Delete',     {'NAME:Selections',     'Selections:=',
'PhaseA_2'});
invoke(Editor,     'Delete',     {'NAME:Selections',     'Selections:=',
'PhaseA2_1'});
invoke(Editor,     'Delete',     {'NAME:Selections',     'Selections:=',
'PhaseA_3'});
invoke(Editor,     'Delete',     {'NAME:Selections',     'Selections:=',
'PhaseA3_1'});
invoke(Editor,     'Delete',     {'NAME:Selections',     'Selections:=',
'PhaseA_4'});
invoke(Editor,     'Delete',     {'NAME:Selections',     'Selections:=',
'PhaseA4_1'});
invoke(Editor,     'Delete',     {'NAME:Selections',     'Selections:=',
'PhaseB'});
invoke(Editor,     'Delete',     {'NAME:Selections',     'Selections:=',
'PhaseB_1'});
invoke(Editor,     'Delete',     {'NAME:Selections',     'Selections:=',
'PhaseB_2'});
invoke(Editor,     'Delete',     {'NAME:Selections',     'Selections:=',
'PhaseB2_1'});
invoke(Editor,     'Delete',     {'NAME:Selections',     'Selections:=',
'PhaseB_3'});
invoke(Editor,     'Delete',     {'NAME:Selections',     'Selections:=',
'PhaseB3_1'});
invoke(Editor,     'Delete',     {'NAME:Selections',     'Selections:=',
'PhaseB_4'});
invoke(Editor,     'Delete',     {'NAME:Selections',     'Selections:=',
'PhaseB4_1'});
invoke(Editor,     'Delete',     {'NAME:Selections',     'Selections:=',
'PhaseC'});
invoke(Editor,     'Delete',     {'NAME:Selections',     'Selections:=',
'PhaseC_1'});
invoke(Editor,     'Delete',     {'NAME:Selections',     'Selections:=',
'PhaseC_2'});
invoke(Editor,     'Delete',     {'NAME:Selections',     'Selections:=',
'PhaseC2_1'});
invoke(Editor,     'Delete',     {'NAME:Selections',     'Selections:=',
'PhaseC_3'});
invoke(Editor,     'Delete',     {'NAME:Selections',     'Selections:=',
'PhaseC3_1'});
invoke(Editor,     'Delete',     {'NAME:Selections',     'Selections:=',
'PhaseC_4'});
```

```
INVOKE(EDITOR, 'DELETE', {'NAME:SELECTIONS', 'SELECTIONS:=',
                          'PHASEC4_1'});
```

BIBLIOGRAPHY

[1] I. Takahashi, T. Koganezawa, G. Su, and K. Ohyama, "A super high speed PM motor drive system by a quasi-current source inverter," IEEE Trans. Ind. Appl., vol. 30, no. 3, pp. 683–690, May/Jun. 1994.

[2] (2008). [Online]. Available: http://www.westwind-airbearings.com/specialist/waferGrinding

[3] (2008). [Online]. Available: http://www.westwind-airbearings.com/pcb/overview

[4] M. Kauf. (2002, Jan.). Microvia formation: Technology and cost comparison [Online]. Available: http://www.circuitree.com. (URL)

[5] (2008). [Online]. Available: http://www.sirona.com/ecomaXL/index.php?site=SIRONA_ COM_s_and_c_handpieces

[6] (2008). [Online]. Available: http://www.miti.cc/

[7] J. R. Bumpy, E. S. Spooner, J. Carter, H. Tennant, G. G. Mego, G. Dellora, W. Gstrein, H. Sutter, and J. Wagner, "Electrical machines for use in electrically assisted turbochargers," in Proc. Power Electron., Mach. Drives Conf., Apr. 2004, vol. 1, pp. 344–349.

[8] I. Kolmanovsky and A. G. Stefanopoulou, "Evaluation of turbocharger power assist system using optimal control techniques," presented at the Society of Automotive Engineers (SAE) World Congress, Detroit, MI, Mar. 2000, SAE Paper 2000-01-0519.

[9] S.M ünz,M. Schier, H. P. Schmalzl, and T. Bertolini. (2008). eBooster design and performance of a innovative electrically driven charging system [Online]. Available: http://www.turbos.bwauto.com/files/library/bwtslibrary 138 325.pdf

[10] S. Kang, S. J. J. Lee, and F. B. Prinz, "Size does matter: The pros and cons of miniaturization," ABB Rev., vol. 2, no. 2, pp. 54–62, 2002.

[11] P. Tsao, M. Senesky, and S. R. Sanders, "An integrated flywheel energy storage system with homopolar inductor motor/generator and high frequency drive," IEEE Trans. Ind. Appl., vol. 39, no. 6, pp. 1710–1725, Nov./Dec. 2003.

[12] W. Wang, "Design of high speed flywheel motor/generator for aerospace applications," Ph.D. dissertation, Pennsylvania State Univ., Philadelphia, 2004.

[13] C. Zwyssig, J. W. Kolar, and S. D. Round, "Megaspeed Drive Systems: Pushing Beyond 1 Million r/min," IEEE/ASME Transactions on Mechatronics, vol. 14, pp. 564-574, 2009.

[14] A. Binder and T. Schneider, "High-speed inverter-fed AC drives," presented at the Int. Aegean Conf. Electr. Mach. Power Electron. (ELECTROMOTION 2007), Bodrum, Turkey, Sep. 10–12.

[15] U. Kafader and J. Schulze, "Similarity relations in electromagnetic motors—Limitations and consequences for the design of small dc motors," in Proc. 9th Int. Conf. New Actuators, ACTUATOR 2004, Bremen, Germany, Jun. 14–16, pp. 309–312.

[16] H. Hayashi, K. Nakamura, A. Chiba, T. Fukao, K. Tungpimolrut, and D. G. Dorrell, “Efficiency improvements of switched reluctance motors with high-quality iron steel and enhanced conductor slot fill,” IEEE Trans. Energy Convers., vol. 24, no. 4, pp. 819–825, Dec. 2009.

[17] C. Zwyssig, S. D. Round, and J. W. Kolar, “Power electronics interface for a 100 W, 500000 rpm gas turbine portable power unit,” in Proc. Appl. Power Electron. Conf., Dallas, TX, Mar. 19–23, 2006, pp. 283–289.

[18] H. Kanebako and Y. Okada, “New design of hybrid-type self-bearing motor for small, high-speed spindle,” IEEE/ASME Trans. Mechatronics, vol. 8, no. 1, pp. 111–119, Mar. 2003.

[19] B. Schneider, M. Bruderer, D. Dyntar, C. Zwyssig, M. Diener, K. Boulouchos, R. S. Abhari, L. Guzzella, and J. W. Kolar, “Ultra-high energy-density converter for portable power,” in Proc. Int. Workshop Micro Nanotechnol. Power Generation Energy Convers. Appl., Tokyo, Japan, Nov. 28–30, 2005, pp. 81–84.

[20] A. Mitra and A. Emadi, "On the suitability of large switched reluctance machines for propulsion applications," in Transportation Electrification Conference and Expo (ITEC), 2012 IEEE, 2012, pp. 1-5.

[21] T. Finken, M. Felden, and K. Hameyer, "Comparison and design of different electrical machine types regarding their applicability in hybrid electrical vehicles," in Electrical Machines, 2008. ICEM 2008. 18th International Conference on, 2008, pp. 1-5.

[22] K. Xiaoguang, W. Fengxiang, and X. Junqiang, "Temperature rise calculation of high speed PM machine based on thermal-circuit method and 3D fluid field method," in Electrical Machines and Systems (ICEMS), 2011 International Conference on, 2011, pp. 1-5.

[23] M. Centner, R. Hanitsch, and U. Schafer, "Comparison of high-speed induction motors employing cobalt-iron and silicon electrical steel," in Electrical Machines, 2008. ICEM 2008. 18th International Conference on, 2008, pp. 1-6.

[24] Y. Zhang, P. Pillay, M. Ibrahim, and M.-C. Cheng, "Magnetic Characteristics and Core Losses in Machine Laminations: High-Frequency Loss Prediction From Low-Frequency Measurements," IEEE Transactions on Industry Applications, vol. 48, pp. 623-629, 2012.

[25] L. T. Mthombeni and P. Pillay, "Core Losses in Motor Laminations Exposed to High-Frequency or Nonsinusoidal Excitation," IEEE Transactions on Industry Applications, vol. 40, pp. 1325-1332, 2004.

[26] M. A. Rahman, A. Chiba, and T. Fukao, "Super high speed electrical machines - summary," in Power Engineering Society General Meeting, 2004. IEEE, 2004, pp. 1272-1275 Vol.2.

[27] J. Dang, Ronald G. Harley, and ect. , “Electromagnetic design considerations for a 50,000 rpm 1kW Switched Reluctance Machine using a flux bridge”, IEEE International Electric Machines and Drives Conference (IEMDC), May 2013, pp. 325-331

[28] W. Li, H. Qiu, X. Zhang, J. Cao, and R. Yi, "Analyses on Electromagnetic and Temperature Field of Super High Speed Permanent Magnet Generator with Different Material Sleeves," IEEE Transactions on Industrial Electronics, vol. PP, pp. 1-1, 2013.

[29] J. Kunz, C. Siwei, D. Yao, J. R. Mayor, R. G. Harley, and T. G. Habetler, "Design of a 750,000 rpm switched reluctance motor for micro machining," in Energy Conversion Congress and Exposition (ECCE), 2010 IEEE, 2010, pp. 3986-3992.

[30] J. Oyama, T. Higuchi, T. Abe, K. Shigematsu, and R. Moriguchi, "The development of small size ultra-high speed drive system," in Proc. Power Convers. Conf., Nagoya, Japan, Apr. 2007, pp. 1571–1576.

[31] (2008). [Online]. Available: http://www.calnetix.com/highspeed.cfm

[32] A. H. Epstein, "Millimeter-scale, MEMS gas turbine engines," in Proc. ASME Turbo Expo., Atlanta, GA, Jun. 2003, pp. 1–28.

[33] S. Das, D. P. Arnold, I. Zana, J. W. Park, M. G. Allen, and J. H. Lang, "Microfabricated high-speed axial-flux multi-watt permanent magnet generators—Part I: Modeling," J. Microelectromech. Syst., vol. 15, no. 5, pp. 1330–1350, Oct. 2006.

[34] D. P. Arnold, S. Das, J. W. Park, I. Zana, J. H. Lang, and M. G. Allen, "Micro-fabricated high-speed axial-flux multi-watt permanent-magnet generators—Part II: Design, fabrication, and testing," J. Microelectromech. Syst., vol. 15, no. 5, pp. 1351–1363, Oct. 2006.

[35] D. E. Hesmondhalgh and D. Tipping, “Design high-speed permanent magnet motor,” in Proc. IEE Colloq. Permanent MagnetMach., Jun. 15, 1988, pp. 6-1–6-2.

[36] (2008). [Online]. Available: http://www.ate-system.de/

[37] J. R. Bumpy, E. S. Spooner, J. Carter, H. Tennant, G. G. Mego, G. Dellora, W. Gstrein, H. Sutter, and J. Wagner, “Electrical machines for use in electrically assisted turbochargers,” in Proc. Power Electron., Mach. Drives Conf., Apr. 2004, vol. 1, pp. 344–349.

[38] C. Zwyssig, S. D. Round, and J. W. Kolar, “Analytical and experimental investigation of a low torque, ultra-high speed drive system,” in Proc. IEEE Ind. Appl. Conf. 2006, Tampa, FL, Oct. 8–12, vol. 3, pp. 1507–1513.

[39] W. Sung Hong, C. Jaehoon, and L. Ju, "Windage Loss Reduction of High-Speed SRM Using Rotor Magnetic Saturation," Magnetics, IEEE Transactions on, vol. 44, pp. 4147-4150, 2008.

[40] D. Gerada, A. Mebarki, N. L. Brown, H. Zhang, and C. Gerada, “Design, modelling and testing of a high speed induction machine drive,” in Proc. ECCE, Sep. 2012, pp. 4649–4655

[41] J.M. Yon, P.H. Mello, R. Wrobel, J.D. Booker, S.G. Burrow, “Analysis of Semipermeable Containment Sleeve Technology for High Speed Permanent Magnet Machines”, IEEE Transactions on Energy Conversion, 2012, vol. 27, issue 3, pp. 646 – 653.

[42] A. Binder, T. Schneider, and M. Klohr, “Fixation of buried and surface-mounted magnets in high-speed permanent-magnet synchronous machines,” IEEE Trans. Ind. Appl., vol. 42, no. 4, pp. 1031–1037, 2006.

[43] A. Tuysuz, A. Looser, J. W. Kolar, and C. Zwyssig, "Novel miniature motors with lateral stator for a wide torque and speed range," in IECON 2010 - 36th Annual Conference on IEEE Industrial Electronics Society, 2010, pp. 1741-1747.

[44] S. H. Mao and M. C. Tsai, “A novel switched reluctance motor with Ccore stators,” IEEE Trans. Magn., vol. 41, no. 12, pp. 4413–4420, Dec. 2005.

[45] D.-H. Lee, T. H. Pham, and J.-W. Ahn, "Design and Operation Characteristics of Four-Two Pole High-Speed SRM for Torque Ripple Reduction," IEEE Transactions on Industrial Electronics, vol. 60, pp. 3637-3643, 2013.

[46] L. Dong-Hee, K. Huynh Khac Minh, and A. Jin-Woo, "The performance of 2-phase high speed SRM with variable air-gap rotor poles for blower system," in Electrical Machines and Systems (ICEMS), 2010 International Conference on, 2010, pp. 1595-1598.

[47] H. Y. Yang, Y. C. Lim, and H. C. Kim, “Acoustic noise/vibration reduction of a single-phase SRM using skewed stator and rotor,” IEEE Trans. Ind. Electron., vol. 60, no. 10, pp. 4292-4300, Oct. 2013.

[48] T.J.E. Miller, "Switched Reluctance Motors and Their Control, " Clarendon Press, Oxford, 1993

[49] R. Krishnan, "Switched Reluctance Motor Drives: Modeling, Simulation, Analysis, Design, and Applications," *CRC Press,* 2001.

[50] Vijayraghavan, "Design of Switched Reluctance Motors and Development of a Universal Controller for Switched Reluctance and Permanent Magnet Brushless DC Motor Drives, " Ph.d Dissertation, Virginia Tech, 2001

[51] T.J.E. Miller and D.A. Staton, "Electric Machine Design using SPEED and Motor-CAD," Motor Design, 2012

[52] Yao Duan, "Method for design and optimization of surface mount permanent magnet machines and induction machines", Ph.d Dissertation, Georgia Tech, 2010

[53] Kra, x, henbu, x, D. hl, C. Zwyssig, et al., "A miniature, 500 000 rpm, electrically driven turbocompressor," in Energy Conversion Congress and Exposition, 2009. ECCE 2009. IEEE, 2009, pp. 3602-3608.

[54] C. Zwyssig, M. Duerr, D. Hassler, and J. W. Kolar, "An Ultra-High-Speed, 500000 rpm, 1 kW Electrical Drive System," in Power Conversion Conference - Nagoya, 2007. PCC '07, 2007, pp. 1577-1583.

[55] C. Wildmann, T. Nussbaumer, and J. W. Kolar, "10 Mrpm spinning ball motor: Preparing the next generation of ultra-high speed drive systems," in Power Electronics Conference (IPEC), 2010 International, 2010, pp. 278-283.

[56] C. Zwyssig, S. D. Round, and J. W. Kolar, "An Ultrahigh-Speed, Low Power Electrical Drive System," IEEE Transactions on Industrial Electronics, vol. 55, pp. 577-585, 2008.

[57] C. Zwyssig and J. W. Kolar, "Design considerations and experimental results of a 100 W, 500 000 rpm electrical generator," J. Micromech. Microeng, vol. 16, pp. S297–S302, Sep. 2006.

[58] S. Kozuka, N. Tanabe, J. Asama, and A. Chiba, "Basic characteristics of 150,000r/min switched reluctance motor drive," in Power and Energy Society General Meeting - Conversion and Delivery of Electrical Energy in the 21st Century, 2008 IEEE, 2008, pp. 1-4.

[59] F. Saint-Eve, C. Sauvey, and G. Abba, "A 100kHz-2kW converter for switched reluctance rnotor used in high speed machining applications," in IEEE Industrial Electronics, IECON 2006 - 32nd Annual Conference on, 2006, pp. 2274-2279.

[60] Y. K. Choi, H. S. Yoon, and C. S. Koh, "Pole-Shape Optimization of a Switched-Reluctance Motor for Torque Ripple Reduction," IEEE Transactions on Magnetics, vol. 43, pp. 1797-1800, 2007.

[61] P. C. Desai, M. Krishnamurthy, N. Schofield, and A. Emadi, "Design and performance evaluation of a novel 6/10 Switched Reluctance Machine," in Electric Machines and Drives Conference, 2009. IEMDC '09. IEEE International, 2009, pp. 755-762.

[62] A. Chiba, Y. Takano, M. Takeno, T. Imakawa, N. Hoshi, M. Takemoto, et al., "Torque Density and Efficiency Improvements of a Switched Reluctance Motor Without Rare-Earth Material for Hybrid Vehicles," IEEE Transactions on Industry Applications, vol. 47, pp. 1240-1246, 2011

[63] K. Kiyota, H. Sugimoto, and A. Chiba, "Comparison of energy consumption of SRM and IPMSM in automotive driving schedules," in Energy Conversion Congress and Exposition (ECCE), 2012 IEEE, 2012, pp. 853-860

[64] Yao Duan and Harley, R.G., "A Novel Method for Multi-objective Design and Optimization of Three Phase Induction Machine", IEEE Transactions on Industry Applications, vol. 47, No. 4, pp. 1707-1715, 2011

[65] Arumugam, R., Lowther, D.A., Krishnan, R. and Lindsay, J.F., "Magnetic field analysis of switched reluctance motor using 2-dimensional finite element model", IEEE Transactions on Magnetics, Vol. MAG-21, No. 5, pp. 1883-1885, 1985

[66] G. Munteanu, A. Binder, and T. Schneider, "Development and test of high-speed bearingless pm synchronous machines," Elektrotechnik and Informationstechnik, 2011.

[67] M. Mekhiche, S. Nichols, J. Kirtley, J. Young, D. Boudreau, and R. Jodoin, "High-speed, high-power density pmsm drive for fuel cell powered hev application," in Electric Machines and Drives Conference, 2001. IEMDC 2001. IEEE International, 2001, pp. 658 –663.

[68] H. Cha, K. T. Vu, S. Choi, and B. moon Han, "Ultra fast pmsm drive for turbo-blower application," in Electrical Machines and Systems, 2008. ICEMS 2008. International Conference on, oct. 2008, pp. 1412 –1416.

[69] T. Noguchi, Y. Takata, Y. Yamashita, and S. Ibaraki, "160,000-r/min, 2.7-kw electric drive of supercharger for automobiles," in Power Electronics and Drives

Systems, 2005. PEDS 2005. International Conference on, vol. 2, 0-0 2005, pp. 1380 – 1385.

[70] R. Lateb, J. Enon, and L. Durantay, “High speed, high power electrical induction motor technologies for integrated compressors,” in Electrical Machines and Systems, 2009. ICEMS 2009. International Conference on, nov. 2009, pp. 1 –5.

[71] J.-W. Ahn, H. K. M. Khoi, and D.-H. Lee, “Design and analysis of high speed 4/2 srms for an air-blower,” in Industrial Electronics (ISIE), 2010 IEEE International Symposium on, july 2010, pp. 1242 –1246.

[72] A. Boglietti, A. Cavagnino, A. Tenconi, and S. Vaschetto, “Key design aspects of electrical machines for high-speed spindle applications,” in IECON 2010 - 36th Annual Conference on IEEE Industrial Electronics Society, nov. 2010, pp. 1735 – 1740.

[73] F. Soares and P. Costa Branco, “Simulation of a 6/4 switched reluctance motor based on matlab/simulink environment,” Aerospace and Electronic Systems, IEEE Transactions on, vol. 37, no. 3, pp. 989 – 1009, jul 2001.

[74] F. Saint-Eve, C. Sauvey, and G. Abba, “A 100khz-2kw converter for switched reluctance rnotor used in high speed machining applications,” in IEEE Industrial Electronics, IECON 2006 - 32nd Annual Conference on, nov. 2006, pp. 2274 –2279.

[75] TI, Switched Reluctance Motor Control Basic Operaion and Example uing the TMS320F240, www.ti.com, 2000.

[76] P. C. Desai, M. Krishnamurthy, N. Schofield, and A. Emadi, "Novel Switched Reluctance Machine Configuration With Higher Number of Rotor Poles Than Stator Poles: Concept to Implementation," IEEE Transactions on Industrial Electronics, vol. 57, pp. 649-659, Feb 2010.

[77] B. Bilgin, A. Emadi, and M. Krishnamurthy, "Switched reluctance generator with higher number of rotor poles than stator poles," in Transportation Electrification Conference and Expo (ITEC), 2012 IEEE, 2012, pp. 1-6.

[78] T. Genda and H. Dohmeki, "Characteristics of 4/2 Switched Reluctance Motor for a high speed drive by the excitation angle," in Proc. 2009 International Conference on Electrical Machines and Systems, pp. 1-6.

[79] C. Yong Kwon, Y. Hee Sung, and K. Chang Seop, "Pole-Shape Optimization of a Switched-Reluctance Motor for Torque Ripple Reduction," IEEE Transactions on Magnetics, vol. 43, pp. 1797-1800, 2007.

[80] Yao Duan and Ionel, D.M., “A Review of Recent Developments in Electrical Machine Design Optimization Methods With a Permanent-Magnet Synchronous Motor Benchmark Study”, IEEE Transactions on Industry Applications, vol. 49, No. 3, pp. 1268-1275, 2013

[82] Y. Sozer, I. Husain, D.A. Torrey, “Advanced Control Techniques for Switched Reluctance Machine Drives in Emerging Applications”, IEEE Energy Conversion Congress and Exposition (ECCE), Sep 2013, pp. 3776-3783.

[83] J. Dang, J.R. Mayor, S.S. Semidey, R. Harley, T. Habetler, J. Restrepo, “Practical Considerations for the Design and Construction of a High Speed SRM with a Flux-

bridge Rotor”, IEEE Energy Conversion Congress and Exposition (ECCE), 2014, pp. 3842-3849.

[84] P. C. Desai, M. Krishnamurthy, N. Schofield, and A. Emadi, "Switched Reluctance Machines with higher rotor poles than stator poles for improved output torque characteristics," in Industrial Electronics, 2009. IECON '09. 35th Annual Conference of IEEE, 2009, pp. 1338-1343.

[85] M. Abbasian, B. Fahimi, and M. Moallem, "High torque double-stator switched reluctance machine for electric vehicle propulsion," in Vehicle Power and Propulsion Conference (VPPC), 2010 IEEE, 2010, pp. 1-5.

[86] B. Fahimi, A. Emadi, and R. B. Sepe, "A Switched Reluctance Machine-Based Starter/Alternator for More Electric Cars," IEEE Transactions on Energy Conversion, vol. 19, pp. 116-124, 2004.

[87] K. Kiyota and A. Chiba, "Design of Switched Reluctance Motor Competitive to 60-kW IPMSM in Third-Generation Hybrid Electric Vehicle," IEEE Transactions on Industry Applications, vol. 48, pp. 2303-2309, 2012.

[88] M. Takeno, K. Kiyota, Y. Murakami, A. Chiba, N. Hoshi, M. Takemoto, et al., "Test results of high torque and high efficiency SRMs designed for 50kW Hybrid Electric Vehicle," in Power and Energy Society General Meeting, 2012 IEEE, 2012, pp. 1-2.

[89] Y. Takano, T. Maeda, M. Takeno, A. Chiba, N. Hoshi, M. Takemoto, et al., "Operating area of a Switched Reluctance Motor with continuous current operation," in Power and Energy Society General Meeting, 2010 IEEE, 2010, pp. 1-4.

[90] B. Fahimi, A. Emadi, and R. B. Sepe, Jr., "Four-quadrant position sensorless control in SRM drives over the entire speed range," IEEE Transactions on Power Electronics, vol. 20, pp. 154-163, 2005.

[91] G. Gallegos-Lopez, P. C. Kjaer, and T. J. E. Miller, "A new sensorless method for switched reluctance motor drives," IEEE Transactions on Industry Applications, vol. 34, pp. 832-840, 1998

VITA

Jie Dang was born in Chongqing, China in 1986. He received a Bachelor of Science degree from Tsinghua University, Beijing China, in 2009 and a Master of Engineering degree from Georgia Institute of Technology, Atlanta Georgia, USA, in 2011, both in Electrical Engineering.

Since August 2010, he has been working on the design and optimization of electrical machines, as a Graduate Research Assistant in the electric power group of Georgia Institute of Technology. In 2013 summer, he worked in the advanced electrification center, Ford Motor, Dearborn MI, as a summer intern. In 2014 summer, he worked in the upstream research company, ExxonMobil, Houston TX, as a summer intern.

His research interests include design and control of electric machines for different applications.